



# ScuDo

Scuola di Dottorato ~ Doctoral School  
WHAT YOU ARE, TAKES YOU FAR

Doctoral Dissertation  
Doctoral Program in Materials science and technology (30<sup>th</sup> Cycle)

# **Oxidation resistance of Ti-Al intermetallic alloys and protection by ceramic coating**

By

**Oxana Ostrovskaya**

\*\*\*\*\*

**Supervisor:**

Prof. Claudio Francesco Badini

**Doctoral Examination Committee:**

Prof. La Vecchia Marina, Referee, Università di Brescia

Prof. Vedani Maurizio, Referee, Politecnico di Milano

Prof. Luca Lusvarghi, Referee, Università Modena e Reggio Emilia

Prof. Graziano Ubertalli, Referee, Politecnico di Torino

Prof. Federico Smeacetto, Referee, Politecnico di Torino

Politecnico di Torino  
2018

## Declaration

I hereby declare that, the contents and organization of this dissertation constitute my own original work and does not compromise in any way the rights of third parties, including those relating to the security of personal data.

Oxana Ostrovskaya

2018

\* This dissertation is presented in partial fulfilment of the requirements for **Ph.D. degree** in the Graduate School of Politecnico di Torino (ScuDo).

*I would like to dedicate this thesis to my son*

## **Acknowledgment**

And I would like to acknowledge: Claudio Badini Francesco, Sara Biamino, Giorgio Baudana and Elisa Padovano (Department of Applied Science and Technology, Politecnico di Torino, Italy); Monica Fabrizio and Enrico Miorin (National Research Council of Italy), Pierluca Boffa Pedro.

## **Abstract**

In recent years, TiAl intermetallic alloys have been widely used in aircraft and automotive industry. With the aim of improving the mechanical behavior and the oxidation resistance at high temperature of the TiAl alloys firstly designed, new intermetallic alloys of second and third generation have been successively developed.

In this work, the oxidation resistance in air of four intermetallic alloys of second generation (Ti-48Al-2Cr-2Nb) and third generation (Ti-48Al-2Nb-0.7Cr-0.3Si, Ti-43.5Al-4Nb-1Mo and Ti-47Al-2Cr-8Nb) was investigated by TGA equipment under isothermal conditions in the range of 800-1000 °C. These alloys were cut from the core of bars, previously processed by Electron Beam Melting and successively heat-treated. The composition of the oxide layers was investigated by XRD, SEM-EDS and XPS. Each alloy showed different oxidation behavior at high temperatures. Layer exfoliation or spallation was observed for many samples, but at very different temperatures for the different alloys. When spallation did not happen in a significant extent the oxide layers grew according to a parabolic law. The kinetic rate constants and the activation energies were calculated. These kinetic parameters allowed to assess a rank of oxidation resistance, which can be correlated with the composition of the alloys.

In order to improve the oxidation resistance of Ti-48Al-2Cr-2Nb, ceramic nitride coatings were deposited by a High Power Impulse Magnetron Sputtering (HiPIMS) method. Differently engineered TiAlN and TaAlN protective films were processed and their performances compared. Samples were submitted to thermal cycling under oxidizing atmosphere up to 850° C (40 cycles) and 950°C (100 and 200 cycles), at high heating and cooling rates. For this purpose, a burner rig able to simulate the operating conditions of the different stages of turbine engines was used.

The microstructure and composition of samples before and after oxidation were investigated by several techniques: microscopy (optical and SEM-EDS), X-ray photoelectron spectrometry (XPS) and X-ray diffraction (XRD).

All the TiAlN coatings differently processed provided a remarkable improvement of oxidation resistance. Good adhesion properties were observed even after repeated thermal shocks. HiPIMS pretreatments of the substrate surfaces, performed before the coating deposition, significantly affected the oxidation rate, the oxide layer composition and the coating/substrate adhesion.

The oxide layers formed on the sample surface showed different thickness, depending on the presence of the protective coating and the processing path adopted for its deposition. The nitride coatings appreciably enhanced the oxidation resistance and sustained repeated thermal shocks without showing damage or spallation. Differently TaAlN coating did not improve the oxidation resistance of TiAl substrate.



# Contents

|  |    |
|--|----|
| 1. Introduction.....   | 1  |
| 1.1 TiAl intermetallic alloys.....   | 3  |
| 1.1.1 Chemical composition of TiAl alloys and phases present in their<br>microstructure..... | 5  |
| 1.1.2 Processing and heat treatments of TiAl intermetallic alloys .....                      | 8  |
| 1.1.3 Mechanical and oxidation resistance of TiAl intermetallic alloys..                     | 22 |
| 1.2 Oxidation protection: surface modification and coating deposition.....                   | 29 |
| 1.2.1 Surface modification and surface alloying .....  | 29 |
| 1.2.2 Aluminizing .....  | 32 |
| 1.2.3 MCrAlY overlay coatings.....   | 34 |
| 1.2.4 Thermal barrier coatings (TBC) .....   | 37 |
| 1.2.5 Metal-based coatings specifically designed for Ti-Al alloys.....                       | 40 |
| 1.2.6 Titanium and aluminium based nitride coatings.....                                     | 45 |
| 1.2.7 Tantalum and aluminium based nitride coatings .....                                    | 48 |
| 1.2.8 Ceramic oxide-based coatings .....   | 53 |
| 2. Experimental part: materials and methods.....   | 55 |
| 2.1 TiAl intermetallic alloys under investigation .....                                      | 55 |
| 2.2 Ceramic coating deposition .....   | 60 |
| 2.3 Techniques of characterization.....  | 72 |
| 2.3.1 X-ray diffraction .....  | 72 |
| 2.3.2 Optical microscopy .....   | 74 |

|  |     |
|--|-----|
| 2.3.3 Scanning Electron Microscopy and Energy Dispersion Spectroscopy .....                        | 75  |
| 2.3.4 X-ray photoelectron spectroscopy .....   | 78  |
| 2.3.5 Thermogravimetric analysis .....   | 81  |
| 2.3.6 Burner rig test .....  | 83  |
| 2.3.7 Scratch test .....   | 84  |
| 3. Experimental part: results .....  | 86  |
| 3.1 Oxidation kinetics of TiAl alloys .....  | 86  |
| 3.2 Oxidation of coated and uncoated intermetallics .....  | 101 |
| 3.2.1 Low-cycling oxidation at 850° C and 950° C of TiAlN coated and uncoated intermetallics ..... | 101 |
| 3.2.2 Long-term cycling oxidation at 950° C of TiAlN coated and uncoated intermetallics .....      | 120 |
| 3.2.3 Oxidation behaviour of TaAlN coated 48-2-2 intermetallic alloy                               | 134 |
| 4. Conclusions.....  | 147 |
| 4.1 Oxidation behaviour of Ti-Al intermetallic alloys .....  | 147 |
| 4.2 TiAlN ceramic coatings.....  | 148 |
| 4.3 TaAlN ceramic coatings .....   | 150 |
| 5. References.....   | 152 |
| References .....   | 152 |



# List of Figures

|   |    |
|---|----|
| Figure 1: Design process of gas turbine engine: estimated temperature, velocity and pressure [1].....   | 1  |
| Figure 2: Expected performance of structural alloys developed for aircraft: temperature and speed [4].....  | 2  |
| Figure 3: BR 715 aero engine. High Pressure Compressor (HPC) and Low Pressure Turbine (LPT) [6].....  | 4  |
| Figure 4: Titanium aluminide turbocharger wheels in service [4]. ....   | 5  |
| Figure 5: Ti-Al phase diagram [4].....  | 6  |
| Figure 6: Cristal structures: a) $\gamma$ -TiAl has L1 <sub>0</sub> structure (ordered face centered tetragonal), and b) $\alpha_2$ -Ti <sub>3</sub> Al has DO <sub>19</sub> structure (hexagonal closed packed) [4]. ...   | 6  |
| Figure 7: Section of the binary Ti–Al-phase diagram (continuous lines). T $\alpha$ : $\alpha$ -transus temperature; Teu: eutectoid temperature. Two vertical dotted lines marked the range of the technical $\gamma$ -TiAl based alloys (45-48 % at. of Al). The broken lines show the effect of Nb (8 at.%) on the position of the phase field regions [17]..... | 7  |
| Figure 8: Processing of TiAl based alloys on an industrial scale [17].....  | 9  |
| Figure 9: Schematic EBM process and technical data for Arcam A2 machine [21].....   | 11 |
| Figure 10: Microstructures of TiAl-based alloys after heat treatment [17]. ...  | 12 |
| Figure 11 : CCT diagram of a Ti-46Al-9Nb alloy and different microstructures formed at specific cooling rates (FC-furnace cooling, AC-air cooling, OC-oil cooling, WC-water cooling) [17].....  | 14 |
| Figure 12: Microstructure of Ti-45Al-(8-9)Nb-(W,B,Y) (at.%): a) SM ingot before HIP, b) SM ingot after HIP, c) PAM ingot [23].....  | 15 |
| Figure 13: Ti-Al quasi phase diagrams with Nb (8% at.) and Nb (10% at.) [23]. ....  | 16 |
| Figure 14: SEM photographs of Ti-45Al-10Nb microstructure: a) Fully Lamellar, b) Nearly Lamellar, c) degraded Fully Lamellar (DFL) [24]. ....   | 16 |

Figure 15: The microstructure of Ti-45Al-2Cr-8Nb alloy obtained by heat treatment at different temperatures in the vicinity of  $T_{\alpha} = 1295$  °C. The yellow dotted line indicates the border (2mm) [21]. ..... 17

Figure 16: SEM image (BSE mode) of TNM microstructure: (a) centrifugal cast Ti-43.5Al-4Nb-1Mo-0.1B, (b) cast and HIPed Ti-43.5Al-4Nb-1Mo-0.1B, (c) cast and HIPed Ti-43.5Al-4Nb-1Mo alloy without boron, (d) HIPed Ti-43.9Al-4Nb-0.95Mo-0.1B gas-atomized powder, (e) Ti-43.5Al-4Nb-1Mo-0.1B +0.5 at.% C showing microstructure different from a) because peritectic solidification, (f) Ti-43.5Al-4Nb-1Mo-0.1B +0.5 at.% C,  $\beta$  solidification due adding high content of Mo. The  $\gamma$  phase appears grey to dark and  $\alpha_2$  light grey,  $\beta$  exhibits the brightest contrast [17]...... 18

Figure 17: Microstructure of Ti-48Al-2Cr-2Nb alloy: (a) after EBM processing, on the left of the picture typical spherical defect inside is present; (b) after EBM processing; (c) after EBM and HIPing; (d) after EBM, HIPing and thermal treatment for 2 h at 1320 °C [18]...... 20

Figure 18: Optical microscopy images of Ti-48Al-2Nb-0.7Cr-0.3Si microstructure: (a) equiaxed morphology after EBM, the arrow indicates the building direction, (b) duplex morphology after HT at 1300°C for 2 h, (c) duplex morphology after HT at 1350°C for 2 h, (d) near lamellar morphology after HT at 1360°C for 2 h, (e) fully lamellar morphology after HT at 1365°C for 2 h, (f) fully lamellar morphology after HT at 1370°C for 2 h with bigger lamellar grains of  $\gamma/\alpha_2$  [19]...... 21

Figure 19: Dependence of mechanical properties (fracture toughness, strength, ductility, impact resistance, creep resistance) and grain size on the microstructure (Near Gamma, Duplex, Nearly lamellar, Fully Lamellar) [4]. ..... 23

Figure 20: Yield strengths of TiAl-based alloys at room temperature and at 650°C [3]...... 24

Figure 21: Oxidation behaviour of coated and uncoated TiAl alloys [3]...... 25

Figure 22: Wagner's parabolic model. .... 28

Figure 23: SEM micrograph of Si-based coating deposited on TiAl alloy: (a) after 100h at 1000°C ( $10^{-6}$  mbar), (b) and (c) after 1000 cycles at 950 °C in air [38]. ..... 30

Figure 24: SEM cross section of  $\gamma$ -TiAl alloy aluminised at 800 °C for 5 h in a low Al activity pack: a) as processed, b) after 10h isothermal oxidation at 900 °C and c) after long term oxidation of 100h at 900°C [59]...... 33

|  |    |
|--|----|
| Figure 25: The oxidation process of aluminised $\gamma$ -TiAl alloy (at 800°C for 3 hours): (a) initial oxidation (b) morphology of the layer after prolonged oxidation [57].....  | 34 |
| Figure 26: CoCrAlY coated $\gamma$ -TiAl after 100 cycles at 1000°C: (a) surface morphology, (b) cross-section microstructure [65]. .....  | 35 |
| Figure 27: SEM (a) as-processed NiCrAlY coated TiAl-4Nb-3Mn (% at.) alloy, (b) oxidized after 10 cycles and (c) 120 cycles, (d) 460 cycles (e) 800 cycles at 1000°C [69].....  | 36 |
| Figure 28: SEM/EDS analysis of NiCrAlY coating deposited on TiAl-4Nb-3Mn (at.%) alloy during cycling oxidation at 1000°C after 800 cycles [69].....  | 36 |
| Figure 29: Diffusion processes occurring in NiCrAlY coated TiAl-4Nb-3Mn (% at.) alloy during cycling oxidation at 1000°C [70]. .....   | 37 |
| Figure 30: The cross-section of thermal barrier coating in a first stage blade [71].....   | 38 |
| Figure 31: SEM images of cross-section of TBC/ $\gamma$ -TiAl alloy (in up of the figure - complex system before oxidation, in down- after oxidation in air at 900 °C): a) aluminized BC, b) substrate pre-oxidation in air, c) substrate pre-oxidation in oxygen [72].....  | 39 |
| Figure 32: Cross section of Ti-50Al-10Cr (at.%) coating deposited on Ti-50Al (at.%): a) after exothermal oxidation-1000 h of at 900° C, b) after 100 cycles at 1000°C [65].....  | 41 |
| Figure 33: SEM images of Ti-51Al-12Cr (% at.) coating deposited on Ti-45Al-8Nb (% at.): (a) after 10 cycles at 900°C in air, (b) after 120 cycles at 900°C in air, (c) after 120 cycles at 950°C in air, (d) after 700 cycles at 900°C in air [6]. .....   | 43 |
| Figure 34: Al-21Ti-23Cr (% at.) coating deposited on Ti-48Al (% at.) alloy after isothermal oxidation at 1000°C: (a) after 2h, (b) after 20 h, (c) after 50 h, (d) after 100 h [78]. .....   | 44 |
| Figure 35: XRD patterns of the (Ti-Al/Ti-Al-N) <sub>n</sub> multilayer coatings deposited on silicon (100): black pattern - 60 multilayer system with a period of 42 nm, and red pattern -100 multilayer system with a period of 25 nm. The positions of TiAlN peaks (JCPDF 00-037-1140), TiAl (JCPDF 00-005-0678) and AlN (JCPDF 00-003-1144) are indicated by dash lines [87]..... | 46 |
| Figure 36: XPS peak fitting for a TiAlN coating: (a) Ti 2p, (b) N 1s, (c) Al 2p and (d) O 1s [88].....   | 47 |

|   |    |
|---|----|
| Figure 37: Schematic presentation of TaAlN deposition on silicon substrate by reactive magnetron co-sputtering [96].  | 49 |
| Figure 38: XRD patterns of as-deposited coatings: (a) Ta <sub>42</sub> Al <sub>8</sub> N <sub>50</sub> , (b) Ta <sub>39</sub> Al <sub>11</sub> N <sub>50</sub> , (c) Ta <sub>35</sub> Al <sub>15</sub> N <sub>50</sub> , and (d) Ta <sub>24</sub> Al <sub>28</sub> N <sub>48</sub> [96].  | 50 |
| Figure 39: SEM cross-section of as-deposited coatings: (a) Ta <sub>42</sub> Al <sub>8</sub> N <sub>50</sub> , (b) Ta <sub>39</sub> Al <sub>11</sub> N <sub>50</sub> , (c) Ta <sub>35</sub> Al <sub>15</sub> N <sub>50</sub> , and (d) Ta <sub>24</sub> Al <sub>28</sub> N <sub>48</sub> [96].   | 51 |
| Figure 40: XRD coatings before and after isothermal oxidation at 600°C, 700°C, 800°C: (up) Ta <sub>35</sub> Al <sub>15</sub> N <sub>50</sub> , and (down) Ta <sub>24</sub> Al <sub>28</sub> N <sub>48</sub> [96].   | 52 |
| Figure 41: Cross-sectional SEM images of Ta-Al-N coatings after isothermal oxidation at 700°C: (a) Ta <sub>42</sub> Al <sub>8</sub> N <sub>50</sub> , (b) Ta <sub>39</sub> Al <sub>11</sub> N <sub>50</sub> , (c) Ta <sub>35</sub> Al <sub>15</sub> N <sub>50</sub> , and (d) Ta <sub>35</sub> Al <sub>15</sub> N <sub>50</sub> [96]. | 53 |
| Figure 42: Microstructures of as-EBM processed TiAl alloys after HIP treatment: Ti-48Al-2Cr-2Nb (48-2-2), Ti-48Al-2Nb-0.7Cr-0.3Si (RNT-650), Ti-43.5Al-4Nb-1Mo (TNM) and Ti-47Al-2Cr-8Nb (HNb)  | 57 |
| Figure 43: GERO furnace   | 58 |
| Figure 44: Optical microscopy images: (a) a fully lamellar microstructure of Ti-48Al-2Cr-2Nb, a near lamellar microstructure of (b) Ti-47Al-2Cr-8Nb and (c) Ti-48Al-2Nb-0.7Cr-0.3Si. SEM image (d): a near lamellar microstructure of Ti-43.5Al-4Nb-1Mo [102].  | 59 |
| Figure 45: Magnetron Sputtering and High Power Impulse Magnetron Sputtering schematic processes [117]   | 61 |
| Figure 46: (a) HiPIMS apparatus, (b) HiPIMS chamber, (c) Plasma Etching, (d) Reactive Deposition  | 63 |
| Figure 47: Roughness profile of TiAlN1 sample surface before coating deposition.  | 64 |
| Figure 48: Roughness profile of TiAlN2 sample surface before coating deposition.  | 65 |
| Figure 49: Roughness profile of TiAlN3 sample surface before coating deposition.  | 65 |
| Figure 50: Cross-section of TiAlN1 sample   | 67 |
| Figure 51: Cross-section of TiAlN2 sample   | 67 |
| Figure 52: Cross-section of TiAlN3 sample   | 68 |

|   |    |
|---|----|
| Figure 53: SEM images. Microstructures of TiAlN coatings (top and cross-section).....   | 69 |
| Figure 54: SEM image of TaAlN coating microstructure.....   | 71 |
| Figure 55: SEM cross-section of TaAlN coating.....  | 71 |
| Figure 56: Bragg's Law ( $2d\sin\theta = n\lambda$ , where n is a whole number of X-ray wavelengths ( $\lambda$ ), d is the spacing between crystallographic planes and $\theta$ is the incident/reflected angle) [127].....  | 72 |
| Figure 57: X'PERT PRO PW3040/60 located at politecnico di Torino (DISAT).....   | 73 |
| Figure 58: Schematic representation of X-Ray diffractometer [128] .....   | 73 |
| Figure 59: Leica DMI 5000 M optical microscope.....   | 74 |
| Figure 60: Schematic SEM apparatus [129] .....  | 76 |
| Figure 61: Schematic principle of SEM. X-ray interaction with the atoms of sample [130] .....   | 77 |
| Figure 62: The electron and X-Ray emissions from sample atoms [131].....  | 78 |
| Figure 63: XPS PHI 5000 Versa Probe apparatus: 1-Scanning x-ray source, 2-sample introduction chamber, 3-argon sputter ion gun, 4-electron energy analyser, 5-optical microscope, 6-five axis automated sample manipulator, 7- optional UHV sample preparation chambers, 8-optional C <sub>60</sub> sputter ion gun, 9-optional UV light source for UPS, 10- optional dual anode X-ray source, 11-optional electron gun for AES,12-Optional 20 keV Argon gas cluster ion gun..... | 79 |
| Figure 64: XPS schematic operating principle [132]. .....   | 80 |
| Figure 65: Electron beam interaction with sample atoms [133] .....  | 81 |
| Figure 66: Schematic Thermogravimetric apparatus Metter Toledo, comprising: 1-baffles, 2-reactive gas capillary, 3-gas outlet, 4-temperature sensors, 5-furnace heater, 6-furnace temperature sensor, 7-adjustment ring weights, 8-protective and purge gas connector, 9-thermostated balance [134].....  | 82 |
| Figure 67: Burner Rig apparatus of Politecnico di Torino (DISAT) .....  | 83 |
| Figure 68: Thermal cycling up to 950°C in Burner Rig apparatus (isothermal step lasting 3 minutes, quenching to 300 °C) .....   | 84 |
| Figure 69: Progressive Load Scratch Test [136], [137] .....   | 85 |

|   |    |
|---|----|
| Figure 70: TGA curves of TiAl alloys recorded under 50 ml/min air flow during heating from 25 to 1000 °C at 5°/min: Ti-48Al-2Cr-2Nb (green line), Ti-48Al-2Nb-0.7Cr-0.3Si (violet line), Ti-43.5Al-4Nb-1Mo (red line), and Ti-47Al-2Cr-8Nb (blue line) [102] .....  | 87 |
| Figure 71: TGA curves of Ti-48Al-2Cr-2Nb (48-2-2) alloy recorded at different temperatures (air flow 50 ml/min, isothermal treatment lasting 10 h): violet line 800 °C, green line 850 °C and red line 900 °C [102]. .....  | 88 |
| Figure 72: TGA curves of Ti-48Al-2Nb-0.7Cr-0.3Si (RNT650) alloy recorded at different temperatures (air flow 50 ml/min, isothermal treatment lasting 10 h): violet line 800 °C, green line 850 °C and red line 900 °C [102]. .....  | 88 |
| Figure 73: TGA curves of Ti-43.5Al-4Nb-1Mo (TNM) alloy recorded at different temperatures (air flow 50 ml/min, isothermal treatment lasting 10 h): green line 850 °C, red line 900 °C and blue line 950 °C [102]. .....   | 89 |
| Figure 74: TGA curves of Ti-47Al-2Cr-8Nb (HNb) alloy recorded at different temperatures (air flow 50 ml/min, isothermal treatment lasting 10 h): green line 850 °C, red line 900 °C, blue line 950 °C and yellow line 1000 °C [102]. .....  | 89 |
| Figure 75: XRD patterns of Ti-48Al-2Cr-2Nb alloy: blue spectrum= as-processed, red spectrum= oxidized at 850°C. Crystalline phases: $\Delta$ TiAl ( $\gamma$ ), $\square$ Ti <sub>3</sub> Al ( $\alpha_2$ ), $\diamond$ Al <sub>2</sub> O <sub>3</sub> ( $\alpha$ ), $\circ$ TiO <sub>2</sub> [102]. .....                                | 90 |
| Figure 76: XRD patterns of Ti-48Al-2Nb-0.7Cr-0.3Si alloy: blue spectrum= as-processed, red spectrum= oxidized at 850°C. Crystalline phases: $\Delta$ TiAl ( $\gamma$ ), $\square$ Ti <sub>3</sub> Al ( $\alpha_2$ ), $\diamond$ Al <sub>2</sub> O <sub>3</sub> ( $\alpha$ ), $\circ$ TiO <sub>2</sub> [102]. .....                        | 90 |
| Figure 77: XRD patterns of Ti-43.5Al-4Nb-1Mo alloy: blue spectrum= as-processed, red spectrum= oxidized at 900 °C. Crystalline phases: $\Delta$ TiAl ( $\gamma$ ), * TiAl ( $\beta$ ), $\square$ Ti <sub>3</sub> Al ( $\alpha_2$ ), $\diamond$ Al <sub>2</sub> O <sub>3</sub> ( $\alpha$ ), $\circ$ TiO <sub>2</sub> , + NbO [102]. ..... | 91 |
| Figure 78: XRD patterns of Ti-47Al-2Cr-8Nb alloy: blue spectrum= as-processed, red spectrum= oxidized at 950 °C. Crystalline phases: $\Delta$ TiAl ( $\gamma$ ), * TiAl ( $\beta$ ), $\square$ Ti <sub>3</sub> Al ( $\alpha_2$ ), $\diamond$ Al <sub>2</sub> O <sub>3</sub> ( $\alpha$ ), $\circ$ TiO <sub>2</sub> , + NbO [102]. .....   | 92 |
| Figure 79: TGA data (50 ml/min in air for 10 h) of Ti-48Al-2Cr-2Nb alloy fitted at different temperatures with straight lines according to a parabolic law: violet line= 800 °C, green line= 850 °C and red line= 900 °C [102]. .....   | 96 |
| Figure 80: TGA data (50 ml/min in air for 10 h) of Ti-48Al-2Nb-0.7Cr-0.3Si alloy fitted at different temperatures with straight lines according to a parabolic law: violet line= 800 °C, green line= 850 °C and red line= 900 °C [102]. .....   | 96 |

|  |     |
|--|-----|
| Figure 81: TGA data (50 ml/min in air for 10 h) of Ti-43.5Al-4Nb-1Mo alloy fitted at different temperatures with straight lines according to a parabolic law: green line= 850 °C, red line= 900 °C and blue line = 950 °C [102].....   | 97  |
| Figure 82: TGA data (50 ml/min in air for 10 h) of Ti-47Al-2Cr-8Nb alloy fitted at different temperatures with straight lines according to a parabolic law: green line= 850 °C, red line = 900 °C, blue line= 950 °C and yellow line = 1000 °C) [102].<br>.....  | 97  |
| Figure 83: Arrhenius plot for oxidation of Ti-48Al-2Cr-2Nb (green line), Ti-48Al-2Nb-0.7Cr-0.3Si (violet line), Ti-43.5Al-4Nb-1Mo (red line), and Ti-47Al-2Cr-8Nb (blue line) [102] .....  | 99  |
| Figure 84: (a) Ti-Al intermetallic alloy, dual phase microstructure (optical microscope, etching by Kroll's reagent); (b) coating surface of TiAlN1 specimen (SEM, InLens); (c) cross section of TiAlN1 sample (SEM InLens, etching with NH <sub>4</sub> OH:H <sub>2</sub> O <sub>2</sub> :H <sub>2</sub> O 1:2:5 volume ratio); (d) Ti-Al intermetallic alloy, colonies of gamma grains (optical microscope, etching by Kroll's reagent); (e) coating surface of TiAlN2 specimen (SEM, InLens); (f) cross section of TiAlN3 sample (SEM SEI, etching with NH <sub>4</sub> OH:H <sub>2</sub> O <sub>2</sub> :H <sub>2</sub> O 1:2:5 volume ratio) [107]..... | 102 |
| Figure 85: Cross section of TiAlN1 sample: coating morphology and nitrogen, titanium and aluminium concentration maps [107]. .....   | 104 |
| Figure 86: XRD patterns of substrate: as-processed Ti-48Al-2Cr-2Nb, and after oxidation in Burner Rig for 40 cycles at 850 or 950°C [107] .....  | 105 |
| Figure 87: XRD patterns of TiAlN coated specimens (TiAlN1 coating): as-processed and after oxidation in Burner Rig for 40 cycles at 850 or 950°C [107] .....   | 105 |
| Figure 88: COF curves recorded during a single scratch test for the TiAlN1 sample and the TiAlN3 sample before and after 40 cycles up to 850°C in burner rig apparatus. ....   | 108 |
| Figure 89: XPS survey spectrum of as processed substrate TiAl after argon surface cleaning. ....   | 109 |
| Figure 90: XPS survey spectrum of TiAl substrate oxidized in Burner Rig (40 cycles at 950 °C), after argon surface cleaning. ....  | 109 |
| Figure 91: XPS survey spectra of as deposited coatings: TiAlN1 (blue line) and TiAlN3 (green line), after surface cleaning [107] .....   | 110 |

|   |     |
|---|-----|
| Figure 92: XPS survey spectra of oxidized coatings after 40 cycles at 950°C in burner rig: TiAlN1 (blue line) and TiAlN3 (green line), after surface cleaning [107] .....   | 110 |
| Figure 93: XPS HR spectra of as-processed samples, where blu line= uncoated TiAl intermetallic alloy, red line =TiAlN 1coating; green line =TiAlN 2 coating, purple line = TiAlN 3 coating. HR TiN XPS pattern of pure TiN also sowed as a reference (black line) [107].....  | 112 |
| Figure 94: XPS HR spectra of TiAlN1 surface: blue line-as processed coating, red line-after 40 cycles at 850°C, green line-after 40 cycles at 950°C [107] .....   | 113 |
| Figure 95: Fitting of Ti2p complex HR spectrum, detected for TiAlN1 sample after 40 burner rig cycles at 850°C [107] .....  | 115 |
| Figure 96: SEM imagines of TiAlN1 cross-section: (a) before and (b) after 200 cycles at 950 °C in Burner Rig apparatus.....   | 121 |
| Figure 97: SEM imagines of TiAlN3 cross-section: (a) before and (b) after 200 cycles at 950 °C in Burner Rig apparatus.....   | 121 |
| Figure 98: XRD patterns of TiAl substrate before and after 100 and 200 oxidation cycles in burner rig [125].....  | 122 |
| Figure 99: XRD patterns of TiAlN1 samples before and after 100 and 200 oxidation cycles in burner rig [125].....  | 123 |
| Figure 100: XPS high-resolution surface spectra of uncoated TiAl: (a) as processed; (b) after 100 thermal cycles at 950 °C; (c) after 200 thermal cycles at 950 °C [125].....   | 126 |
| Figure 101: XPS HR spectrums of TiAlN1 sample: (a) as processed; (b) after 100 thermal cycles at 950°; (c) after 200 thermal cycles at 950°. XPS HR N1s not observed after cyclic oxidation (Curves (b) and (c) not reported) [125] .....   | 128 |
| Figure 102: XPS HR of TiAlN3 sample: (a) as processed; (b) after 100 thermal cycles at 950°C; (c) after 200 thermal cycles at 950°C. XPS HR N1s not observed after cyclic oxidation (Curves (b) and (c) not reported) [125] .....   | 129 |
| Figure 103: XPS depth profiles, after 200 thermal cycles at 950 °C: red line = TiAl (uncoated alloy), blue line = TiAlN1 coated sample, green line = TiAlN3 coated sample. The dashed lines show the extrapolation of the curves toward the concentration of titanium, aluminium and nitrogen found in the TiAlN coatings. [125]..... | 131 |
| Figure 104: EDS of as-processed Ti-48Al-2Cr-2Nb surface.....  | 135 |

|  |     |
|--|-----|
| Figure 105: EDS of Ti-48Al-2Cr-2Nb oxidized at 900°C for 30 min .....  | 135 |
| Figure 106: EDS cross-section of Ti-48Al-2Cr-2Nb oxidized at 900°C for 30 minutes.....   | 135 |
| Figure 107: SEM imagine of surface of intermetallic alloy after oxidation at 900°C for 30 minutes.....   | 136 |
| Figure 108: SEM imagine of cross-section of uncoated 48-2-2 intermetallic alloy after oxidation at 900 °C for 30 minutes (oxide layer a bit less than 2 μm thick).....   | 136 |
| Figure 109: EDS spectrum of surface of as-processed TaAlN coated sample .....  | 137 |
| Figure 110: EDS of TaAlN coated sample after oxidation at 900°C for 30 minutes.....  | 137 |
| Figure 111: SEM surface imagine of TaAlN coated sample after oxidation at 900°C for 30 minutes.....  | 138 |
| Figure 112: SEM cross-section imagine of TaAlN coated sample after oxidation at 900°C for 30 min (the up layer is an oxide scale about 2 μm thick grown on remaining TaAlN coating 1.2 μm thick, and the lower layer is the TiAl interlayer about 0.4 μm thick). ..... | 138 |
| Figure 113: EDS cross-section of sample with TaAlN coating oxidized at 900°C for 30 minutes.....   | 139 |
| Figure 114: XRD plot of surface of as-processed samples with TaAlN coating .....   | 140 |
| Figure 115: XRD plot of surface of with TaAlN coating after oxidation at 900°C for 30 min in air.....  | 140 |
| Figure 116: Survey spectrum of as-processed sample with TaAlN coating .  | 142 |
| Figure 117: Survey spectrum of sample with TaAlN coating oxidised at 900°C for 30 min.....   | 142 |
| Figure 118: XPS HR spectra of as-processed samples with TaAlN coating  | 143 |
| Figure 119: XPS HR spectra of samples with TaAlN coating oxidised at 900°C for 30 min.....   | 144 |

# List of Tables

|   |     |
|---|-----|
| Table 1: XPS spectra analysis of as-deposited TiAlN layers [88].  | 47  |
| Table 2: Parameters for the HiPIMS process [106]  | 62  |
| Table 3: Substrate pre-treatment for TiAlN deposition   | 64  |
| Table 4: Average superficial roughness (Sa) before the coating deposition   | 64  |
| Table 5: Thickness of coatings measured by Calo tester  | 66  |
| Table 6: Parameters for the TaAlN HiPIMS deposition   | 70  |
| Table 7: XPS analyses of the sample surfaces after isothermal oxidation (argon and contaminants percentages not reported, balancing 100%).                          | 93  |
| Table 8: EDS analyses of the sample surfaces after isothermal oxidation (argon and contaminants percentages not reported, balancing 100%).                          | 93  |
| Table 9: Parabolic rate constant $K_p$ ( $\text{kg}^2\text{m}^{-4}\text{s}^{-1}$ ) at specific temperatures (800°C-1000°C) for the TiAl alloys under investigation. | 98  |
| Table 10: Coating adhesion and coefficient of friction for TiAlN film/TiAl systems.   | 107 |
| Table 11: XPS surface analysis of specimens before and after burner rig test (40 cycles up to 850° C and 950° C) [107].   | 116 |
| Table 12: Chemical bonds and species detected by XPS in the samples before and after burner rig test (40 cycles up to 850° C and 950° C) [107]                      | 117 |
| Table 13: XPS surface analysis after 40 cycles at 950°C, comparison after different sputtering times  | 119 |
| Table 14: XPS elemental analysis of as processed and oxidized samples [125]   | 124 |
| Table 15: Binding energies for Al, Ti, O and N chemical bonds [125]   | 127 |
| Table 16: Binding energies for Ta, Al, N and O chemical bonds   | 145 |



# Chapter 1

## Introduction

From the last century to today, a fair amount of advancements has been achieved in aeronautical industry. The development of propulsion systems or structural part of gas turbine aero engines was increased significantly. The **Figure 1** shows different thermodynamic parameters at different locations in gas turbine engine.

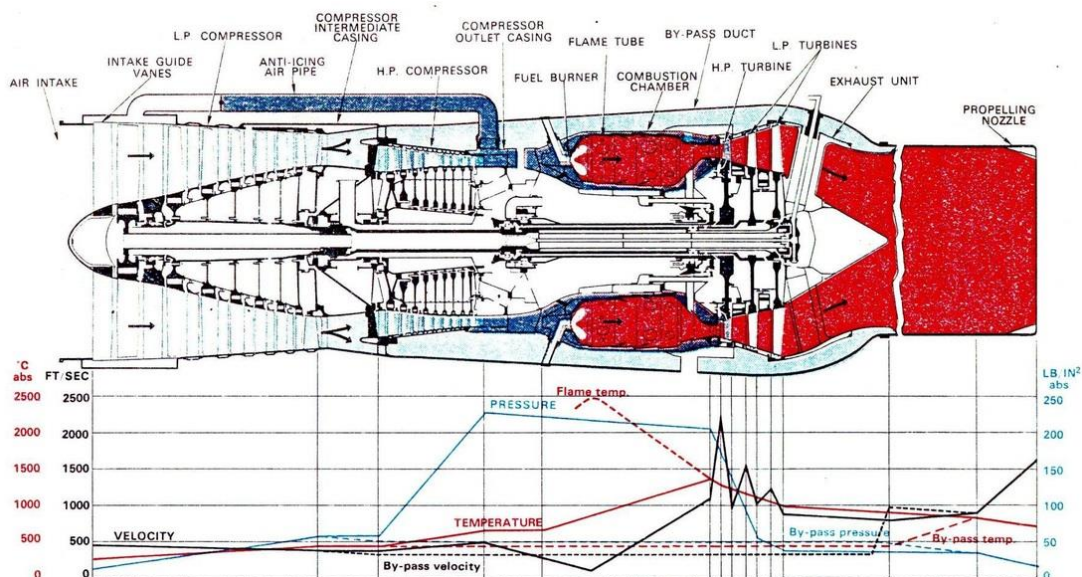


Figure 1: Design process of gas turbine engine: estimated temperature, velocity and pressure [1].

In the last few decades, the titanium aluminides (TiAl) have been considered as promising materials because of their excellent behaviour at high temperatures. The

intermetallic alloys have played a key role in automotive and aircraft sectors because of their low densities (about 3.8-4.2 mg/cm<sup>2</sup> [2],[3], half of that of Ni-based superalloys), very good mechanical properties such as high strength up to 800 °C [3], excellent stiffness, very well creep and fatigue resistance, rather good oxidation resistance and good corrosion behaviour.

The TiAl intermetallic alloys can replace the nickel-based superalloys in different parts of gas turbines, and this would result in a reduction of weight (20-30%) [4], fuel consumption (20%), noise (50%) and of NOx emissions (80%) [3]. The **Figure 2** shows different intermetallic alloys that were developed for noise attenuation and exhaust reduction [4].

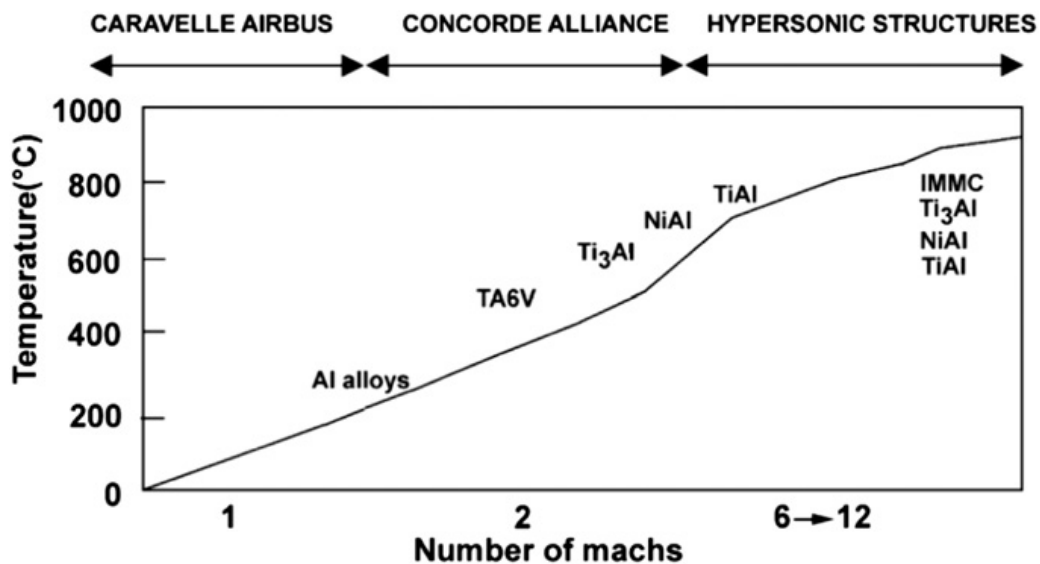


Figure 2: Expected performance of structural alloys developed for aircraft: temperature and speed [4].

The important limitation of these alloys is the low ductility and fracture toughness at room temperature, but in recent years, this problem was faced through significant improvements in manufacture processes, thermal treatments and microalloying. The oxidation resistance of TiAl alloys above 850°C still represents a strong restriction for their more extensive application in automotive and aerospace fields. Therefore these alloys are currently used for the blades of the low pressure turbine engines where the operating temperature is between 750-800°C. The lifetime of turbine engine components depends on the different operating conditions and it is expected to be some thousands of hours. Anyway turbine components are periodically disassembled and submitted to repair in order to increase their lifetime.

These intermetallics sustain operating temperature up to 950°C in turbocharge gasoline engines and around 800°C in valves of engines.

A further improvement of mechanical properties and oxidation resistance at temperatures ranging between 850°C and 1000°C would allow to use TiAl intermetallics as a convenient alternative of other materials (like Ni-based superalloys) in turbine engines.

In order to increase the maximum operating temperature of turbine engines, the deposition of protective coatings on hot structural parts can be adopted [5],[6],[7]. However, to date, the long-term stability of the coatings and then their effectiveness in service has not yet been proved. Suitable ceramic coatings designed for this specific application should be developed for titanium aluminide protection.

The aim of this work is to study the oxidation behaviour of several TiAl-based intermetallic alloys, and to develop consequently protective coatings able to improve the oxidation resistance of intermetallic components of aircraft engines. In order to test the performance of the protective coatings under investigation, a burner rig, designed to simulate the operating conditions of gas turbines, was also used. In particular TiAlN and TaAlN coatings have been studied because their effectiveness for oxidation protection of TiAl intermetallics was never studied before. On the other hand such a kind of protective layer seems very promising because of chemical and physical compatibility with the TiAl substrate: for instance the thermal expansion coefficient of TiAlN ( $7.5 \cdot 10^{-6} \text{ K}^{-1}$ ) is rather similar to that of Ti-48Al-2Cr-2Nb alloys ( $10 \cdot 10^{-6} \text{ K}^{-1}$ ). Even though TiAlN coating deposited on some TiAl substrate and TaAlN coating deposited on conventional Ti alloys was formerly investigated the HiPIMS technique was never adopted for the coating deposition. Actually this technique is expected to show advantages over conventional magnetron sputtering since it can provide smoother, harder and denser surface films than the conventional magnetron sputtering. Finally, as far as I know, the combination of the HiPIMS coatings and intermetallic substrate was never tested by the burner rig apparatus.

## 1.1 TiAl intermetallic alloys

In the literature, several authors reported investigations about TiAl intermetallic alloys and their state of the art [3],[4],[8]. The alloys initially developed were used in automotive sector for turbocharger exhaust gas turbines and valves [8],[9],[10] (**Figure 3** and **Figure 4**). As it is well known, the maximum operating temperature for turbocharger turbine is about 850°C, but in new gasoline engines, engineered to

improve fuel efficiency, the exhaust gas temperature should increase up to 1050°C. For this reason, a new Ti-31Al-8Nb-1Cr-0.5Si-0.03C wt.% alloy (DAT-TA2 by Daido) has been developed for this application [11]. Recently TiAl alloys have found applications in aircraft engines too. At the present time, GE is using Ti-48Al-2Nb-2Cr at.% (48-2-2) for the low pressure turbine (LPT) blades of GENx engine [3],[12] and, currently, there are about 190,000 blades flying on Boeing 787 and Boeing 747-8. Pratt and Whitney is also using the Ti-43.5Al-4Nb-1Mo-0.1B at.% alloy (TNM) [3] in the LPT stage of GTF engine [13], [14].

The materials requirements for the applications mentioned above consist of a suitable combination of high temperature strength, fatigue and creep resistance, ductility and oxidation resistance. In spite of the efforts spent to improve the Ti-Al intermetallic alloys to date their main lacks deal with the low ductility at room temperature and the oxidation resistance that limits the maximum operating temperature.

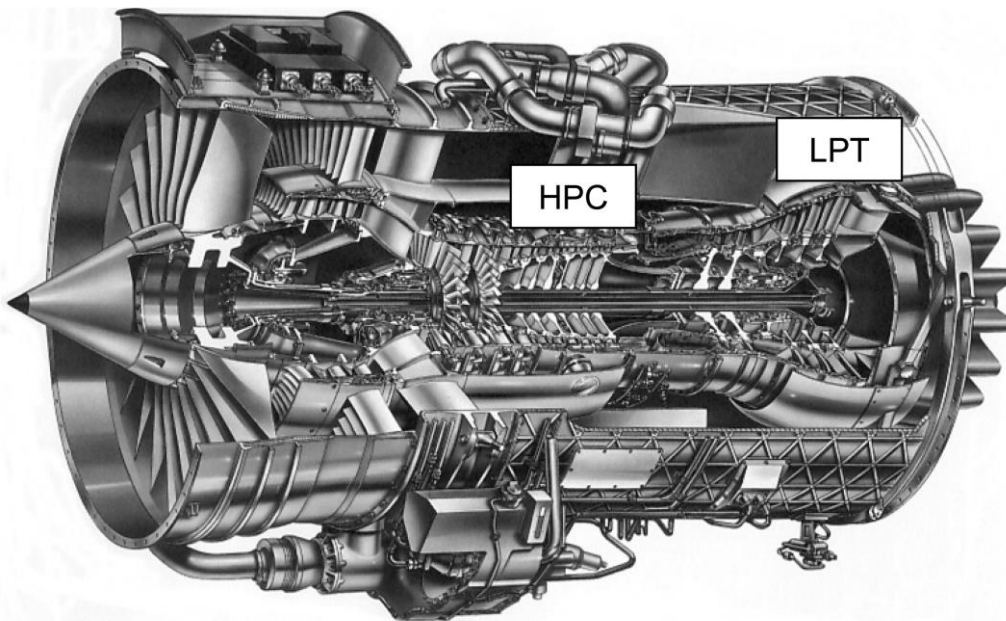


Figure 3: BR 715 aero engine. High Pressure Compressor (HPC) and Low Pressure Turbine (LPT) [6].

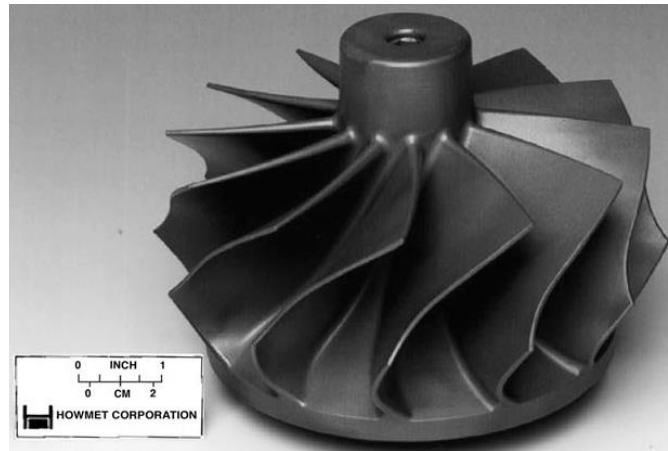


Figure 4: Titanium aluminide turbocharger wheels in service [4].

### 1.1.1 Chemical composition of TiAl alloys and phases present in their microstructure

Chemical composition and microstructure of TiAl-based intermetallic alloys were designed with the aim of improving both mechanical and oxidation resistance for engineering applications. Among the first generation TiAl alloys, the Ti-48Al-1V-(0.1C) was widely investigated. However, this alloy showed poor mechanical characteristics, not completely suitable for hot structural parts of turbines [15].

Today, TiAl intermetallic alloys of second and third generation are currently used for aeronautic applications. The composition of the TiAl-based alloys of second generation can be described as follow (at.%): Ti-(45-48)Al-(1-3)X-(2-5)Y-( $<1$ )Z; where: X= Cr, Mn, V; Y= Nb, Ta, W, Mo; Z= B, C, Si [3].

The third-generation can be classified as: Ti-(45-48)Al-(0-10)X-(0-3)Y-(0-1)Z-(0-0.5)RE; where: X= Cr, Mn, Nb, Ta; Y= W, Mo, Hf, Zr; Z= B, C, Si; RE= rare earths [3].

According to the Ti-Al-phase diagram in **Figure 5**, the TiAl-based alloys (45-48 % at. of Al) at room temperature consist of two principal phases: the predominant phase  $\gamma$ -TiAl (ordered face centered tetragonal) and the  $\alpha_2$ -Ti<sub>3</sub>Al phase (ordered hexagonal close packed).

L1<sub>0</sub> and DO<sub>19</sub> crystal structures are shown in **Figure 6**. The tetragonality ratio of TiAl is 1.02 for stoichiometric compound. This tetragonality ratio decreases to 1.01 when aluminium concentration decreases, and the ratio increases to 1.03 with increasing aluminium concentration [4].

In addition, small amounts of dispersed  $\beta$ -TiAl phase (body-centered cubic, disordered at room temperature) can be present in some alloys like  $\text{Ti}_2\text{AlMo}$  [16].

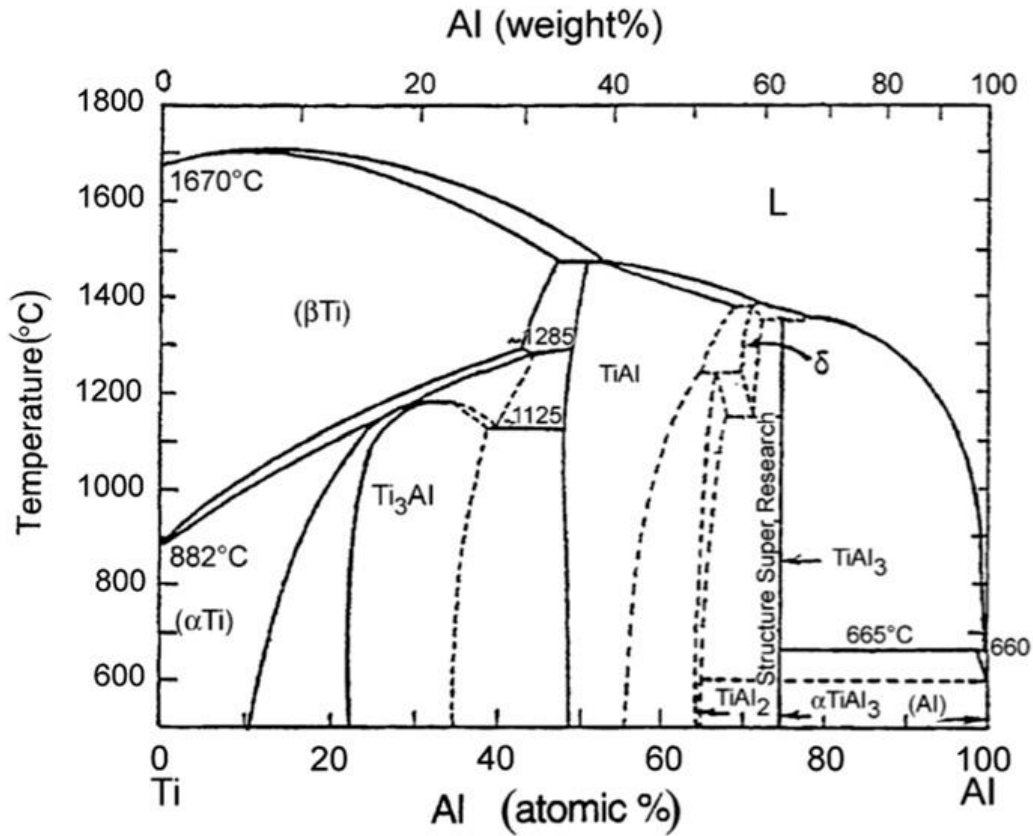


Figure 5: Ti-Al phase diagram [4].

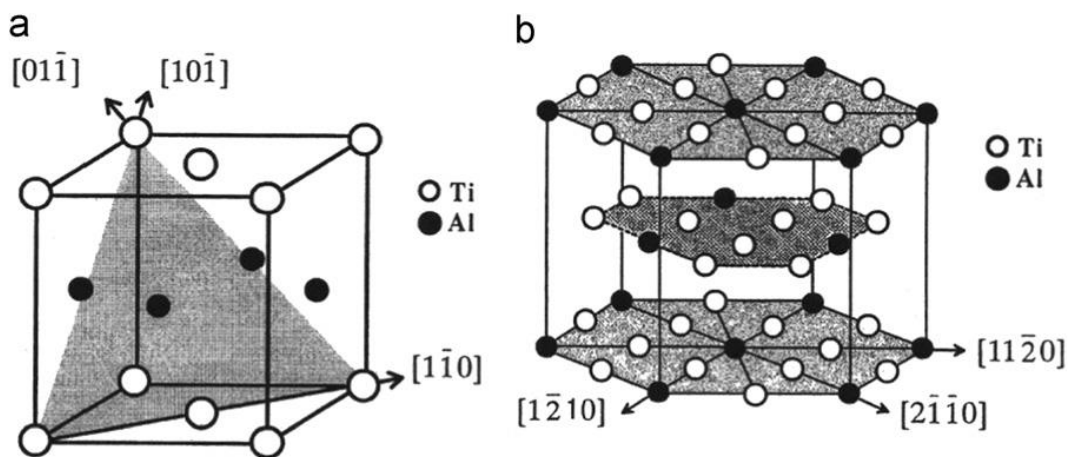


Figure 6: Crystal structures: a)  $\gamma$ -TiAl has L1<sub>0</sub> structure (ordered face centered tetragonal), and b)  $\alpha_2$ -Ti<sub>3</sub>Al has DO<sub>19</sub> structure (hexagonal closed packed) [4].

During casting and solidification, the  $\gamma$ -TiAl alloys show the transformations described in the following (**Figure 7**).

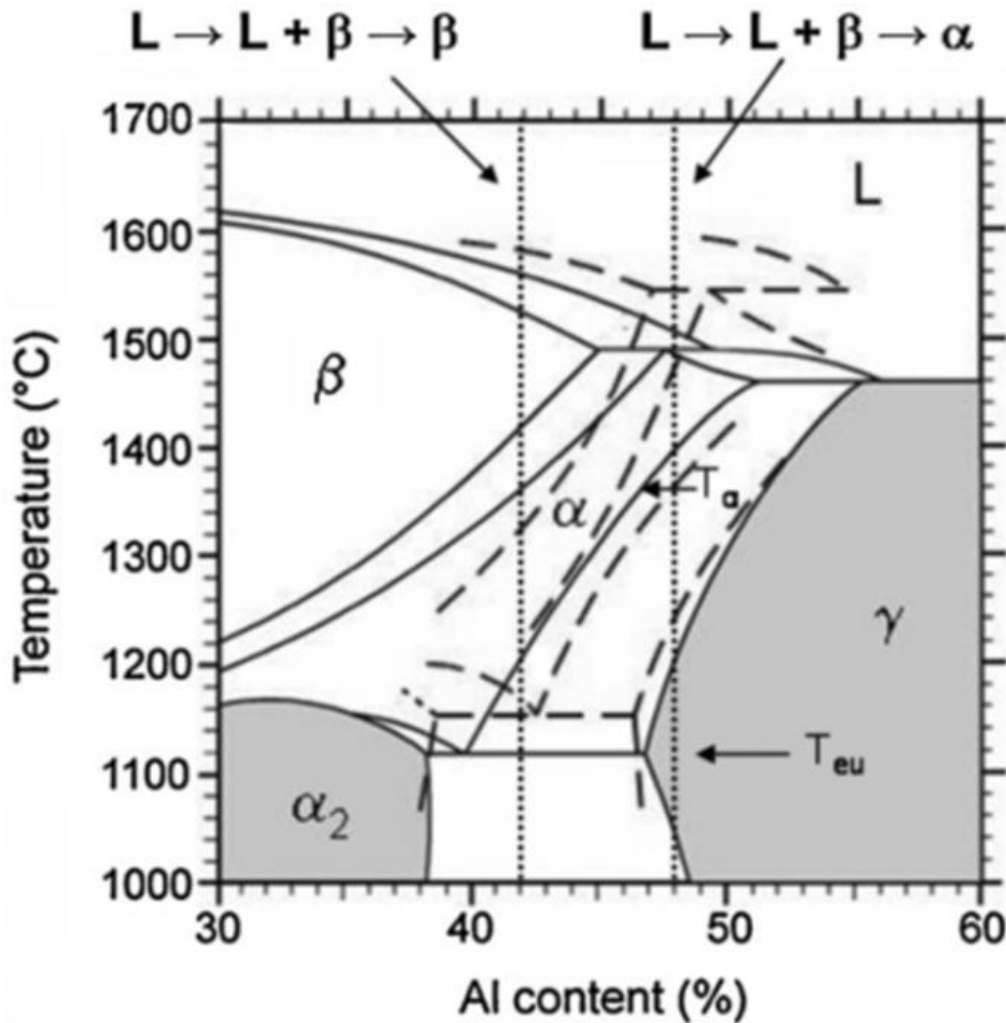


Figure 7: Section of the binary Ti–Al-phase diagram (continuous lines).  $T_\alpha$ :  $\alpha$ -transus temperature;  $T_{eu}$ : eutectoid temperature. Two vertical dotted lines marked the range of the technical  $\gamma$ -TiAl based alloys (45-48 % at. of Al). The broken lines show the effect of Nb (8 at.%) on the position of the phase field regions [17].

The solidification of TiAl binary alloys with an Al concentration below 45% at. takes place via  $\beta$  formation from the liquid and subsequent  $\beta$ -transformation ( $L \rightarrow L + \beta \rightarrow \beta \rightarrow \dots$ ). A higher Al concentration leads to a peritectic solidification reaction ( $L \rightarrow L + \beta \rightarrow \alpha + \beta \rightarrow \dots$ ). In case of binary alloy (Ti-46Al % at.), the solidification of the  $\beta$ -TiAl phase begins at 1535°C ( $L \rightarrow L + \beta$ ). Subsequently, cooling leads to a peritectic solidification reaction at 1482°C ( $L + \beta \rightarrow \alpha + \beta$ ). Between

1479°C and 1332 °C the alloy completely consists of  $\alpha$ -Ti<sub>3</sub>Al phase. The  $\alpha$ -Ti<sub>3</sub>Al phase shows a lattice similar to that of  $\alpha_2$ -Ti<sub>3</sub>Al phase, but it has disordered structure. The formation of  $\alpha_2$  from  $\alpha$  during cooling entails a disorder-order transformation. The  $\alpha$ -transus temperature is placed at 1332 °C (below  $T_\alpha$  the transformation  $\alpha \rightarrow \gamma$  occurs). In temperature range 1332°C-1136°C  $\gamma$ -TiAl phase progressively forms and the ratio between the amounts of  $\alpha$  and  $\gamma$  decreases with the temperature decrease (e.g. about 75% of  $\gamma$  at 1136°C). At the eutectoid temperature (1135°C) the transformation  $\alpha + \gamma \rightarrow \alpha_2 + \gamma$  happens, and a characteristic lamellar structure forms due to the transformation of  $\alpha$  into  $\alpha_2 + \gamma$ . After the eutectoidic transformation, the alloy microstructure consists of grains of primary  $\gamma$  and domains with  $\alpha_2/\gamma$  lamellar structure. At 1134 °C, the lamellar structure coming from the transformation of  $\alpha$  (40%at. of Al) contains alternating lamellae of  $\gamma$ -phase (containing about 47.2%at. of aluminium and constituting about 17 % of the domain) and  $\alpha_2$ - phase (containing about 38.5%at. of aluminium and constituting about 83 % of the domain). After the eutectoidic transformation and during the cooling from 1134 °C, the total amount of  $\gamma$  decreases because part of it transforms to  $\alpha_2$ . For instance at 1000 °C, the  $\gamma$  phase becomes 73% of the whole microstructure.

### 1.1.2 Processing and heat treatments of TiAl intermetallic alloys

The TiAl engineering components can be produced by numerous manufacturing techniques: casting or centrifugal casting (horizontal or vertical form) and investment casting (lost-wax casting), metal injection moulding (MIM), hot extrusion, isothermal forging or conventional forging with subsequent annealing treatment, powder metallurgy (PM) including hot isostatic pressing, additive manufacturing etc. [3],[4],[8],[9],[11],[17],[18],[19],[20].

In **Figure 8**, some of industrial processes for  $\gamma$ -TiAl base alloy transformation are summarized [17].

The casting method is a very well-known route for production of turbine blades. This method is followed by different complex thermo-mechanical processing which causes recrystallization. In order to improve chemical homogeneity by diffusion and to reduce casting porosity, the alloys can undergo a hot isostatic pressing (HIPing, deformation rate  $5 \times 10^{-3} \text{ s}^{-1}$ ). For instance, the parameters of HIPing for TNM alloy are given bellow: working temperature 1200°C for 4 h, pressing force 200 MPa and cooling in furnace [17].

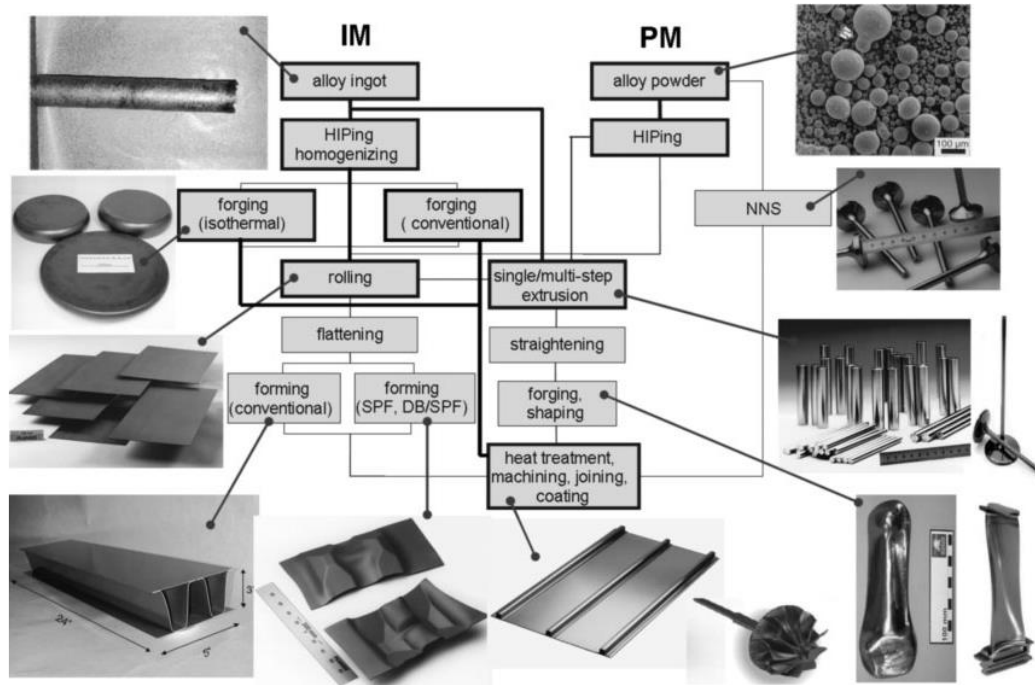


Figure 8: Processing of TiAl based alloys on an industrial scale [17].

The hot isothermal forging and conventional forging at high temperatures ( $1200^{\circ}\text{C}$ -  $1350^{\circ}\text{C}$ ) are conducted at a rather high deformation rate. During the deformation at high temperature and pressure, the starting microstructure modifies owing to dynamic recrystallization. Usually the present grains align perpendicularly to the forging direction and the alloy morphology exhibits elongated grains. The cooling rate is very important in this case, since phase transformations and ulterior crystallization can take place [17].

The hot isostatic pressing of powders (powder metallurgy) is commonly used for production TiAl billets. The mix of powder is degassed at  $500^{\circ}\text{C}$  and compacted at around  $1200^{\circ}\text{C}$  to  $1400^{\circ}\text{C}$  for 2-6 h. The desired microstructure can be obtained during the pressing by selecting the temperature or by using post processing steps [4].

The powder metallurgical method is very promising for large-scale production. The PM has been successfully adopted for producing near-net shape objects with minimal post processing. All the powder metallurgy techniques require a personalised research for each alloy and further heat treatment and mechanical

machining to produce the final TiAl engineering parts. Three principal processes of PM have been studied: Spark Plasma Sintering (SPS), Selective Laser Melting (SLM) or Direct Metal Laser Melting (DMLM) and Electron Beam Melting (EBM). The SPS process is a method based on internal Joule heating which promotes the densification of powder compacts. The SPS process is usually used for making duplex microstructures. The DMLM (using laser beam) and EBM (using electron beam) are metal powder techniques where the alloy powder (TiAl) is deposited and melted layer by layer, according to a process based on a CAD file. EBM has been developed by Arcam AB in Sweden and it is commercially available since 2002 [3].

The turbine TiAl blades of aircraft engines have been formerly processed by casting techniques. In more recent years other production process have been investigated and the attention have been focusing on EBM process in particular. In fact this last production process shows some advantages with respect to casting: reduction or elimination of scraps, more homogeneous chemical composition and microstructure in every component part, no contamination from atmosphere and crucible.

In this work the TiAl intermetallic alloys were processed by EBM and their final microstructure and mechanical properties were obtained by heat treatment.

In **Figure 9**, the schematic drawing of Arcam A2 machine and its technical data are reported. The EBM process is available online on Arcam AB's website [20].

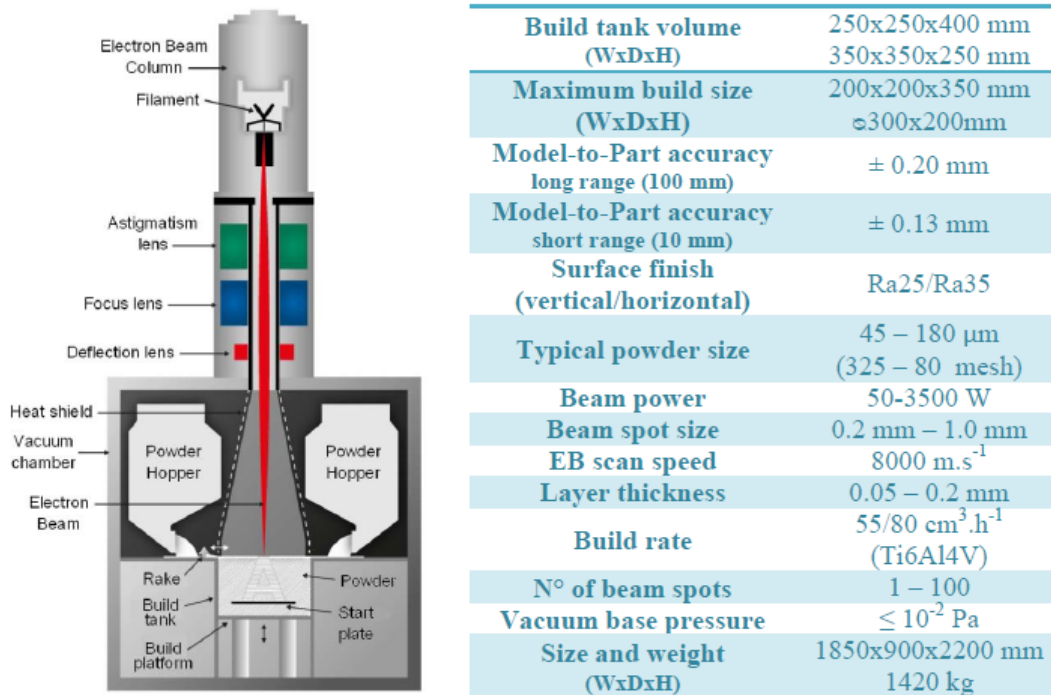


Figure 9: Schematic EBM process and technical data for Arcam A2 machine [21].

The principle of EBM is very similar to a scanning carried out in an electron microscope. A heated tungsten filament emits electrons (on top of the machine). The electrons are collimated and accelerated until they achieve a kinetic energy of about 60 keV. The magnetic coils control the electron beam. Magnetic lens focus the beam to the desired diameter, and other lens deflect the focused beam to the desired point on the building table. The electron beam gun is placed in fixed position and the electron beam is reflected by lens. The diameter of electron beam is about 0.1mm and the beam current is in the range 1–50mA. The equipment of last generation are multi-beams and can melt contemporary the powders placed in different points of the building table. The metal powder layers are deposited on the building table and the powder bed is made flat by a raking mechanism. Usually the thickness of layer is in the range 0.05– 0.2mm. In order to obtain good layer packing, efficient flow, and successively melt uniformity, suitable particle size distribution and near-spherical powders are used. The electron beam is controlled by a computer and interacts with the powder which melts and then solidifies into dense and solid metal. After the processing of a layer, the building is lowered, a new layer of powder is deposited and treated by the laser beam. The components are built layer-by-layer. The powder is preheat by the beam (about up to 80 % of melting temperature) by scanning at high rate ( $\sim 10^4$  mm/s) and medium beam

current ( $\sim 30$  mA-50 mA). After the beam melts the powder (scanning rate  $\sim 10^2$  mm/s and beam current 5 – 21 mA). The EBM process is conducted under high vacuum ( $10^{-2}$  Pa- $10^{-4}$  Pa in different parts of Arcan machine). During the melting process, inert helium gas ( $10^{-2}$  Pa) is sent to the vacuum chamber. Helium gas avoids accumulation of electrical charge in the powder and favours the subsequent cooling. When the building process is completed the chamber is filled by helium to cool quickly the powder bed. The component is taken out of the powder and rest of powder is recovered, sieved and recycled [20],[21].

In every case (for all the PM methods), a final heat treatment can be adopted to modify the  $\gamma$ -TiAl alloy microstructure. Different characteristic microstructures of TiAl-based alloys can be obtained by heat treatment. The first step of the heat treatment consists in annealing performed within the  $\alpha$  or  $\alpha+\gamma$  phase field. The TiAl-based alloys after the heat treatment can show four different microstructures depending on the annealing temperature: duplex, near gamma, near lamellar and fully lamellar [17],[22] (**Figure 10**).

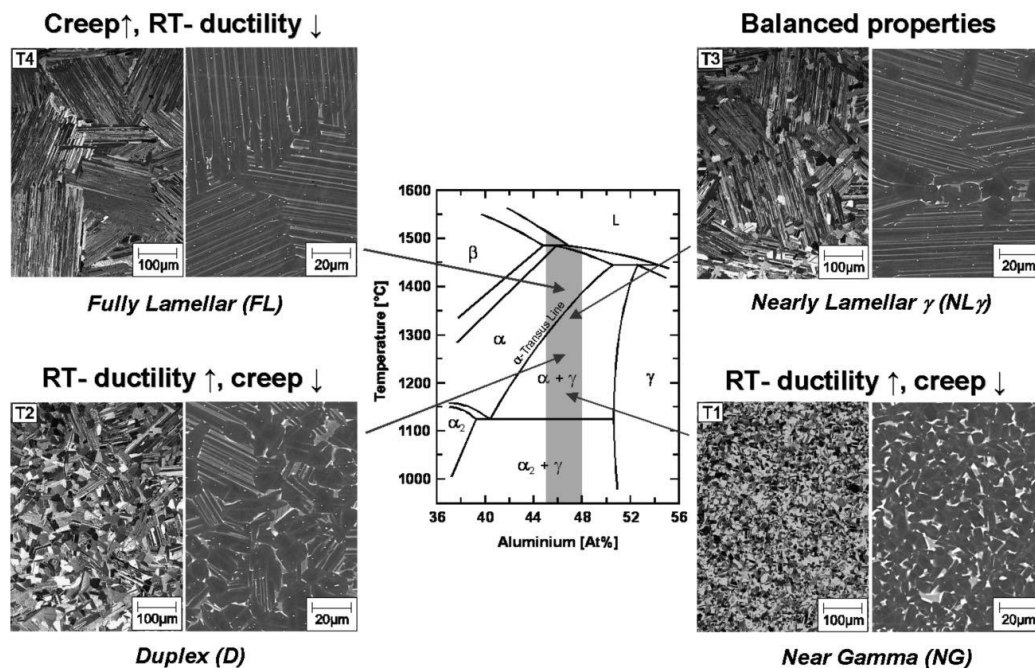


Figure 10: Microstructures of TiAl-based alloys after heat treatment [17].

The heat treatment starting from a temperature just a little bit above the eutectoid temperature, that is in the  $\alpha+\gamma$  field, leads to formation of a near gamma microstructure. The same microstructure can be obtained starting from a

temperature below the eutectoid temperature, that is in  $\alpha_2+\gamma$  field [4]. The final microstructure mainly consists of equiaxed  $\gamma$  grains with a small content of  $\alpha_2$  phase placed at grain boundaries and triple points [4],[17]. The duplex microstructure forms after annealing well above the eutectoid temperature, that is in the centre of  $\alpha+\gamma$  zone, and subsequent cooling to room temperature. The duplex microstructure is composed of alternating lamellae ( $\gamma/\alpha_2$  phases) and globular  $\gamma$ -phase grains placed at the grain boundaries of  $\gamma/\alpha_2$  colonies. In addition, there are also some small grains of  $\alpha_2$  phase situated at the boundaries of lamellar zones [7]. Near and fully lamellar microstructures ( $\gamma/\alpha_2$  phases) respectively form after annealing about 10 °C below and 10-20 °C above the  $\alpha$ -transus temperature, and subsequent cooling. The near lamellar microstructure comprises  $\gamma/\alpha_2$  lamellar domains and primary  $\gamma$  grains, while the fully lamellar consists of  $\gamma/\alpha_2$  domains only. The volume fraction of lamellar colonies increases with the growing of the annealing temperature in the  $\alpha+\gamma$  field (because during a continuous cooling from the annealing temperature the system does not change exactly according to the phase diagram), while the lamellar spacing in the domains depends on the cooling rate [17]. The lamellar microstructure is composed of alternating lamellae of  $\alpha_2$  and  $\gamma$  with the following crystallographic relationship:  $(111)\gamma// (0001)\alpha_2$  and  $(110)\gamma// (1120)\alpha_2$  [17].

The microstructure of  $\gamma$ -TiAl alloy does not depend only on the annealing temperature (above  $\alpha$ -transus temperature or in  $\alpha+\gamma$  two phase field), but on the cooling rate too. In the same manner also the microstructure obtained after annealing at a temperature above the  $\alpha$ -transus depends on the cooling rate. The CCT curves (continuous cooling transformations) were investigated for several TiAl alloys. For example, in the **Figure 11**, the CCT diagram of a HNb  $\gamma$ -TiAl alloy is reported. In this figure the different curves refer to more or less quick cooling rates, these curves cut the curves of formation start for lamellar (L),  $\gamma_m$  and  $\alpha_2$  structures. The intersections between the cooling curves and the curves of formation starts show at which temperature the different structures appear during cooling [17].

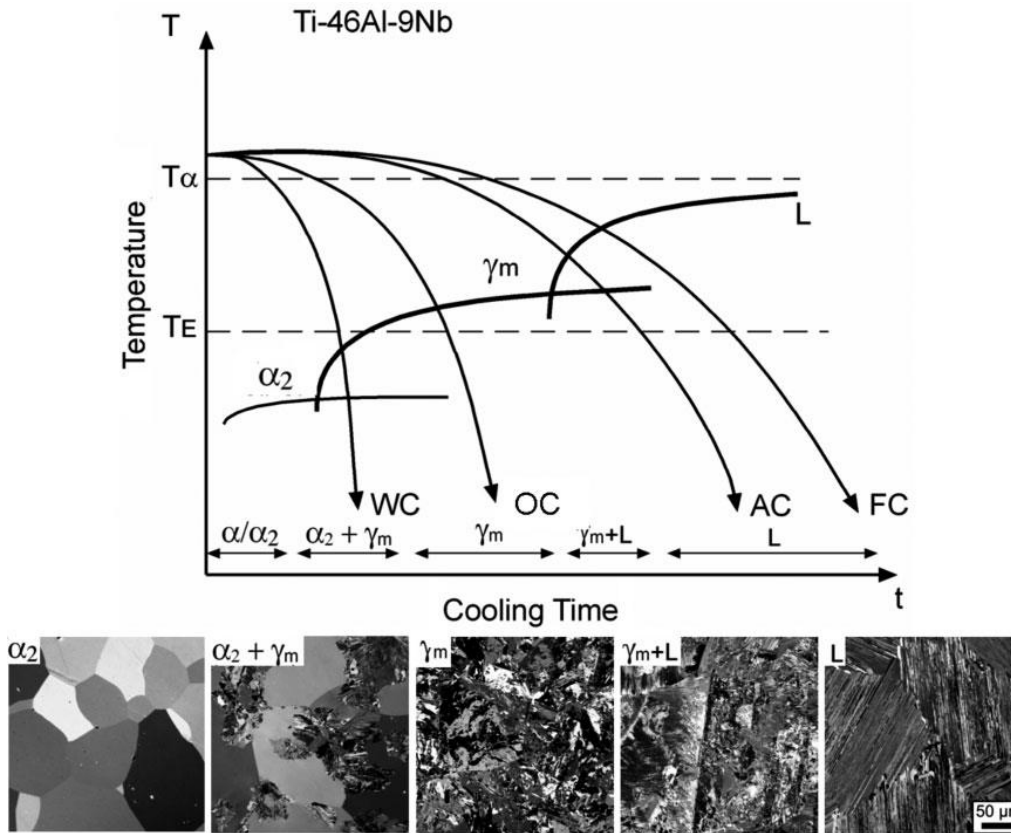


Figure 11 : CCT diagram of a Ti-46Al-9Nb alloy and different microstructures formed at specific cooling rates (FC-furnace cooling, AC-air cooling, OC-oil cooling, WC-water cooling) [17].

The full lamellar microstructure ( $\alpha_2/\gamma$ ) forms at the slow furnace cooling from the single  $\alpha$  phase field (FC curve). The average lamellar spacing in  $\alpha_2/\gamma$  colonies decreases when the air-cooling is adopted (AC curve). In this case, the microstructure can consist of lamellar colonies and  $\gamma_m$ -TiAl grains localized at colony boundaries. During oil cooling, the disordered  $\alpha$ -phase completely transforms into the  $\gamma_m$  phase (face-centered cubic) (OC curve). The massive transformation of  $\alpha$  into  $\gamma_m$  phase is suppressed by water quenching (WC curve). According to Figure 11, the supersaturated  $\alpha_2$  phase also forms after water-cooling. A disorder-order transformation of  $\alpha$  phase happens without composition change and formation  $\alpha_2$ . A subsequent ageing treatment at the temperature below the eutectic temperature results in partial transformation of  $\alpha_2$  phase into a lamellar structure [17]. In fact, the aluminium content of  $\alpha_2$  phase obtained by quenching  $\alpha$  is well over the equilibrium percentage of Al at room temperature, therefore the  $\alpha_2$  is partially converted into the aluminium rich  $\gamma$  phase.

In the following, the more common microstructures resulting from processing and heat treatments for typical TiAl alloys (including those under investigation in this work) will be presented.

The Figure 12 shows the microstructure of the HNb TiAl alloy Ti-45Al-(8-9)Nb-(W,B,Y) (at.%) processed by different techniques [23].

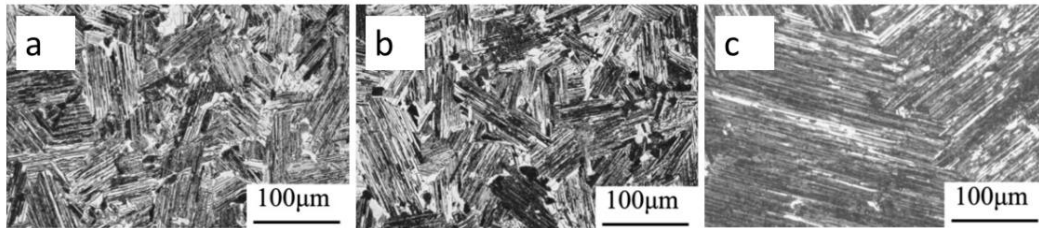


Figure 12: Microstructure of Ti-45Al-(8-9)Nb-(W,B,Y) (at.%): a) SM ingot before HIP, b) SM ingot after HIP, c) PAM ingot [23].

The SM ingots (diameter 120 mm x high 420 mm) were prepared by vacuum arc remelting (VAR) plus scull melting (SM) technologies. Double-melted PAM ingots (diameter 160 mm x high 470 mm) were prepared by cold hearth plasma arc melting (PAM). In order to eliminate casting defects, a hot isostatic press (HIP) under argon pressure of 140 MPa at 1250°C was used for SM ingots. A near lamellar structure (colony size 10 µm) was obtained by SM showing some porosity, but after HIP treatment, the porosity greatly decreased. PAM ingot exhibits fully lamellar structure with colony size about 200 µm - 1200 µm. The cooling process leads to a difference in the microstructure between SM and PAM ingots. In the case of PAM ingots, the material spent more time in the temperature range where  $\beta$  and  $\alpha$  phase exist. During this period of time, big  $\alpha$  grains grew and then they transformed during quick cooling into large size FL colony ( $\alpha_2+\gamma$ ) [23].

In **Figure 13**, the dotted lines show the modified phase diagram, which depicts the microstructures practically observed when the Ti-45Al contains 8-10% at. Nb. It is clear that solidification of alloys with 44-45%at Al occurs via  $\beta$  formation ( $L \rightarrow L+\beta \rightarrow \beta \rightarrow \beta+\alpha$ ). If the addition of niobium is high enough,  $\beta$  phase is present also at room temperature (**Figure 13**, 10% Nb). During cooling niobium can segregate at the grain boundaries, where the enhanced concentration of Nb causes the  $\beta$ -formation at room temperature [23]. Other alloying elements like W and Mo act as  $\beta$  stabilizers in the same manner of Nb.

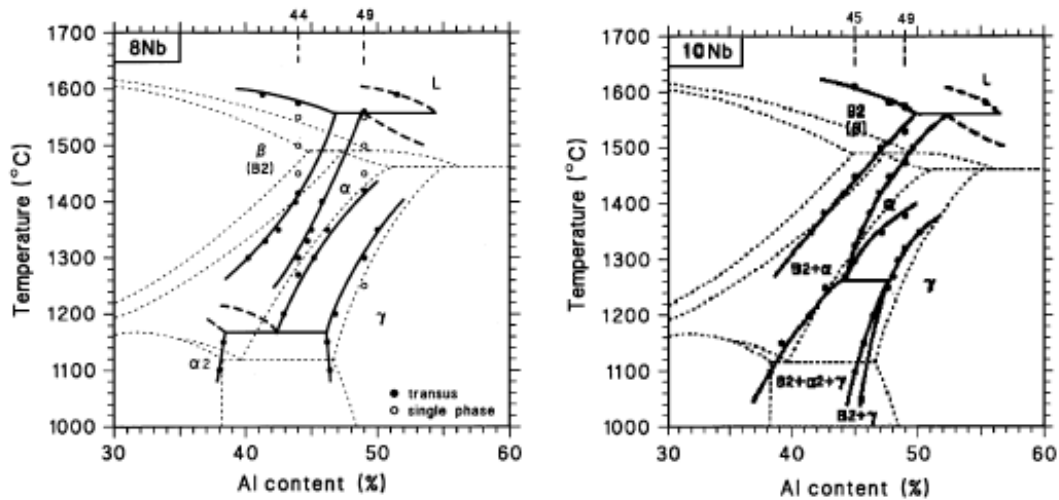


Figure 13: Ti-Al quasi phase diagrams with Nb (8% at.) and Nb (10% at.) [23].

In **Figure 14** three microstructures of Ti-45Al-10Nb alloy obtained with different thermal treatments are showed. The Ti-45Al-10Nb alloy was produced by non-consumable argon arc melting. In order to obtain the homogenised composition of HNb alloy the ingots were remelted four times. Successively the ingots were maintained at 1200°C for 168 h to homogenise the microstructure and then forged at 1250°C [24].

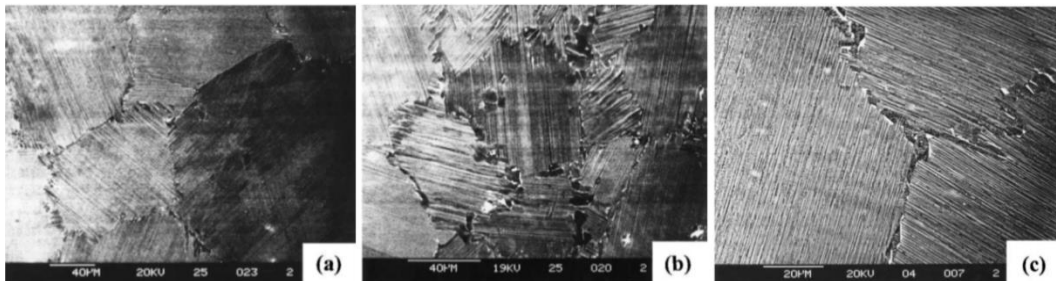


Figure 14: SEM photographs of Ti-45Al-10Nb microstructure: a) Fully Lamellar, b) Nearly Lamellar, c) degraded Fully Lamellar (DFL) [24].

The Fully Lamellar microstructure was obtained by using the following heat treatment: annealing at 1318°C, cooling down to 900°C in 15 minutes, isotherm at 900° for 30 minutes, air cooling. This FL microstructure has colony size of lamellar structure about 150  $\mu\text{m}$  and a lamellar spacing about 0.22  $\mu\text{m}$ . In the case of Near Lamellar microstructure the heat treatment was: annealing at 1300°C, cooling down to 900°C in 60 minutes, isotherm at 900° for 30 minutes, air cooling. The NL microstructure contains small equiaxed  $\gamma$  grains at the grain boundaries, the colony

size of lamellar structure was about  $90\ \mu\text{m}$  and the lamellar spacing was about  $0.25\ \mu\text{m}$ . After 30 h at  $1050^\circ\text{C}$ , the FL microstructure obtained by heat treatment described above, was degraded due to the changing of the grain boundary structure and the coarsening of the lamellar laths [24].

The **Figure 15** shows the evolution of Ti-45Al-2Cr-8Nb microstructure in correspondence to the heat treatment temperature [21].

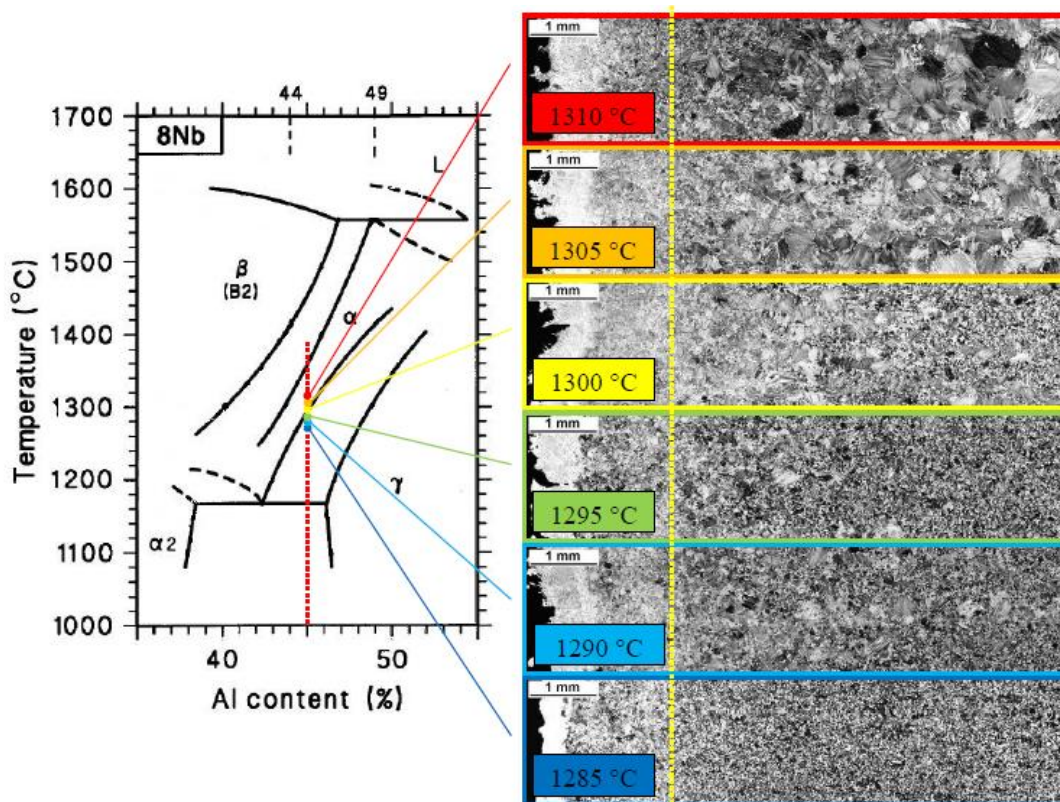


Figure 15: The microstructure of Ti-45Al-2Cr-8Nb alloy obtained by heat treatment at different temperatures in the vicinity of  $T_\alpha = 1295^\circ\text{C}$ . The yellow dotted line indicates the border (2mm) [21].

At  $1285^\circ\text{C}$ , the HNb alloy shows fine equiaxed as-EBM microstructure. The first lamellar grains is observed after heat treatment at  $1290^\circ\text{C}$ . After heat treatment at  $1295^\circ\text{C}$ , under 50 % lamellar grains were observed. At  $1300^\circ\text{C}$ , over 50 % of lamellar grains were more homogeneously distributed among fine equiaxed  $\alpha$  and  $\gamma$  grains. At  $1305^\circ\text{C}$  the lamellar grains ratio and average lamellar grain size increased. The microstructure was homogeneous and lamellar grains were uniformly distributed. After treatment at  $1310^\circ\text{C}$  for 2 hours, the microstructure was nearly lamellar, which consisting in 90 % of coarse lamellar grains pinned

mostly at grain boundaries by fine equiaxed grains. The fully lamellar microstructure, which composed by coarse (300-500  $\mu\text{m}$ ) lamellar  $\gamma/\alpha$  colonies, was observed over 1315  $^{\circ}\text{C}$  [21].

In **Figure 16** the different microstructure of TNM alloy obtained by several production processes are showed [17].

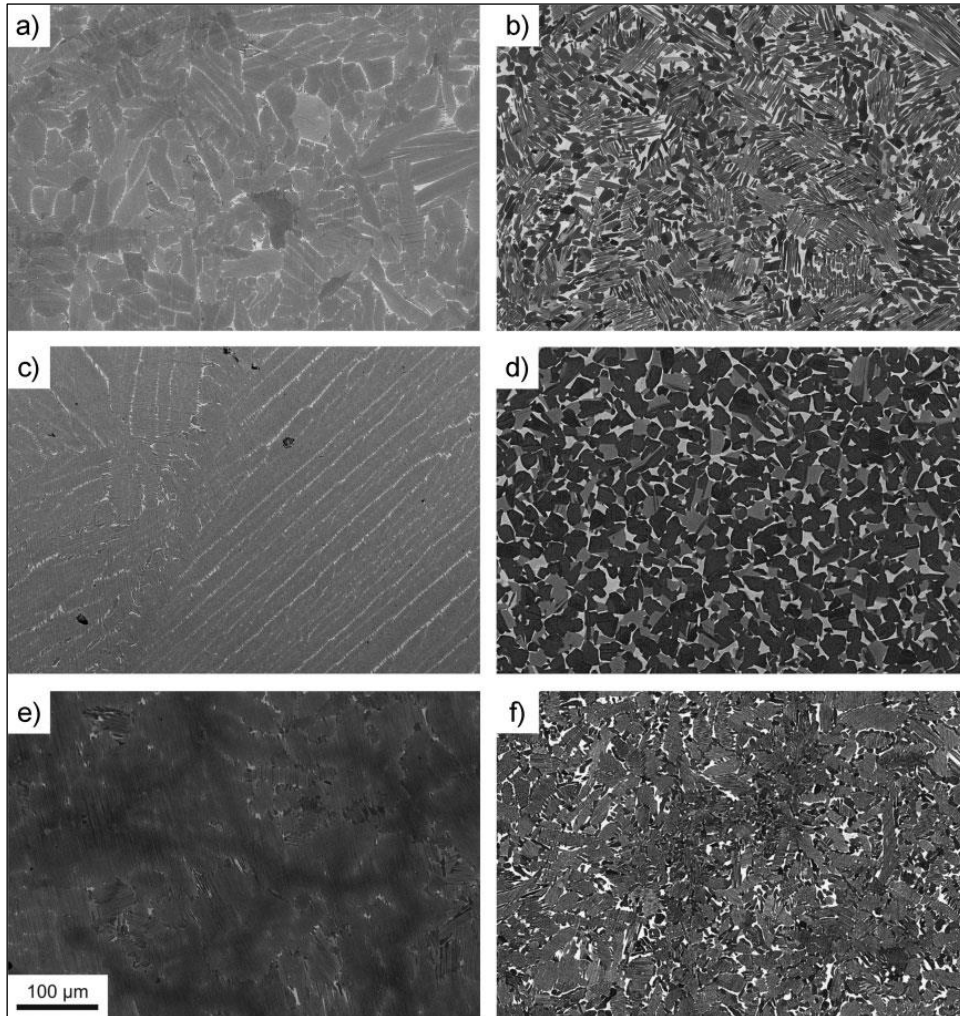


Figure 16: SEM image (BSE mode) of TNM microstructure: (a) centrifugal cast Ti-43.5Al-4Nb-1Mo-0.1B, (b) cast and HIPed Ti-43.5Al-4Nb-1Mo-0.1B, (c) cast and HIPed Ti-43.5Al-4Nb-1Mo alloy without boron, (d) HIPed Ti-43.9Al-4Nb-0.95Mo-0.1B gas-atomized powder, (e) Ti-43.5Al-4Nb-1Mo-0.1B +0.5 at.% C showing microstructure different from a) because peritectic solidification, (f) Ti-43.5Al-4Nb-1Mo-0.1B +0.5 at.% C,  $\beta$  solidification due adding high content of Mo. The  $\gamma$  phase appears grey to dark and  $\alpha_2$  light grey,  $\beta$  exhibits the brightest contrast [17].

The morphology of as cast Ti-43.5Al-4Nb-1Mo-0.1B alloy is mainly composed by lamellar colonies ( $\gamma+\alpha_2$ ) and very fine  $\beta$  globular grains at the boundaries of  $\gamma/\alpha_2$ . The lamellar structure is not well visible because the lamellar spacing is small (**Figure 16**, (a)). According to phase diagram, this microstructure derived from solidification path:  $L \rightarrow L+\beta \rightarrow \beta \rightarrow \beta+\alpha \rightarrow \alpha+\gamma+\beta \rightarrow \alpha+\alpha_2+\gamma+\beta \rightarrow \alpha_2+\gamma+\beta$ . The  $\gamma$  grains at the  $\gamma/\alpha_2$  colony boundaries form due to the  $\beta \rightarrow \gamma$  transformation. The  $\beta$  phase shows semi-coherent interfaces with  $\alpha_2$  and  $\gamma$  phases; at the interfaces the following crystallographic relationship exists:  $(0001)\alpha_2// (101)\beta// (111)\gamma$  and  $[1120]\alpha_2// [111]\beta// [101]\gamma$ . It can be noticed that the TNM microstructure after HIPing shows grain reduction in comparison with TNM after casting. (**Figure 16**, (b)). The B refining agent plays a beneficial role in cast TNM alloy, the grains became coarse in TNM alloy without B (**Figure 16**, (c)). In this case, the grains are coarse in spite of HIP treatment. The HIPed Ti-43.9Al-4Nb-0.95Mo-0.1B powder, obtained by gas atomization, has homogenous microstructure consisting of globular  $\gamma$ ,  $\alpha_2$  and  $\beta$  grains (**Figure 16**, (d)). The addition of C improves the high-temperature capability of TNM alloy and increases the strength and creep resistance. However, the microstructure of TNM dramatically changed after small addition of alfa stabilizer (C, 0.5% at.) into the alloy (**Figure 16**, (e)). The solidification pathway does not involve the initial  $\beta$  formation. In order to promote  $\beta$  formation, the detrimental effect of C can be compensated by Mo which is  $\beta$ -phase stabilizer (**Figure 16**, (f)) [17].

The various microstructures of Ti-48Al-2Cr-2Nb alloy, that are obtained after different processing paths starting from metal powders, are shown in **Figure 17** [18]. The microstructure of this alloy after the EBM process is always extremely fine and homogenous, but it usually contains only very small spherical pores (**Figure 17**, (a) and (b)). During powder atomization, the gaseous Ar entrapped inside the alloy created the residual porosity, that can be quantified less 2%. After HIPing the porosity can be reduced to 1%. In addition, the HIPed alloy is subjected to a full recrystallization; the growth of near equiaxed grains is clearly observed in **Figure 17**, (c). A duplex microstructure can be formed after ulterior thermal treatment. In this case, after 2 h at 1320 °C, about 40% of equiaxed grains is transformed into lamellar colonies of  $\gamma/\alpha_2$ , and the average colony size is about 100  $\mu\text{m}$ . The rest of fine equiaxed grains (approximately 15  $\mu\text{m}$ ) show that grain growth did not occurred during heat treatment (**Figure 17** (d)) [18].

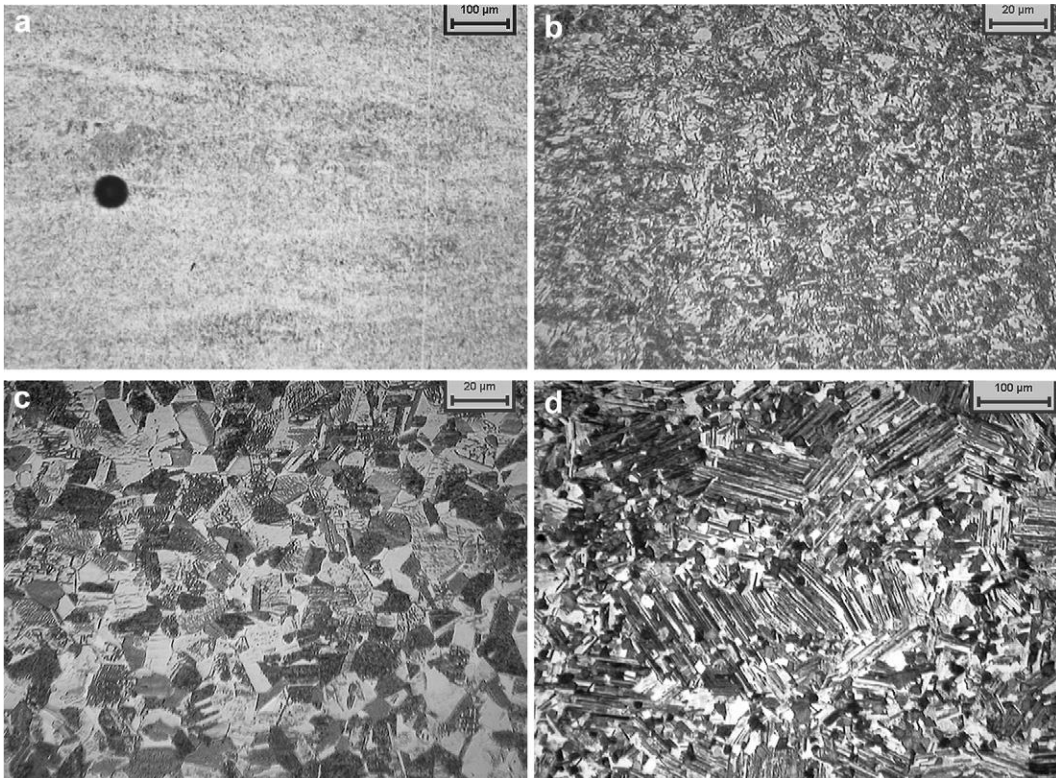


Figure 17: Microstructure of Ti-48Al-2Cr-2Nb alloy: (a) after EBM processing, on the left of the picture typical spherical defect inside is present; (b) after EBM processing; (c) after EBM and HIPing; (d) after EBM, HIPing and thermal treatment for 2 h at 1320 °C [18].

The **Figure 18** shows different microstructures of Ti-48Al-2Nb-0.7Cr-0.3Si after engineering processing. The very fine gamma equiaxed grains, generally parallel to powder layers, with coarser grains represent the typical microstructure after EBM process (**Figure 18**, (a)). The near gamma microstructure forms after melting and rapid cooling, while the linear bands with big grains are due to re-melting of previously deposited layer as a consequence of heat diffusion phenomena during EBM processing. The **Figure 18** (b) shows a duplex microstructure: some lamellar grains formed after heat treatment at 1300°C for 2 h (below the alpha transus temperature). Only few lamellar colonies can be observed in this microstructure (red and yellow arrows (**Figure 18**, (b))). The quantity of lamellar colonies and the dimension of grains increased when the temperature of HT grew (**Figure 18**, (c)). The near lamellar microstructure appeared after HT at 1360°C for 2 h (**Figure 18**, (d)). Fully lamellar formation was obtained at 1365°C and 1370°C for 2 h (**Figure 18**, (e) and (f) respectively). The small difference in

temperature (only 5°C) changed the connection between lamellar colonies (the total connection was present at 1370 °C) [19].

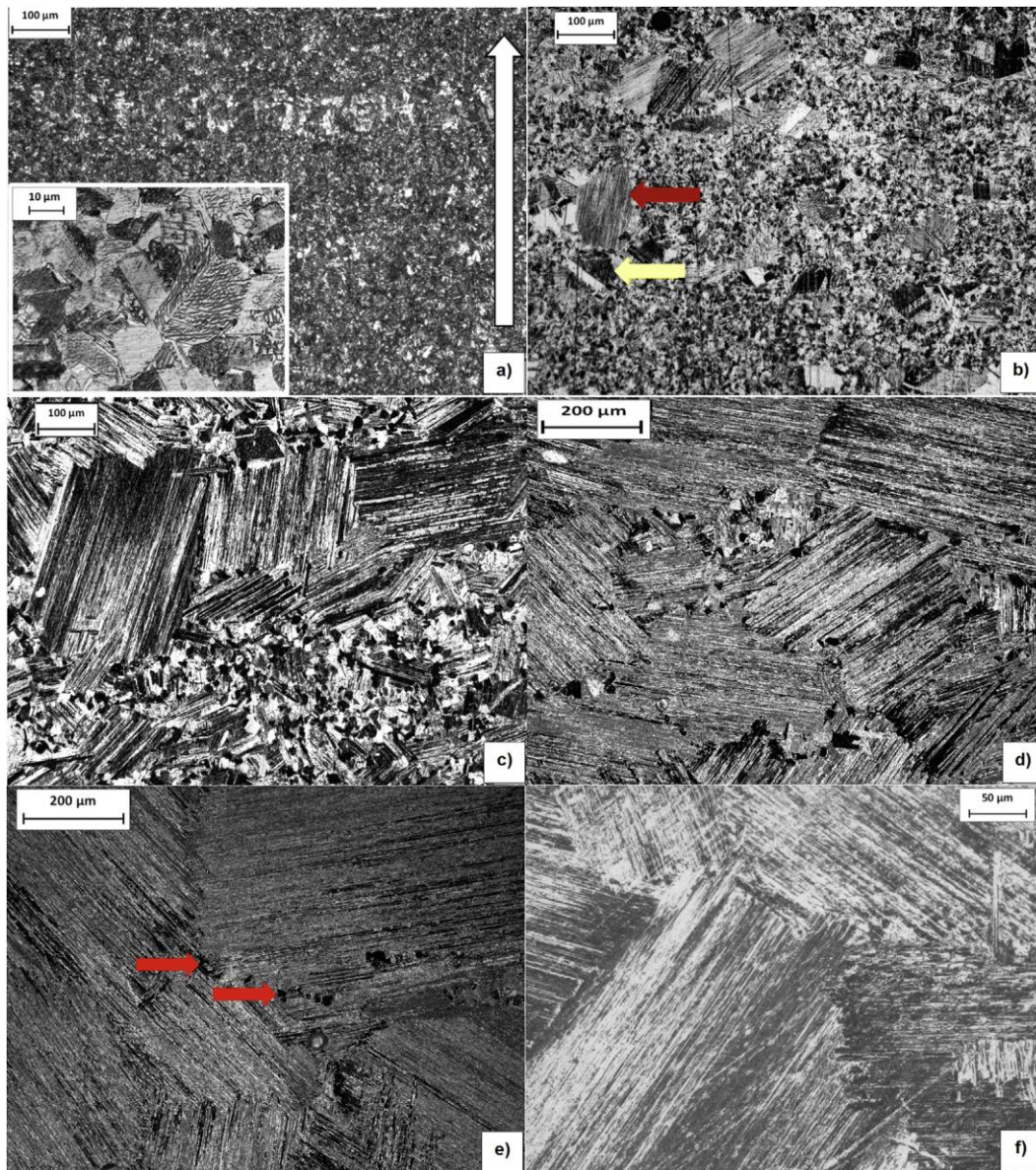


Figure 18: Optical microscopy images of Ti-48Al-2Nb-0.7Cr-0.3Si microstructure: (a) equiaxed morphology after EBM, the arrow indicates the building direction, (b) duplex morphology after HT at 1300°C for 2 h, (c) duplex morphology after HT at 1350°C for 2 h, (d) near lamellar morphology after HT at 1360°C for 2 h, (e) fully lamellar morphology after HT at 1365°C for 2 h, (f) fully lamellar morphology after HT at 1370°C for 2 h with bigger lamellar grains of  $\gamma/\alpha_2$  [19].

### 1.1.3 Mechanical and oxidation resistance of TiAl intermetallic alloys

In order to improve the mechanical properties and high temperature capabilities of TiAl intermetallic alloys, during the last years many researchers designed novel TiAl alloys with alloying elements suitable for optimizing their microstructure. The main components of all microstructures are  $\alpha_2$  and  $\gamma$  phases. The  $\alpha_2$  phase ( $\text{Ti}_3\text{Al}$ ) has good high temperature strength, but very low ductility. The  $\gamma$  phase (TiAl) has excellent strength at high temperature (600 °C - 700 °C) and its room temperature ductility is limited, but better than  $\alpha_2$  phase [4]. The addition into the alloy of Nb, Ta, W and Mo, stabilizers of  $\beta$ -phase, improves the creep resistance. The Cr, Nb and Mo alloying elements in TiAl alloy make easier forging and extrusion at high temperature [3]. In fact, Nb and Mo favour the formation of the cubic  $\beta$ -phase, which becomes ordered at high temperature and for this reason facilitates forging and extrusion. The room temperature poor ductility and strength of the fully lamellar microstructure is due to its coarse grains. The elements Cr, Mn and V are used to reduce the grain size in TiAl alloys in order to increase the ductility [8],[25].

The relationship between microstructures and some mechanical properties is showed in the **Figure 19** [4].

The fully lamellar structure (alternating  $\gamma/\alpha_2$  phases) has excellent fracture toughness, but low ductility and strength. In addition this structure shows very good fatigue and creep resistance [4]. The duplex microstructure is preferred for most of structural applications, because its improved ductility and fatigue resistance. On the other hand, the duplex microstructure shows limited fracture toughness and creep resistance, while near lamellar and fully lamellar microstructures exhibit better creep resistance and fracture toughness [3],[22]. The near gamma has good strength and ductility, but impact resistance and creep resistance are poor. For example, literature reports that the fracture toughness for the duplex microstructure ranges from 10 MPa m<sup>1/2</sup> to 16 MPa m<sup>1/2</sup>, while the fracture toughness for fully lamellar microstructures is about 30 MPa m<sup>1/2</sup> [4]. From the above it is clear that it is not possible to maximize all the mechanical properties, but the best compromise should be adopted for each specific applications.

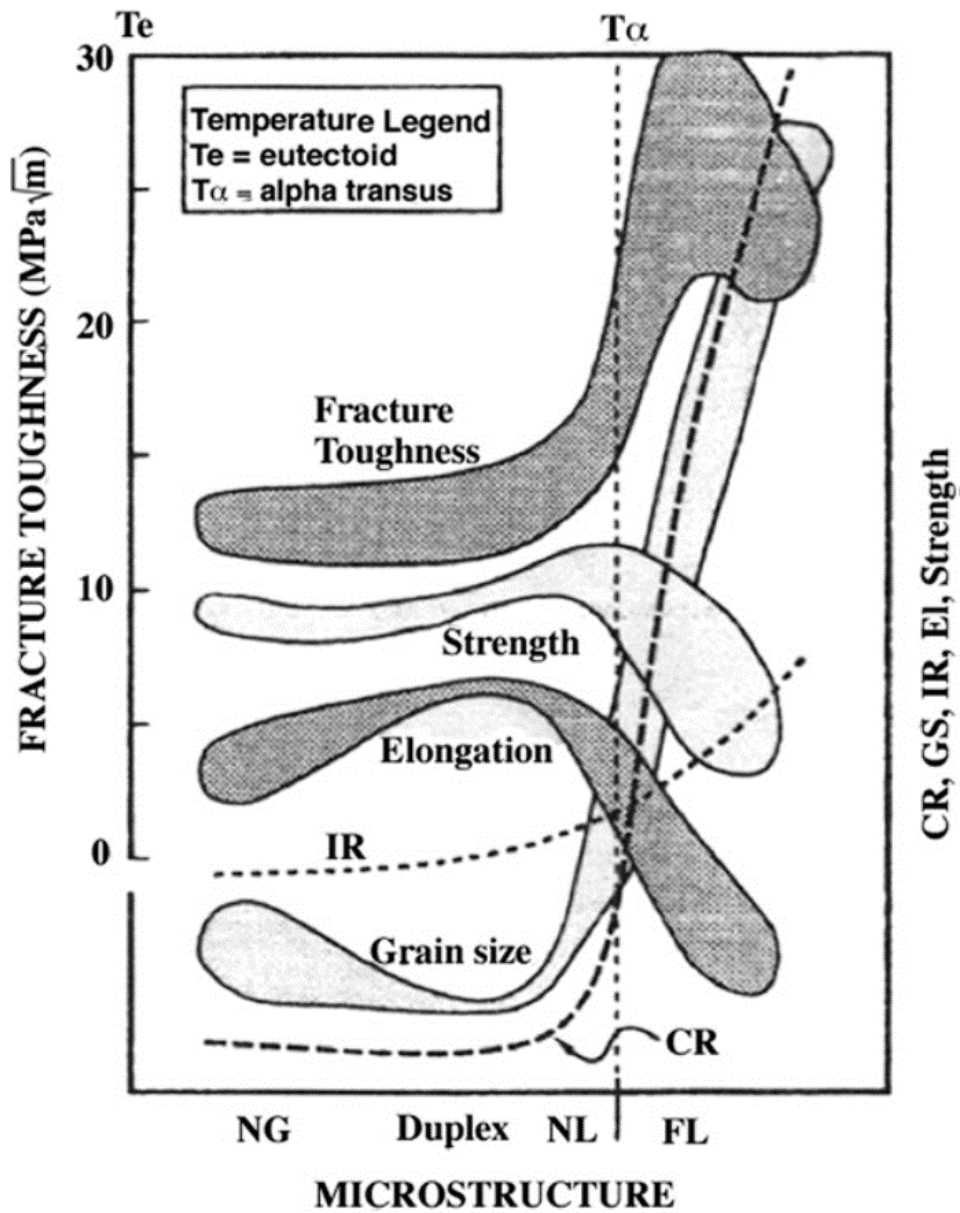


Figure 19: Dependence of mechanical properties (fracture toughness, strength, ductility, impact resistance, creep resistance) and grain size on the microstructure (Near Gamma, Duplex, Nearly lamellar, Fully Lamellar) [4].

In **Figure 20** the comparison of tensile yield strengths at different temperatures of various  $\gamma$ -TiAl alloys is reported [3].

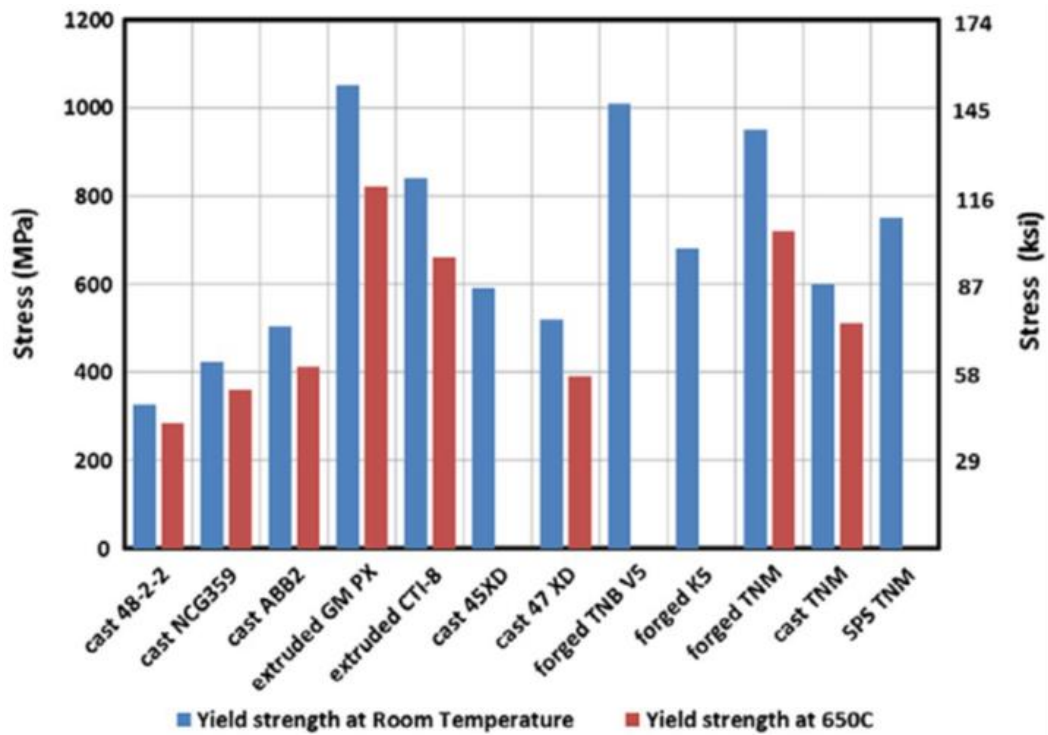


Figure 20: Yield strengths of TiAl-based alloys at room temperature and at 650°C [3].

The yield strength greatly depends from chemical compositions and method of production of the TiAl alloys. In every case, the yield strength decreases with the temperature increases.

The typical oxidation performances of second, third generation TiAl alloys and coated TiAl alloys are compared in **Figure 21** [3].

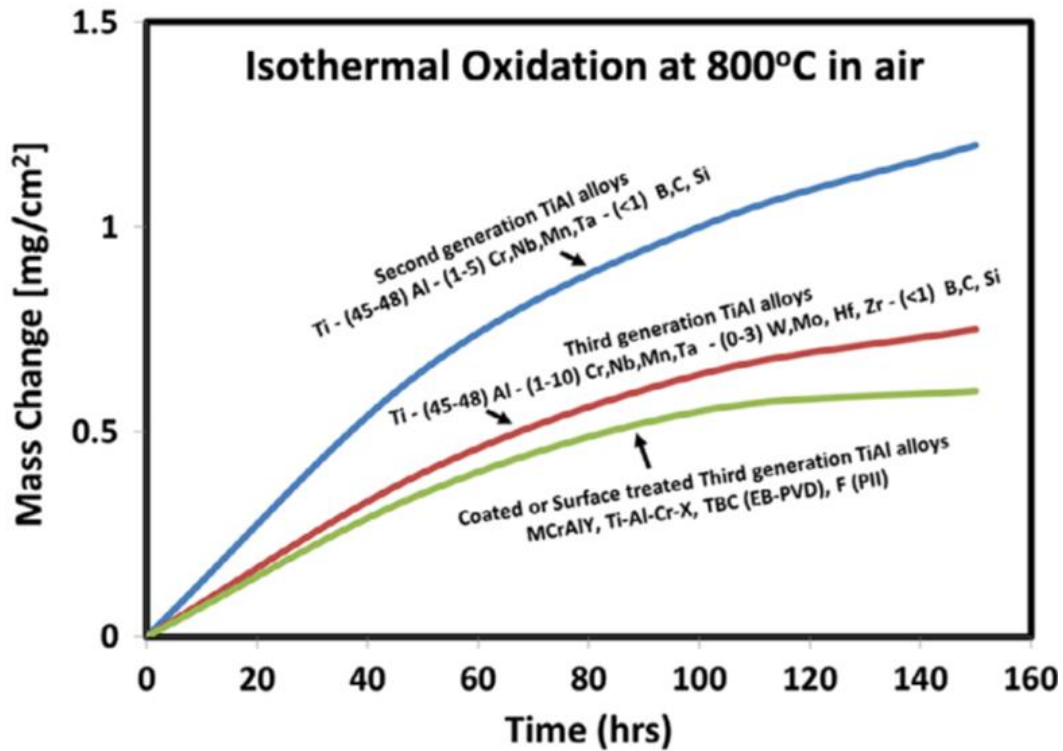


Figure 21: Oxidation behaviour of coated and uncoated TiAl alloys [3].

According to previous studies [3],[5],[22],[26],[27] the oxidation behaviour of TiAl intermetallic alloys very often depends on many factors such as: Ti/Al ratio, alloying elements, different microstructures, temperature, atmosphere conditions ect.

The aluminium concentration in TiAl alloys [26],[28] plays a very important role, because aluminium can form protective oxide scale ( $\text{Al}_2\text{O}_3$ ) on the surface and, as a consequence, this barrier hinders inward diffusion of oxygen and further oxidation [5]. Titania ( $\text{TiO}_2$ ) and alumina form on surface at the same time. As it is known, the titania, a fast-growing oxide, does not provide long-term oxidation protection [22] because the diffusion of oxygen and metal ions through titania is faster than through alumina [29]. The activation energy for titania formation is lower than that of alumina and this leads to faster growth of  $\text{TiO}_2$  with respect to  $\text{Al}_2\text{O}_3$  [5],[30],[27]. Only an increase of Al to Ti atomic ratio limits the growth of both  $\text{TiO}_2$  and the whole oxide layer [27]. For example, the activation energy for oxidation of the binary Ti-50Al (% at.) alloy is 423 kJ/mol, while for pure Ti alloy is 239 kJ/mol [27].

In addition, a higher activation energy may be attributed to formation of the  $\gamma$  phase (TiAl), which exhibits significantly better oxidation resistance than  $\alpha_2$  phase (Ti<sub>3</sub>Al). The oxidation resistance of  $\alpha_2$  and  $\gamma$  phases depends on several factors: solubility of oxygen in these phases and diffusion of aluminium and titanium. Both  $\gamma$  and  $\beta$  phases show a low level of oxygen solubility, while  $\alpha_2$ -phase shows an higher level [7]. According to the literature, the oxygen solubility in  $\alpha_2$  phase is 12-15% and in  $\gamma$  phase is 2-3% [2], this means that oxygen penetrates faster into  $\alpha_2$  phase than into  $\gamma$  and  $\beta$  phases. The  $\alpha_2$  phase (Ti<sub>3</sub>Al) contains less aluminium than  $\gamma$  (TiAl). The diffusion coefficient of aluminium at 800 °C in  $\alpha_2$  phase ( $1.6 \times 10^{-20} \text{m}^2 \text{s}^{-1}$ ) is lower than in  $\gamma$  ( $8 \times 10^{-20} \text{m}^2 \text{s}^{-1}$ ) and  $\beta$  phase ( $1.1 \times 10^{-14} \text{m}^2 \text{s}^{-1}$ ). The lower oxygen solubility, the higher aluminium content and aluminium diffusion rate (that could promote the formation of alumina) in  $\gamma$  phase with respect to  $\alpha_2$  phase could be responsible for the better oxidation resistance of  $\gamma$  phase. On the other hand also the diffusion coefficient of titanium at 800 °C in  $\alpha_2$  phase ( $2.1 \times 10^{-19} \text{m}^2 \text{s}^{-1}$ ) is lower than in  $\gamma$  phase ( $9.9 \times 10^{-19} \text{m}^2 \text{s}^{-1}$ ) and  $\beta$  phase ( $1.3 \times 10^{-14} \text{m}^2 \text{s}^{-1}$ ), and this is not favourable for the formation of a passive layer on the surface in the case of  $\gamma$  and  $\beta$  phases. However, the diffusion rate of Ti in  $\alpha_2$ ,  $\gamma$  and  $\beta$  phases is bigger than that of Al in these phases [7]. Therefore, on the basis of the diffusion rate of metallic elements, TiO<sub>2</sub> should form preferentially in the initial oxidation step of both  $\alpha_2$ ,  $\gamma$  phases. The limited aluminium diffusion, in particular in the case of  $\alpha_2$  phase, leads to poor formation of aluminium oxide protective layer during initial oxidation [31]. After the formation of an initial oxide layer, the oxidation progress depends on the diffusion of oxygen, titanium and aluminium through the preformed oxide. The activation energy for the diffusion of oxygen in TiO<sub>2</sub> (234 kJ/mol) is lower than the oxygen diffusion in Al<sub>2</sub>O<sub>3</sub> (587 kJ/mol) [27]. The activation energy for the diffusion of the titanium in TiO<sub>2</sub> (257 kJ/mol) is lower than the activation energy for aluminium diffusion in Al<sub>2</sub>O<sub>3</sub> (477 kJ/mol) [27]. Conclusively, the diffusion of both oxygen and metal occurs faster inside TiO<sub>2</sub>, which should grow more quickly than Al<sub>2</sub>O<sub>3</sub>. Therefore the only way to limit the formation of TiO<sub>2</sub> in a binary Ti-Al alloy is to increase the Al:Ti atomic ratio.

Potentially, the binary Ti-Al alloys with very high aluminium concentration should display excellent oxidation resistance. Unfortunately, these alloys show poor mechanical properties, and therefore they are not suitable for high temperature applications in aerospace and automotive sectors. Better mechanical behaviour can be achieved by adding alloying elements and designing ternary and quaternary alloys. Some of these alloying elements are detrimental for oxidation resistance, but other alloying elements can counterbalance their effects.

The effect of Cr, Si, Nb, Mo, Ta and W addition on the oxidation resistance has been well investigated [4],[8],[5],[22],[32]. The relative effectiveness of beneficial elements follows the order: W>Mo>Nb>Si [20],[29]. For example, the activation energy for oxidation of TiAl alloys with Nb high content was founded about 296 kJ/mol and 268 kJ/mol for Ti-43Al-11Nb and Ti-30Al-2.7Nb respectively [24], then Nb increases the activation energy, but it still remain lower

that the activation energy for Ti-50Al (423 kJ/mol) [27]. The Nb ions inside the oxide scale slows the diffusion of oxygen. In addition, the thermodynamic activity of aluminium enhances compared to that of titanium, which reduces the rutile growth rate and facilitates the alumina formation [25],[33]. Unfortunately a content of Nb over 10 % at. favours the formation of Ti-Nb and Al-Nb mixed oxides, which decreases the oxidation resistance. The Mo significantly reduces the oxygen solubility in the TiAl-based alloys and enhances the aluminium diffusion, thus enabling the alumina formation on the surface [7],[22],[16]. The silicon can play a beneficial effect on the oxidation resistance at low temperature, since it forms silicides and silica, which acts as a barrier for oxygen diffusion [32],[16],[34]. However, an excessive content of Si causes the oxide layer exfoliation [34]. A chromium content below 4% leads to a detrimental effect on the oxidation resistance. On the contrary, a beneficial effect of Cr is observed when its percentage ranges between 8 % at. and 10 % at., even though over 10% at. it worsens the mechanical properties [28],[27]. In fact, the formation of a Cr<sub>2</sub>O<sub>3</sub> diffusion barrier, inhibiting ion mass transport, improves the high temperature oxidation resistance of TiAl alloys [5]. According to the literature, several combinations of alloying elements create a synergistic effect in quaternary TiAl-based alloys. For example, the couples Cr with Nb [16], Nb (5-10% at.) with Si (1-5% at.) [35] and Mo with Nb [7],[36] display this synergistic effect which results in the accelerated growth of alumina. However, the contemporary presence of Cr, Nb and Mo together in TiAl alloys was not found to improve the oxidation resistance, contrary to the couples Nb-Cr and Nb-Mo [28].

After the primary formation of mixed oxides, the oxidation mechanism of TiAl system completely depends on inward and outward transport processes: the thermal diffusion of metal and oxygen ions in bulk and grain boundaries of oxide layer and the transport of electrons and holes through the oxide scale (Wagner's oxidation theory). The **Figure 22** shows the diffusion process inside the oxide layer, where the diffusion of O<sup>-2</sup> ions across the oxide layer was caused by Nernst potential coming from the difference in partial pressure of oxygen. On the base of diffusion processes Wagner proposed the parabolic law for the growth of the oxide layer.

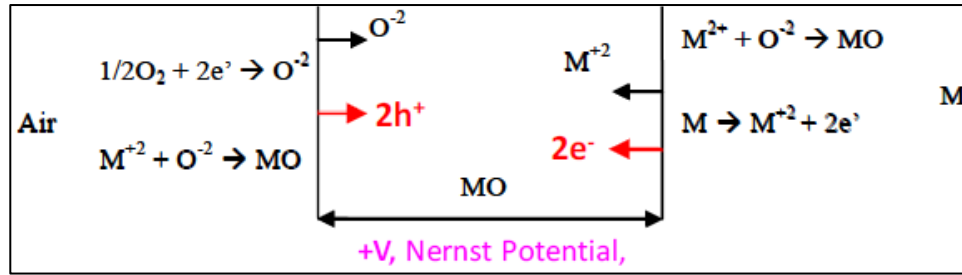


Figure 22: Wagner's parabolic model.

The kinetic parameters (parabolic constant rate and activation energy) for the oxidation of complex intermetallic TiAl alloys in the temperature range of interest could be investigated according to Wagner's theory.

Since the oxide layer growth on TiAl alloy is controlled by diffusion the velocity of mass gain decreases with the time, because the thickness of the oxide layer increases. The Wagner's law for oxide layer growth is represented below:

$\left(\frac{\Delta m}{A}\right)^2 = K_p t$ , where the  $K_p$  is parabolic rate constant,  $\Delta m/A$  is weight gain of the sample per unit of surface area and  $t$  is the time.

The  $K_p$  value increases with the temperature growth.

The relation between the parabolic rate constant  $K_p$ , the temperature and the activation energy can be expressed by the Arrhenius equation:  $K_p = K_0 e^{\left(-\frac{Q}{RT}\right)}$ , where  $K_0$  is a constant,  $Q$  is the activation energy for the oxidation,  $R$  is the gas constant and  $T$  is the temperature in K.

The Arrhenius equation can be also written (taking the natural logarithms of both parts) as:  $\ln(K_p) = \ln(K_0) - \frac{Q}{RT}$ .

By plotting  $\ln(K_p)$  versus  $1/T$  the activation energy for oxidation  $Q$  can be calculated from the slope of the straight line fitting the experimental data [22].

A high value of activation energy  $Q$  indicates that the alloy has good oxidation resistance.

## **1.2 Oxidation protection: surface modification and coating deposition**

The surface modification or the adoption of protective coatings can significantly improve the oxidation resistance of TiAl alloy [22]. After an initial oxidation, an oxide layer forms on the modified surface or coating. This oxide scale becomes a diffusion protective barrier that reduces the oxidation kinetics of complex intermetallic substrate. Unfortunately, after the prolonged oxidation most of thermal barrier systems tends to form inherently brittle phases that lead to a deterioration of the mechanical properties of surfaces or spallation.

In general for TiAl alloys several anti-erosion and oxidation protection surface treatments have been proposed: thermal diffusion (plasma carburization, nitriding, sulphidation, and cc.), low-oxidation partial pressure treatment, ion implantation, laser surface alloying, aluminizing, sol-gel process [8],[22].

At present, these surface treatments should be further investigated, and improved for long period applications.

### **1.2.1 Surface modification and surface alloying**

The thermal diffusion is very convenient and most used technique for surface microalloying and development of modified surfaces. Several thermal diffusion methods have been developed: solid, liquid, or gas thermal diffusion, plasma thermal diffusion and compound thermal diffusion. The main advantage of thermal diffusion is the excellent metallurgical bonding between new-alloyed surface and substrate. The alloying elements penetrate into the surface under heat action, thus modifying the surface composition. The diffusion of Al, Si, Cr, Nb, C, S and Mo elements can improve the oxidation behaviour of titanium aluminides forming suitable modified surfaces. After oxidation, the alloyed surfaces transform into compact protective oxidised scales, where the oxygen and metal ions diffusion is rather difficult [5].

The thermal diffusion of Si results in the formation of  $Ti_5Si_3$  and  $TiSi_2$  phases on TiAl surfaces. After oxidation up to 1000°C mainly alumina and silicon dioxide form on Ti-Si compounds. The complex protective scale impedes the Ti outward-diffusion and O inward-diffusion, which improves the oxidation resistance. In addition, the Ti-Si compounds have very similar thermal expansion coefficients

with respect to the TiAl substrate, which hinders spallation and results in good thermal cycling resistance [37],[38].

The oxidised scale formed after 1000 cycles at 950°C was continuous, adherent and without cracks (**Figure 23**)[38].

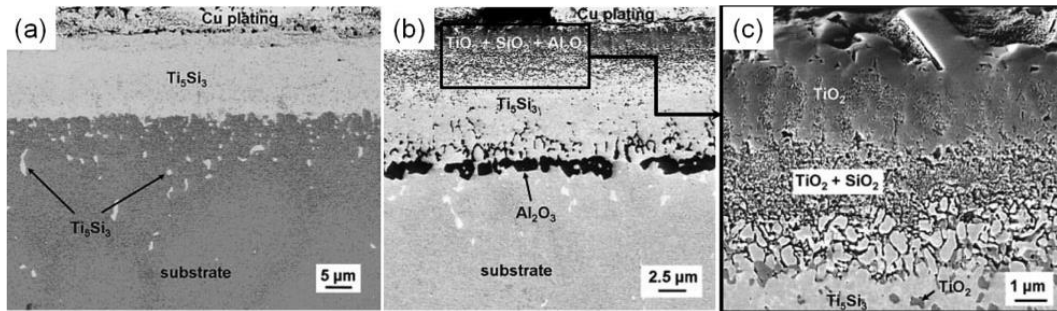


Figure 23: SEM micrograph of Si-based coating deposited on TiAl alloy: (a) after 100h at 1000°C ( $10^{-6}$  mbar), (b) and (c) after 1000 cycles at 950 °C in air [38].

The chromizing of Ti-6Al-4V alloy by double glow plasma creates a dense chromized coating and Ti-Cr mutual diffusion layer. After 100 h at 850°C, on the surface a  $\text{Cr}_2\text{O}_3$  external layer and a  $\text{TiO}_2$  internal layer form. The compact chromium oxide inhibited the oxygen diffusion [39].

Also a Nb alloying coating was deposited on Ti-6Al-4V [40] and Ti-Al [41] alloys by double glow plasma thus improving significantly their oxidation resistance.

Carburized samples of Ti-Al alloys showed good oxidation resistance at 900°C owing to the formation of a complex multilayer made of (from outside to inside):  $\text{TiC}/(\text{Al}_3\text{Ti})\text{C}_{1-x}/\text{carbide}/(\text{Ti}_3\text{Al})\text{C}_{1-x}/\text{carbide}/\text{the substrate}$  [42].

The Mo surface alloying provided good oxidation resistance below 650 °C of Ti-6Al-4V alloy, unfortunately at 850°C the molybdenum protective coating lost any protective effect [43].

In the S alloyed coatings, S reacted with Ti forming  $\text{TiS}_2$  and favouring the  $\text{TiAl}_3$  and  $\text{TiAl}_2$  Al-rich phase's formation. Sulfurizing resulted in enhanced oxidation resistance at 900° C [44].

Oxidation treatments under low oxygen partial pressure or pre-oxidation of Ti-Al-based alloy are suitable for the initial formation of a protective scale. According

to thermodynamic equilibrium conditions, mainly alumina formation can be observed under low oxygen partial pressure. An initial oxide layer that contains alumina and several other oxides ( $\text{Al}_2\text{TiO}_5$ ,  $\text{TiO}_2$  etc.) improves the high temperature oxidation resistance, but it is not effective for very long periods [5].

Ion implantation is a surface modification process, which involves the impact on the sample surface of ions accelerated by an electrical field. The main advantage of this process is that it is a low temperature method, which allows the perfect implantation on TiAl surface of the almost all elements and their combinations such as: metallic ions (Al, Nb, Mo and Si), non-metallic ions (C, Cl, F, I) or combined ions (C+Nb, Al+Nb and Si+Nb). The concentration of implanted ions can be controlled and reproducible, the bonding with the substrate is quite good but the process is rather expensive [5].

The Al, Si, or Mo ion implantation favours the alumina formation during initial oxidation [45].

In addition, the Nb implantation promotes the formation of an Al enriched layer on the oxidized surface decreasing the content of titania [46].

Combined ion implantation of Nb with other elements (C, Al or Si) into the surface of TiAl based alloys, improves oxidation resistance of alloy and stabilizes the beneficial presence of these elements in the extremal scale [47],[48],[49].

The halogen elements such as F, Cl, Br and I implanted into the surface lead to improved oxidation resistance of TiAl alloys. The halogen elements depress the oxygen ions diffusion and react with Ti giving compounds that volatilize during oxidation. The titanium halide become gas at high temperature and therefore mainly alumina forms on TiAl surface. In addition, aluminium halides at high temperature concentrate at the interface between oxide scale and substrate via diffusion through pores/cracks, and they successively oxidise into alumina. The compact scale of alumina improves the oxidation behaviour of TiAl alloy. Anyway the ion implantation of halides shows some drawbacks: formation of very thin films (about  $0.5 \mu\text{m}$ ) that limits the application for long-term, and high cost of production [50],[51],[52],[53].

Laser surface alloying is a surface engineering process, which exploits the short-time interaction between a directed energy laser beam and a pre-deposited layer of alloying elements or compounds and can affect the underlying substrate.

The final coating has good metallurgical bonding with the underlying material, dense microstructure and controllable thickness. This technique permits the deposition of many different coatings on several substrates, including Ti-Al traditional and intermetallic alloys [5].

The TiAl laser surface alloyed with C and C-Nb resulted in good oxidation resistance at 870 °C [54].

The Ti-6Al-4V laser surface alloyed with Al+Nb mixture exhibited good oxidation resistance due to the formation of a complex coating consisting of TiAl<sub>3</sub>/TiAl/Al. In fact, a continuous and dense alumina protective scale appeared after oxidation of this laser surface alloyed material [55]. Similarly, laser surface alloying with aluminium powders in nitrogen atmosphere was adopted to greatly improve the oxidation resistance, at high temperature and for long time, of Ti-6Al-4V. Unfortunately, this kind of coating shows poor wear behaviour [56].

Generally speaking, the laser surface alloying seems a very promising method for processing protective coatings, but further process improvement is necessary for practical applications. In fact, the shielding gas or gas formed during the reaction with the substrate easily cause the formation of defects as pores, while the high heating and cooling rate during deposition creates cracks inside the coating [5].

In the following a more detailed presentation of some protective coatings for oxidation protection is given. Alternative methods for processing more or less thick protection coatings frequently consist in the surface deposition of metal-based coatings and complex thermal barrier coatings, formerly developed for the oxidation protection of nickel superalloys.

### **1.2.2 Aluminizing**

The aluminising of TiAl surface, resulting in an Al rich layer (TiAl<sub>3</sub>), also can improve the oxidation resistance by promoting alumina formation [57].

The aluminised layer can be obtained in different ways: aluminium deposition by ion-beam-assisted-deposition, aluminium cladding, PVD deposition of TiAl<sub>3</sub> and pack cementation (PC) [22].

For PC process powder mixtures containing pure and alloyed aluminium are commonly used, with the addition of inert filler (for example alumina) and an activator (halide salt e.g a fluoride). For instance the diffusion of Al, leads to TiAl<sub>3</sub>

formation on the Ti-Al surface. Unfortunately, some cracks form inside the oxide layer and the substrate made of brittle  $\text{TiAl}_3$ . This happens because of the thermal mismatch between  $\text{TiAl}_3$  and the substrate. In order to reduce the thermal stresses and decrease the cracks formation, a  $\text{TiAl}_3/\text{TiAl}_2$  multilayer can be adopted [58].

Also the inter-diffusion between substrate and coating results in the formation of a  $\text{TiAl}_2$  intermediate layer (**Figure 24,(a)**)[59].

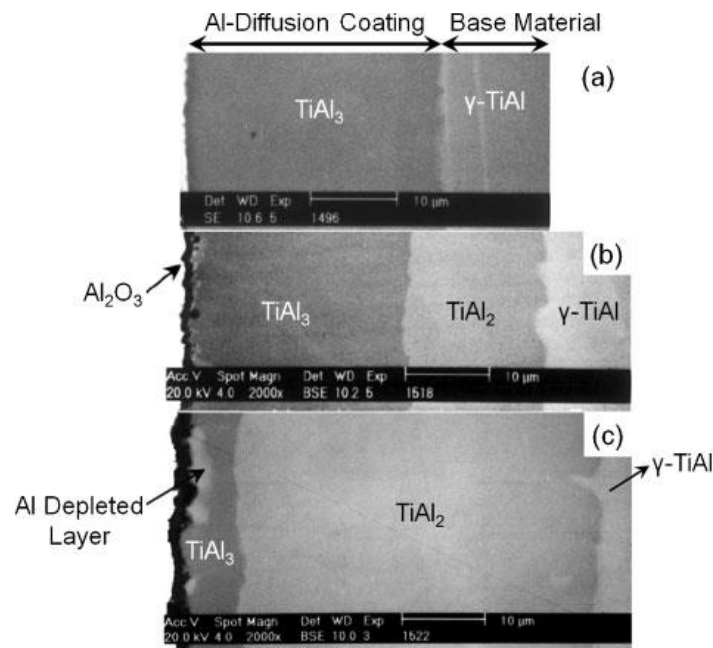


Figure 24: SEM cross section of  $\gamma\text{-TiAl}$  alloy aluminised at 800 °C for 5 h in a low Al activity pack: a) as processed, b) after 10h isothermal oxidation at 900 °C and c) after long term oxidation of 100h at 900°C [59].

After oxidation, the external part of the coating gives rise to alumina formation (with traces of  $\text{TiO}_2$ ), while progressively  $\text{TiAl}_3$  transforms into  $\text{TiAl}_2$  (**Figure 24, b and c**). In addition,  $\text{TiAl}_3$  is rather brittle and shows poor cracking resistance due to the low symmetry of its tetragonal  $\text{DO}_{22}$  structure [59].

Some alloying element of TiAl alloys (Nb or Cr) showed beneficial effects on the aluminised layer in terms of coating stability and microstructure. In fact, the aluminising rate of TiAl alloys increases with small content of Nb or Cr, aluminising kinetics promotes the Al diffusion and leads to the formation of a stable  $\text{TiAl}_3$  layer with less surface cracks [60].

The oxidation mechanism of aluminised surface, based on the diffusion of several elements, is depicted in **Figure 25**. After long term oxidation (e.g. at 800-1000°C) the surface layer consists of four different layers: external alumina scale with contamination of rutile, underlying  $\text{TiAl}_2$  layer coming from Al depletion of  $\text{TiAl}_3$ , two layers containing Al and Ti with an aluminium concentration decreasing with the distance from the surface [57].

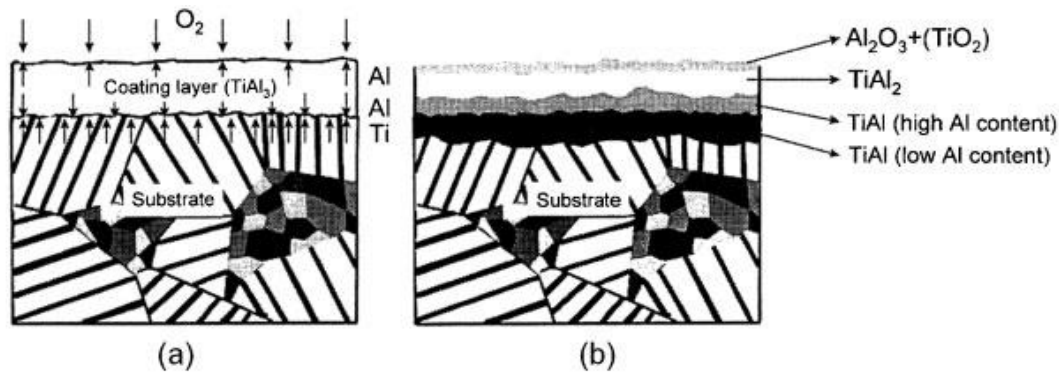


Figure 25: The oxidation process of aluminised  $\gamma$ -TiAl alloy (at 800°C for 3 hours): (a) initial oxidation (b) morphology of the layer after prolonged oxidation [57].

### 1.2.3 MCrAlY overlay coatings

In addition to aluminizing, also MCrAlY overlay coatings have been traditionally used for the oxidation protection of materials for high temperature applications. For this reason these kind of coatings, that are very effective when deposited on the surface of nickel superalloys, have been tested for the oxidation protection of the TiAl intermetallic alloys too. The overlay coatings can be deposited by using to main techniques: electron beam physical vapour deposition (EB-PVD) and low-pressure plasma spray (LPPS). In both cases the surface layer (about 100  $\mu\text{m}$  thick) is deposited at high temperature under vacuum and controlled atmosphere. EB-PVD process is based on the evaporation of coating material by means electron beam and subsequent deposition on the substrate. During the LPPS process a plasma containing drops of molten MCrAlY is sent to the surface where it solidifies.

The MCrAlY overlay coatings ( $M=\text{Co}$ ,  $\text{Ni}$  and  $\text{Ni}+\text{Co}$ ) at 800-900°C in air suffer oxidation giving rise to a complex structure [61],[62].

The MCrAlY coatings are currently used to protect Fe-, Co-, Ni-based superalloys [63],[64],[65]. When deposited on surface of  $\gamma$ -TiAl alloys they oxidize giving mainly  $\text{Al}_2\text{O}_3$ ,  $\text{Cr}_2\text{O}_3$  and nickel oxides on the surface. Cr promotes the

formation of alumina while even little amounts of Y strengthen the interfacial bonds between the oxide layer and the substrate [22]. During the oxidation, Al and Ti diffuse towards the surface and Ni and Co diffuse towards the substrate. The diffusion of these elements causes the formation of a diffusion interlayer placed between the MCrAlY and the substrate. The interlayer shows a complex composition as it contains intermetallic phases like AlNi<sub>2</sub>Ti or AlCo<sub>2</sub>Ti and other ternary components. The formation of the interlayer worsens the mechanical properties and this can cause crack growth [66],[65].

For instance from **Figure 26** it can be observed that some cracks formed on the CoCrAlY surface after 100 cycles at 1000°C [65].

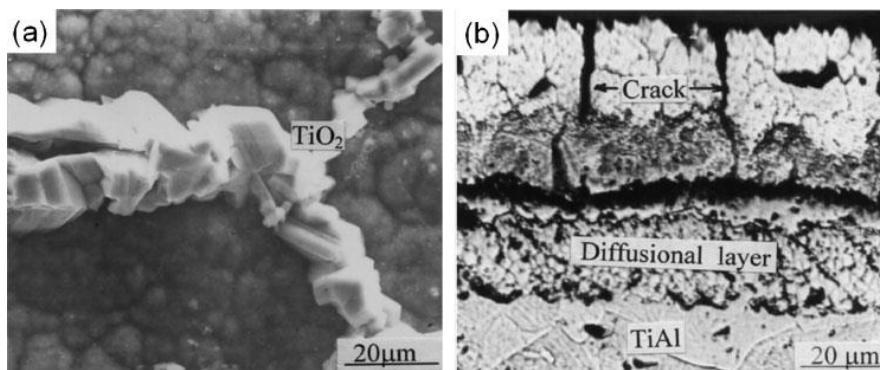


Figure 26: CoCrAlY coated  $\gamma$ -TiAl after 100 cycles at 1000°C: (a) surface morphology, (b) cross-section microstructure [65].

After prolonged cycling (100 cycles at 1000°C), the harmful TiO<sub>2</sub> also appeared on the surface of the CoCrAlY and NiCrAlY deposited on the surface of an intermetallic alloy [65].

In order to prevent the above mentioned inter-diffusion suitable barriers can be put between MCrAlY coating and  $\gamma$ -TiAl [67],[68].

For example, after the isothermal oxidation at 900°C, the Al/Al<sub>2</sub>O<sub>3</sub>/NiCoCrAlY coating system deposited on the Ti-48Al-2Cr-2Nb surface granted better oxidation resistance than the monolithic NiCoCrAlY coating. In this case, the Al/Al<sub>2</sub>O<sub>3</sub> interlayer avoided the Ti outward-diffusion and Ni/Co inward-diffusion. The AlCo<sub>2</sub>Ti and AlNi<sub>2</sub>Ti brittle intermetallic phases were not formed inside of the NiCoCrAlY coating. In addition, a compact scale made of alumina only formed on the coating surface [68].

The NiCrAlY coating plasma sprayed on TiAl-4Nb-3Mn (% at.) and TiAl-2Nb-2Mo (% at.) beta gamma alloys sustained very well cyclic oxidation up to 1000°C [69],[70]. The **Figure 27** depicts the coating modification with the number of cycles [69].

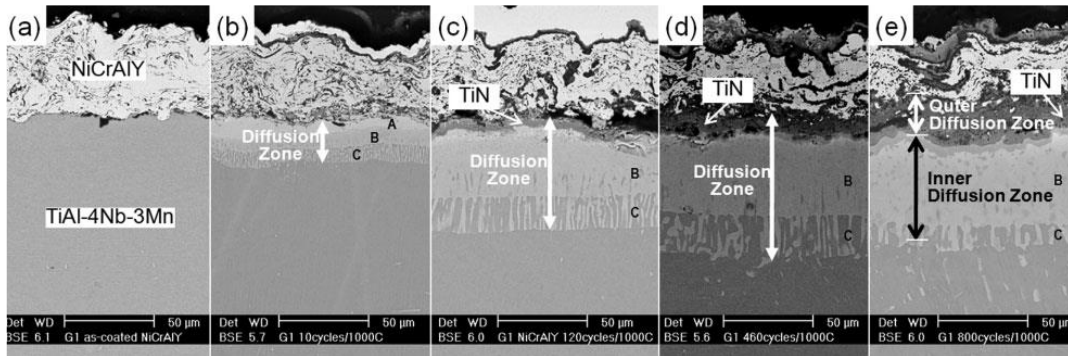


Figure 27: SEM (a) as-processed NiCrAlY coated TiAl-4Nb-3Mn (% at.) alloy, (b) oxidized after 10 cycles and (c) 120 cycles, (d) 460 cycles (e) 800 cycles at 1000°C [69].

A TiN layer grew in any direction at interface between coating and substrate. The  $N_2$  passed very easily through porous NiCrAlY coating (obtained by plasma spray) and reacted with Ti diffusing from the substrate. The formed TiN interfacial layer, when enough thick, blocked both inward Ni diffusion and outward Ti diffusion (**Figure 28**) [69].

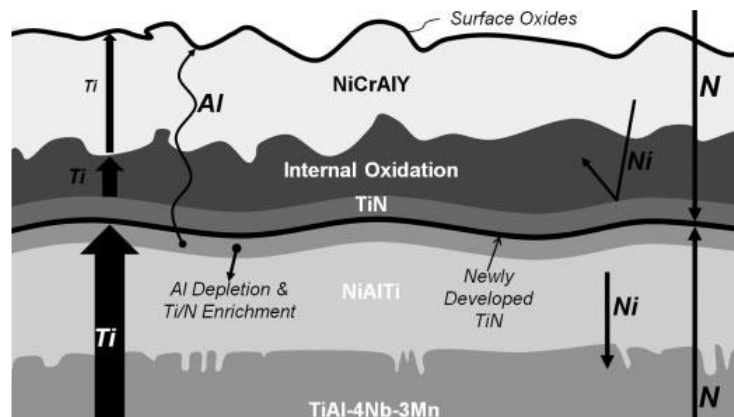


Figure 28: SEM/EDS analysis of NiCrAlY coating deposited on TiAl-4Nb-3Mn (at.%) alloy during cycling oxidation at 1000°C after 800 cycles [69].

Generally, the severe Ni inward diffusion created a complex diffusion zone of  $Ni_2TiAl/NiTiAl/(NiTiAl+TiAl)$  between TiAl alloy and NiCrAlY coating. The

$\text{Ni}_2\text{TiAl}$  external part of the diffusion zone is progressively converted to  $\text{TiN}$  with the time [69],[70].

The  $\text{TiAl-4Nb-3Mn}$  (% at.) alloy coated with  $\text{NiCrAlY}$  showed a similar oxidation mechanism dominated by inward and outward diffusion of several elements (**Figure 29**) [70].

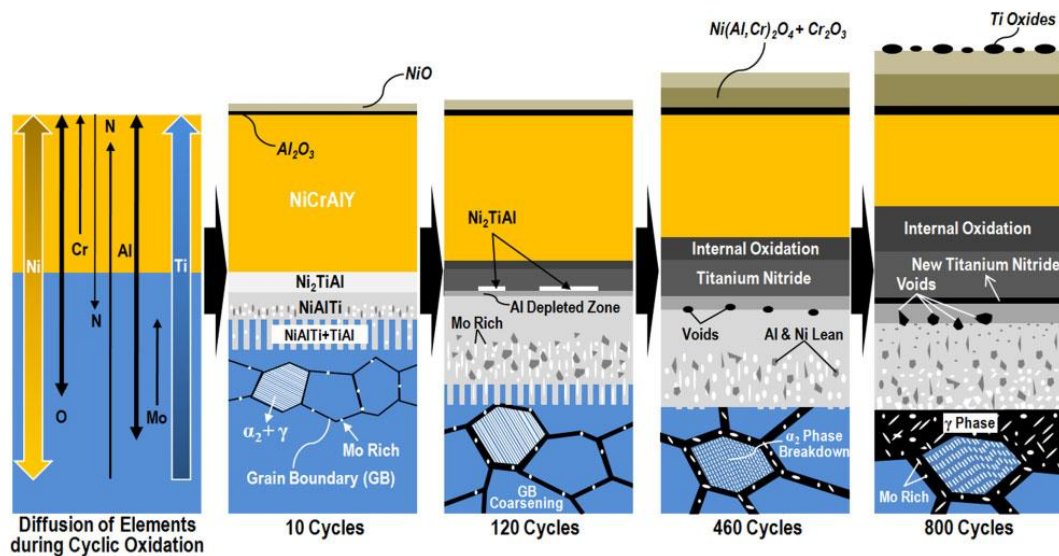


Figure 29: Diffusion processes occurring in  $\text{NiCrAlY}$  coated  $\text{TiAl-4Nb-3Mn}$  (% at.) alloy during cycling oxidation at  $1000^\circ\text{C}$  [70].

Nickel diffused not only inward but also outward leading to the formation of  $\text{NiO}$  phase in top of surface. A bright globular phase of  $\text{Mo}$  formed in the inner-diffusion zone. The  $\text{Mo}$  diffusion also caused the widening of the grain boundary regions of  $\text{TiAl-4Nb-3Mn}$  (% at.) alloy. After long term oxidation, the outward diffusion of  $\text{Al}$  through the  $\text{TiN}$  interlayer created pores below the  $\text{TiN}$  layer (**Figure 29**)[70].

### 1.2.4 Thermal barrier coatings (TBC)

This kind of protection systems have been developed for the components of turbine engines (typically turbine blades) that operate at the highest temperatures and are traditionally fabricated by using nickel-based alloys [61],[62].

The TBC is composed of two coatings deposited of the surface of the component: an internal layer that can be either an aluminium rich layer obtained by

aluminizing or a MCrAlY deposited by plasma spray, and an external ceramic layer made of zirconia partially stabilized by yttria, deposited by plasma spray or electron beam assisted physical vapour deposition [5],[6],[61],[71]. According to current industrial practice the zirconia layer is deposited by EB-PVD on an aluminized bond coat while low pressure plasma spray ( or vacuum plasma spray are used for depositing the ceramic layer on the MCrAlY bond coat.

The structure of a TBC is represented in **Figure 30** [71].

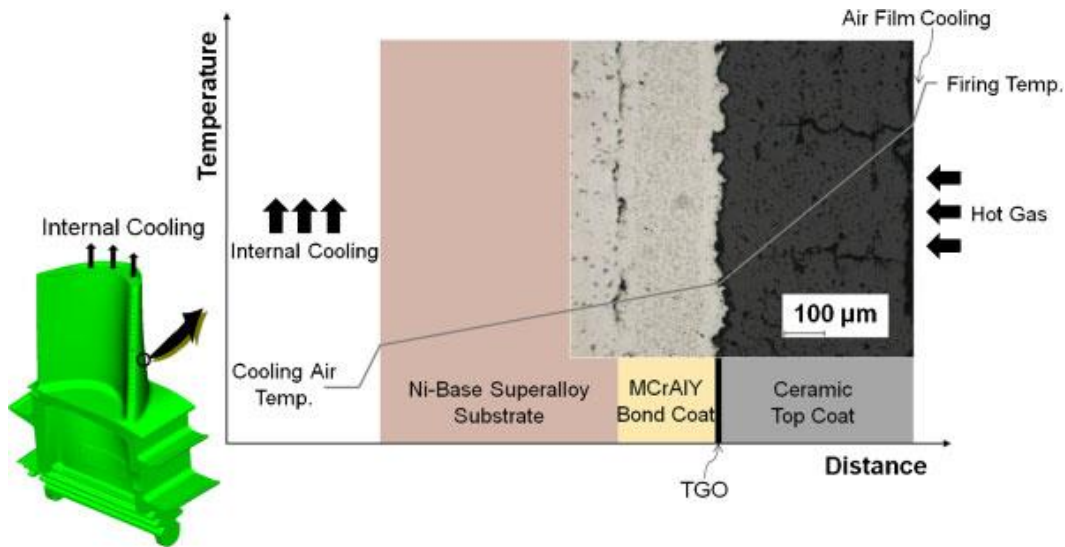


Figure 30: The cross-section of thermal barrier coating in a first stage blade [71].

The external ceramic layer (Top Coat-TC) exerts an insulating effect and creates a temperature gradient within the TBC, thus lowering the temperature of the substrate. The Top Coat is porous and therefore does not grant any protection from oxidation. The underlying layer rich of alumina (aluminized or MCrAlY layer called Bond Coat-BC) reacts with the oxygen easily diffusing through the Top Coat and it gives rise to an intermediate alumina layer called Thermally Growth Oxide (TGO). The interfacial bonds between the TC and the MCrAlY is generally better (because of the roughness of the MCrAlY surface) than those between the TC and the aluminized layer, but this last more easily oxidises to alumina. The thermal expansion of the TC is very similar to that of the BC, but strong thermal mismatch exists between TGO and BC, which results in important thermal stresses. The thermal stresses increase with the growth of the alumina layer, and cause the failure of the TBC when the thickness of the alumina layer reaches a critical value. The TBCs were also tested for the protection of  $\gamma$ -TiAl alloys, and in this case, the TBC

failure also occurred after the growth of the alumina layer up to a critical thickness [5],[71].

**Figure 31** shows the cross section of a TBC deposited on  $\gamma$ -TiAl before and after 100 h of oxidation in air at 900 °C [72].

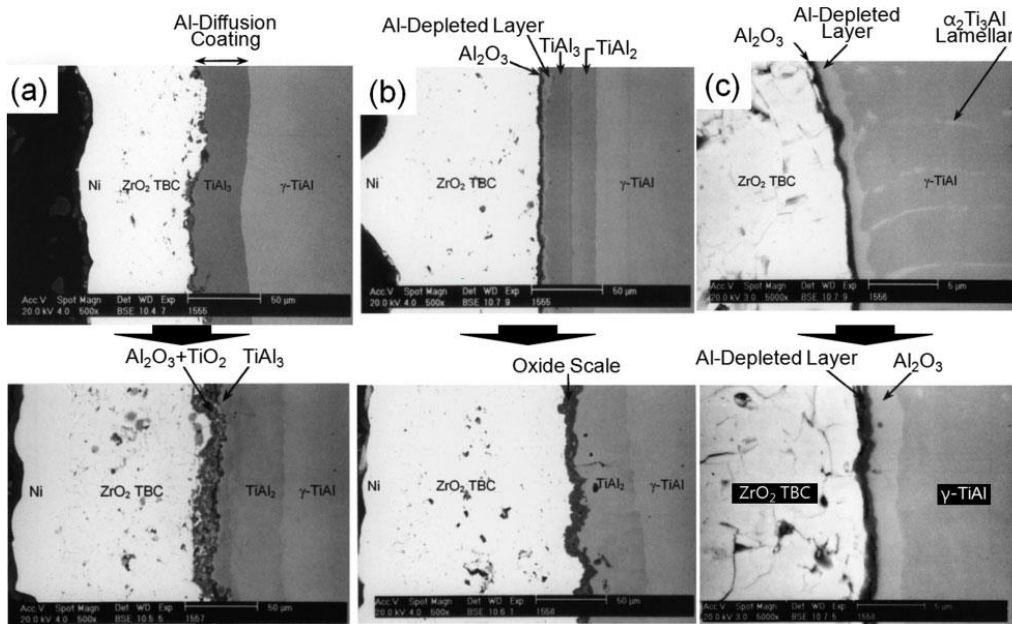


Figure 31: SEM images of cross-section of TBC/  $\gamma$ -TiAl alloy (in up of the figure - complex system before oxidation, in down- after oxidation in air at 900 °C): a) aluminized BC, b) substrate pre-oxidation in air, c) substrate pre-oxidation in oxygen [72].

Sample “a” was processed by using an aluminized layer as BC, sample “b” was obtained by performing a pre-oxidation in air of the substrate before the aluminizing treatment and sample “c” was obtained by performing this preliminary pre-oxidation in oxygen. The best oxidation protection was obtained for sample “c” which showed the best interfacial bonds between the TGO (containing not only alumina but titania too) and the BC. The aluminized BC consists of  $\text{TiAl}_3$  and  $\text{TiAl}_2$ , but it transforms progressively in  $\gamma$ -TiAl because of the diffusion of aluminium towards the substrate. Other kinds of BC (Ti-Al-Cr-Y-N, Ti-Al-Cr) were tested as an alternative to aluminized BC. In general the BCs provide oxidation protection to  $\gamma$ -TiAl alloys (e.g. Ti-45Al-8Nb at.%) for several hundreds of thermal cycles up to 850-950° C. The failure of these protection systems entails crack formation and spallation, which is promoted by the possible presence of porosity inside the BC

and the TGO. In addition, the presence of Ti inside the BC and then the presence of TiO<sub>2</sub> inside the TGO decreases the oxidation protection capability. The BCs based on aluminides unfortunately show great brittleness, which is detrimental for the mechanical behaviour (crack formation under limited thermal stress). These kind of TBCs should be optimized in terms composition and processing path in order to ensure long-term oxidation protection of  $\gamma$ -TiAl alloys. Finally, it should be considered that the processing of complex TBCs is quite expensive and they are successfully adopted for components that are internally cooled. In addition the processing of circuits for internal cooling in  $\gamma$ -TiAl alloys represents a big challenge because of their intrinsic brittleness [72].

### 1.2.5 Metal-based coatings specifically designed for Ti-Al alloys

Since the overlay coatings show poor chemical and physical (thermal expansion) compatibility with both Titanium alloys and Ti-Al intermetallic alloys, alternative metal-based coatings have been investigated.

These metal-based coatings can be used as an alternative of surface modification and aluminizing. Various coatings (Al-X, Ti-Al-X, Ti-Al-Cr-X) can be deposited by different technics: PVD, CVD, ion plating, thermal spraying, laser cladding, sol-gel etc. [3],[5],[6],[22],[73].

The metal-based coatings Al-X (X=Si, Nb, Cr, Y) have been formerly developed to improve the oxidation resistance of traditional Ti-Al based alloys, and more recently have been considered for oxidation protection of intermetallics. These coatings have excellent thermal stability and their high content of aluminium leads to formation of a scale rich in alumina [3],[5].

The Al-Si coating deposited on Ti-6Al-4V by low oxygen partial pressure fusing method after cyclic oxidizing showed the formation of a continuous layer of alumina on the top of surface. The formed Si-enriched layer impeded the diffusion into the coating of elements detrimental for oxidation resistance. The Al-Cr coating fabricated by low oxygen partial pressure self-fusing technique on Ti-6Al-4V showed excellence oxidation resistance at 600°C [74].

The TiAl-based alloy with Al+Y coating, co-deposited by the single EB-PVD process, during oxidation at 900°C and 1000°C formed an interlayer of alumina and an outer layer of (Y,Al)O. The (Y,Al)O external layer acts as a stabiliser of the

coating and leads to a compact oxide scale which greatly enhances the oxidation resistance [75].

More complex Al-based coatings were also investigated. The Ti-2.5Al-5V-5Mo alloy was coated by low-pressure plasma spraying with quasi-crystalline coating Al-Cu-Fe-Cr (mix of icosahedral quasi-crystalline phases  $\text{Al}_{65}\text{Cu}_{20}\text{Fe}_{15}$ ,  $\text{Al}_{65}\text{Cr}_5\text{Cu}_{20}\text{Fe}_{10}$  and crystalline  $\text{Al}_2\text{Cu}$ ). After cycling oxidation test at  $650^\circ\text{C}$  and  $800^\circ\text{C}$ , the stable and compact scale (showing no spallation) consisted of  $\text{Al}_2\text{O}_3$  in the external part and a mixture of  $\text{Cr}_2\text{O}_3$ ,  $\text{CuO}$  and  $\text{FeO}$  in the inner part [76].

However, the Al-X coatings shows thermal expansion coefficient different from that of the substrate and, for this reason, suffer of rapid degradation and cracking [5].

The metal-based Ti-Al-X (X=Nb, Cr) coatings can provide excellent oxidation protection for  $\gamma$ -TiAl alloys under isothermal and cyclic oxidation, because they have compositions and thermal expansion coefficients similar to the substrate [63],[77].

The magnetron sputtered Ti-50Al-10Cr (% at.) coating deposited on  $\gamma$ -TiAl alloy was tested under isothermal and cyclic conditions. After testing at  $900^\circ\text{C}$  for h 1000 and at  $1000^\circ\text{C}$  for 100 cycles, a continuous and adherent alumina layer was formed on the surface, while chromium and titanium oxides were present inside the scale and gave rise to the growth of a very thick layer (**Figure 32**). It was proposed that chromium can promote the alumina formation [64],[65].

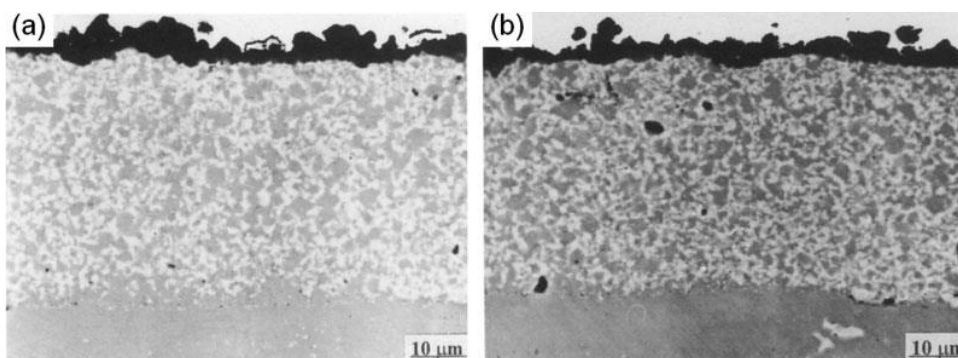


Figure 32: Cross section of Ti-50Al-10Cr (at.%) coating deposited on Ti-50Al (at.%): a) after exothermal oxidation-1000 h of at  $900^\circ\text{C}$ , b) after 100 cycles at  $1000^\circ\text{C}$  [65].

A Ti-51Al-12Cr (% at.) coating deposited by low-pressure plasma spray (LPPS) demonstrated thermal and chemical properties very similar to those of Ti-48Al-2Cr-2Nb (% at.) substrate, and alumina grew on this surface in the temperature range 800-1000°C in air. A Ti-51Al-12Cr (% at.) coating was also applied by magnetron sputtering onto Ti-45Al-8Nb (% at.). This coating provided oxidation protection during cycling (350 cycles) in the temperature range 750-900°C in air, while the oxide layer grown on the uncoated alloy quickly underwent spallation under these test conditions [63].

Both Ti-37Al-14Cr and Ti-50Al-10Cr coatings were tested showing good compatibility with TiAl substrate and excellent cyclic oxidation resistance without crack and spallation [5].

These Ti-Al-Cr coatings proved to be effective for oxidation protection, but their lifetime is limited. The main components of the coating are  $\gamma$ -TiAl and Ti(Cr,Al)<sub>2</sub> Laves phase, which become unstable after long period oxidation. In fact, after long-term oxidation at 900°C the degradation of Ti-Al-Cr coating occurred: the alumina formation caused the depletion of Al in the coating under the oxide scale and the  $\gamma$ -TiAl phase transformed into the cubic Al-Ti-O (Z-phase); the Cr inward-diffusion unto substrate caused depletion of Cr and the dissolution of Laves phase in the coating. In particular, the degradation of Z phase leads to rapid oxidation as shown in **Figure 33** [6].

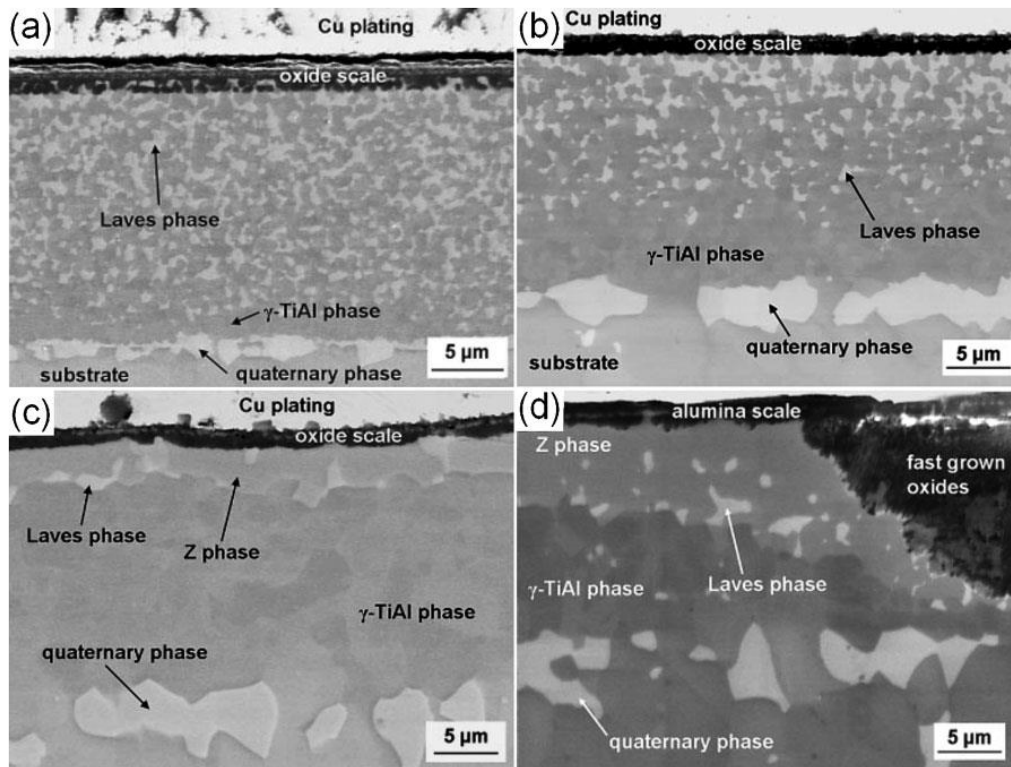


Figure 33: SEM images of Ti-51Al-12Cr (% at.) coating deposited on Ti-45Al-8Nb (% at.): (a) after 10 cycles at 900°C in air, (b) after 120 cycles at 900°C in air, (c) after 120 cycles at 950°C in air, (d) after 700 cycles at 900°C in air [6].

In addition, also Ti-Al-Cr coatings with higher aluminium concentration were investigated. An amorphous Al-21Ti-23Cr (% at.) coating, deposited on the Ti-48Al (% at.) substrate by magnetron sputtering, after isothermal oxidation at 1000°C for 100h transformed into a mixture of  $\text{Cr}_2\text{Al}$  and  $\text{Ti}(\text{Cr},\text{Al})_2$  phases, during the contemporaneous formation of a continuous scale of alumina. After further oxidation at high temperature the  $\text{Cr}_2\text{Al}$  phase disappeared while  $\gamma\text{-TiAl}$  became the main component of the coating (**Figure 34**). Obviously, the high aluminium content is responsible for the excellent protective film, in particular the  $\text{Ti}(\text{Cr},\text{Al})_2$  phase helps alumina formation [78].

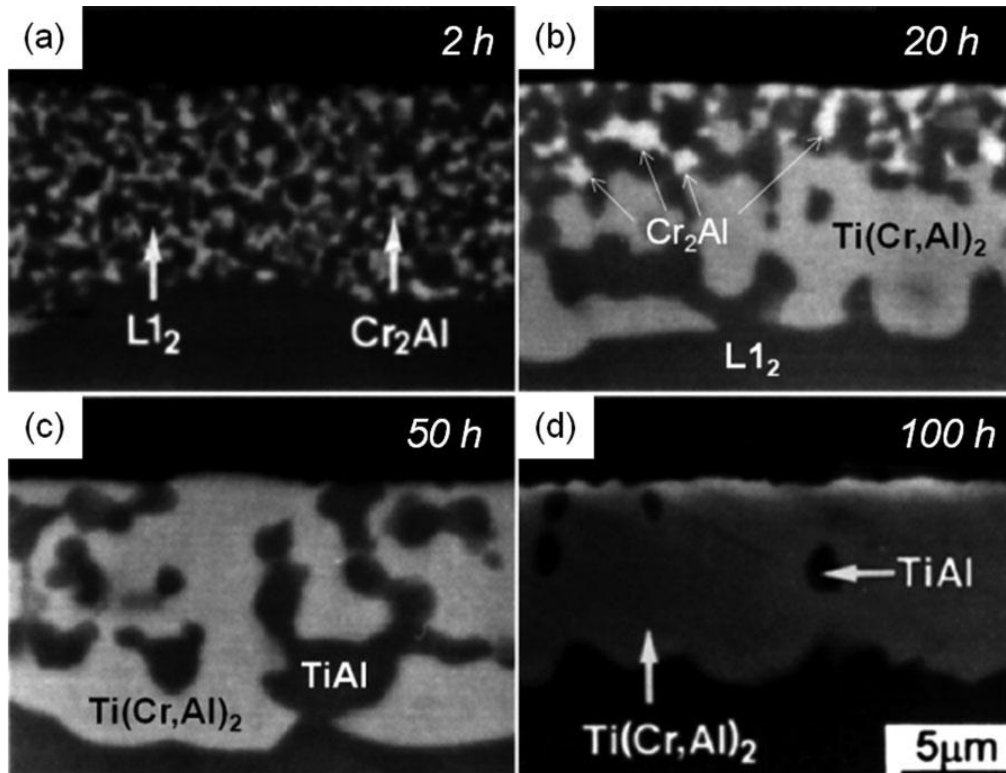


Figure 34: Al-21Ti-23Cr (% at.) coating deposited on Ti-48Al (% at.) alloy after isothermal oxidation at 1000°C: (a) after 2h, (b) after 20 h, (c) after 50 h, (d) after 100 h [78].

The substitution of Cr with Nb in Ti-Al-X coatings was investigated, but it did not result in any advantage. The Ti-46Al-5Nb and Ti-46Al-14Nb coatings deposited on Ti-48Al-2Cr-2Nb substrate were tested for 100 h at 900°C in air. A mixture of rutile and alumina formed after oxidation of the coatings containing Nb, which were initially constituted by  $\gamma$ -TiAl and  $Ti_3Al$  phases. These coatings provided a slight improvement of oxidation resistance with respect to the uncoated alloy, but the weight gain due to oxidation was a bit higher than that observed for Ti-Al-Cr coatings and spallation of the surface layer was observed [5],[77].

Also a Ti-Al-Cr (-Y) coating was tested for effective protection from oxidation of titanium aluminides. After oxidation, in the top of the surface a compact and continue alumina scale formed [79],[80],[81].

### 1.2.6 Titanium and aluminium based nitride coatings

More or less complex nitride coatings have been proposed for oxidation protection of Ti-Al intermetallic alloys. Some of them were obtained by adding nitrogen to the metal-based coatings discussed in the previous section.

The oxidised surface of a Ti-Al-Cr-Y-N coating after up to 3000 h of isothermal oxidation at 750°C showed very complex structure: it was composed by subsequent sub-layers made of a mix of titania and alumina with different ratio between the two oxides, and only small amounts of chromium and yttrium. Nitrogen was not found inside the external oxidized layer, but it concentrated inside the not-oxidized coating where no oxygen was detected [82]. However, the maximum useful temperature for Ti-Al-Cr-Y-N coating was 850°C, in fact at 900°C this coating showed scale spallation [6]. The Ti-Al-Cr-Y-N nitride coating granted excellent oxidation protection for 3000 h at 750 °C [82] and was rather effective up to 850 °C, but this coating is not suitable for long-term application at higher temperatures [6].

Nitride coatings TiAlN and TiAlxN have high temperature oxidation resistance, excellent wear resistance, and very high micro-hardness. The TiN/TiAlN composite coatings like  $Ti_{0.5}Al_{0.5}N/Ti_{0.7}Al_{0.3}N$  as well as simpler nitride coatings ( $Ti_{0.5}Al_{0.5}N$ ,  $Ti_{0.75}Al_{0.25}N$ ,  $Ti_{0.6}Al_{0.3}Si_{0.1}N$ ) were successfully deposited on Ti-based alloys by arc ion plating technique. [83],[84],[85],[86].

A (Ti-Al/Ti-Al-N)<sub>n</sub> multilayers coating was deposited on silicon and steel substrates by magnetron co-sputtering in Ar/N<sub>2</sub> gas mixture. In **Figure 35**, the XRD analyses of two different (Ti-Al/Ti-Al-N)<sub>n</sub> multilayer systems deposited onto silicon (100) are reported [87].

From the JCPDF 00-037-1140 (blue dash lines), the TiAlN phase has several peaks (hkl): (111) located at 37.5 (2θ°), (200) located at 43.72 (2θ°), (210) corresponded at 49.5(2θ°), (220) situated at 64 (2θ°), (311) located at 77(2θ°) and (222) situated at 81(2θ°). Only few of them can be clearly detected in the XRD pattern. A shift of diffraction angles in XRD spectrum was due to the compressive residual stress induced during a magnetron sputtering deposition of those complex multilayer systems, **Figure 35**.

According to JCPDF 00-005-0678 (black dash lines), TiAl phase has six diffraction peaks: (110) at 31.8 ( $2\theta^\circ$ ), (111) at 38.8 ( $2\theta^\circ$ ), (200) at 45.5 ( $2\theta^\circ$ ), (220) at 66 ( $2\theta^\circ$ ), (221) at 70.8 ( $2\theta^\circ$ ) and (301) at 75 ( $2\theta^\circ$ ), **Figure 35**.

Red dash lines (JCPDF 00-003-1144) refer to AlN phase: (100) at 33 ( $2\theta^\circ$ ), (002) at 35.8 ( $2\theta^\circ$ ), (102) at 59.5 ( $2\theta^\circ$ ), (204) at 61.5 ( $2\theta^\circ$ ) and (112) at 71.6 ( $2\theta^\circ$ ), **Figure 35** [87].

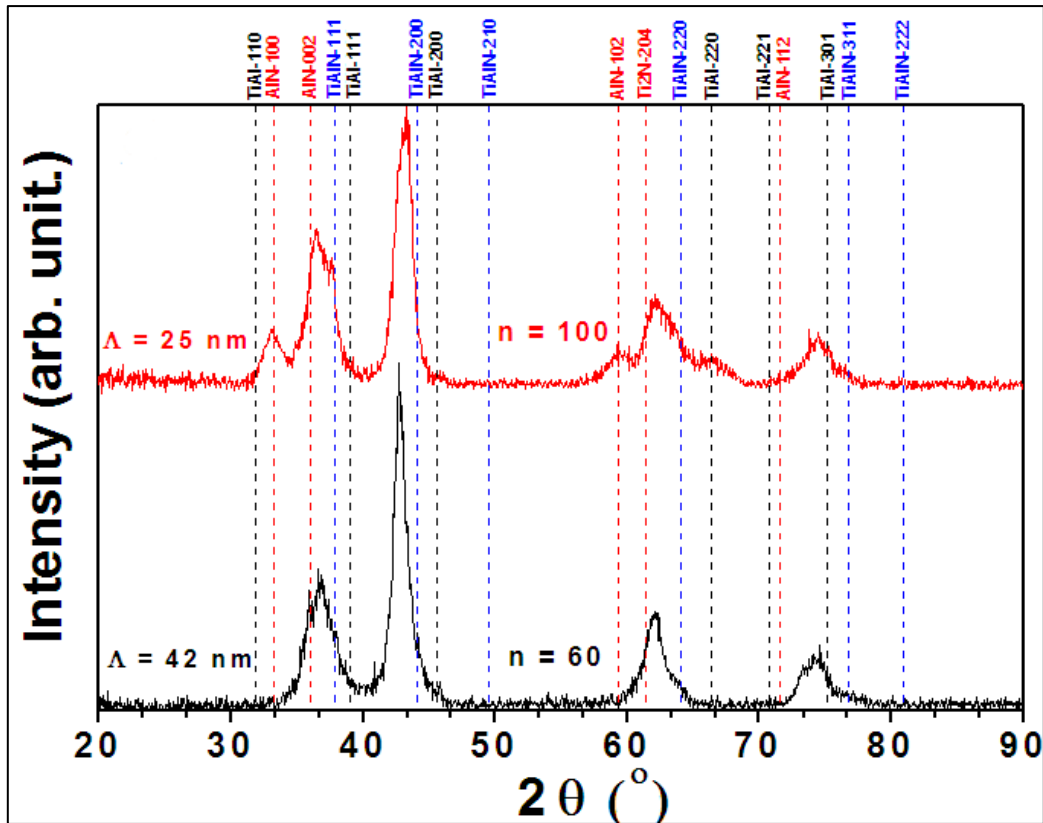


Figure 35: XRD patterns of the  $(\text{Ti-Al/Ti-Al-N})_n$  multilayer coatings deposited on silicon (100): black pattern - 60 multilayer system with a period of 42 nm, and red pattern - 100 multilayer system with a period of 25 nm. The positions of TiAlN peaks (JCPDF 00-037-1140), TiAl (JCPDF 00-005-0678) and AlN (JCPDF 00-003-1144) are indicated by dash lines [87].

The **Figure 36** shows the high resolution (HR) XPS spectra after oxidation (Ti 2p, Al 2p, N 1s and O 1s) of TiAlN coating deposited by a magnetron sputtering system on Si wafer substrate from Ti and Al targets, in nitrogen and argon atmosphere. The binding energies and the relative spectral areas for all TiAlN species that formed after deposition are reported in **Table 1**.

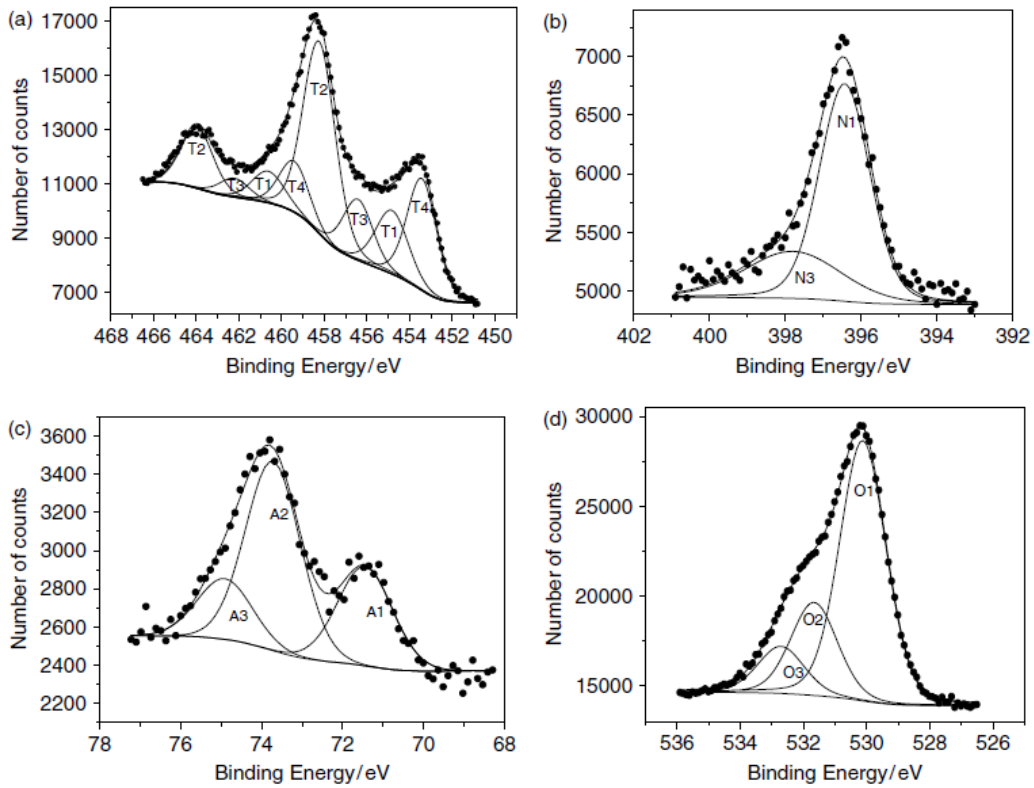


Figure 36: XPS peak fitting for a TiAlN coating: (a) Ti 2p, (b) N 1s, (c) Al 2p and (d) O 1s [88].

**Table 1:** XPS spectra analysis of as-deposited TiAlN layers [88].

| Element | Contribution      | Core level        | Binding energy (eV) | Relative spectral area (%) | Assignment                                       |
|---------|-------------------|-------------------|---------------------|----------------------------|--|
| Ti      | T1                | 2p <sub>3/2</sub> | 454.9               | 13                         | Ti in TiAlN                                      |
|         |                   | 2p <sub>1/2</sub> | 460.8               |                            |  |
|         | T2                | 2p <sub>3/2</sub> | 458.3               | 45                         | TiO <sub>2</sub>                                 |
|         | T3                | 2p <sub>1/2</sub> | 463.8               |                            |  |
|         |                   | 2p <sub>3/2</sub> | 456.4               | 14                         | Ti oxynitrides and/or satellite structure of TiN |
| T4      | 2p <sub>1/2</sub> | 462.2             |                     |                            |  |
|         | 2p <sub>3/2</sub> | 453.5             | 28                  | TiAl alloy                 |  |
| N       | N1                | 2p <sub>1/2</sub> | 459.5               |                            |  |
|         |                   | 1s                | 396.4               | 71                         | N in TiAlN                                       |
| Al      | A1                | 1s                | 397.8               | 29                         | N in Ti or TiAl oxynitrides                      |
|         |                   | 2p                | 71.5                | 29                         | Al in TiAl alloy                                 |
|         | A2                | 2p                | 73.7                | 54                         | Al in TiAlN                                      |
| A3      | 2p                | 74.8              | 17                  | Al-O bonds                 |  |

From the Ti 2p HR XPS, the dominant component is T2, corresponding to TiO<sub>2</sub>. The spin-orbit doublet of T2 is positioned at 458.3 eV (2p<sub>3/2</sub>) and 463.8 eV (2p<sub>1/2</sub>). The second intense peak is T4, attributed to Ti-Al metallic bonds. The binding energies of T4 are 453.5 eV (2p<sub>3/2</sub>) and 459.5 eV (2p<sub>1/2</sub>). T1 and T3 peaks have similar intensity. T1 corresponds to TiN or TiAlN and T3 can be attributed to TiN oxide or satellite signal of TiN. The binding energies of T1 are 454.9 eV (2p<sub>3/2</sub>) and 460.8 eV (2p<sub>1/2</sub>). The binding energies of T3 are 456.4 eV (2p<sub>3/2</sub>) and 462.2 eV (2p<sub>1/2</sub>). The N1s HR XPS plot shows N1 and N3 contributions: a dominant peak of TiAlN (N1), and a small peak that can be attributed to TiAlN satellite or TiAl oxynitrides. The binding energy of N1 is positioned at 396.4 eV and for N3 is placed at 397.8 eV. Al2p HR XPS plot shows three contributions (A1, A2 and A3). Binding energy of A1 at 71.5 eV, correspond to Ti-Al bond. The principal component is A2, probably attributable to TiAlN, with binding energy of 73.7 eV. The binding energy placed at 74.8 eV (A3) can be attributed to Al<sub>2</sub>O<sub>3</sub>. The O1s HR XPS plot consisted of 3 species: O1 (530.0 eV) refers to Ti-O bonds, O2 (531.6 eV) refers to OH<sup>-</sup> and O3 (532.8 eV) refers to adsorbed water [88].

According to some literature after oxidation at high temperature, alumina preferentially forms on the top of TiAlN system coatings. This alumina external layer hindered the inward oxygen diffusion and the underlying nitrogen rich coating impeded the diffusion of oxygen towards the substrate [5].

In addition, a TiAlCrN coating, deposited on the TC11 titanium alloy by arc ion plating method, showed excellent oxidation protection at 700°C for 100 h. The chromium addition led to (Ti,Al)N and (Ti,Cr)N nitrides formation. These phases inhibited the oxygen diffusion [89].

However, on the surface of these nitride coatings cracks formed after long-term oxidation at high temperatures; these cracks represented an easy path for oxygen diffusion and for this reason they caused severe oxidation of Ti-based alloy [5].

### **1.2.7 Tantalum and aluminium based nitride coatings**

Tantalum nitride is believed to display better properties with respect to titanium nitride because of its better corrosion resistance [90],[91], wear resistance [92], and hardness [92]. For these reasons tantalum nitride coatings were deposited on different substrates including Ti-6Al-4V alloy [43],[93].

Tantalum was also used for doping Ti-Al-N coatings with the aim of enhancing their oxidation resistance [94],[95]. However, at our knowledge, this kind of coatings was never tested in combination with TiAl intermetallic alloys.

For instance, Ta-Al-N coatings ( $Ta_{42}Al_8N_{50}$ ,  $Ta_{39}Al_{11}N_{50}$ ,  $Ta_{35}Al_{15}N_{50}$ ,  $Ta_{24}Al_{28}N_{48}$ ) were deposited on silicon substrates by magnetron sputtering at room temperature. In the **Figure 37**, the reactive magnetron co-sputtering method of TaAlN coating is shown [96].

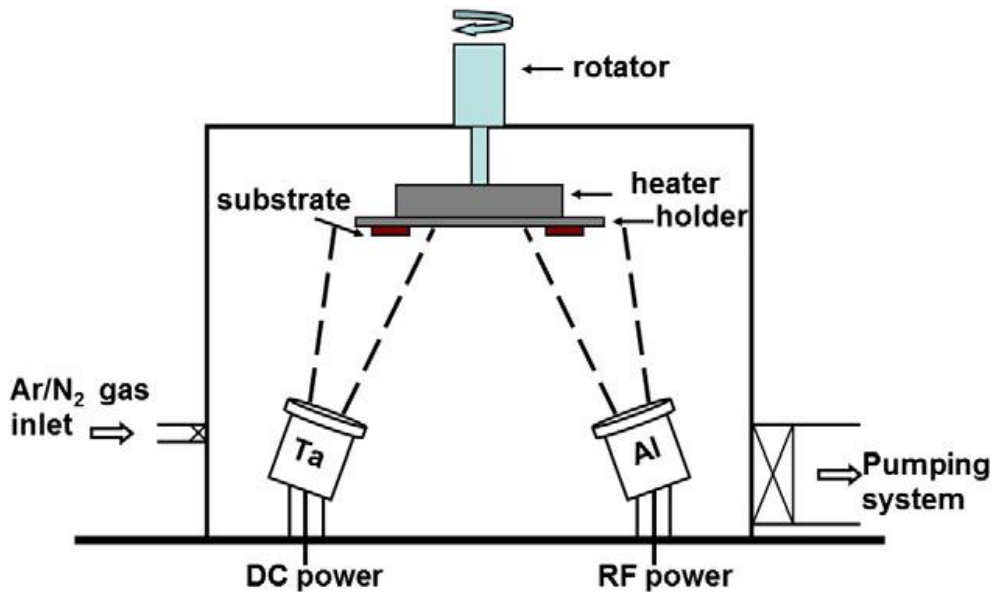


Figure 37: Schematic presentation of TaAlN deposition on silicon substrate by reactive magnetron co-sputtering [96].

Pure tantalum (99.95%) and aluminium (95.95%) with a diameter of 50.8 mm were used as the targets. The distance between targets and substrate was 90 mm. During the deposition, argon and nitrogen were used in the chamber, the flow rates were 12 and 8 cm<sup>3</sup>/min respectively, working pressure was 0.7Pa. The silicon substrate was fixed on rotated holder and during sputtering it swung at a speed of 5 rpm. The TaAlN coating was deposited for 40 minutes [96].

In **Figure 38**, the XRD patterns illustrates that all Ta-rich coatings have a face-centered-cubic crystalline structure (TaN); and Al-rich coating ( $Ta_{24}Al_{28}N_{48}$ ) probably has a near-amorphous structure, formed by crystallites of hexagonal AlN phase [96].

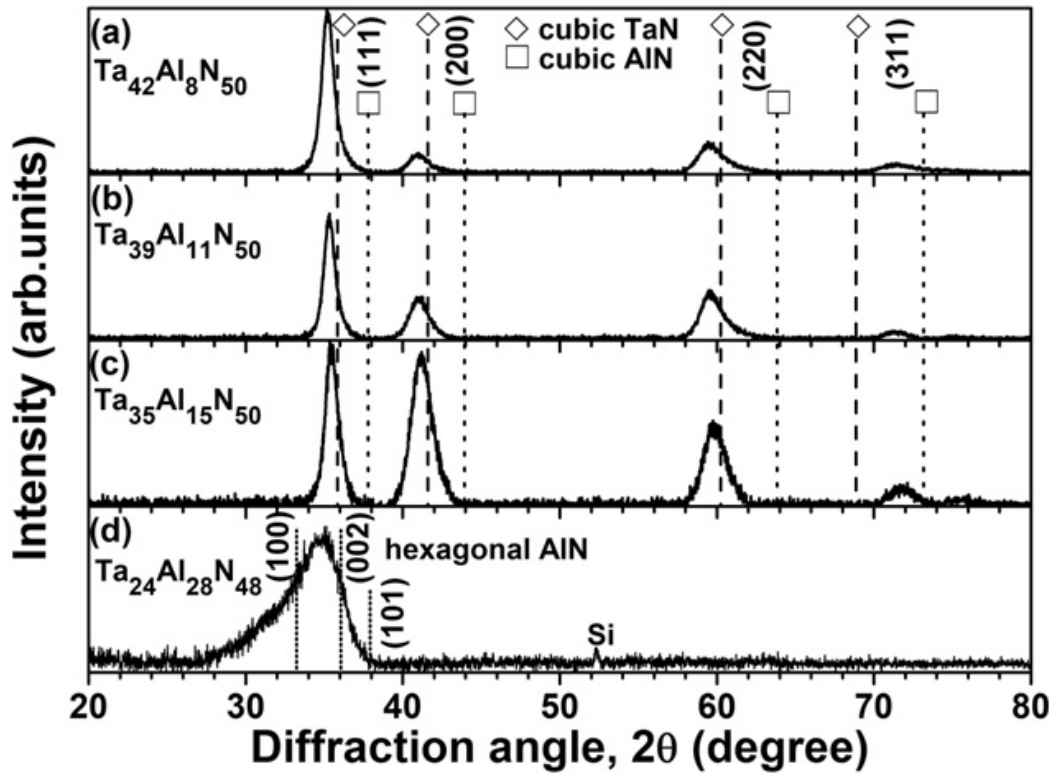


Figure 38: XRD patterns of as-deposited coatings: (a)  $\text{Ta}_{42}\text{Al}_8\text{N}_{50}$ , (b)  $\text{Ta}_{39}\text{Al}_{11}\text{N}_{50}$ , (c)  $\text{Ta}_{35}\text{Al}_{15}\text{N}_{50}$ , and (d)  $\text{Ta}_{24}\text{Al}_{28}\text{N}_{48}$  [96].

The  $\text{Ta}_{42}\text{Al}_8\text{N}_{50}$ ,  $\text{Ta}_{39}\text{Al}_{11}\text{N}_{50}$ ,  $\text{Ta}_{35}\text{Al}_{15}\text{N}_{50}$ ,  $\text{Ta}_{24}\text{Al}_{28}\text{N}_{48}$  coatings showed a columnar structure, and the  $\text{Ta}_{24}\text{Al}_{28}\text{N}_{48}$  coating exhibited a near-amorphous structure (**Figure 39**) [96].

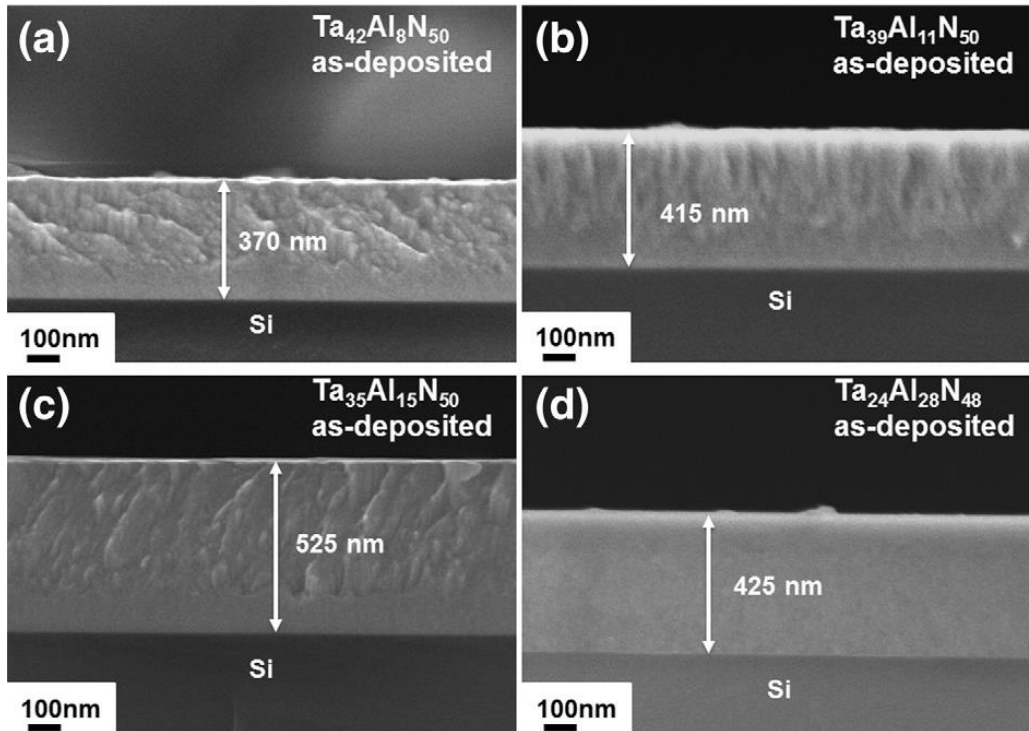


Figure 39: SEM cross-section of as-deposited coatings: (a)  $\text{Ta}_{42}\text{Al}_8\text{N}_{50}$ , (b)  $\text{Ta}_{39}\text{Al}_{11}\text{N}_{50}$ , (c)  $\text{Ta}_{35}\text{Al}_{15}\text{N}_{50}$ , and (d)  $\text{Ta}_{24}\text{Al}_{28}\text{N}_{48}$  [96].

In **Figure 40**, the XRD patterns of Ta-rich ( $\text{Ta}_{35}\text{Al}_{15}\text{N}_{50}$ ) and Al-rich ( $\text{Ta}_{24}\text{Al}_{28}\text{N}_{48}$ ) coatings are reported.

The XRD patterns of other Ta-rich coatings ( $\text{Ta}_{42}\text{Al}_8\text{N}_{50}$  and  $\text{Ta}_{39}\text{Al}_{11}\text{N}_{50}$ ) exhibited a similar trend to  $\text{Ta}_{35}\text{Al}_{15}\text{N}_{50}$ , for this reason they are not reported here. After exposition until  $600^\circ\text{C}$ , the Ta-rich coatings showed  $\delta$ -TaN structure. An amorphous dominant structure appeared at  $700^\circ\text{C}$  on Ta-rich coatings. After oxidation at  $800^\circ\text{C}$ , the Ta-rich coatings oxidized, and in the top tantalum oxide ( $\text{Ta}_2\text{O}_5$ ) formed. In case of Al-rich coating ( $\text{Ta}_{35}\text{Al}_{15}\text{N}_{50}$ ), aluminium oxide begins to form at  $600^\circ\text{C}$  after 16h [96].

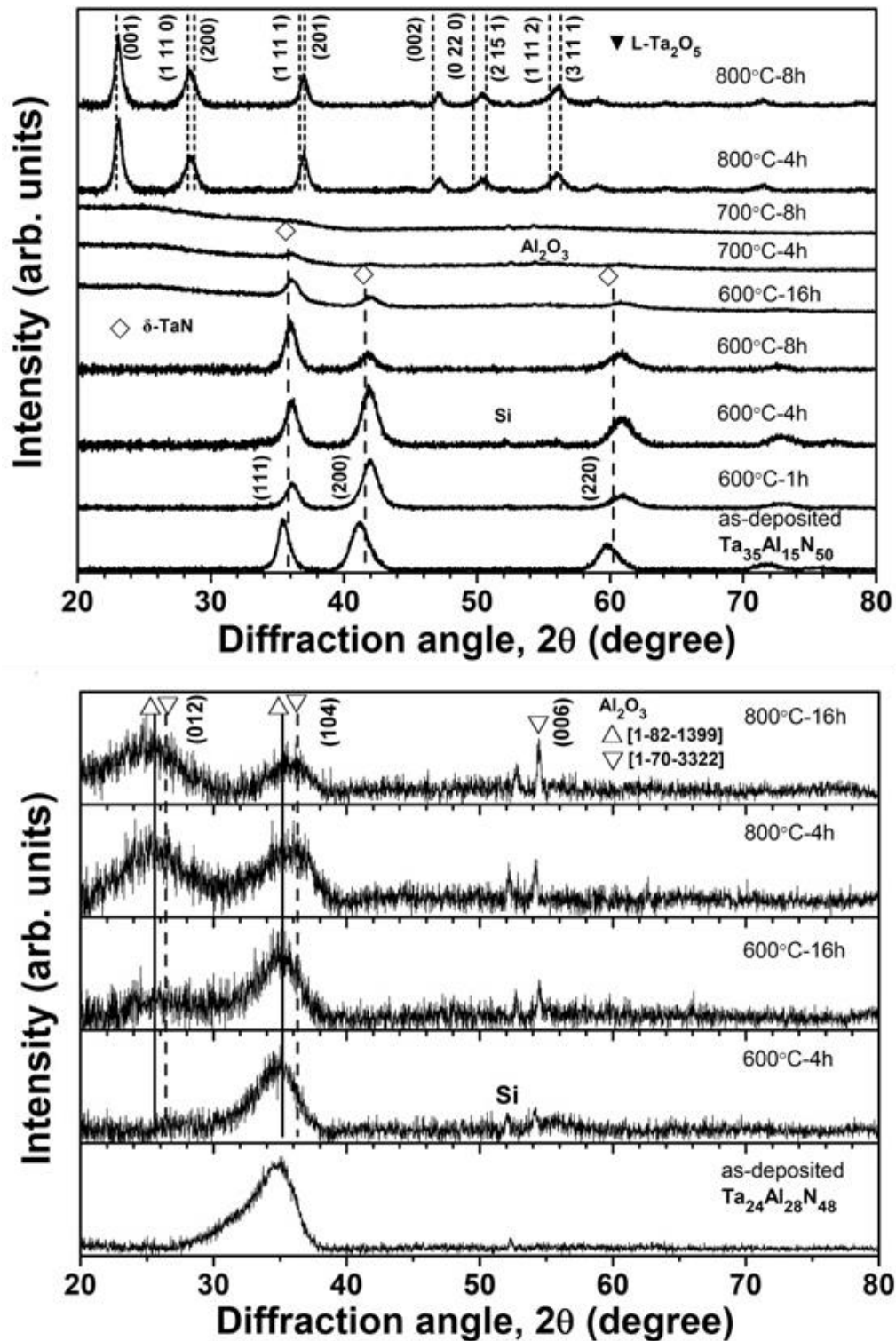


Figure 40: XRD coatings before and after isothermal oxidation at 600°C, 700°C, 800°C: (up)  $Ta_{35}Al_{15}N_{50}$ , and (down)  $Ta_{24}Al_{28}N_{48}$  [96].

Those Ta–Al–N coatings displayed good oxidation resistance in temperature range from 600 °C to 700 °C. The Ta<sub>35</sub>Al<sub>15</sub>N<sub>50</sub> coating exhibited a superior oxidation resistance with respect to similar coatings with a higher tantalum content when treated at 700 °C for 4 h. **Figure 41** [96].

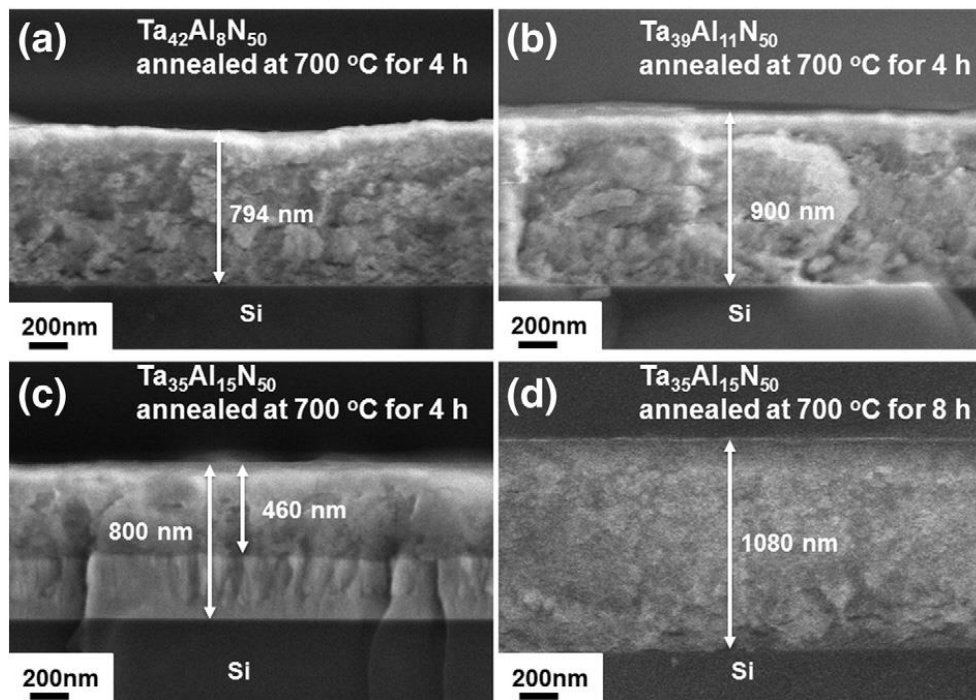


Figure 41: Cross-sectional SEM images of Ta-Al-N coatings after isothermal oxidation at 700°C: (a) Ta<sub>42</sub>Al<sub>8</sub>N<sub>50</sub>, (b) Ta<sub>39</sub>Al<sub>11</sub>N<sub>50</sub>, (c) Ta<sub>35</sub>Al<sub>15</sub>N<sub>50</sub>, and (d) Ta<sub>35</sub>Al<sub>15</sub>N<sub>50</sub> [96].

### 1.2.8 Ceramic oxide-based coatings

Ceramic system coatings as oxide coatings and enamel coatings have excellent thermal stability and oxidation resistance at high temperature. The oxide protective coatings deposited on the surface of titanium aluminides commonly are based on Al<sub>2</sub>O<sub>3</sub>, SiO<sub>2</sub> and Cr<sub>2</sub>O<sub>3</sub> [5].

The Ti-22Al-25Nb alloy covered by sol gel processing with silica coating and oxidized at 900 °C showed that the oxygen inward diffusion and titanium outward diffusion are hindered by the coating. This greatly limits the growth of a reaction layer made of AlNbO<sub>4</sub> at interface between substrate and the coating and of TiO<sub>2</sub> at the top surface. A chromia coating deposited on  $\gamma$ -TiAl alloy by multi arc ion platinum method promoted the growth of alumina at the interface with the

intermetallic substrate and retarded the titanium outward diffusion and the subsequent  $\text{TiO}_2$  formation. It is believed that the preferential formation of alumina at the interface with the substrate is due to the low oxygen activity. However, these simple oxide coatings are generally not well compatible with titanium aluminides and intrinsically brittle, which promotes cracking and spallation [97].

Enamel protective coatings have good compatibility with the intermetallic substrate as their thermal expansion coefficient is similar to that of titanium-based and TiAl intermetallic alloys. Enamel coatings show optimal high temperature stability, low cost and easy processing [5].

After 300 h at  $800^\circ\text{C}$ , glass-ceramic coatings as  $\text{Na}_2\text{O-CaO-SiO}_2$  and  $\text{SiO}_2\text{-Al}_2\text{O}_3\text{-CaO-Na}_2\text{O}$  deposited on TIMETAL 834 and TA1 alloys showed that no weight gains occurred and no novel oxide formed on the surface of the coatings. The glass-ceramic coatings ( $\text{MgO-SiO}_2\text{-TiO}_2$ ,  $\text{BaO-MgO-SiO}_2$ ,  $\text{ZnO-Al}_2\text{O}_3\text{-SiO}_2$  and  $\text{Ba-SiO}_2$ ) processed by vitreous enamelling on the  $\gamma\text{-TiAl}$  alloys ensured excellent oxidation resistance at  $800^\circ\text{C}$  up to 100h [98],[99].

Both  $\text{SiO}_2\text{-B}_2\text{O}_3\text{-Al}_2\text{O}_3\text{-MgO-TiO}_2\text{-K}_2\text{O}$  and  $\text{SiO}_2\text{-BaO-CaO-Al}_2\text{O}_3\text{-TiO}_2$  glass-ceramic coatings significantly protected from oxidation the  $\gamma\text{-TiAl}$  alloys at  $1000^\circ\text{C}$  up to 25h [100].

A  $\text{SiO}_2\text{-Al}_2\text{O}_3\text{-ZrO}_2\text{-ZrO-B}_2\text{O}_3\text{-CaO-Na}_2\text{O}$  coating deposited on the Ti24Al14Nb3V alloy improved oxidation behaviour at  $900^\circ\text{C}$ , and showed good chemical stability and thermal expansion coefficient similar to the substrate. However, even if spallation or cracking were not observed, these glass-ceramic coatings start to peel off after long-term oxidation at high temperature. [101].

In addition, the presence of rather thick coatings made of glass-ceramics oxides is detrimental for the mechanical properties of titanium aluminides, and this feature represents the main limit for their practical exploitation [5].

## Chapter 2

# Experimental part: materials and methods

In this chapter, the material processing and characterization of samples under investigation are described. Optical microscopy and Scanning Electron Microscopy were used for microstructure and morphology investigations. Crystalline phases constituting the alloys and the ceramic coatings were identified by X-ray diffraction. X-ray Photoelectron Spectroscopy and Energy Dispersive Spectroscopy were used for the chemical characterization of samples. The kinetics of isothermal oxidation of intermetallic alloys was studied by Thermogravimetric analysis. Oxidation tests in air were preliminarily carried out in order to check the suitability of coatings for oxidation protection. Cycling oxidation of coated and uncoated intermetallic alloys was performed in Burner Rig apparatus, with the aim of evaluating the combined effect of oxidation and thermal shock. Scratch testing checked the adhesion of coatings before and after the thermal cycling. Burner rig apparatus was used for evaluating the performance of the most promising coatings under condition simulating the operation of turbine engine components.

### 2.1 TiAl intermetallic alloys under investigation

Ti-48Al-2Cr-2Nb at.% (Ti-33.3Al-2.7Cr-4.8Nb wt.%), Ti-48Al-2Nb-0.7Cr-0.3Si at.% (Ti-33.5Al-4.8Nb-0.9Cr-0.2Si wt.%), Ti-43.5Al-4Nb-1Mo at. % (Ti-28.6Al-9.1Nb-2.3Mo wt.%) and Ti-47Al-2Cr-8Nb at.% (Ti-30.4Al-2.5Cr-17.8Nb wt.%) intermetallic alloys were investigated.

The alloys under investigation have been produced by electron beam melting. The general features of Electron Beam Method are presented in chapter 2 of this thesis, dealing with processing and heat treatments of TiAl intermetallic alloys.

The processing paths for the intermetallic alloys have been well investigated during the last years and the advancements in this field have been widely reported in the literature. Also the processing methods of the alloys used in this work as well as the relevant microstructures have been described in several papers previously

published [18],[19],[20],[21],[102],[103],[104],[105]. For sake of clarity some basic information on this subject are summarized in the following and references are given in order to allow the readers to achieve further data.

The chemical compositions of powder alloys (in wt.% and at.%) was checked by inductively coupled plasma (ICP), while a LECO instrument was used to measure oxygen concentration.

The Ti-48Al-2Cr-8Nb (at.%) alloy was obtained from powder with nominal particle size distribution between 45  $\mu\text{m}$  and 180 $\mu\text{m}$  (-80/+325 mesh). The flowability ( $28\pm 1\text{s}$ ) was measured according to ASTM B213-03, while the ASTM B212-99 was used for apparent density measurement ( $2.31\pm 0.23\text{g/cm}^3$ ) [20].

A nominal size distribution between 45 $\mu\text{m}$  and 150 $\mu\text{m}$  (-100/+325 mesh) was utilized for the Ti-48Al-2Cr-2Nb (at. %) alloy. The cumulative gran size distributions of the  $\gamma$ -TiAl powder was obtained according to ASTM B214-07 [18].

In order to produce the Ti-48Al-2Nb-0.7Cr-0.3Si (at.%) alloy, a powder with nominal particle size distribution between 45 $\mu\text{m}$  and 180 $\mu\text{m}$  (-100/+325 mesh) was used (ASTM B214-07). According to ASTM B213-13 the Ti-48Al-2Nb-0.7Cr-0.3Si powder flowability ( $30\pm 1\text{ s}$ ) was measured. The apparent powder density was  $2.22\text{ g/cm}^3$  (ASTM B212-99) and the alloy density was  $3.98\text{ g/cm}^3$  [19].

The Ti-43.5Al-4Nb-1Mo (at. %) alloy was obtained from powder with nominal particle size distribution between 45  $\mu\text{m}$  and 145 $\mu\text{m}$  (-80/+325 mesh), according to ASTM B214-07. According to ASTM B213-13, the Ti-43.5Al-4Nb-1Mo (at. %) powder flowability was ( $27 \pm 1$ ). The apparent density was  $2.29 \pm 0.03\text{ g/cm}^3$  (ASTM B212-99) [103].

In order to reduce the amount of defects, as residual porosity, and improve the homogeneity, the EBM samples were hot isostatic pressed (HIPed) for 4h at 1260°C under a pressure of 1700 bar in argon [18],[19],[20],[21],[103].

The microstructures of TiAl alloys under investigation after HIPing are represented in **Figure 42**. The microstructures show very fine equiaxed  $\gamma$ -grains in all TiAl alloys.

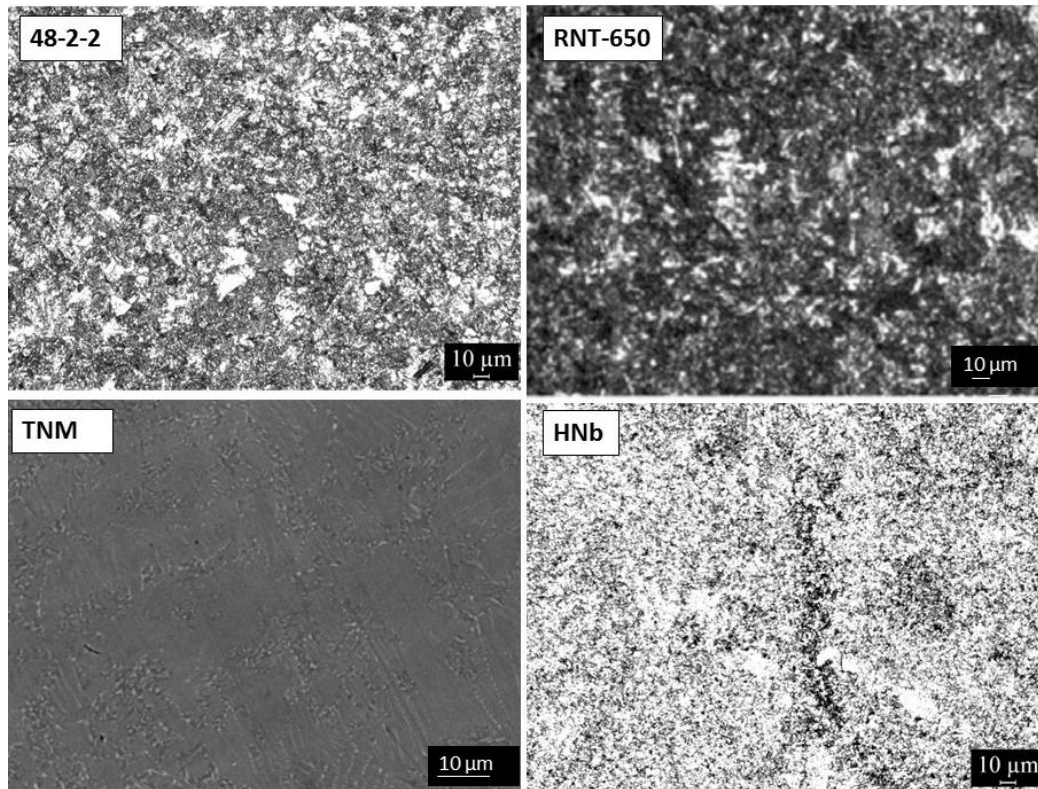


Figure 42: Microstructures of as-EBM processed TiAl alloys after HIP treatment: Ti-48Al-2Cr-2Nb (48-2-2), Ti-48Al-2Nb-0.7Cr-0.3Si (RNT-650), Ti-43.5Al-4Nb-1Mo (TNM) and Ti-47Al-2Cr-8Nb (HNb).

The TiAl alloys under investigation were finally thermally treated in a GERO carbon-free oven (**Figure 43**), in order to obtain a balanced set of mechanical properties.

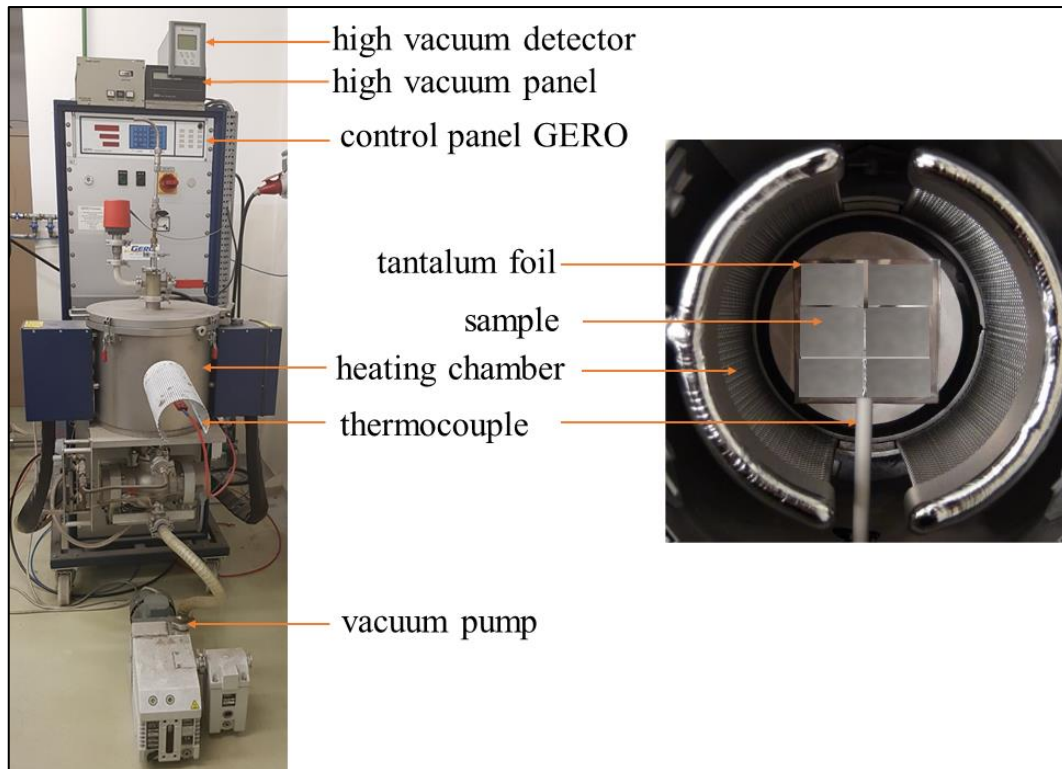


Figure 43: GERO furnace.

The electric GERO furnace operates under high vacuum ( $10^{-4}$  mbar) or in inert gas flow (argon) to avoid oxidation. The furnace has a stainless steel double wall, in order to cool the chamber during the heating by water. A tungsten resistance, placed inside the chamber, heats the chamber zone. A molybdenum and a stainless steel layers insulate the chamber. A thermocouple placed inside the chamber controls the temperature. During the heat treatment, the samples are positioned on a tantalum foil, in centre of chamber.

Only few information about the heat treatment of the alloy under investigation can be given because the exact heat treatments are of industrial interest and therefore confidential.

Similar heat treatments were adopted for 48-2-2 and HNb as both of them show the  $\alpha$ -transus temperature at around  $1295^{\circ}\text{C}$  [21]. Therefore, the samples were annealed for 2 hours at  $1320^{\circ}\text{C}$  and quickly cooled to room temperature. In this manner a microstructure mostly constituted by lamellar structure can be obtained.

Also the thermal treatment of RNT-650 alloy consisted in the annealing at a temperature above the  $\alpha$ -transus. Annealing was performed for 2 hours at 1360°C as previously reported in the literature [103].

The heat treatment of TNM [103] consisted in an annealing performed just above the  $\gamma$ -solvus, which is ranges around 1240°C depending on the chemical composition of TNM. After annealing, the sample was quickly cooled to room temperature thus obtaining a near lamellar structure.

The optimized microstructures of TiAl alloys under investigation are reported in **Figure 44**.

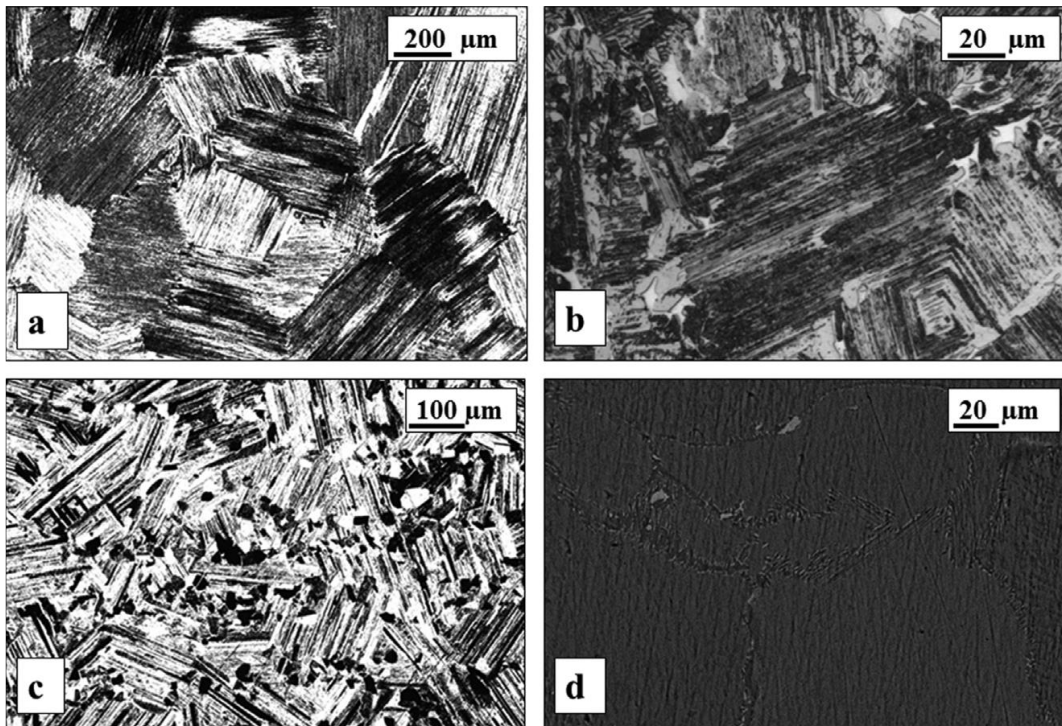


Figure 44: Optical microscopy images: (a) a fully lamellar microstructure of Ti-48Al-2Cr-2Nb, a near lamellar microstructure of (b) Ti-47Al-2Cr-8Nb and (c) Ti-48Al-2Nb-0.7Cr-0.3Si. SEM image (d): a near lamellar microstructure of Ti-43.5Al-4Nb-1Mo [102].

A fully lamellar microstructure was obtained for Ti-48Al-2Cr-2Nb (**Figure 44**, a). From the literature, the fully lamellar microstructure of TiAl intermetallic alloy shows the best creep resistance [4]. Ti-47Al-2Cr-8Nb, Ti-48Al-2Nb-0.7Cr-0.3Si and Ti-43.5Al-4Nb-1Mo alloys show a near lamellar microstructure (**Figure 44**, b and c). The SEM image of Ti-43.5Al-4Nb-1Mo alloy (**Figure 44**, d) clearly

shows mainly lamellar microstructure ( $\gamma/\alpha_2$  colonies), with some globular  $\beta_0$  and  $\gamma$  grains localised at the grain boundaries.

## 2.2 Ceramic coating deposition

In order to improve the oxidation resistance of second-generation TiAl-based alloys, TaAlN and TiAlN coatings were deposited on Ti-48Al-2Cr-2Nb heat-treated alloy. In this work, the High Power Impulse Magnetron Sputtering (HiPIMS) process is used for very thin ceramic coatings deposition.

The TaAlN and TiAlN coatings under investigation were deposited by research team ( Silvia M. Deambrosis, Monica Fabrizio, Enrico Miorin, Francesco Montagner, Valentina Zin) of National Research Council (CNR) of Italy, Istituto di Chimica della Materia Condensata e di Tecnologie per l'Energia (ICMATE), Corso Stati Uniti 4, 35127 Padova, Italy. Before the coating deposition the substrate was etched and the resulting roughness was measured at ICMATE by a mechanical profilometer. The roughness measurements were obtained according to UNI ISO 4287.

In recent years, the Reactive HiPIMS technology attracted attention as a promising sputtering-based ionized physical vapour deposition (PVD) process suitable for processing thin coatings with improved characteristics [106]. The HiPIMS is a simple process that combines the advantages of conventional magnetron sputtering and arc evaporation, because it produces a highly ionized droplet-free plasma. In comparison with conventional magnetron sputtering techniques, the HiPIMS plasma conditions considerably improve the flux of energetic ionized species [107].

A most important advantage of the HiPIMS technique is to perform efficient etching of different substrates, and to deposit several compounds (i.e., oxides or nitrides) [108],[109],[110],[111],[112],[113],[114],[115],[116]. During the reactive sputtering a mixture of gases reacts with the target material, and coating can be obtained with different chemical composition [107]. The HiPIMS technique uses the "cooler plasma", which means that the substrate does not suffer the action of high temperatures during the coating deposition [117].

In HiPIMS, a fraction of the plasma ions comes from the target material. During the etching process some of the bombarding metal ions may be implanted into an intermediate region [107]. The high-energy ion bombardment creates a smooth

surface, which results in good adherence of the coating with substrate. HiPIMS can cover large areas of a certain amount of micrometres. The film obtained by HiPIMS exhibit a uniform smooth surface and ultra-dense microstructure. In addition, the HiPIMS films can be deposited on complex-shaped substrates [107], [117].

The comparison between conventional Magnetron Sputtering and High Power Impulse Magnetron Sputtering is shown in **Figure 45**.

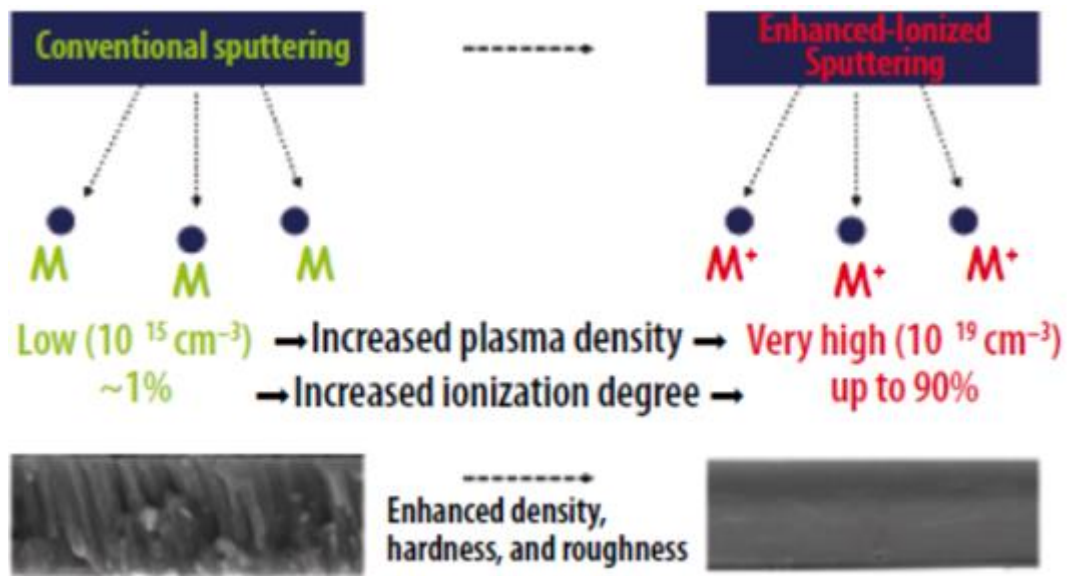


Figure 45: Magnetron Sputtering and High Power Impulse Magnetron Sputtering schematic processes [117].

The **Figure 45** shows that HiPIMS coating has ultra-dense microstructure and a very smooth surface, while a conventionally grown coating presents less hardness, density than HiPIMS film, and shows inhomogeneous microstructure [117].

The good quality coating is due to the high ionization factor of the sputtered surfaces. The electron impact ionization is obtained by the high plasma (electron) densities [118]. The ionization fraction in HiPIMS is a function of the peak target power [119] and the target material [120]. The sputtering gas influences the plasma chemistry and ionization during HiPIMS process. When argon-sputtering gas is used in HiPIMS the ionization is low if species has a high ionization potential (IPA) and a low electron impact ionization cross-section ( $Q_i$ ). High ionization has been found when IPA value is low and materials has a high  $Q_i$  value [117].

A summary of some important parameters for the HiPIMS discharge is reported in **Table 2**. The plasma parameters are calculated for the dense plasma regions at the target, where the ionization is the strongest [106].

**Table 2:** Parameters for the HiPIMS process [106].

| Parameter                           | Value  |
|-------------------------------------|--|
| Peak power density                  | $10^3 \text{ W cm}^{-2}$                           |
| Average power density               | $1\text{--}10 \text{ W cm}^{-2}$                   |
| Peak current density                | $1\text{--}10 \text{ A cm}^{-2}$                   |
| Discharge voltage                   | $500\text{--}1000 \text{ V}$                       |
| Pulse frequency                     | $10\text{--}1000 \text{ Hz}$                       |
| Pulse width                         | $10\text{--}500 \mu\text{s}$                       |
| Process gas pressure                | $10^{-3}\text{--}10^{-2} \text{ Torr (0.1--1 Pa)}$ |
| Magnetic field strength             | $0.010\text{--}0.100 \text{ T}$                    |
| Electron density                    | $10^{18}\text{--}10^{19} \text{ m}^{-3}$           |
| Electron temperature                | $1\text{--}5 \text{ eV}$                           |
| Ion energy (average for metal ions) | $20 \text{ eV}$                                    |
| Debye length                        | $10^{-6}\text{--}10^{-5} \text{ m}$                |
| Electron gyroradius                 | $10^{-4}\text{--}10^{-3} \text{ m}$                |
| Ion gyroradius                      | $10^{-1} \text{ m}$                                |
| Ionization mean free path           | $10^{-2} \text{ m}$                                |

The variation of the deposition parameters permits to control the energy of HiPIMS deposition, and allows the manipulation of film properties (mechanical, optical and electrical) [106]. During the film growth, the bombarding energy, the ions flux, the flux composition and the incidence angle of flux affect the plasma-film interface [121], [122]. The high pulsed ion flux parameters determinate the efficiency of the moment transfer to the film atoms and influence the growth and microstructure of film [123]. Another characteristic of HiPIMS is the possibility to increase the plasma density in front of a sputtering source in order to decrease the mean ionization distance for the sputtered particles [107]. The increase in plasma density is simply achieved by applying a high electrical power in pulses with a low duty factor (low ratio pulse on time/cycle time) [114],[107]. In addition, in order to obtain a novel structure of film with superior properties [115], the HiPIMS allows to control the direction of the deposition flux [124].

In this work a reactive HiPIMS (TRUMPF-Hüttinger, True Plasma High Pulse 4002 power supply and 18 kW model 3018 HBP bias unit, Freiburg, Germany) was used for coating deposition (**Figure 46**).

This apparatus is available at the laboratories of National Research Council (CNR) of Italy, “Istituto di Chimica della Materia Condensata e di Tecnologie per l’Energia” (ICMATE), Corso Stati Uniti 4, Padova 35127, Italy.

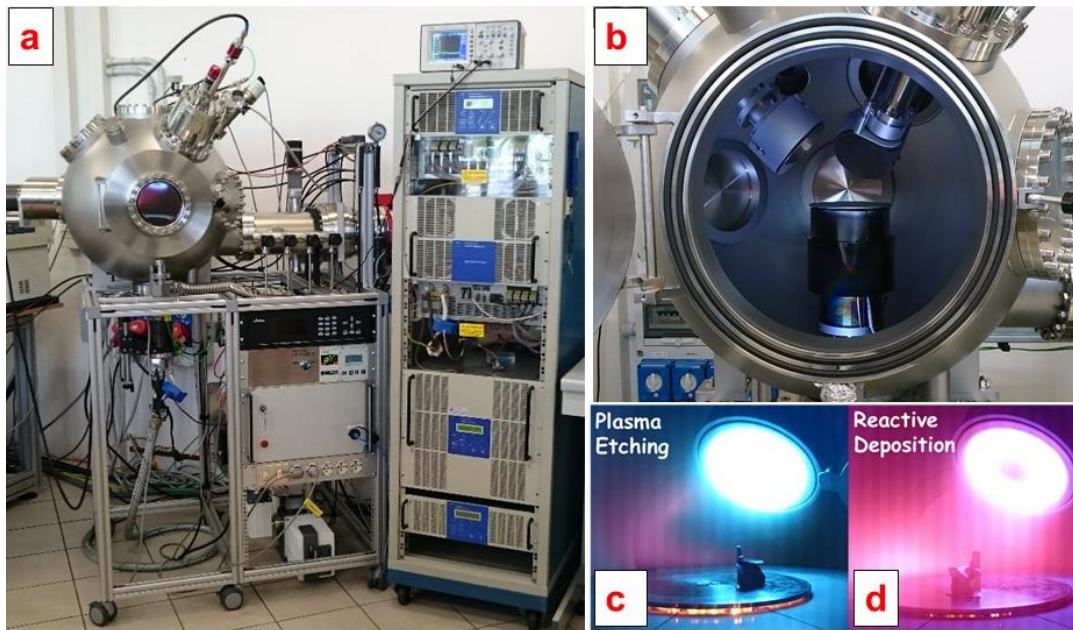


Figure 46: (a) HiPIMS apparatus, (b) HiPIMS chamber, (c) Plasma Etching, (d) Reactive Deposition.

Before the coating deposition, the Ti-48Al-2Cr bars (about 25 mm of diameter) obtained by EBM process and successively heat treated, were cut in order to obtain the cylindrical specimen (about 20 mm high).

In order to avoid the cutting defects, the upper surface of cylinders was metallographically polished to a 1 $\mu$ m diamond finishing.

All samples were ultrasonically cleaned in alcohol bath for 20 min.

After the surface preparation described above, three different pre-treatments were used for TiAlN coating deposition. The pre-treatment parameters are shown in **Table 3** [107],[125]. The roughness resulting from surface preparation of the substrate is reported in **Table 4**. The three roughness profiles (Ra) of the surface of

samples differently treated before coating depositions are shown in **Figure 47**, **Figure 48** and **Figure 49**.

**Table 3:** Substrate pre-treatment for TiAlN deposition.

| Substrate pre-treatment             | TiAlN1 | TiAlN2 | TiAlN3 |
|-------------------------------------|--------|--------|--------|
| Ultrasound cleaning in alcohol bath | yes    | yes    | yes    |
| HiPIMS plasma etching               | no     | 60 min | 10 min |
| TiAl interlayer deposition          | no     | no     | yes    |

**Table 4:** Average superficial roughness (Sa) before the coating deposition.

| Sample | Etching | Interlayer | average superficial roughness Sa ( $\mu\text{m}$ ) |
|--------|---------|------------|--|
| TiAlN1 | no      | no         | 0.014 $\pm$ 0.001                                  |
| TiAlN2 | 60 min  | no         | 0.04 $\pm$ 0.02                                    |
| TiAlN3 | 10 min  | yes        | 0.012 $\pm$ 0.002                                  |

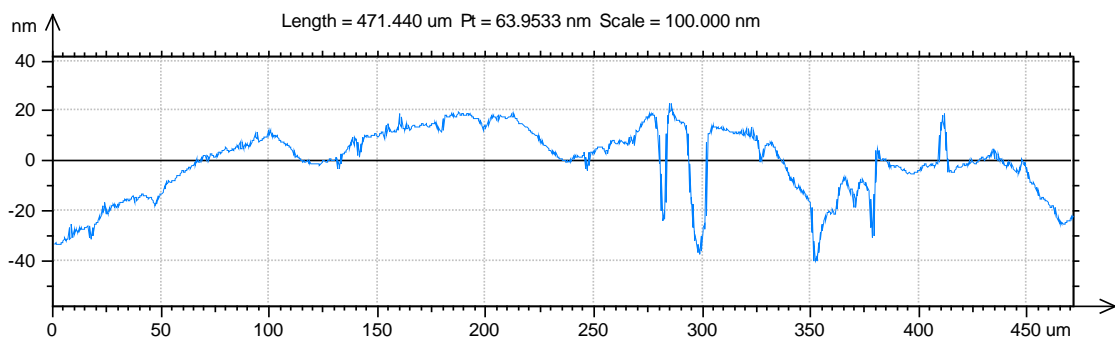


**Figure 47:** Roughness profile of TiAlN1 sample surface before coating deposition.

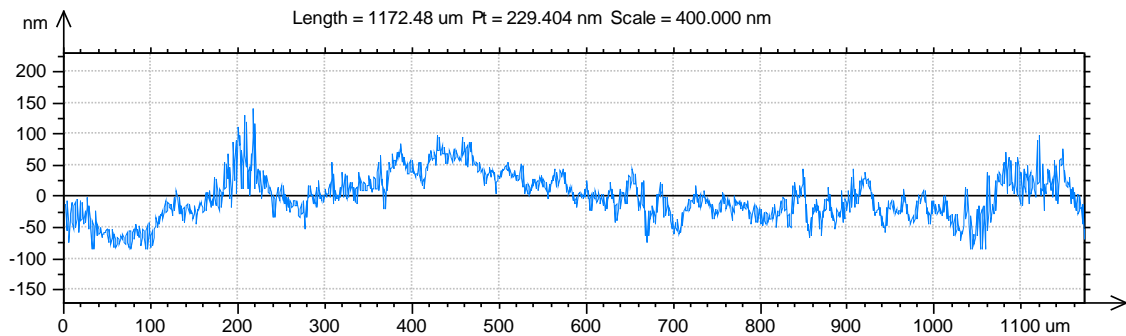


Figure 48: Roughness profile of TiAlN2 sample surface before coating deposition.

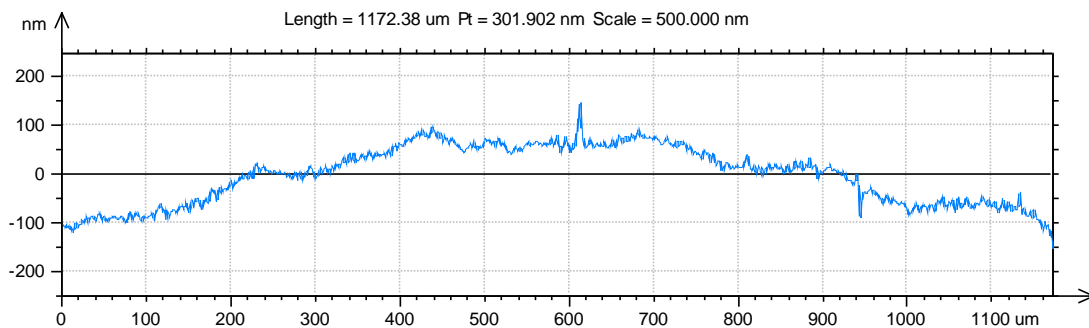


Figure 49: Roughness profile of TiAlN3 sample surface before coating deposition.

In case of TiAlN2 specimens, the sample surface was plasma etched for 60 minutes. HiPIMS etching conditions were: Ti<sub>0.5</sub>Al<sub>0.5</sub> cathode, average power 100 W, bias voltage -1200 V, Ar pressure  $1.0 \times 10^{-2}$  mbar, frequency 500 Hz and pulse length 25  $\mu$ s [107], [125]. The HiPIMS plasma etching aimed at the removal of the natural oxide layer [116] and improving the adhesion [110],[126].

The TiAlN3 surface was plasma etched by Argon ions for 10 minutes (the same etching condition of TiAlN2) and subsequently coated with a TiAl interlayer. The TiAl interlayer was deposited by using a TiAl target (Ti:Al atomic ratio 1:1, 4" in diameter, 6 mm thick, and 99.9% purity) fixed on a weakly unbalanced magnetron cathode. The substrates were placed 100 mm below the target and heated up to 400 °C. The TiAl interlayer deposition was performed under the following conditions: mean cathode power density 12.5 W/cm<sup>2</sup>, mean cathode power 1000 W, pulse length 25  $\mu$ s, frequency 500 Hz, gas Ar, pressure  $1.0 \times 10^{-2}$  mbar, substrate bias voltage -50 V, deposition duration 10 min. The TiAl interlayer was expected to improve the quality of the TiAlN coating [107], [125].

The TiAlN coating deposition was performed in a high-vacuum chamber (base pressure lower than  $1 \times 10^{-7}$  mbar). The inert gas (Ar, 99.9997% purity) and the reactive gas (N, 99.998% purity) were passed through dedicated mass flow controllers. The pressure of sputtering gas mixture (50%Ar +50%N) was set at  $1 \times 10^{-2}$  mbar. A TiAl target (Ti<sub>0.5</sub>Al<sub>0.5</sub> 99.9% purity) was used for TiAlN deposition. The substrates were placed 100 mm below the target and heated up to 400 °C. Other important HiPIMS conditions for TiAlN deposition were: mean cathode power 1000 W, mean cathode power density 12.5 W/cm<sup>2</sup>, pulse length 25 μs, frequency 500 Hz, substrate bias voltage -50 V, deposition duration 180 min [107], [125].

In the **Table 5** the thickness of TiAlN coatings measured by Calo tester (at ICMATE) are reported. These thickness values were also measured on the cross-section of the specimens by SEM and by FIB/SEM (at University "Roma Tre", Engineering Department, in the frame of a joint research project funded by the Italian National Research Council – Italian Ministry of Economic Development agreement “Ricerca di Sistema Elettrico Nazionale”).

**Table 5:** Thickness of coatings measured by Calo tester.

| sample        | Thickness of coatings<br>(μm)             |
|---------------|---|
| <b>TiAlN1</b> | 2.19±0.03                                 |
| <b>TiAlN2</b> | 2.13±0.04                                 |
| <b>TiAlN3</b> | Coating 2.12±0.06<br>Interlayer 0.30±0.02 |

The cross-sections of these coatings are shown in **Figure 50**, **Figure 51**, **Figure 52** and **Figure 53**.

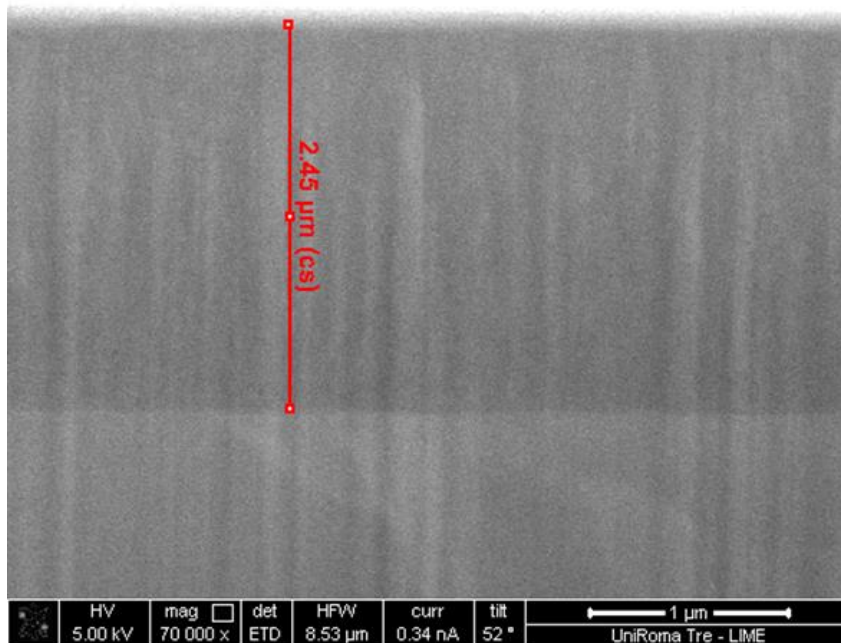


Figure 50: Cross-section of TiAlN1 sample.

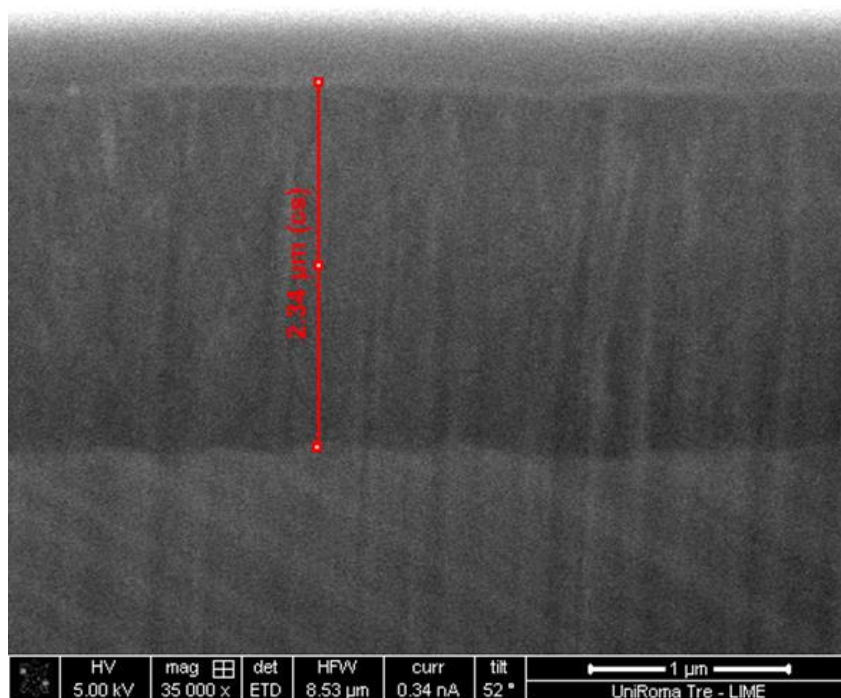


Figure 51: Cross-section of TiAlN2 sample.

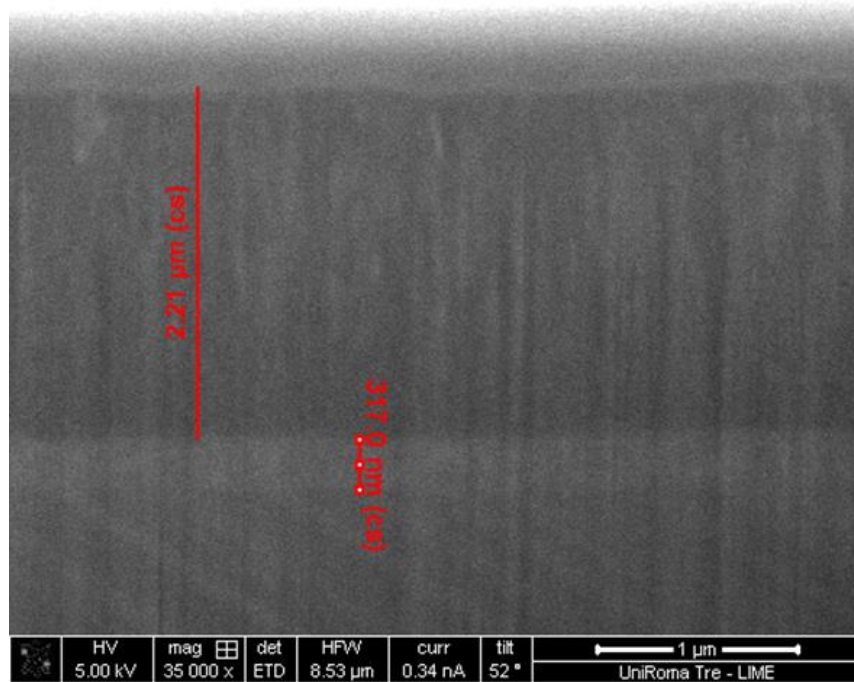


Figure 52: Cross-section of TiAlN3 sample.

The microstructures of TiAlN coatings are also shown in **Figure 53**.

The TiAlN1 coating showed good compact microstructure without defects. The TiAlN2 coating exhibited TiAl lamellar microstructure, probably due to very long ions etching (60 min) before the coating deposition. The TiAlN3 coating showed very soft lamellar microstructure.

All TiAlN specimens were about  $3\mu\text{m}$  thick (**Figure 50**, **Figure 51**, **Figure 52** and **Figure 53**).

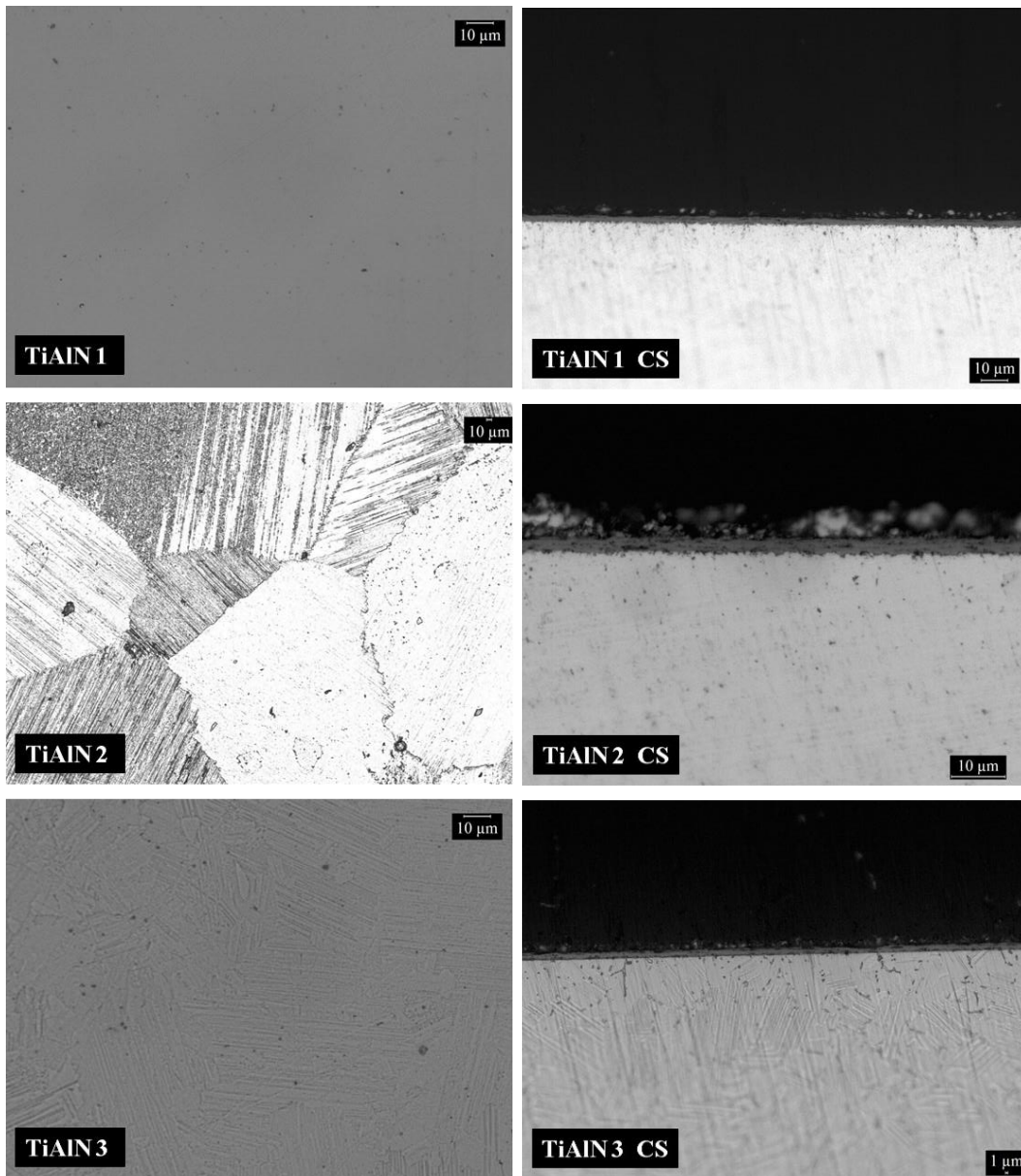


Figure 53: SEM images. Microstructures of TiAlN coatings (top and cross-section).

Also a TaAlN coating was deposited on the surface of Ti-48Al-2Cr-2Nb heat-treated alloy.

The HiPIMS parameters used for TaAlN deposition are summarized in **Table 6**.

**Table 6:** Parameters for the TaAlN HiPIMS deposition.

|   |   |                           |
|---|---|---------------------------|
| <b>Substrate<br/>pre-<br/>treatment</b>   | Ultrasound cleaning                                   | yes                       |
|   | HiPIMS plasma etching (min)                           | 10                        |
|   | TaAl Interlayer                                       | yes                       |
| <b>Film<br/>deposition<br/>parameters</b> | Mean cathode power (W)                                | 500                       |
|   | Mean cathode power density ( $\text{W}/\text{cm}^2$ ) | 6.25                      |
|   | Pulse length ( $\mu\text{s}$ )                        | 25                        |
|   | Frequency (Hz)  | 500                       |
|   | Gas   | Ar + N <sub>2</sub> (50%) |
|   | Ta and Al targets                                     | Ta+Al (50%)               |
|   | Pressure (mbar)                                       | $1 \times 10^{-2}$        |
|   | Substrate bias voltage (V)                            | -100                      |
|   | Duration (min)  | 130                       |

The microstructure of TaAlN coating is shown in **Figure 54** and cross-section of TaAlN is reported in **Figure 55**. The TaAlN coating was homogenous and did not exhibit any defect.

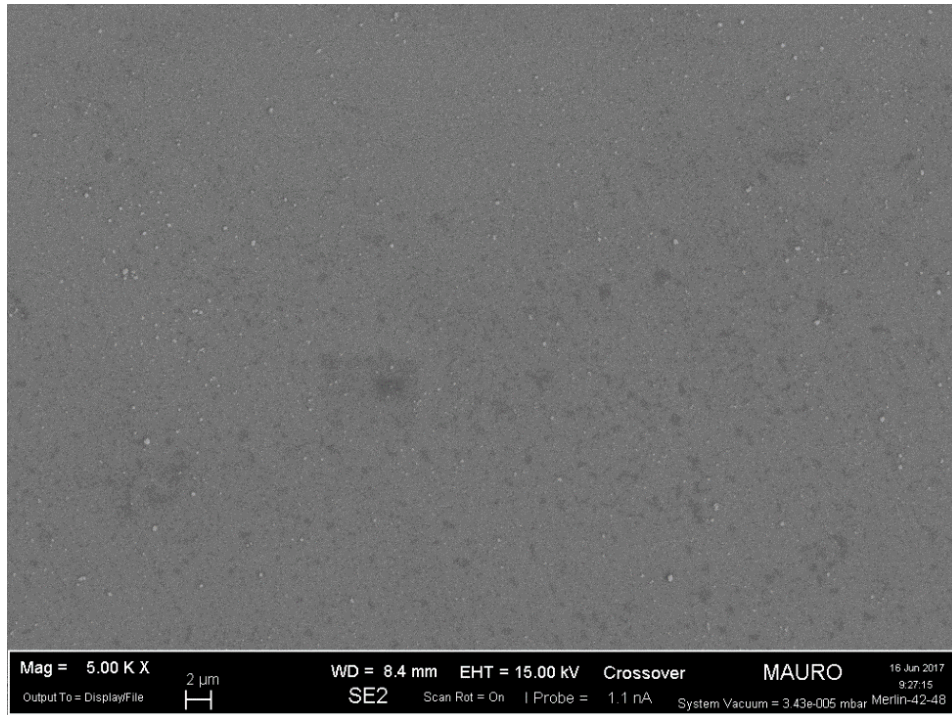


Figure 54: SEM image of TaAlN coating microstructure.

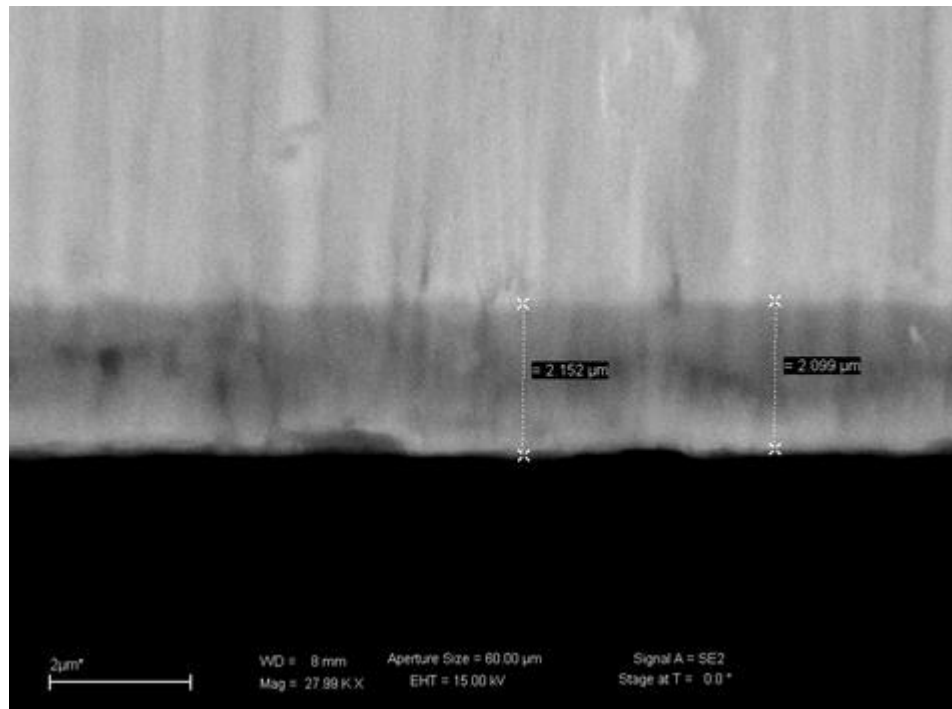


Figure 55: SEM cross-section of TaAlN coating.

## 2.3 Techniques of characterization

In order to analyse the chemical composition and microstructure before and after oxidation, different tests and characterization techniques were adopted in this work. The isothermal and cycling oxidation treatments are also described in this chapter.

### 2.3.1 X-ray diffraction

X-ray diffraction (XRD) technique is a semiquantitative analysis currently used for microstructure characterization of crystalline materials. In a crystalline solid, the lattice planes are separated by inter-planar distance  $d$ . An incident X-ray beam interacts with crystal lattice of phases contained in a sample, and it is diffracted from atomic planes in a certain direction. The diffraction occurs according to the Bragg's law or equation (**Figure 56**).

Each crystalline material has its own characteristic structure consisting of a stacking of crystallographic planes, therefore X-ray diffraction results in a unique XRD pattern.

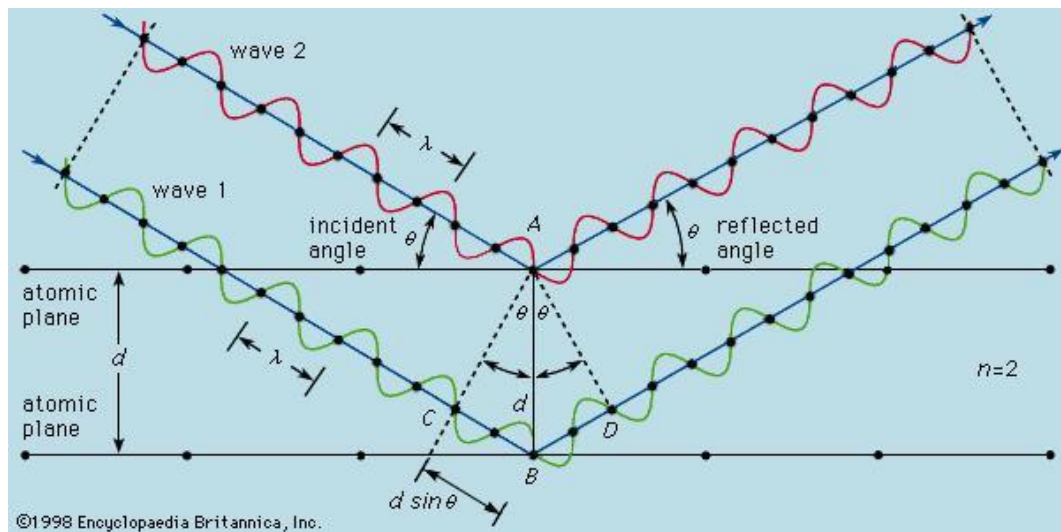


Figure 56: Bragg's Law ( $2d\sin\theta = n\lambda$ , where  $n$  is a whole number of X-ray wavelengths ( $\lambda$ ),  $d$  is the spacing between crystallographic planes and  $\theta$  is the incident/reflected angle) [127].

In this work, the Panalytical X'PERT PRO PW3040/60 (Bragg Brentano geometry, Cu  $K\alpha$  radiation, operating conditions 40 kV and 40 mA) and Micro-

XRD Rigaku D/max (Cu  $K\alpha$  radiation, probe 100 micron) diffractometers were used (**Figure 57**).



Figure 57: X'PERT PRO PW3040/60 located at politecnico di Torino (DISAT).

A schematic description of XRD equipment is shown in **Figure 58**.

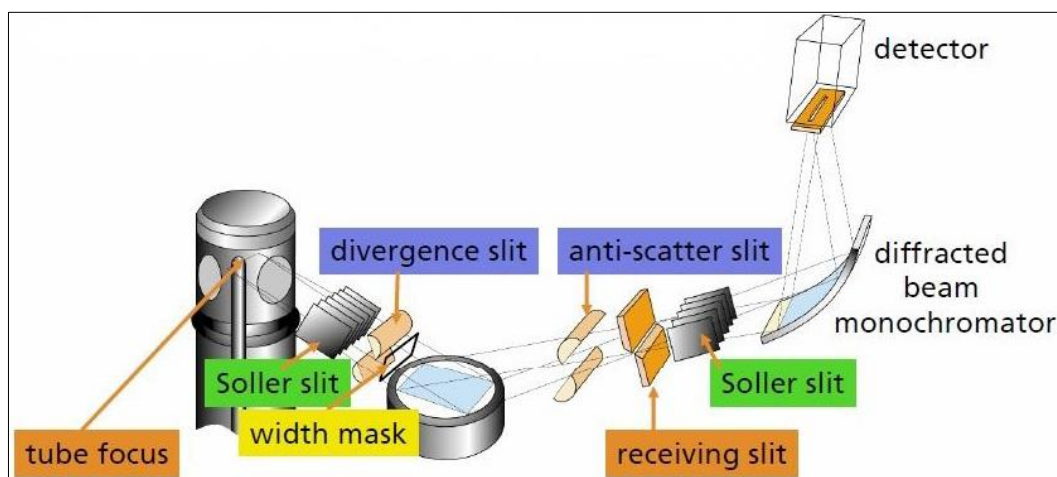


Figure 58: Schematic representation of X-Ray diffractometer [128].

X-rays are generated by a cathode ray source (x-ray tube) and treated by a window (or a monochromator) in order to produce monochromatic X-rays ( $K\alpha$

wavelength). X-rays pass through soller slits and divergence slit, in order to collimate incident beam on the sample surface. The interaction between incident ray and the sample surface produces a refracted ray ( in case of a crystalline sample). Anti-scatter slit selects the beam reflected by the sample surface. X-ray beam is filtered by a monochromator thus reducing background noise. After X-ray is collected by X-ray detector (proportional, Geiger, scintillation, semiconductor). The detector records and processes the X-ray signal diffracted according to Bragg Equation, and converts the signals in a XRD spectrum.

### 2.3.2 Optical microscopy

Before the microscopic analysis, the sample surface was polished to a 1 $\mu$ m diamond finishing. In order to observe the microstructure of uncoated alloys, etching by Kroll's reagent (6% vol. nitric acid and 3% vol. hydrofluoric acid, 91% vol. deionized water) was performed for Ti-48Al-2Cr-2Nb, Ti-47Al-2Cr-8Nb and Ti-48Al-2Nb-0.7Cr-0.3Si alloys. Differently the coated surfaces were only cleaned by ultrasounds in alcohol bath.

In this work, a Leica DMI5000 M inverted microscope equipped with an integrated camera was used. The Leica LAS software was employed for image analysis of microstructure (**Figure 59**).



Figure 59: Leica DMI 5000 M optical microscope.

### 2.3.3 Scanning Electron Microscopy and Energy Dispersion Spectroscopy

The electron microscopy permits to investigate the morphology and microstructure of the samples, while EDS allows to analyse their composition. In this work, a scanning electron microscope (SEM-FEG Assing SUPRA 25) was used and energy dispersive spectroscopy was performed at 15 kV (EDS Oxford INCA). The EDS analysis and the EDS elemental maps were carry out on the cross-section of specimens (with and without coating) before and after oxidation. With the aim of avoiding rounding of the sample edge, possibly occurring during cutting, the sample was embedded into a resin and its cross section was carefully polished before the EDS analysis.

The **Figure 60** shows the schematic SEM/EDS apparatus.

In Electron Gun, the electrons are emitted by the heated cathode filament and ejected into a vacuum tube. Successively the cathode ray passes through an anode, acting as a collimator. After the focused and accelerated beam is condensed by condenser lens (one or two). The spray apertures and condenser lens work together. The magnetic condenser lenses apply a magnetic field to the beam and a helical path focuses the beam into a spot. The deflection coils deflect electron beam and objective lens focus the electron beam in very fine spot. The primary electron beam scans the sample surface in a raster pattern. The Backscattered Electron Detectors, the secondary Electron Detector and the Energy dispersive X-ray Detector allow to create the imagine of the sample and detect information for SEM-EDS analysis.

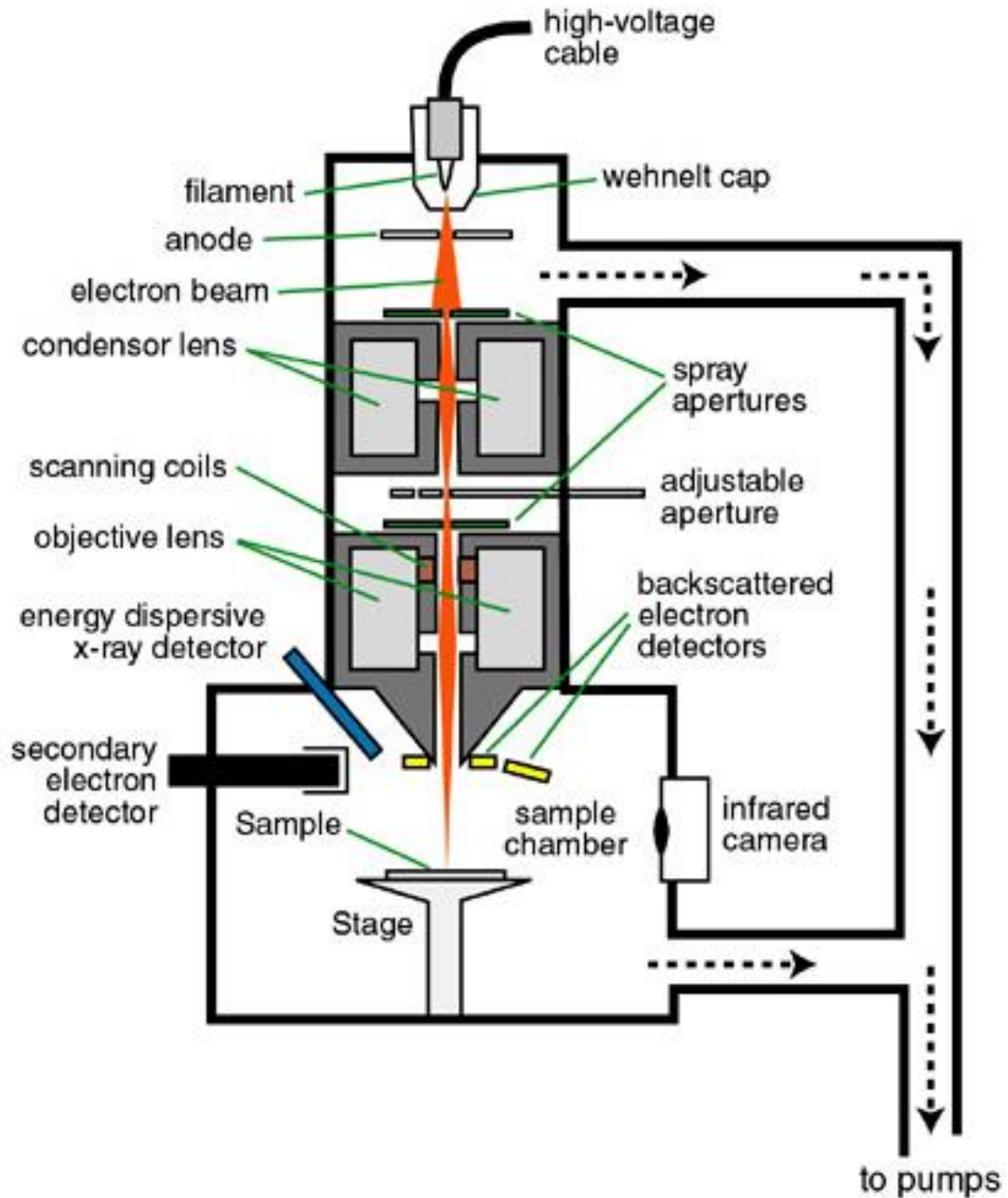


Figure 60: Schematic SEM apparatus [129].

The **Figure 61** shows the Electron beam interaction with the atoms of sample surface. The electron beam source shot the sample surface, thus causing the emission of X-Rays and other electrons.

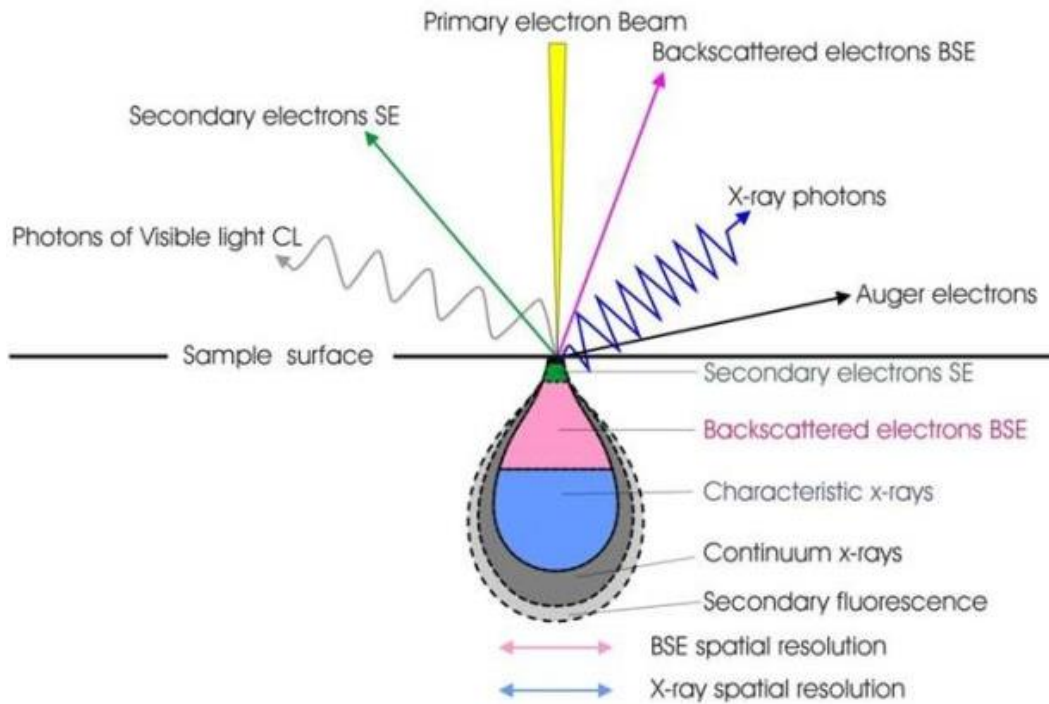


Figure 61: Schematic principle of SEM. X-ray interaction with the atoms of sample [130].

The primary accelerated electrons penetrate in electron shells of the sample atoms and later elastically backscattered electrons (BSE) with lower energy are ejected from the sample surface. Due to inelastic collisions, the secondary electrons (SE) can be emitted from the k-orbital of the specimen's atoms. The Auger electrons and X-ray effects are observed when an electron from higher energy orbital moves to compensate an inner shell electron free position, the excess of energy created during the reorganization in electronic shells produces the Auger effect and x-rays emission (**Figure 62**).

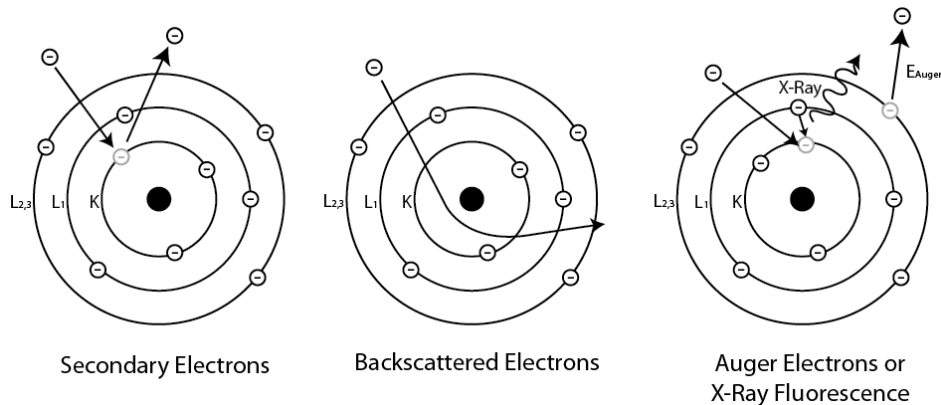


Figure 62: The electron and X-Ray emissions from sample atoms [131].

In fact, the high-energy electron beam can cause the removal of a core state electron leaving a hole. If the core hole is filled by an outer electron, this electron loses an energy amount equal to the difference in energy of the orbitals involved. This energy can be also used by a second electron that can be ejected if the energy is greater than its binding energy.

The BSE electrons give information about atomic number of atoms and their distributions in the sample, while SE allow for the morphological analysis and give rise to very high resolution SEM images. The Auger electrons can be used for quantitative analysis, Auger Electron Spectroscopy (AES) is a surface sensitive technique. X-rays give the characteristic chemical information of the emitting atoms. EDX analysis usually affects zones of sample around 1-3  $\mu\text{m}$  wide.

### 2.3.4 X-ray photoelectron spectroscopy

The X-ray photoelectron spectroscopy (XPS) is a sensitive quantitative analysis of chemical composition of the sample surface (few atomic layers interested by the analysis, maximum probe penetration of 10 nm).

In this work, XPS PHI 5000 Versa Probe apparatuses was used **Figure 63**.

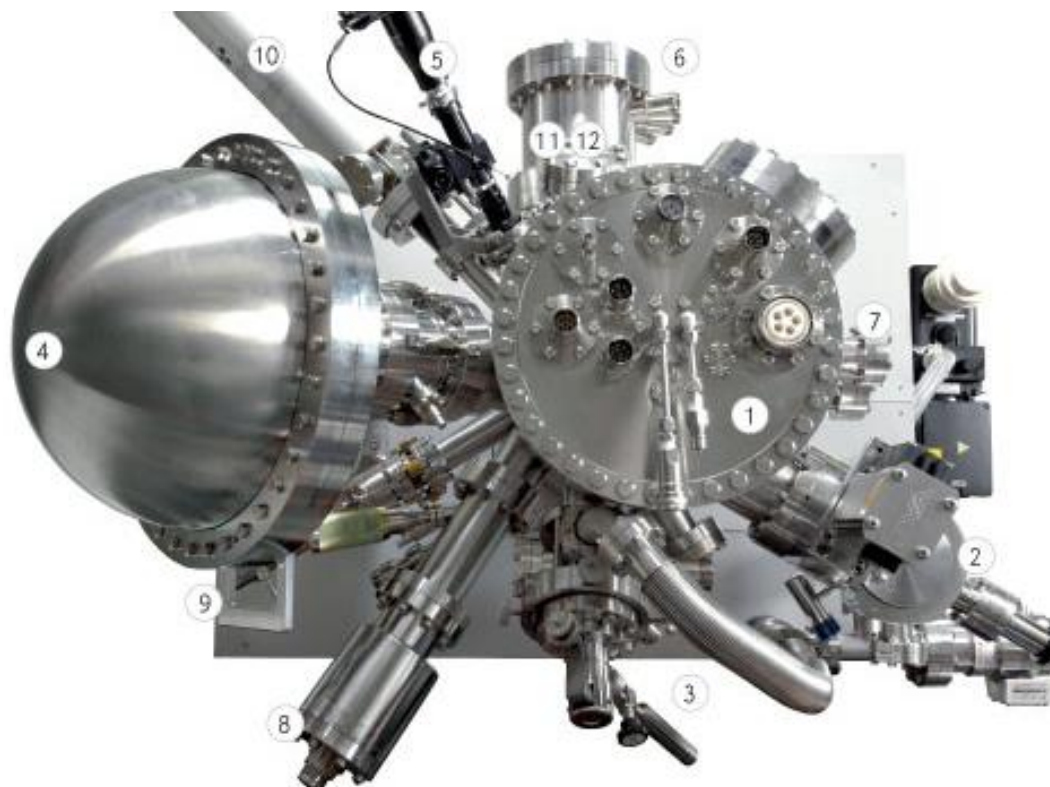


Figure 63: XPS PHI 5000 Versa Probe apparatus: 1-Scanning x-ray source, 2-sample introduction chamber, 3-argon sputter ion gun, 4-electron energy analyser, 5-optical microscope, 6-five axis automated sample manipulator, 7- optional UHV sample preparation chambers, 8-optional C<sub>60</sub> sputter ion gun, 9-optional UV light source for UPS, 10- optional dual anode X-ray source, 11-optional electron gun for AES,12-Optional 20 keV Argon gas cluster ion gun.

XPS PHI 5000 Versa probe apparatus with Al K-alpha works at 1486.6 eV energy, 15 kV voltage and 1 mA anode current. A spot size of 100  $\mu\text{m}$  was used to collect the photoelectron signal for the survey spectra. The pass energy value of 187.85 eV and 23.5 eV was employed for survey and high resolution spectra respectively. Calibration of XPS equipment was performed by matching the literature binding energy values of Au 4f<sub>7/2</sub>, Cu 2p<sub>3/2</sub> and Ag 3d<sub>5/2</sub> peaks. XPS is performed in ultrahigh vacuum ( $10^{-9}$  mbar).

Before the XPS analysis, the samples were cleaned by ultrasounds in an alcohol bath. Each sample surface was analysed after argon ion cleaning (2kV) in the XPS chamber until the carbon content became negligible. The deconvolution of High Resolution XPS spectrum was done by using Multipack 9.6 software.

The schematic operating principle of XPS technique is shown in **Figure 64**.

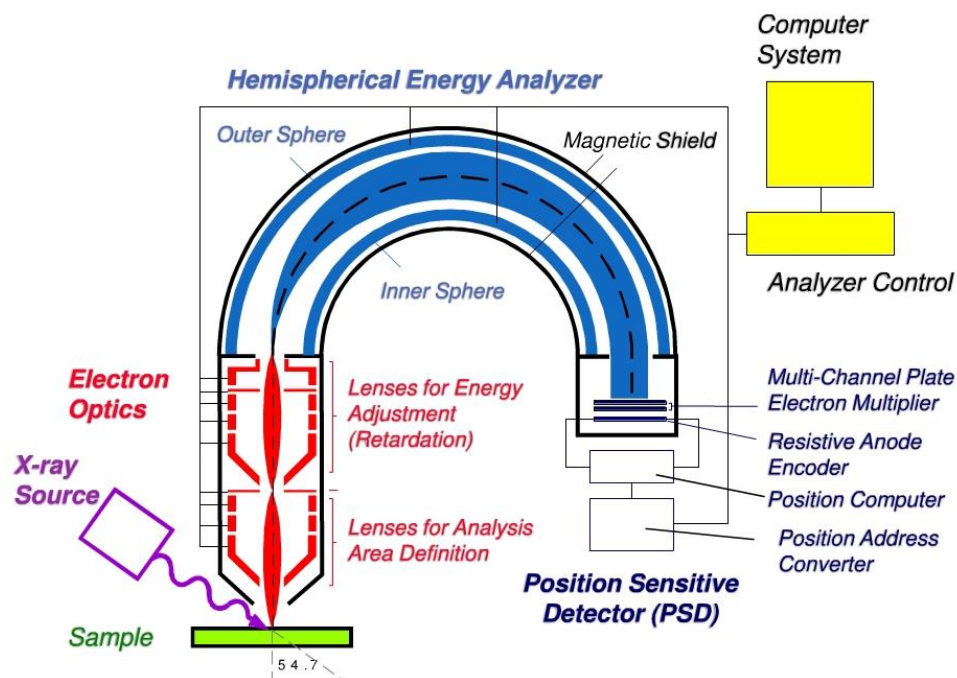


Figure 64: XPS schematic operating principle [132].

A monochromatic X-ray source (1.5 kV) irradiates the surface sample. After beam-surface interaction, some quantity of core-level electrons escape from the sample atoms. Lens system collects the escaped photoelectrons from sample surface. Hemispherical Energy Analyser filters the electron energies. Position Sensitive Detector counts the number of electrons. The Electron Energy Analyser measures the kinetics energies of electrons ejected from the sample surface, and electron detector elaborates the data in XPS spectrum.

The X-ray source interaction with an atom of the sample is shown in **Figure 65**.

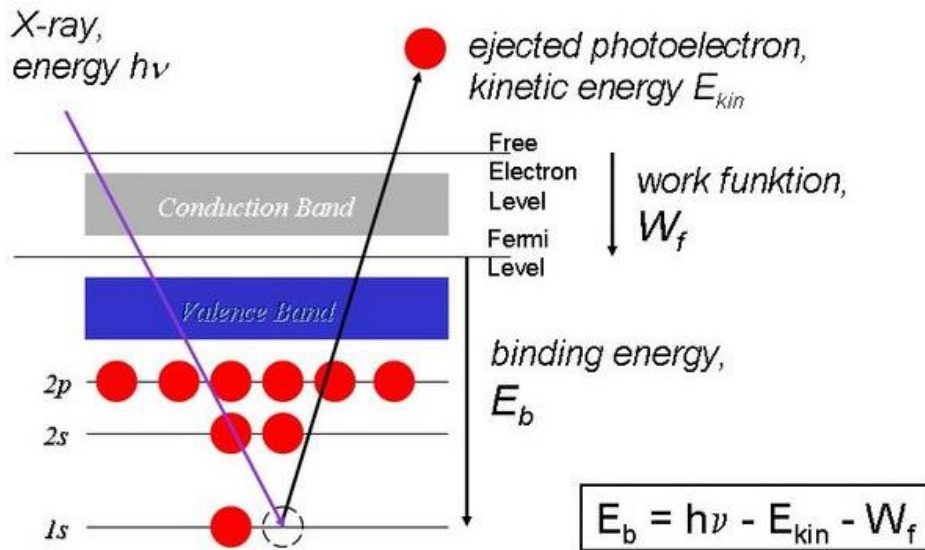


Figure 65: X-ray source interaction with an atom of the sample [133].

The kinetic energy ( $E_{kin}$ ) of emitted electron depends from photon energy ( $h\nu$ ) and binding energy ( $E_b$ ) of emitted electron:  $E_{kin} = h\nu - E_b - W_f$ , where  $W_f$  is a work function depending on the spectrometer.

The binding energy of emitted electron results from different parameters concerning the chemical element (positive charge on nucleus, that is number of protons acting on the electron), the orbital hosting the electron (energy level that electron occupies), and the chemical environment (type of chemical bond, orbital energy, valence state, etc.).

### 2.3.5 Thermogravimetric analysis

The thermogravimetric analysis is an analytical method to study the weight alteration (growth or loss sample mass), which depends on the temperature change.

In this work, thermogravimetric analysis (TGA) was performed in a Mettler Toledo AG-TGA/STDA851.

The TGA apparatus is schematically shown in **Figure 66**.

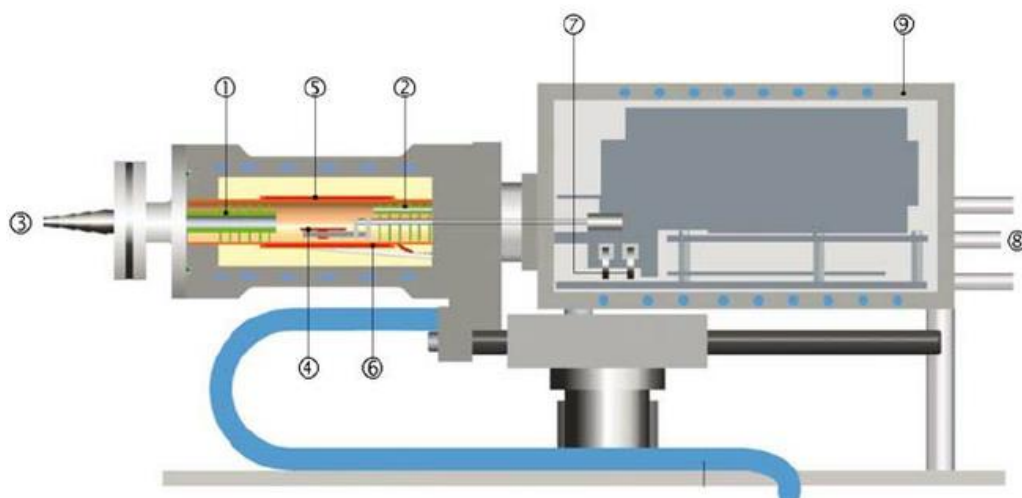


Figure 66: Schematic Thermogravimetric apparatus Mettler Toledo, comprising: 1-baffles, 2-reactive gas capillary, 3-gas outlet, 4-temperature sensors, 5-furnace heater, 6-furnace temperature sensor, 7-adjustment ring weights, 8-protective and purge gas connector, 9-thermostated balance [134].

During TGA test, the furnace temperature sensor and thermostated balance measure respectively temperature (during continuous heating) and weight changes against time or temperature (isothermal experiments or temperature run). The thermogravimetric data are usually compiled into a plot x-axis versus y-axis, where the mass or percentage of initial mass is reported on the y-axis and the temperature or time is shown on the x-axis.

The intermetallic bars (about 25 mm in diameter) of EBM alloys after heat treatment processing were cut, in order to obtain small cubic specimens (about  $2.5 \times 2.5 \times 2.5 \text{ mm}^3$ ). Successively, each face of the cubic samples was polished up to 4000 grit. The alloy samples were cleaned by ultrasound in an alcohol bath for 10 minutes. An alumina crucible (150  $\mu\text{l}$ ) was used as sample holder.

At the beginning, the TGA runs were performed from 25 °C to 1000 °C. The test parameters for the first TGA measurement were: 50 ml/min air flow, heating rate of 5 °C/min. In this manner, the temperature above which the oxidation of each alloys happens with an appreciable rate was detected. Based on these TGA curves, the oxidation behaviour of the four alloys under investigation was studied in isothermal conditions at 800 °C, 850 °C, 900 °C, 950 °C and 1000 °C. The experimental conditions for isothermal TGA tests were: heating rate of 5 °C/min up to the isothermal temperature, holding for 10 hours in isothermal conditions,

average cooling rate about 25°C/min (each samples was cooled inside the TGA chamber down to room temperature) [102].

### 2.3.6 Burner rig test

For cycling oxidation of uncoated and coated TiAl samples, a Burner Rig apparatus was used (**Figure 67**). At least three samples for each kind of specimen (uncoated or coated with every TiAlN film) were contemporaneously tested in this apparatus.



Figure 67: Burner Rig apparatus of Politecnico di Torino (DISAT).

The burner rig facility was specifically designed in order to simulate the operating conditions (atmosphere, temperatures and temperature variation) of real turbine engines.

The chamber of Burner Rig can hold ten samples contemporaneously. During the test, the half-moon refractory doors closed the BR chamber. The temperature of each sample was recorded by a thermocouple placed near of the sample surface and another thermocouple positioned below the sample. Methane and air (volume ratio 1:17) were used to feed a flame, positioned in centre of chamber. Compressed air was used for quenching, the air flow was directed toward the sample surface by using one nozzle for each sample.

The **Figure 68** shows the temperature variation recorded during first twenty cycles up to 950°C. During each cycle the temperature change all for coated and uncoated sample was regular and repetitive. In this case, each thermal cycle consisted of three steps: heating up to 950°C, isothermal treatment for 3 minutes and quench down to 300 °C.

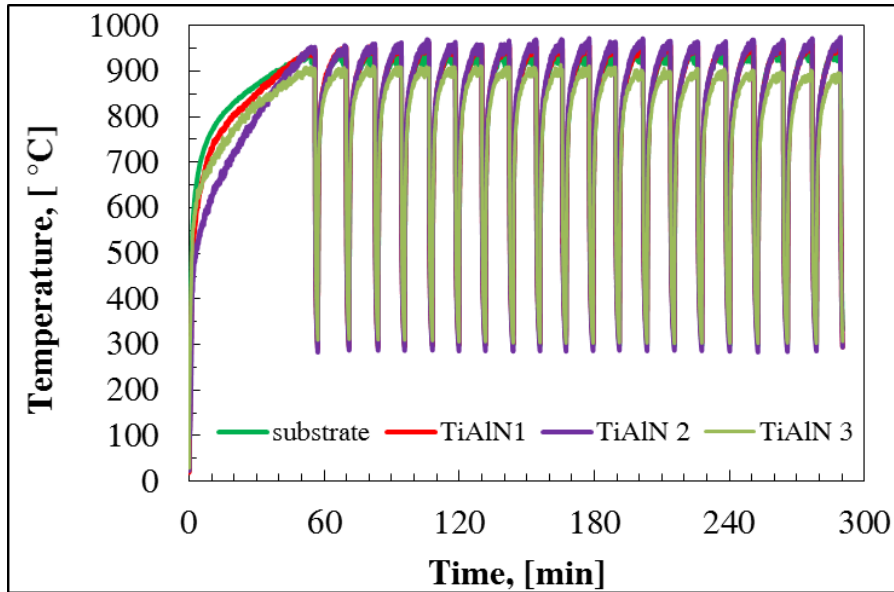


Figure 68: Thermal cycling up to 950°C in Burner Rig apparatus (isothermal step lasting 3 minutes, quenching to 300 °C).

### 2.3.7 Scratch test

Scratch test is one effective method for investigating the adhesion between a coating and the substrate on which it has been deposited.

Scratch test parameters were chosen according to ISO 1071-3:2005 standard [135] for ceramic materials in progressive loading scratch test (PLST) mode.

A scratch tester (CETR-UMT-2, Bruker, ISMATE laboratory), equipped with a standard Rockwell C diamond tip, was used for advanced scratch testing of TiAlN/Ti-48Al-2Cr-2Nb systems (**Figure 69**).

The normal force ( $F_z$ ) and the friction coefficient (COF) were recorded as a function of time. The coating/substrate adhesion was quantified determining the failure critical load  $L_{c3}$ , at which adhesive failure was initiated due to the coating delamination.  $L_{c3}$  was estimated by combining detected signals with microscope images of scratch tracks (Wild/Leica M3Z stereomicroscope equipped with a Lumenera Infinity lite camera). In particular a sharp variation of the coefficient of friction occurs at the failure critical load.

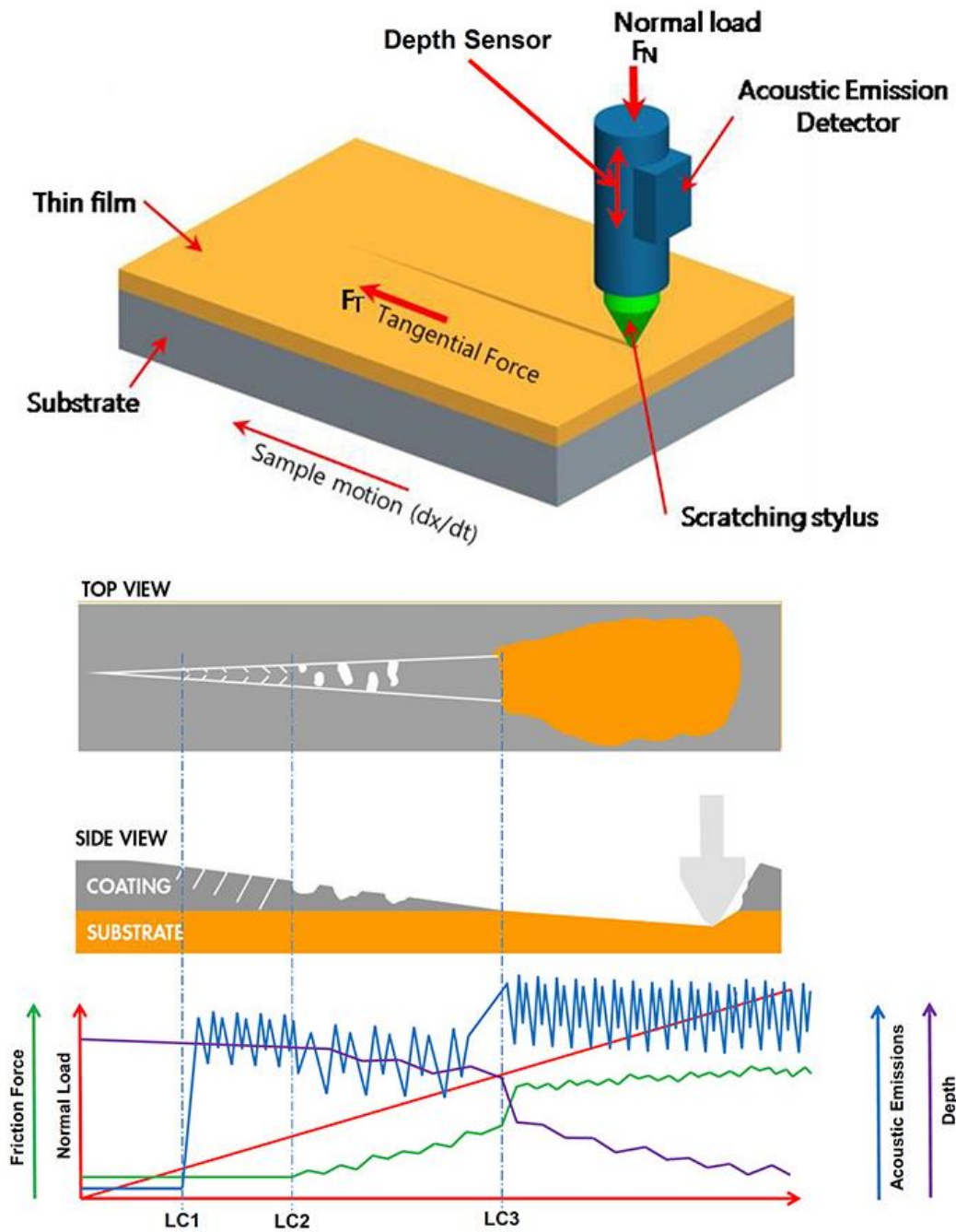


Figure 69: Progressive Load Scratch Test [136], [137].

# Chapter 3

## Experimental part: results

In this chapter, the oxidation behaviour of uncoated and coated TiAl-based intermetallic alloys is discussed. Different oxidation tests were performed in order to study the oxidation kinetics of TiAl alloys, the effectiveness of ceramic coatings for oxidation protection and the level of oxidation, which occurred at high temperatures.

### 3.1 Oxidation kinetics of TiAl alloys

The oxidation resistance of four TiAl alloys with different chemical compositions (Ti-48Al-2Cr-2Nb at.%, Ti-48Al-2Nb-0.7Cr-0.3Si at.%, Ti-43.5Al-4Nb-1Mo at.% and Ti-47Al-2Cr-8Nb at.%) was compared by submitting these materials to TGA thermal oxidation tests in the same experimental conditions.

Initially, these four TiAl-based intermetallic alloys were oxidized in TGA furnace during a temperature run. The TGA test was performed in the temperature range from 25° C to 1000 °C under airflow of 50 ml/min, and heating rate of 5°/min. The TGA results are shown in **Figure 70**, where the mass gain versus time recorded during a temperature run is depicted. After this TGA test, all TiAl based alloys under investigation exhibited more or less significant spallation.

According to TGA curves in **Figure 70**, the good oxidation resistance of all TiAl intermetallic alloys was observed until 800°, while the significant oxidation of each TiAl alloy is present up to 800°C. In fact, the TiAl intermetallic alloys are currently used for low-pressure stages of aircraft turbines or for turbocharger of car engines operating at temperatures not exceeding 750 °C and 850 °C respectively.

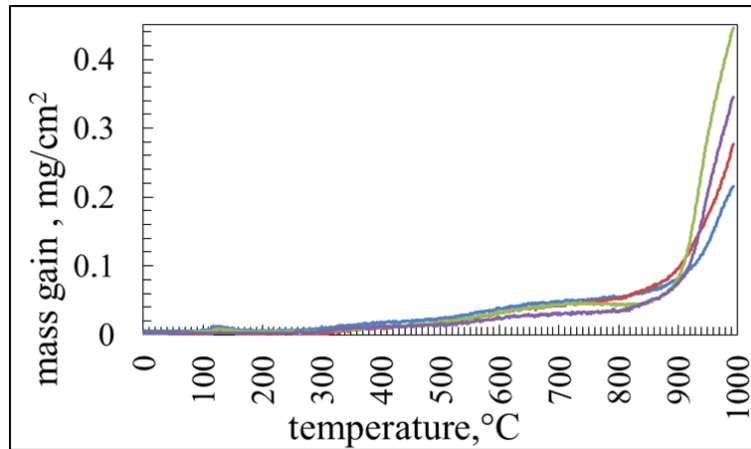


Figure 70: TGA curves of TiAl alloys recorded under 50 ml/min air flow during heating from 25 to 1000 °C at 5°/min: Ti-48Al-2Cr-2Nb (green line), Ti-48Al-2Nb-0.7Cr-0.3Si (violet line), Ti-43.5Al-4Nb-1Mo (red line), and Ti-47Al-2Cr-8Nb (blue line) [102].

The oxidation kinetics of intermetallic alloys at high temperature are usually controlled by the diffusion rate of oxygen and alloying elements, which increases with the temperature increase [102].

In order to study the oxidation kinetics of each TiAl intermetallic alloy under investigation, several isothermal TGA tests were performed at different temperatures (800 °C, 850 °C, 900 °C, 950 °C and 1000 °C) under air flow (50 ml/min) and adopting a dwelling time of 10 h. The TGA curves recorded for each alloy at different temperatures are shown in **Figure 71**, **Figure 72**, **Figure 73** and **Figure 74**.

The first part of the relevant TGA curves, showing an almost linear trend, corresponds to the heating up to the temperature chosen for the subsequent isothermal oxidation treatment. During the heating to the pre-fixed temperature selected for the isothermal oxidation treatment an initial oxide layer forms on the top of sample surface. During the subsequent isothermal oxidation, the oxide layer grows due to the inward diffusion of oxygen and the outward diffusion of metallic elements from the substrate, as a consequence of the oxide layer growth some spallation of oxide scales can occur at high temperature. This phenomenon was clearly observed after 10 hours of oxidation above 900°C for Ti-48Al-2Cr-2Nb (48-2-2) and Ti-48Al-2Nb-0.7Cr-0.3Si (RNT650). The oxide grown on Ti-43.5Al-4Nb-1Mo (TNM) suffered slight exfoliation after 10h at 950°C, and only negligible spallation was observed for Ti-47Al-2Cr-8Nb (HNb) after 10h at 1000°C. For an

accurate investigation of the kinetic law, only the TGA curves referring to well measurable mass gain occurring without significant exfoliation phenomena were considered [102].

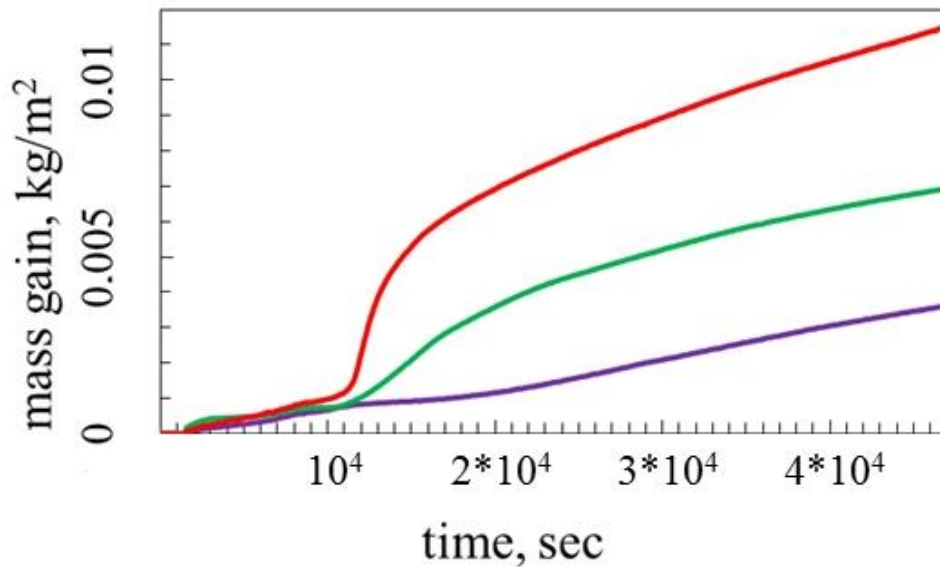


Figure 71: TGA curves of Ti-48Al-2Cr-2Nb (48-2-2) alloy recorded at different temperatures (air flow 50 ml/min, isothermal treatment lasting 10 h): violet line 800 °C, green line 850 °C and red line 900 °C [102].

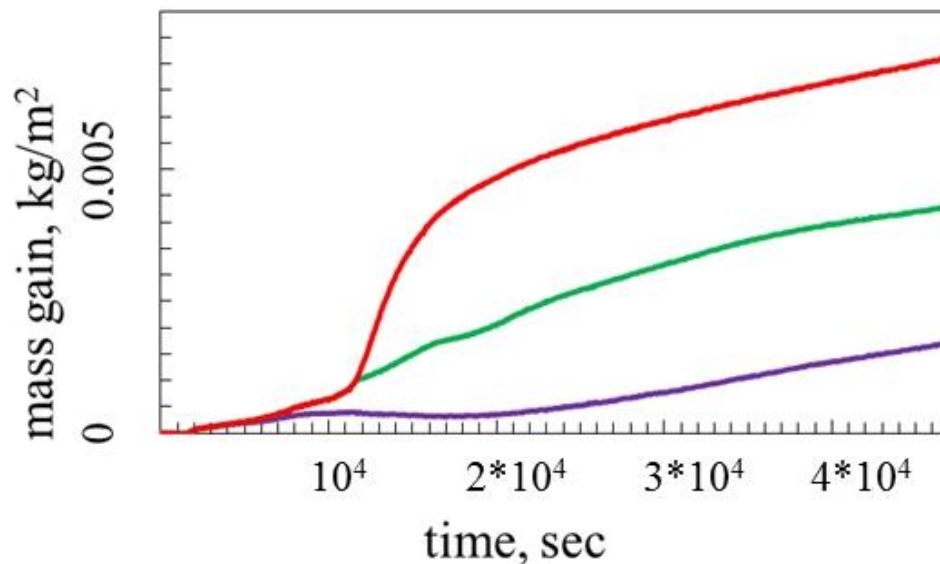


Figure 72: TGA curves of Ti-48Al-2Nb-0.7Cr-0.3Si (RNT650) alloy recorded at different temperatures (air flow 50 ml/min, isothermal treatment lasting 10 h): violet line 800 °C, green line 850 °C and red line 900 °C [102].

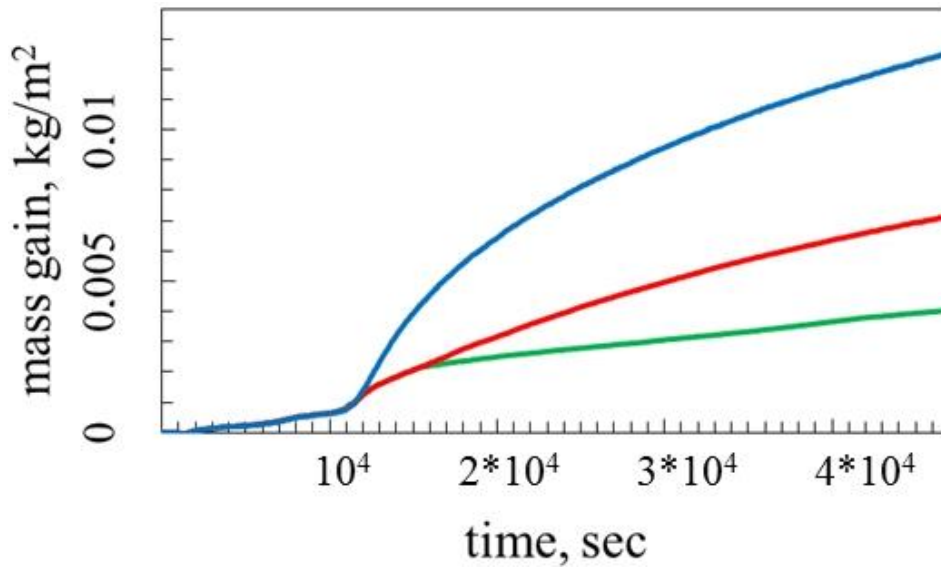


Figure 73: TGA curves of Ti-43.5Al-4Nb-1Mo (TNM) alloy recorded at different temperatures (air flow 50 ml/min, isothermal treatment lasting 10 h): green line 850 °C, red line 900 °C and blue line 950 °C[102].

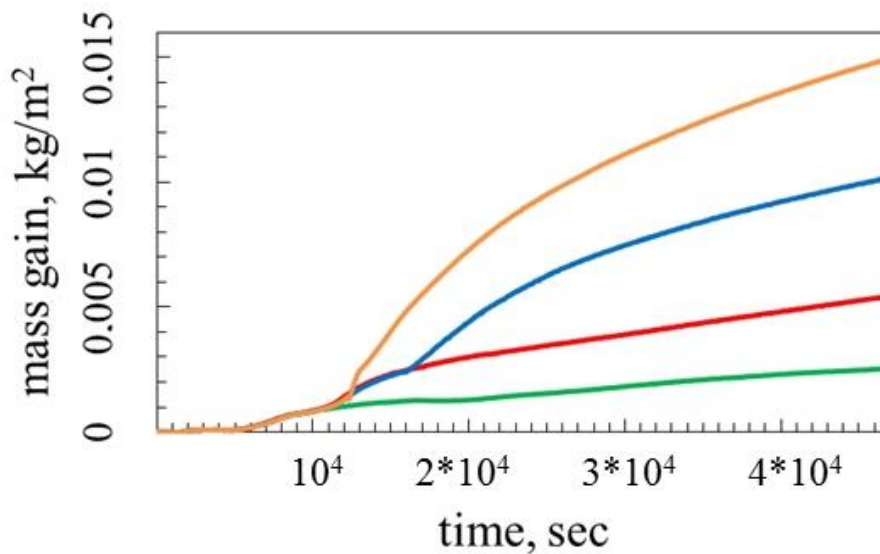


Figure 74: TGA curves of Ti-47Al-2Cr-8Nb (HNb) alloy recorded at different temperatures (air flow 50 ml/min, isothermal treatment lasting 10 h): green line 850 °C, red line 900 °C, blue line 950 °C and yellow line 1000 °C [102].

For the same reason, the XRD patterns of as-processed intermetallic alloys are compared in the following with those of samples oxidized at a temperature that does

not cause exfoliation of the oxidized layers (**Figure 75**, **Figure 76**, **Figure 77** and **Figure 78**).

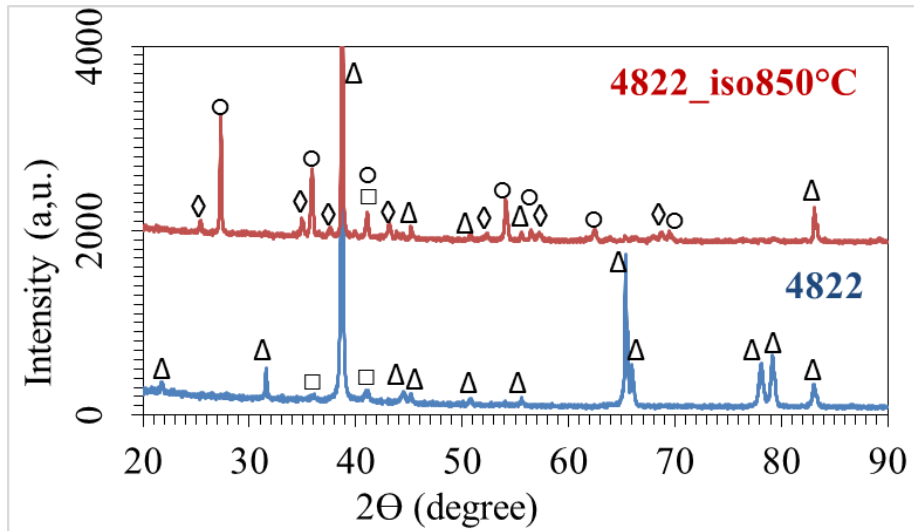


Figure 75: XRD patterns of Ti-48Al-2Cr-2Nb alloy: blue spectrum= as-processed, red spectrum= oxidized at 850°C. Crystalline phases:  $\Delta$  TiAl ( $\gamma$ ),  $\square$   $\text{Ti}_3\text{Al}$  ( $\alpha_2$ ),  $\diamond$   $\text{Al}_2\text{O}_3$  ( $\alpha$ ),  $\circ$   $\text{TiO}_2$  [102].

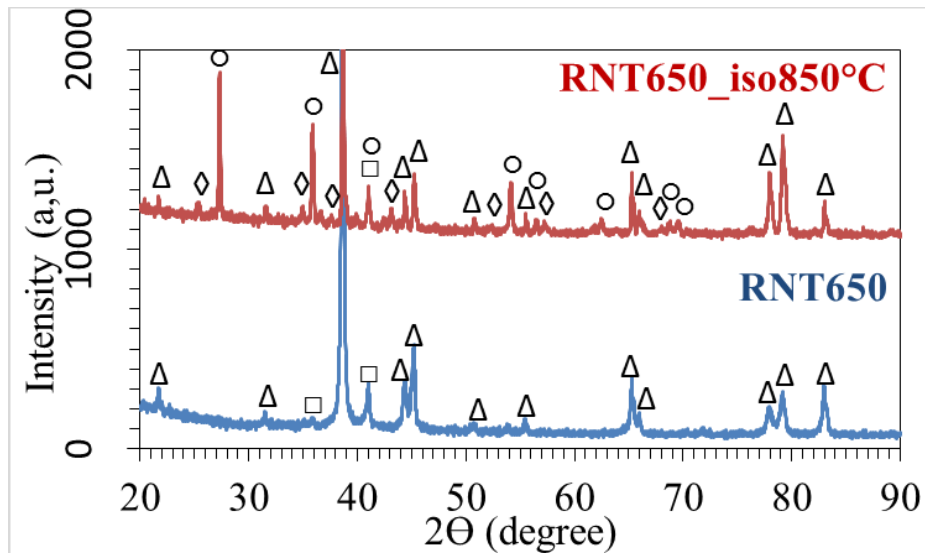


Figure 76: XRD patterns of Ti-48Al-2Nb-0.7Cr-0.3Si alloy: blue spectrum= as-processed, red spectrum= oxidized at 850°C. Crystalline phases:  $\Delta$  TiAl ( $\gamma$ ),  $\square$   $\text{Ti}_3\text{Al}$  ( $\alpha_2$ ),  $\diamond$   $\text{Al}_2\text{O}_3$  ( $\alpha$ ),  $\circ$   $\text{TiO}_2$  [102].

Before the oxidation, the 48-2-2 and RNT alloys mainly contained  $\gamma$ -TiAl ( $\Delta$ ) and a lower amount of  $\alpha_2$ -Ti<sub>3</sub>Al ( $\square$ ).

After isothermal oxidation, some  $\alpha$ -alumina ( $\diamond$ ) and rutile ( $\circ$ ) formed on the surface of these alloys. In addition, in XRD spectra of oxidized samples the peaks of  $\gamma$  and  $\alpha_2$  phases are also present. This means that the thickness of the oxide layer is not sufficient to prevent the penetration of the X-ray beam down to the metal substrate (**Figure 75** and **Figure 76**).

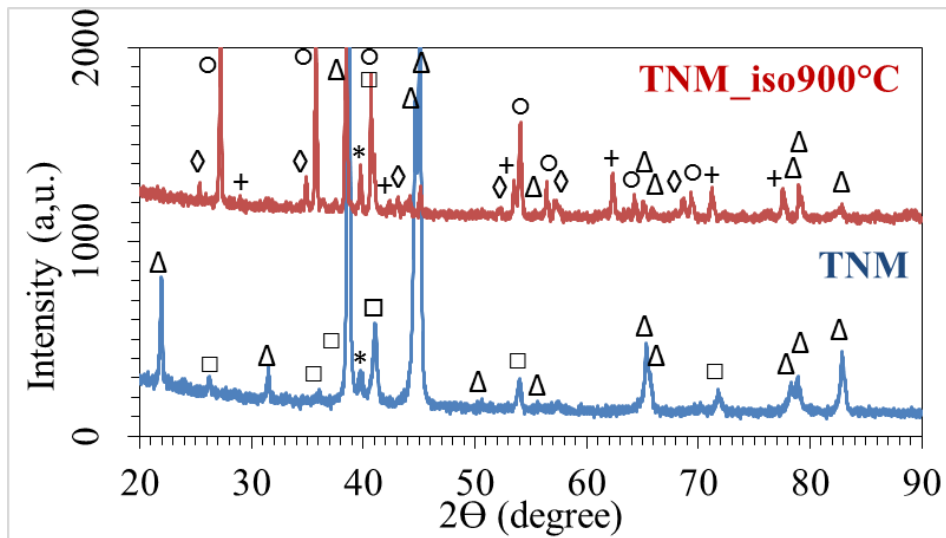


Figure 77: XRD patterns of Ti-43.5Al-4Nb-1Mo alloy: blue spectrum= as-processed, red spectrum= oxidized at 900 °C. Crystalline phases:  $\Delta$  TiAl ( $\gamma$ ), \* TiAl ( $\beta$ ),  $\square$  Ti<sub>3</sub>Al ( $\alpha_2$ ),  $\diamond$  Al<sub>2</sub>O<sub>3</sub> ( $\alpha$ ),  $\circ$  TiO<sub>2</sub>, + NbO [102].

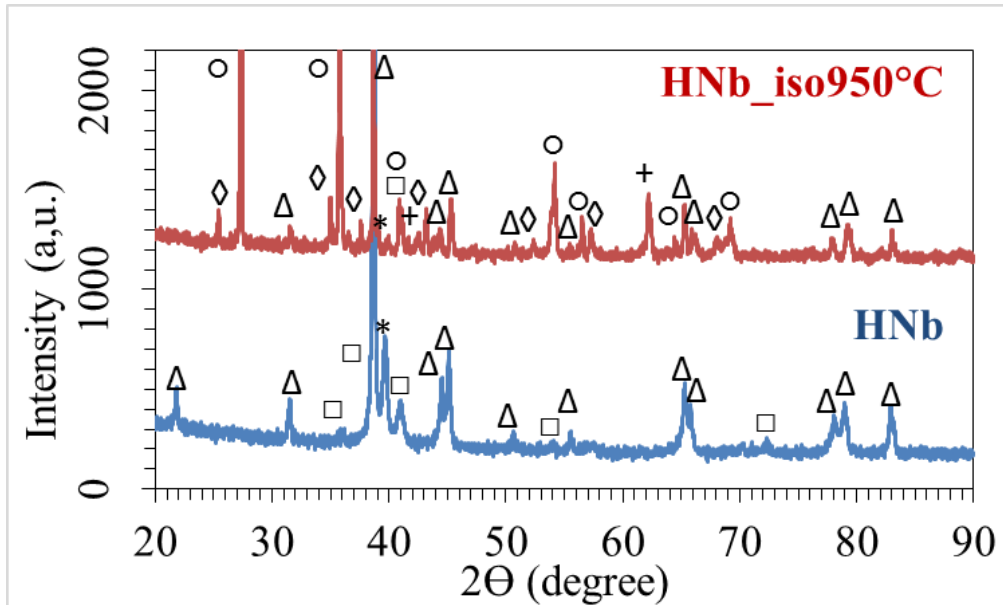


Figure 78: XRD patterns of Ti-47Al-2Cr-8Nb alloy: blue spectrum= as-processed, red spectrum= oxidized at 950 °C. Crystalline phases:  $\Delta$  TiAl ( $\gamma$ ), \* TiAl ( $\beta$ ),  $\square$  Ti<sub>3</sub>Al ( $\alpha_2$ ),  $\diamond$  Al<sub>2</sub>O<sub>3</sub> ( $\alpha$ ),  $\circ$  TiO<sub>2</sub>, + NbO [102].

The as-processed TNM and HNb alloys were mainly composed of  $\gamma$ -TiAl phase ( $\Delta$ ), but some contents of  $\alpha_2$ -Ti<sub>3</sub>Al ( $\square$ ) and  $\beta$  TiAl (\*) phases were present as well. The presence of  $\beta$  phase in these alloys is consistent with their rather high content of  $\beta$  stabilizers (Nb and Mo). The higher Nb content (8% at.) in HNb alloy resulted in the higher intensity of  $\beta$ -TiAl peak with respect to TNM alloy (4% at. Nb). (**Figure 77** and **Figure 78**).

It is evident that several oxides formed on the surfaces of alloys containing Mo and Nb. In addition, in this case, rutile and alumina mainly formed after TGA oxidation test, but also niobium oxide formed after oxidation of alloys containing at least 4% at of Nb.

Conclusively, in every case, the principal oxide formed after TGA oxidation test was rutile, and therefore it can be inferred that the oxide layer cannot provide passivation effect since it contains mixed crystals of rutile and alumina. On the other hand, a gradient of composition through the layer thickness could occur and the alumina concentration could be higher on the surface, but XRD cannot allow neither to confirm nor to exclude this possibility. For this reason, XPS analyses were carried out.

In addition to XRD investigation, the oxidized samples were analysed by XPS and EDS techniques. The results of these investigations are compared in **Table 7** and **Table 8**.

**Table 7:** XPS analyses of the sample surfaces after isothermal oxidation (argon and contaminants percentages not reported, balancing 100%).

| Alloys                         | XPS analysis (at.%) |     |     |     |     |     |      |
|--------------------------------|---------------------|-----|-----|-----|-----|-----|------|
|                                | Ti                  | Al  | Cr  | Nb  | Mo  | Si  | O    |
| <b>Ti-48Al-2Cr-2Nb</b>         | 29.8                | 3.8 | 2.1 | 0.1 | -   | -   | 62.5 |
| <b>Ti-48Al-2Nb-0.7Cr-0.3Si</b> | 29.0                | 2.3 | 2.6 | 0.1 | -   | 0.5 | 63.6 |
| <b>Ti-43.5Al-4Nb-1Mo</b>       | 29.0                | 4.5 | -   | 0.1 | 0.1 | -   | 64.7 |
| <b>Ti-47Al-2Cr-8Nb</b>         | 31.9                | 2.0 | 1.8 | 0.1 | -   | -   | 62.1 |

**Table 8:** EDS analyses of the sample surfaces after isothermal oxidation (argon and contaminants percentages not reported, balancing 100%).

| Alloys                         | EDS analysis (at.%) |      |     |     |     |     |      |
|--------------------------------|---------------------|------|-----|-----|-----|-----|------|
|                                | Ti                  | Al   | Cr  | Nb  | Mo  | Si  | O    |
| <b>Ti-48Al-2Cr-2Nb</b>         | 17.7                | 18.1 | 0.5 | 0.2 | -   | -   | 63.6 |
| <b>Ti-48Al-2Nb-0.7Cr-0.3Si</b> | 19.0                | 18.3 | 0.2 | 0.3 | -   | 0.1 | 62.2 |
| <b>Ti-43.5Al-4Nb-1Mo</b>       | 19.2                | 16.5 | -   | 0.5 | 0.1 | -   | 63.7 |
| <b>Ti-47Al-2Cr-8Nb</b>         | 17.9                | 18.4 | 0.5 | 0.5 | -   | -   | 62.8 |

The EDS and XPS analyses were performed on samples already investigated by XRD, whose patterns are shown in the relevant figures. The comparison of XPS and EDS analysis can give information about the distribution of elements within

the oxide scale formed on surfaces of different TiAl alloys. As well known, the electron beam penetration in SEM-EDS analysis is enormously higher than that of XPS beam. For this reason, SEM-EDS method shows the average composition of oxide scale, while the XPS analysis gives information about few atomic layers placed on the top of oxide layers.

In every case, the formation of oxides is evident from both analyses. Both EDS and XPS show that the ratio between oxygen and metallic elements detected within the scale is consistent with the formation of a mixture of oxides of Ti, Al, Cr, Si, Nb and Mo. The XRD patterns reported before showed that the alumina, rutile and niobium oxide (in case of TNM and HNb alloys) formed after oxidation. The average value of the atomic ratio between Ti and Al found in the scale is consistent with the atomic ratio of these elements in the alloys, which means that there is not a preferential oxidation of one of the two main elements constituting the TiAl alloys. On the other hand, XPS analysis puts in evidence that the outermost part of the oxide layer is mostly constituted by rutile with an additional much lower amount of alumina.

The percentage of chromium on the surface of oxidized alloys was about 2 % at. (XPS analysis), but the average concentration (EDS analysis) was much lower. This means that the chromium mainly concentrated in the outermost part of the oxide layer. Differently the percentage of silicon with respect to the total of metallic elements is higher in the scale than in the bulk of Ti-48Al-2Nb-0.7Cr-0.3Si alloy, in particular at the oxide surface. Therefore, this element concentrates in the scale and in particular in the external part of it.

Both EDS and XPS outcomes concur to show that Nb and Mo do not diffuse easily from the substrate towards the oxide layer; however, they take part in the formation of the scale as put in evidence by the formation of NbO in TNM and HNb alloys. The comparison of EDS and XPS analyses shows that the concentration of these elements is higher in the inner part of the oxide layer.

Very likely diffusion phenomena affect the distribution within the oxide layer of elements that form oxides.

The diffusion phenomena is based on capacity of atoms to move from a high concentration region towards a region of low concentration, in addition to concentration gradient also the energy of activation for the diffusion of alloy elements (Al, Ti, Cr, Mo, Nb, Si) can play very important role. In fact, on the basis

of free energy for oxide formation alumina should form more easily than the oxides of all the other elements contained in the alloys under investigation (Ti, Cr, Mo, Nb, Si). In spite of thermodynamics, the oxide layer was composed by a complex mixture of several oxides distributed in inhomogeneous manner inside of whole oxide layer [102]. Alumina is not the main component of the scale and the concentration of this oxide greatly decreases moving towards the surface that is mainly constituted by rutile.

Assuming that the oxide layer growth is controlled by diffusion, the trend of the experimental TGA curves, shown in **Figure 71**, **Figure 72**, **Figure 73** and **Figure 74**, should be explained by using the Wagner's theory.

In particular, the mass gain recorded during the isothermal step lasting ten hours should be fitted according to the parabolic rate relationship, as proposed by the Wagner's theory:

$$\left(\frac{\Delta m}{A}\right)^2 = K_p t \text{ [138].}$$

Where  $\Delta m/A$  is the weight gain of the sample per unit of surface area,  $t$  is the time and  $K_p$  is the parabolic rate constant.

In **Figure 79**, **Figure 80**, **Figure 81** and **Figure 82**, the parabolic plots for the part of TGA curves obtained during the isothermal step are showed. The mass gain was transformed into  $(\Delta m/A)^2$  and plotted versus isothermal oxidation time. Black straight lines fitting the experimental data were superimposed to the experimental curves. The slope of the fitting lines corresponds to the values of the parabolic rate constant for each alloy and experimental condition (temperature). The  $R^2$  is the correlation coefficient of these curves.

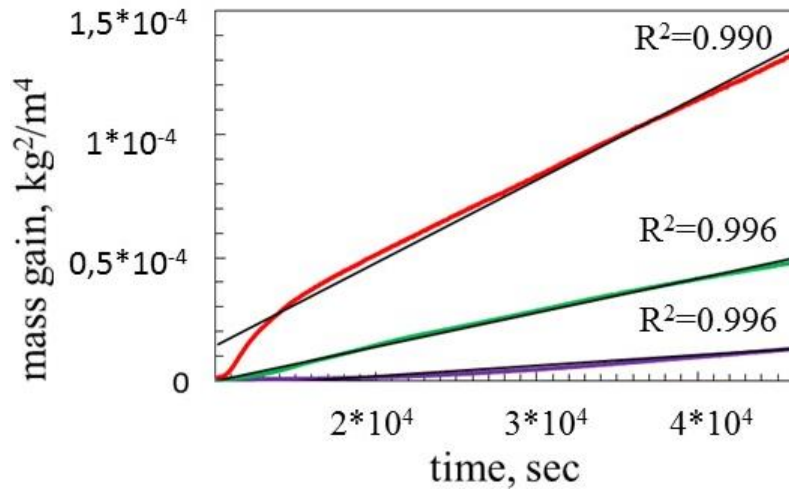


Figure 79: TGA data (50 ml/min in air for 10 h) of Ti-48Al-2Cr-2Nb alloy fitted at different temperatures with straight lines according to a parabolic law: violet line= 800 °C, green line= 850 °C and red line= 900 °C [102].

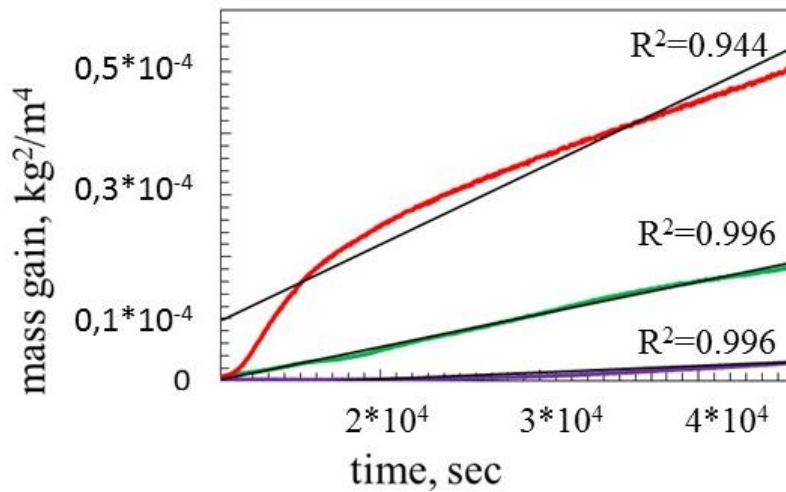


Figure 80: TGA data (50 ml/min in air for 10 h) of Ti-48Al-2Nb-0.7Cr-0.3Si alloy fitted at different temperatures with straight lines according to a parabolic law: violet line= 800 °C, green line= 850 °C and red line= 900 °C [102].

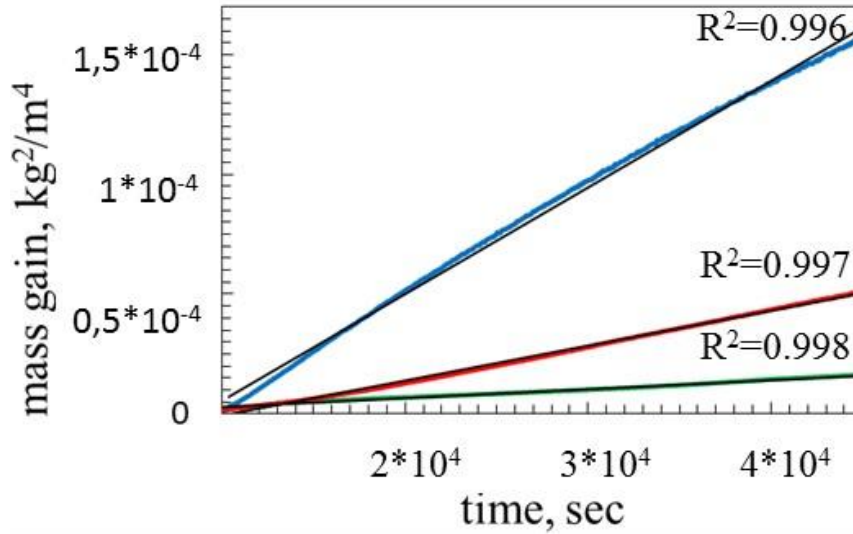


Figure 81: TGA data (50 ml/min in air for 10 h) of Ti-43.5Al-4Nb-1Mo alloy fitted at different temperatures with straight lines according to a parabolic law: green line= 850 °C, red line= 900 °C and blue line = 950 °C [102].

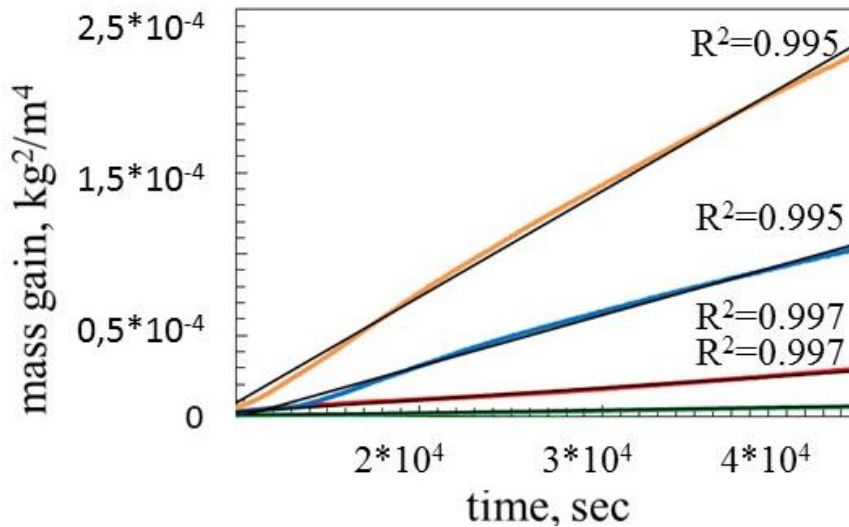


Figure 82: TGA data (50 ml/min in air for 10 h) of Ti-47Al-2Cr-8Nb alloy fitted at different temperatures with straight lines according to a parabolic law: green line= 850 °C, red line = 900 °C, blue line= 950 °C and yellow line = 1000 °C [102].

According to TGA fitted plots, the experimental data well match with the parabolic law, as the correlation coefficient ( $R^2$ ) is always greater than 0.940 and in most of case near to one. Very little deviations were only observed for Ti-48Al-2Cr-2Nb and Ti-48Al-2Nb-0.7Cr-0.3Si alloys ( $R^2=0.990$  and  $R^2=0.994$

respectively) when oxidized at 900°C. Probably these deviations are due to the little spallation of oxide layers grown on 48-2-2 and RNT-650 alloys at 900°C. The parabolic rate constant for oxidation of TiAl alloys under investigation at different temperatures were obtained from TGA fitted plots (**Table 9**).

**Table 9:** Parabolic rate constant  $K_p$  ( $\text{kg}^2\text{m}^{-4}\text{s}^{-1}$ ) at specific temperatures (800°C-1000°C) for the TiAl alloys under investigation.

| T<br>(°C) | 48-2-2                |       | RNT-650               |       | TNM                   |       | HNb                   |       |
|-----------|-----------------------|-------|-----------------------|-------|-----------------------|-------|-----------------------|-------|
|           | $K_p$                 | $R^2$ | $K_p$                 | $R^2$ | $K_p$                 | $R^2$ | $K_p$                 | $R^2$ |
| 800       | $4.26 \cdot 10^{-10}$ | 0.996 | $1.07 \cdot 10^{-10}$ | 0.996 | -                     | -     | -                     | -     |
| 850       | $1.38 \cdot 10^{-9}$  | 0.996 | $5.29 \cdot 10^{-10}$ | 0.996 | $3.67 \cdot 10^{-10}$ | 0.998 | $1.63 \cdot 10^{-10}$ | 0.997 |
| 900       | $3.36 \cdot 10^{-9}$  | 0.990 | $1.23 \cdot 10^{-9}$  | 0.944 | $1.46 \cdot 10^{-9}$  | 0.997 | $7.39 \cdot 10^{-10}$ | 0.997 |
| 950       | -                     | -     | -                     | -     | $4.45 \cdot 10^{-9}$  | 0.996 | $3.14 \cdot 10^{-9}$  | 0.995 |
| 1000      | -                     | -     | -                     | -     | -                     | -     | $6.51 \cdot 10^{-9}$  | 0.995 |

As expected the parabolic rate constant raises with the temperature growth for all the TiAl alloys. In addition, the comparison of parabolic rate constant at different temperatures shows that the oxidation resistance of these alloys changes significantly for temperature variations of 50 °C. The Ti-47Al-2Cr-8Nb alloy exhibited the best oxidation resistance, while the Ti-48Al-2Cr-2Nb showed the worst result. The RNT-650 and TNM alloys showed a similar oxidation resistance, and their  $K_p$  placed between the best and worst values at an intermediate level. The oxidation behaviour of Ti-43.5Al-4Nb-1Mo and Ti-47Al-2Cr-8Nb at 950 °C alloys appeared very similar, while  $K_p$  of these alloys was different at 900°C. The Ti-43.5Al-4Nb-1Mo alloys at 1000°C showed significant spallation, and therefore the parabolic rate constant was not calculated at this temperature. The Ti-47Al-2Cr-8Nb alloy exhibited  $K_p$  values of the same order of magnitude at 1000°C and at 950°C; these values are similar to those showed by 48-2-2 at 900°C. The best oxidation resistance seems related to the molybdenum and niobium alloying elements. In addition, aluminium plays a role since its concentration is higher in HNb alloy than in TNM alloy, and this can justify their different behaviour. In addition, the parabolic rate constants of the alloys under investigation at 900°C is placed between  $K_p$  for the growth of titania (at 900°C is  $10^{-7} \text{ kg}^2\text{m}^{-4}\text{s}^{-1}$ ) and  $K_p$  for alumina (at 900°C is  $10^{-10} \text{ kg}^2\text{m}^{-4}\text{s}^{-1}$ ) [30]. At this temperature, the parabolic rate

constant of Ti-47Al-2Cr-8Nb is very similar to that for the formation of a pure alumina scale.

The relation between the temperature and the parabolic rate constant  $K_p$  can be represented by the Arrhenius equation:

$K_p = K_0 e^{-\frac{Q}{RT}}$ , where  $K_0$  is a constant,  $Q$  is the activation energy for the oxidation,  $R$  is the gas constant and  $T$  is temperature in K.

The Arrhenius equation can be transformed by taking the natural logarithm of both parts as:

$$\ln(K_p) = \ln(K_0) - \frac{Q}{RT} .$$

The Arrhenius plot of the logarithm of parabolic rate constant at different temperatures versus  $1/T$  for oxidation of TiAl alloys under investigation is shown in **Figure 83**.

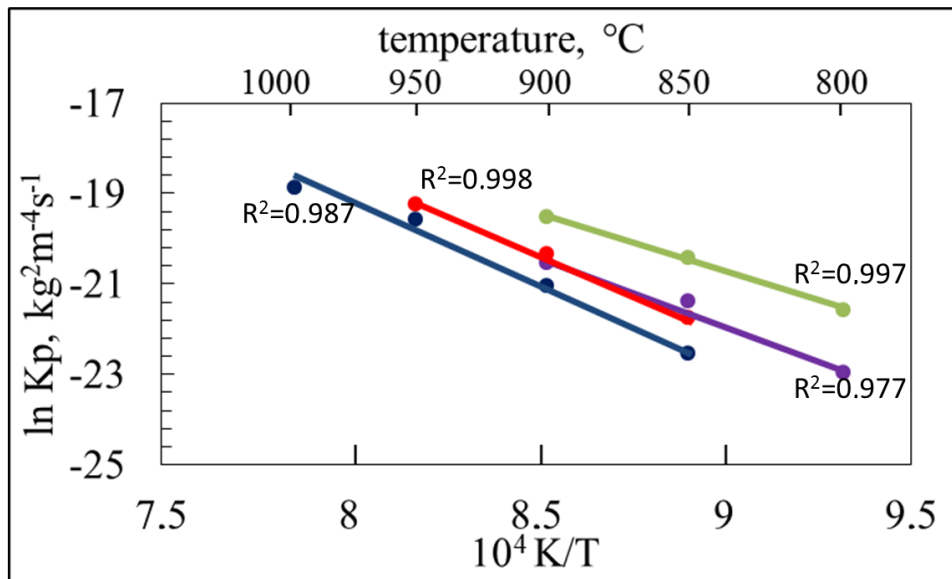


Figure 83: Arrhenius plot for oxidation of Ti-48Al-2Cr-2Nb (green line), Ti-48Al-2Nb-0.7Cr-0.3Si (violet line), Ti-43.5Al-4Nb-1Mo (red line), and Ti-47Al-2Cr-8Nb (blue line) [102].

The activation energies for oxidation ( $Q$ ) of TiAl alloys under investigation were calculated from the slope of the straight line fitting the experimental data represented in the **Figure 83**. The following values were obtained: 216.30 kJmol<sup>-1</sup>

(Ti-48Al-2Cr-2Nb), 256.57 kJmol<sup>-1</sup> (Ti-48Al-2Nb-0.7Cr-0.3Si), 285.12 kJmol<sup>-1</sup> (Ti-43.5Al-4Nb-1Mo) and 298.4 kJmol<sup>-1</sup> (Ti-47Al-2Cr-8Nb).

According to literature, the activation energies of oxidation for TiAl binary alloys greatly depend on the aluminium content (about 250 kJmol<sup>-1</sup> for Ti-26Al alloy and 400 kJmol<sup>-1</sup> for Ti-48.6Al alloy) [22]. Based on these literature outcomes the Ti-Al binary alloy with an aluminium content around 48 % at. shows an oxidation resistance higher than quaternary alloys with similar aluminium concentration (like most of the alloys under investigation).

Unfortunately, the TiAl binary alloy cannot be used in structural parts, designed for working at high temperatures. Complex intermetallic alloys, showing improved mechanical properties required for industrial application, have been developed by using several alloying elements. These alloys always show lower activation energy for oxidation than the binary TiAl alloy with a high aluminium content. Nevertheless, the different alloying elements used for improving mechanical behaviour are believed to display beneficial or detrimental effects on oxidation resistance. In fact, according to literature, the oxidation behaviour of complex TiAl intermetallic alloys (Ti-48Al, at.%) in air within the temperature range between 800-1000°C can be appreciably improved by using some alloying elements [22],[32]. The relative effectiveness of these beneficial elements followed the order: Mo > Nb > Si [22]. High percentages of both Al and Nb alloying elements, when contemporaneously present in TiAl intermetallic alloys, grant a beneficial effect on oxidation resistance (activation energy values Ti-43Al-11Nb is 296 kJ mol<sup>-1</sup> and of Ti-30Al-2.7Nb 268 kJ mol<sup>-1</sup>) [26].

However literature also reports activation energy values for Ti-Al-Nb alloys that are significantly lower (200 kJ mol<sup>-1</sup> for Ti-45.9Al-8Nb [139]) and similar to that of pure titanium (180-230 kJ mol<sup>-1</sup>).

In any case, the activation energies of alloys under investigation seem appreciably good, being higher than that for pure titanium, at least in the case of Ti-48Al-2Nb-0.7Cr-0.3Si, Ti-43.5Al-4Nb-1Mo and Ti-47Al-2Cr-8Nb alloys. The synergetic effect of Nb (4% at.) and Mo (1% at.) in TNM alloy (43.5% at.) plays a positive role on oxidation resistance, in fact the activation energy for oxidation was similar to that of Nb alloy with higher concentrations of both Al (47% at.) and Nb (8% at.). These outcomes are fully consistent with the useful effect that these elements are believed to exert on the mechanism of formation of the oxide layer: decrease of the diffusion rate of oxygen and increase of the aluminium outward

diffusion rate due to Nb, decrease of the oxygen solubility within the substrate due to Nb and Mo. The presence of chromium (2% at.) inside Ti-48Al-2Cr-2Nb alloy led to a detrimental effect on the oxidation resistance, while the small amount of silicon (0.3% at.), partially replacing Cr into Ti-48Al-2Nb-0.7Cr-0.3Si, improved the oxidation resistance. The Si, Nb and Mo elements display a positive effect on oxidation resistance since they hinder the diffusion of oxygen and, as a consequence, the oxide formation [2], [30], [34],[140], [141].

Conclusively the kinetic parameters (both parabolic rate constant and activation energy) significantly changed with the alloy composition and allowed to establish the following ranking (from the worst to the best) for the oxidation resistance of the TiAl alloys examined: Ti-48Al-2Cr-2Nb, Ti-48Al-2Nb-0.7Cr-0.3Si, Ti-43.5Al-4Nb-1Mo, Ti-47Al-2Cr-8Nb.

## **3.2 Oxidation of coated and uncoated intermetallics**

In order to improve the oxidation resistance of Ti-48Al-2Cr-2Nb intermetallic alloy, the TaAlN or TiAlN coating were proposed as protective oxidation coating. The Ti-48Al-2Cr-2Nb alloy that, among the Ti-Al alloys under investigation, showed the worst oxidation resistance was selected for checking the suitability of the coatings. First the effectiveness of the coatings was tested by oxidation in air. When this preliminary test put in evidence the capability of the coating to give some protection against oxidation, cyclic oxidation tests were performed at different temperatures by using burner rig apparatus. These last experimental tests allowed to compare the oxidation resistance of coated and uncoated alloy under conditions simulating the real operating conditions suffered by components of turbine engines, (high temperature, oxidative environment, thermal shock).

### **3.2.1 Low-cycling oxidation at 850° C and 950° C of TiAlN coated and uncoated intermetallics**

In this part of the work the coating thermal stability, adhesion and effectiveness were evaluated in relation to the experimental conditions (temperature and duration of the test) and the method adopted for processing the TiAlN coatings [107].

According to the literature, the Ti<sub>0.54</sub>Al<sub>0.46</sub>N phase is stable up to 900°C, while it starts to undergo decomposition from 1000°C and shows a great instability over 1200°C [107].

The titanium aluminium nitride is a supersaturated solid solution with a cubic crystal lattice similar to that of TiN. The TiAlN solid solution is believed to be metastable, since annealing can result in its spinodal decomposition with the formation of cubic Ti-rich and Al-rich domains. The Al-rich domains further transform into an AlN wurtzite-like structure. The decomposition is favoured by a high Al:Ti ratio in the nitride and high temperature exposure [107], [142], [143], [144].

Firstly, microscopy and XRD analysis were adopted to study the microstructure of TiAlN coated and TiAl uncoated specimens.

The Ti-48Al-2Cr-2Nb intermetallic alloy, used as reference material in burner rig test and adopted as substrate for the HiPIMS deposition of TiAlN coatings, shows a typical duplex microstructure (**Figure 84** 1a, 1d). This microstructure is believed to ensure the best compromise between strength, ductility and fracture toughness [4]; such a kind of appropriate combination of properties is required for structural components of turbines [107].

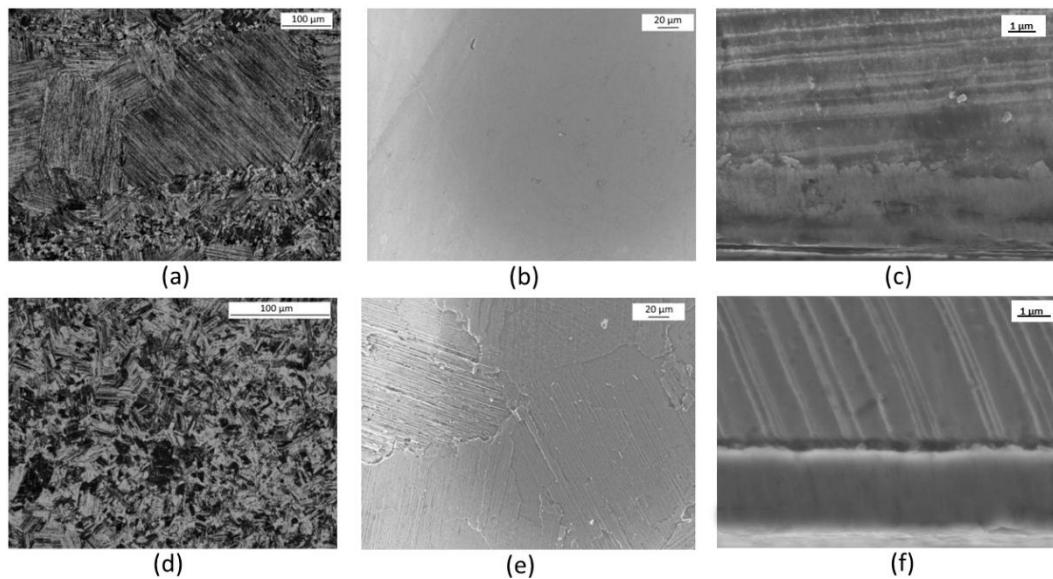


Figure 84: (a) Ti-Al intermetallic alloy, dual phase microstructure (optical microscope, etching by Kroll's reagent); (b) coating surface of TiAlN1 specimen (SEM, InLens); (c) cross section of TiAlN1 sample (SEM InLens, etching with  $\text{NH}_4\text{OH}:\text{H}_2\text{O}_2:\text{H}_2\text{O}$  1:2:5 volume ratio); (d) Ti-Al intermetallic alloy, colonies of gamma grains (optical microscope, etching by Kroll's reagent); (e) coating surface of TiAlN2 specimen (SEM, InLens); (f) cross section of TiAlN3 sample (SEM SEI, etching with  $\text{NH}_4\text{OH}:\text{H}_2\text{O}_2:\text{H}_2\text{O}$  1:2:5 volume ratio) [107].

The duplex microstructure is made of regions showing fine lamellar colonies and regions mainly containing equiaxed gamma grains. The lamellar structure consists of a mixture of alternate plates of  $\gamma$  phase (cubic TiAl) and plates of  $\alpha_2$  (Ti<sub>3</sub>Al with hexagonal lattice and ordered structure). The dual phase microstructure is achieved by using a proper Al:Ti atomic ratio as well as by adopting a specifically designed thermal treatment. The lamellar structure provides creep resistance and fracture toughness while the dual phase structure, arising from the combination of lamellar regions with the gamma equiaxed grains, ensures the necessary ductility at room temperature. Chromium is added to improve ductility too and Nb enhances the oxidation resistance. The microscopic examination of the surface of the TiAlN coatings shows that they are continuous, flat and not porous (**Figure 84**, b and e).

The coatings do not completely hide the microstructure of the substrate from microscopic observation. This is particularly evident in the case of sample TiAlN<sub>2</sub> since the high-energy metallic ions bombardment performed before the coating deposition etched the substrate surface putting in evidence the duplex microstructure (**Figure 84** e). The cross sections of the coated specimens (**Figure 84**, c and f) allowed measuring their thicknesses, which were similar for the three coatings under investigation and almost uniform all over the sample surfaces (ranging between 2  $\mu\text{m}$  and 2.2  $\mu\text{m}$ ).

Elemental maps recorded on the sample cross sections (**Figure 85**) showed that nitrogen is present within the coating, where the total concentration of metallic elements (Ti and Al) is about the 50% of that observed in the TiAl alloy substrate. Chromium and niobium were not detected inside the coating, which means that any diffusion from the substrate towards the surface did not occur during HiPIMS deposition.

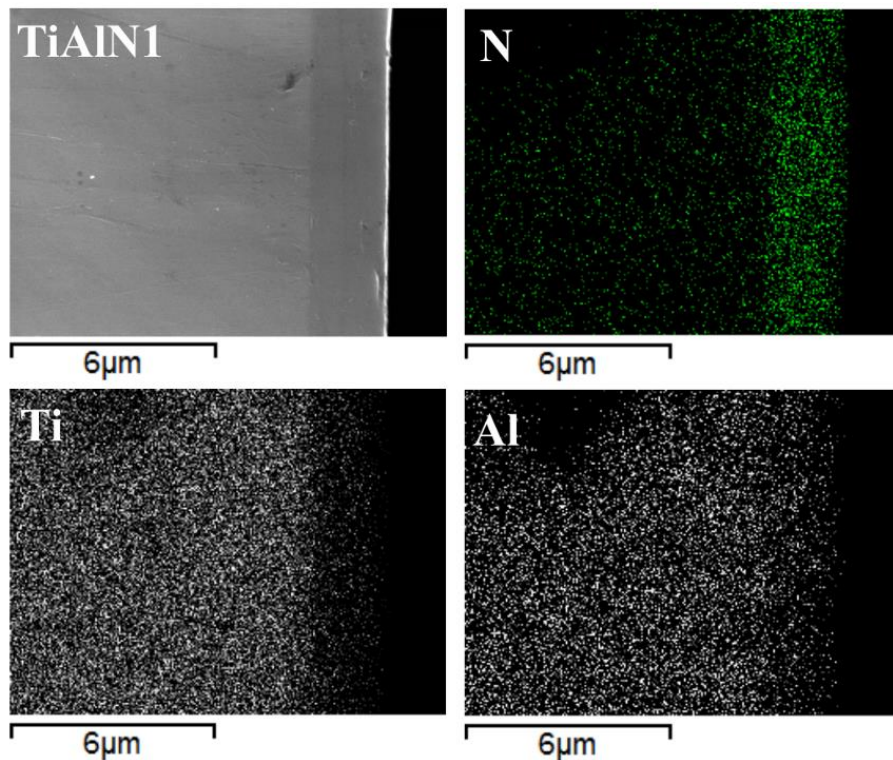


Figure 85: Cross section of TiAlN1 sample: coating morphology and nitrogen, titanium and aluminium concentration maps [107].

After burner rig test the morphology of the surface changed because of the growth of an oxide layer. This was well evident for sample TiAlN2 because the growing oxide film hid the intermetallic alloy microstructure. A microscopic inspection of the oxidized surfaces suggested that the white oxide film is not fully homogeneous. This behaviour is in agreement with the pitting mechanism of corrosion reported in the literature for the initial corrosion step of TiAlN end TiN surface coatings [87]. Actually, it is very hard to determine accurately the thickness of the oxide layer using microscopy. Indeed, even if the specimen is mounted using a thermoset resin before cutting and polishing, the oxide film (a few tenths of nanometres thick) can suffer damage and partial removal from the sample cross section during the sample preparation for the microscopic examination. Nevertheless, the SEM-EDS analysis of the oxidized surfaces confirmed the formation of the oxide scale and allowed making comparisons between bare and coated specimens. Indeed, after burner rig test involving 40 cycles up to 950°C the content of oxygen detected on the surface of the uncoated alloy was 51% at., while it ranged between 17% at. and 21% at. for the specimens carrying the TiAlN coatings. This outcome represents a first evidence of the coating effectiveness.

The XRD patterns of uncoated TiAl substrate and TiAlN coated specimens before and after short-term cycling oxidation in Burner Rig are reported in **Figure 86** and **Figure 87** [107].

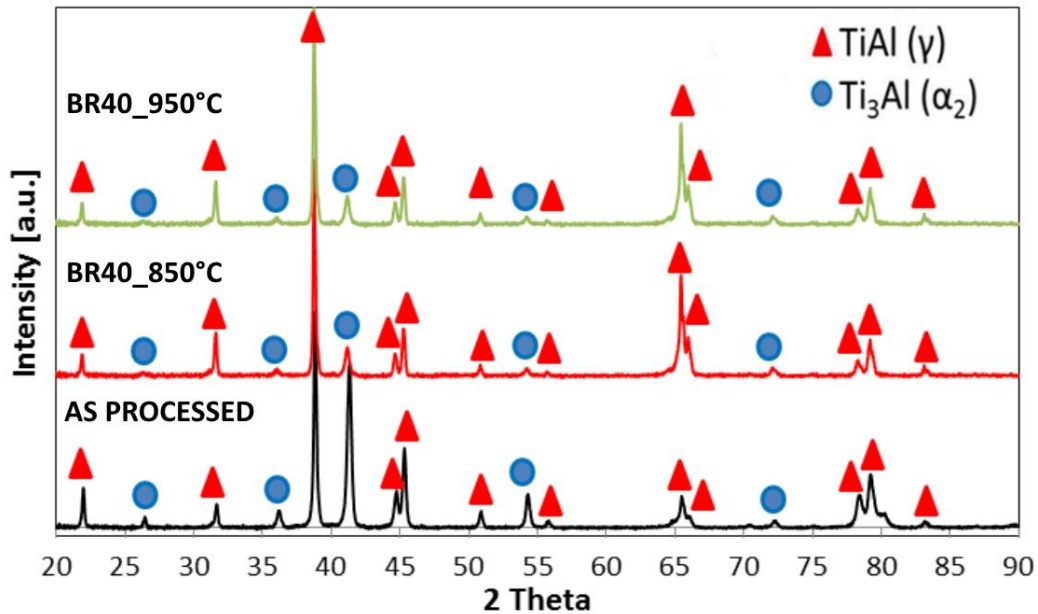


Figure 86: XRD patterns of substrate: as-processed Ti-48Al-2Cr-2Nb, and after oxidation in Burner Rig for 40 cycles at 850 or 950°C [107].

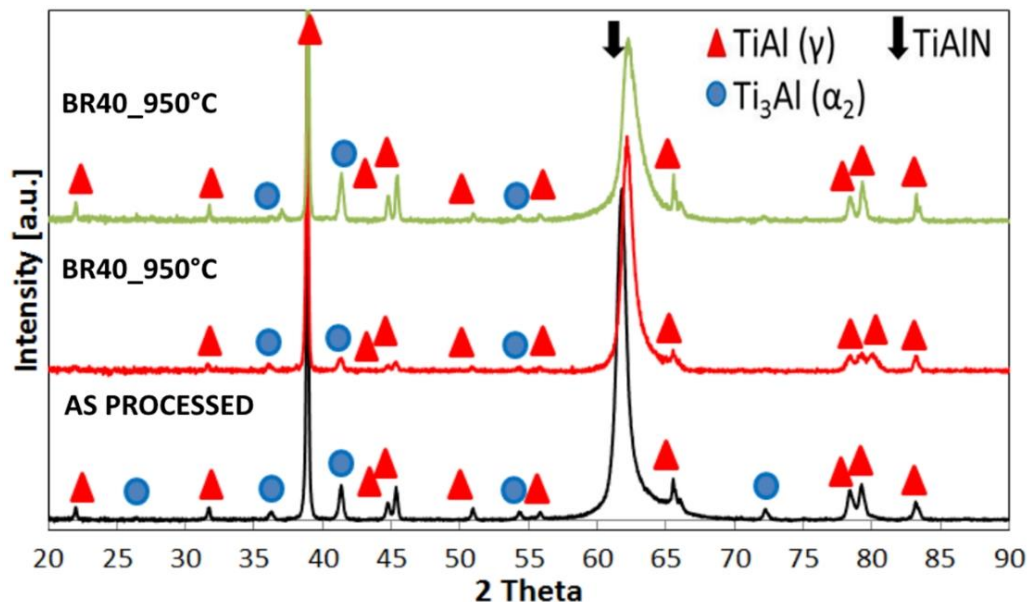


Figure 87: XRD patterns of TiAlN coated specimens (TiAlN1 coating): as-processed and after oxidation in Burner Rig for 40 cycles at 850 or 950°C [107].

Before oxidation, the TiAl substrate shows the characteristic peaks of TiAl ( $\gamma$ ) and Ti<sub>3</sub>Al ( $\alpha_2$ ) phases. After oxidation, the morphology of the substrate changed, the quantity of Ti<sub>3</sub>Al ( $\alpha_2$ ) decreased (**Figure 86**).

The XRD patterns detected on coated samples are compared before and after oxidation in **Figure 87**. In this Figure, only the patterns of coated TiAlN1 sample are reported since the XRD patterns of TiAlN2 and TiAlN3 specimens were similar.

The XRD pattern of as-processed TiAlN coating exhibits an intense peak at  $2\theta = 62.24^\circ$ , which can be attributed to (220) reflex of TiAlN. The (111), (200), (311) and (222) diffraction peaks of TiAlN could not be observed in the XRD pattern in **Figure 87** because they were overlapped with the reflexes of  $\gamma$  and  $\alpha_2$  phases or they were not enough intense to exceed the background. Moreover the literature shows that the 220 texture usually appeared after magnetron sputtering deposition of TiAlN coating [87], [88], [145].

The titanium aluminium nitride, where the Ti atoms in the TiN lattice (NaCl-type, B1) are substituted by Al atoms [146], can be indexed with the (AlTi)N phase according to the card number # 58012 of the ICSD database [147]. The peaks of TiAl ( $\gamma$ ) and Ti<sub>3</sub>Al ( $\alpha_2$ ) phases are also present in these XRD patterns of TiAlN coated samples, that is due to the deep X-ray penetration (several micrometres below the sample surface) that allows the X-ray beam to reach the intermetallic substrate.

After 40 cycles at 850°C in Burner Rig, the X-ray pattern of TiAlN coated samples remained unchanged. Only a little change was observed after 40 cycles at 950°C in Burner Rig, because the intensity of TiAlN peaks slightly decreased. In every case, oxidation did not result in the appearance of oxide peaks on the XRD patterns of both uncoated and coated specimens after 40 cycles at 850°C and 950°C. It means that probably a very thin and not well-crystallized oxide layer forms under these conditions. XRD allows only crystalline phases to be detected and only if their amount inside the volume of material affected by the analysis exceeds the detection limits of this technique. The absence in the XRD patterns of oxidized samples of peaks belonging to oxides suggests that the amount of oxides and therefore the thickness of the oxide layer are quite small. In addition, the TiAlN peak still remained in the XRD spectra detected after oxidation.

In this work, the thermal stability of nitride coatings was also considered in relation to their exploitation for oxidation protection. TiAlN is a supersaturated

solid solution with a cubic crystal lattice similar to that of TiN. This solution is believed to be metastable, since annealing can result in its spinodal decomposition with the formation of cubic Ti-rich and Al-rich domains. The decomposition is favored by a high Al:Ti ratio in the nitride and high temperature exposure. For instance, according to the literature, the  $\text{Ti}_{0.54}\text{Al}_{0.46}\text{N}$  phase is stable up to  $900^\circ\text{C}$ , while it starts to undergo decomposition from  $1000^\circ\text{C}$  and shows a great instability over  $1200^\circ\text{C}$ . Stability depends on the synthesis method, too. In the present work, no evidence of decomposition was found even after exposure of the TiAlN coatings to temperatures of up to  $950^\circ\text{C}$  for quite a long period (forty burner rig cycles entailed isothermal steps at  $950^\circ\text{C}$  lasting 2 hours in total).

In addition, the nitride coatings proved to remain well adherent to the substrate after 40 thermal cycles and oxidation at  $850^\circ\text{C}$  occurred in the burner rig apparatus.

The film/substrate adhesion results are reported in **Table 10**, that summarizes the Lc3 critical load values, associated to the coating adhesion failures. The average value was obtained considering three different tests for each sample. The critical normal load could be detected when the film started to delaminate by the appearance of a discontinuity in the friction coefficient curve (**Figure 88**).

**Table 10:** Coating adhesion and coefficient of friction for TiAlN film/TiAl systems.

| Sample    | Critical Load Lc3, (N) |  | COF          |  |
|-----------|------------------------|--|--------------|--|
|           | As deposited           | After 40 BR cycles up to $850^\circ\text{C}$ | As deposited | After 40 BR cycles up to $850^\circ\text{C}$ |
| Substrate | /                      | /  | 0.60         | 0.56   |
| TiAlN1    | $-34.0 \pm 0.5$        | $-31 \pm 1$                                  | 0.95         | 0.58   |
| TiAlN2    | $-35 \pm 2$            | $-38 \pm 2$                                  | 0.84         | 0.67   |
| TiAlN3    | $-42 \pm 3$            | $-38 \pm 2$                                  | 0.84         | 0.69   |

As reported in the **Table 10**, the plasma etching treatment performed on TiAlN2 samples did not significantly affect the Lc3 critical load values. Instead, the plasma etching treatment followed by the deposition of a glue made of TiAl

metallic interlayer clearly improved the film/substrate adhesion properties (see TiAlN3 sample) [148]. The average Lc3 value increased from  $(34.0 \pm 0.5)$  N for TiAlN1 sample to  $(42 \pm 3)$  N for TiAlN3 sample. The burner rig thermal treatment did not weaken the adhesion of the film to the substrate. Indeed, the Lc3 load values after 40 cycles at  $850^\circ\text{C}$  were not far from the ones detected on the as deposited samples.

In **Figure 88**, as an example, one scratch test output for the TiAlN1 sample as deposited and after the burner rig test and one for the TiAlN3 sample are shown.

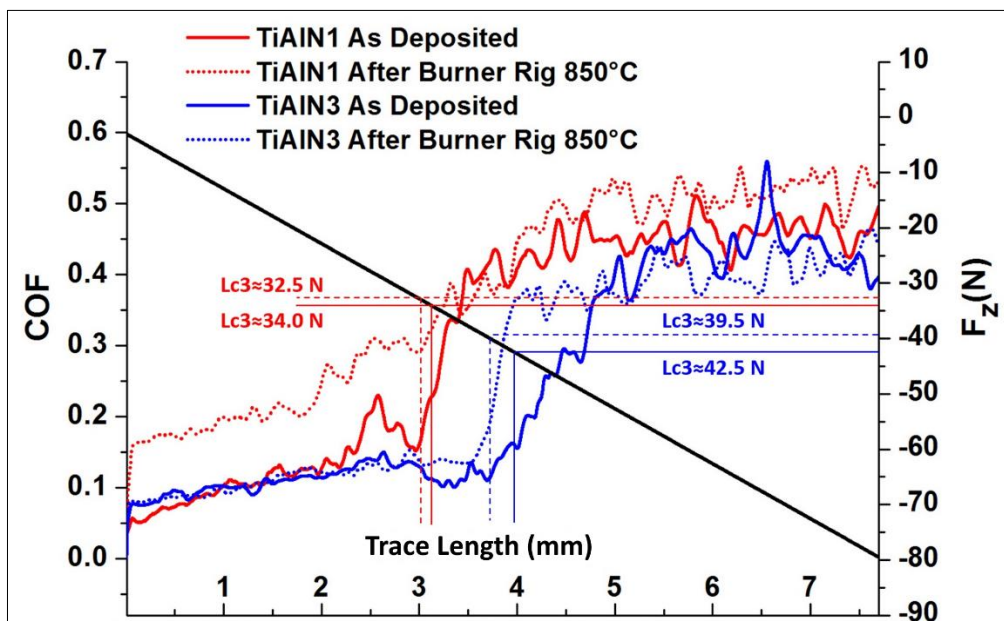


Figure 88: COF curves recorded during a single scratch test for the TiAlN1 sample and the TiAlN3 sample before and after 40 cycles up to  $850^\circ\text{C}$  in burner rig apparatus [107].

In order to investigate the oxidation of coated and uncoated surfaces at high temperature, the XPS analysis was adopted. XPS is currently widely used for investigating very thin surface coatings since the probe enters the sample only for a few atomic layers. In addition, the XPS analysis can also investigate the amorphous phases, while XRD allows only crystalline phases to be detected, and only if their amount inside the volume affected by the analysis exceeds the detection limits of this technique. The **Figure 89** exhibits the XPS survey spectrum of as processed TiAl substrate.

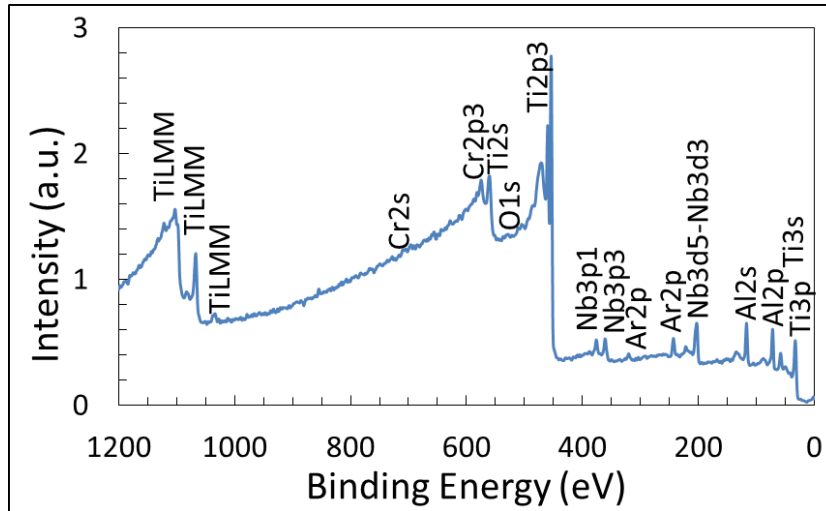


Figure 89: XPS survey spectrum of as processed substrate TiAl after argon surface cleaning.

The peaks of Al<sub>2</sub>s, Al<sub>2</sub>p, Ti<sub>3</sub>s, Ti<sub>2</sub>p, Ti<sub>3</sub>p, Nb<sub>3</sub>p, Nb<sub>3</sub>d, Cr<sub>2</sub>p, O<sub>1</sub>s and Ar<sub>2</sub>p were observed in the survey spectrum of the uncoated Ti-Al intermetallic alloy, while the N<sub>1</sub>s peak obviously was not present in XPS spectrum of Ti-48Al-2Cr-2Nb alloy. Before XPS analysis all surfaces was cleaned by argon, which caused the appearance of the Ar<sub>2</sub>p signal instead (**Figure 89**).

After cycling in burner rig apparatus, the XPS survey spectrum of TiAl substrate modifies as showed in **Figure 90**.

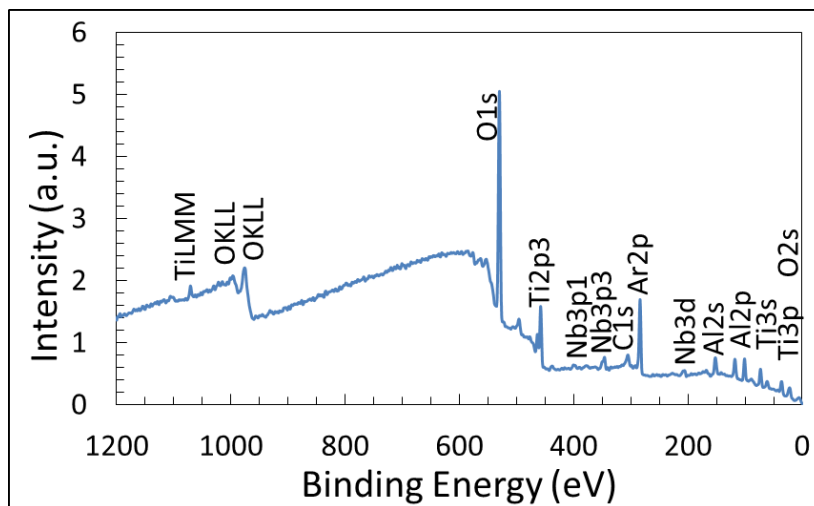


Figure 90: XPS survey spectrum of TiAl substrate oxidized in Burner Rig (40 cycles at 950 °C), after argon surface cleaning.

The peaks of O1s and O2s appeared after oxidation to confirm the surface oxidation of TiAl alloy.

The XPS survey spectra for coated samples (TiAlN1 and TiAlN3) before and after the burner rig test are represented in **Figure 91** and **Figure 92**. These Figures show the survey spectra of samples with TiAlN1 and TiAlN3 coatings, which are similar to that recorded for specimen with TiAlN2 coating [107].

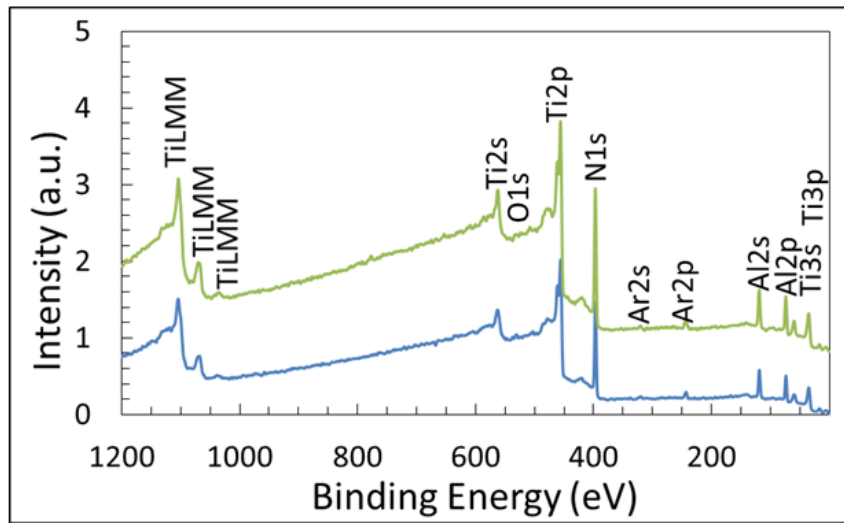


Figure 91: XPS survey spectra of as deposited coatings: TiAlN1 (blue line) and TiAlN3 (green line), after surface cleaning [107].

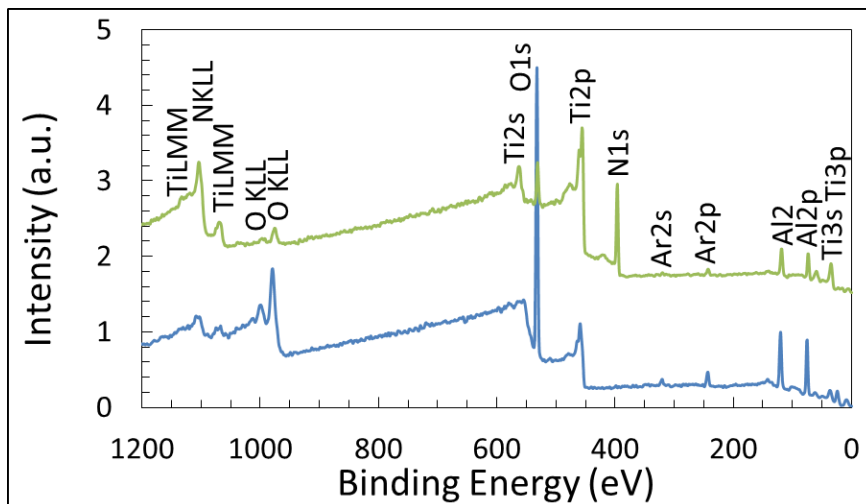


Figure 92: XPS survey spectra of oxidized coatings after 40 cycles at 950°C in burner rig: TiAlN1 (blue line) and TiAlN3 (green line), after surface cleaning [107].

As expected, the intensity of oxygen and nitrogen peaks strongly depends on the relative amount of nitride and oxides present on the surfaces, which is very different for as processed and oxidized samples respectively. In any case, the comparison of the survey spectra for oxidized coatings TiAlN1 and TiAlN3 shows that the peak of oxygen is higher in TiAlN1 survey spectra than in TiAlN3 survey spectra, and the peak of nitrogen present inside the TiAlN1 coating is lower than the nitrogen peak for TiAlN3 coating. Probably, the coating TiAlN1 was more oxidized than TiAlN3 coating.

The peaks corresponding to the binding energies (BEs) of Al2p, N1s, Ti2p and O1s (clearly visible only after burner rig test) are well evident and they were used for investigating more in detail the chemical bonds formed by these elements through the high resolution spectra. Peaks belonging to Nb3d and Cr2p were observed only in the survey spectrum of the uncoated Ti-Al intermetallic alloy, while the N1s peak obviously is not present in this case. The high resolution (HR) spectra of Al2p, N1s, Ti2p and O1s were generally fitted by several peaks with the aim of achieving information about the chemical composition and bonding characters of surface films before and after burner rig test. In principle, the integral of the deconvoluted peaks can be used to estimate quantitatively the bond contents. Unfortunately, the tight overlapping of peaks belonging to different bonds, that occurs mainly after the formation of oxides, and some uncertainties in the literature about the binding energies made this estimation difficult to be done with accuracy. Nevertheless, significant semi-quantitative indications about the importance of the different bonds can be obtained by fitting and integrating the high-resolution (HR) spectra.

The chemical species, which are present in substrate and coatings, before the oxidation in Burner Rig apparatus, are shown in **Figure 93**.

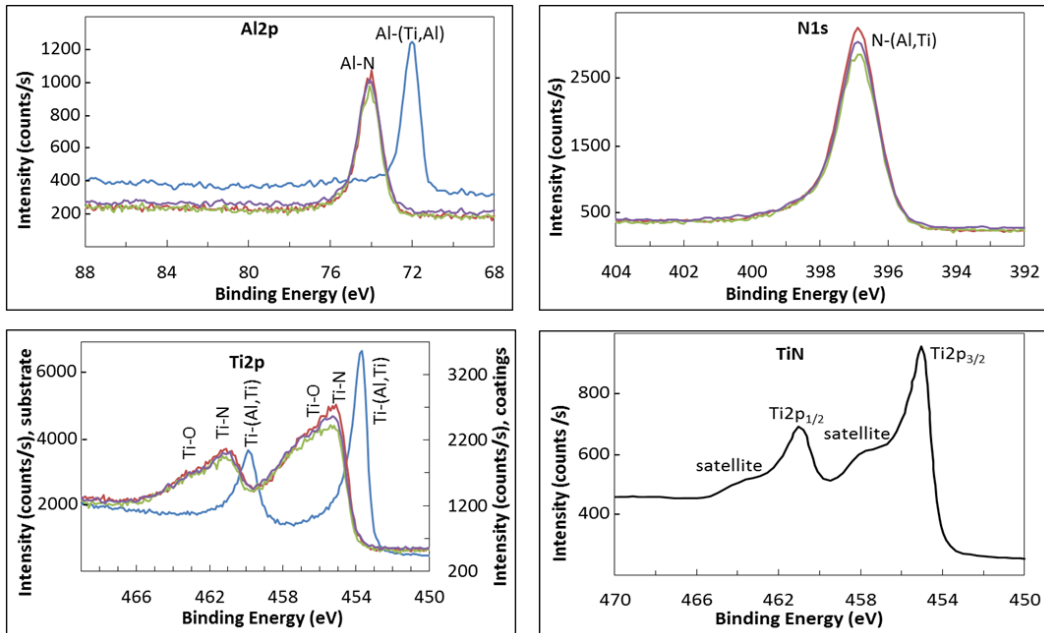


Figure 93: XPS HR spectra of as-processed samples, where blu line= uncoated TiAl intermetallic alloy, red line =TiAlN 1coating; green line =TiAlN 2 coating, purple line = TiAlN 3 coating. HR TiN XPS pattern of pure TiN also sowed as a reference (black line) [107].

The uncoated alloy showed a single peak at 71.9 eV in Al<sub>2</sub>p HR XPS spectrum. This peak can be attributed to metallic bond. According to literature, the binding energies (BEs) of Al-A and Al-Ti metallic bonds are 72.8 eV [87] and 71.5 eV [149] respectively. In Al<sub>2</sub>p HR XPS spectrum, the coated specimens show a Al-N single peak at 74.2 eV. In the literature, the binding energy of Al<sub>2</sub>p 3/2 peak was observed between 73.7 eV and 74.3 eV [87],[88],[145],[149],[150]. The peak position for Al-N bond very likely depends on stoichiometry of the nitride.

The N<sub>1s</sub> HR XPS spectrum confirmed the presence of N-(Al,Ti) bonds in TiAlN samples, the relevant peak was placed at 396.9 eV. According to literature the N-(Al,Ti) peak was observed in range between 396.4 eV and 398.6 eV. In literature the binding energies are also reported for both N-Al and N-Ti bonds, which are placed at 396.8-398.6 eV and at 396.7-398.0 eV respectively [87], [145], [149]. The BEs variation of N-(Al,Ti) species can be attributed to possible oxygen contamination and changes in the nitride stoichiometry [88], [151].

The Ti<sub>2</sub>p HR XPS spectrum shows different species, which are represented by doublets consisting of Tip<sub>3/2</sub> and Ti<sub>2</sub>p<sub>1/2</sub> peaks. In case uncoated surface, the Ti-(Al, Ti) metallic bonds, appear at 453.7 eV and at 459.8 eV [152]. In TiAlN

surfaces, the titanium nitride shows the Ti2p 3/2 peak for Ti-N bond between 454.4eV and 455.8 eV [87], [88], [145], [149], [150], [153], while the component of the doublet Ti2p 1/2 was detected at 460.2 eV [88] or at 461.1 eV [149]. In this work, the Ti-N bond of TiAlN coatings resulted in a doublet at 455.1 eV and 461.0 eV in Ti2p HR XPS spectrum. In addition some Ti-O bond appeared on TiAlN surfaces, probably due to partial oxidation of the nitride [145], [149], [150], [151]. The HR spectra are further made complex by the presence of weak satellites of Ti-N doublet, as showed in the spectrum of TiN (**Figure 93**).

As put in evidence by XPS survey analysis, after burner rig test the uncoated and coated samples were oxidized. In **Figure 94** the HR XPS plots show the comparison of as-processed and TiAlN1 samples oxidized at different temperatures. The TiAlN1 coated sample was taken as an example in order to compare the changes in chemical composition before and after short-term cyclic oxidation. The progressive oxidation of TiAlN coating occurring during the burner rig test resulted in a strong modification of the HR XPS spectrum for Al2p, O1s and Ti2p.

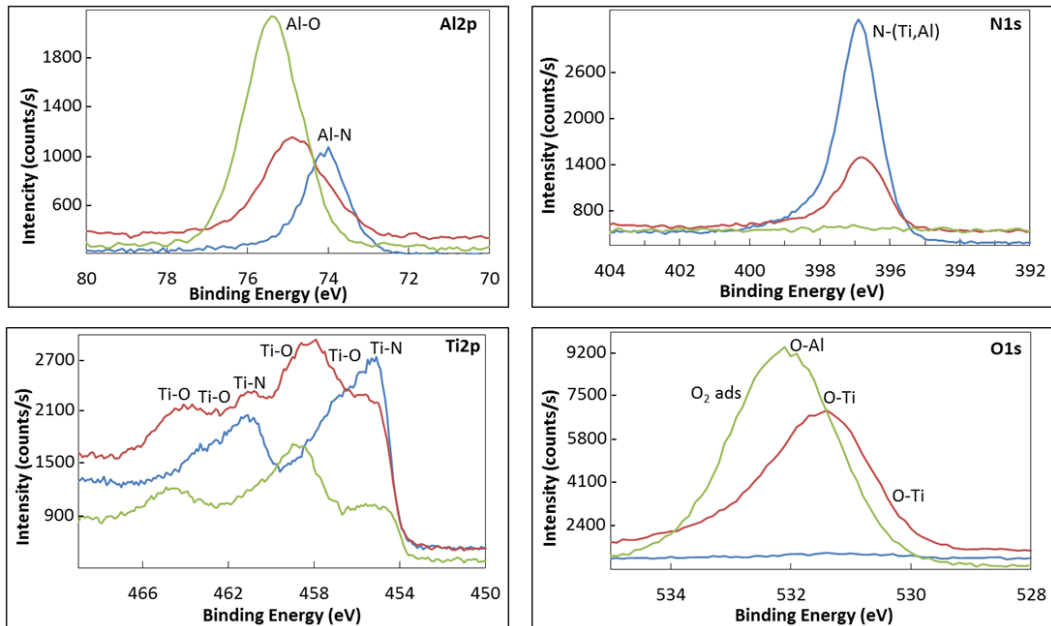


Figure 94: XPS HR spectra of TiAlN1 surface: blue line-as processed coating, red line-after 40 cycles at 850°C, green line-after 40 cycles at 950°C [107].

Before the cyclic oxidation, the Al-N peak dominates in Al2p HR spectrum of as-processed TiAlN coating. After oxidation, the Al-O peak progressively grows with advancement of oxidation.

The N1s HR XPS plot shows only a very strong N-(Ti,Al) peak for as processed TiAlN samples, but after 40 oxidation cycles at 850°C the N-(Ti,Al) peak intensity decreased and after 40 cycles at 950 °C this peak completely disappeared. Clearly this trend shows that the nitride coating is progressively covered by the oxide layer and not interested any longer by XPS analysis.

In principle, the O1s HR XPS spectrum could consist of three or four peaks attributable to: O<sub>2</sub> adsorbed on the surface, O-Ti<sup>4+</sup>, O-Ti<sup>2+</sup> and O-Al<sup>3+</sup> bonds. The as-processed coating is uncontaminated by oxygen (blue line), the coating after 40 cycles at 850 °C shows mainly the presence of O-Ti bonds and the coating after 40 cycles at 950°C shows oxygen adsorbed, O-Ti and O-Al bonds. It is clear that the intensity, the shape and the position of the peak in the O1s spectrum changes with the progress in oxidation. After 40 cycles at 950° C, the O-Al peak at 532.2 eV was dominating, while after 40 cycles at 850° C the contribution of the peaks of O-Ti bonds (at 531.2 eV and 530.3 eV) was also very important.

In the Ti2p HR spectrum of as processed TiAlN coating only the doublet related to Ti-N bond was present. The intensity of this doublet progressively decreased with the oxidation advancement while several peaks relevant to the formation of several titanium oxides progressively grew. In oxidized TiAlN coating, the formation of several titanium oxides with different Ti-O bonds gave rise to several doublets. The deconvolution of the complex Ti2p HR curve is reported in **Figure 95** [107].

In the **Figure 95**, the titanium spectrum can be deconvoluted in four curves (each consisting of a doublet), which correspond to four chemical states of titanium forming the compounds: TiN, TiO, Ti<sub>2</sub>O<sub>3</sub>, TiO<sub>2</sub>. Each of these curves consists of Ti2p<sub>1/2</sub> and Ti2p<sub>3/2</sub> peaks.

After oxidation for 40 cycles at 850°C, the titanium formed three oxides, corresponding to three doublets, which are partially superimposed. In addition, also the doublet belonging to Ti-N bond is still visible in the HR spectrum.

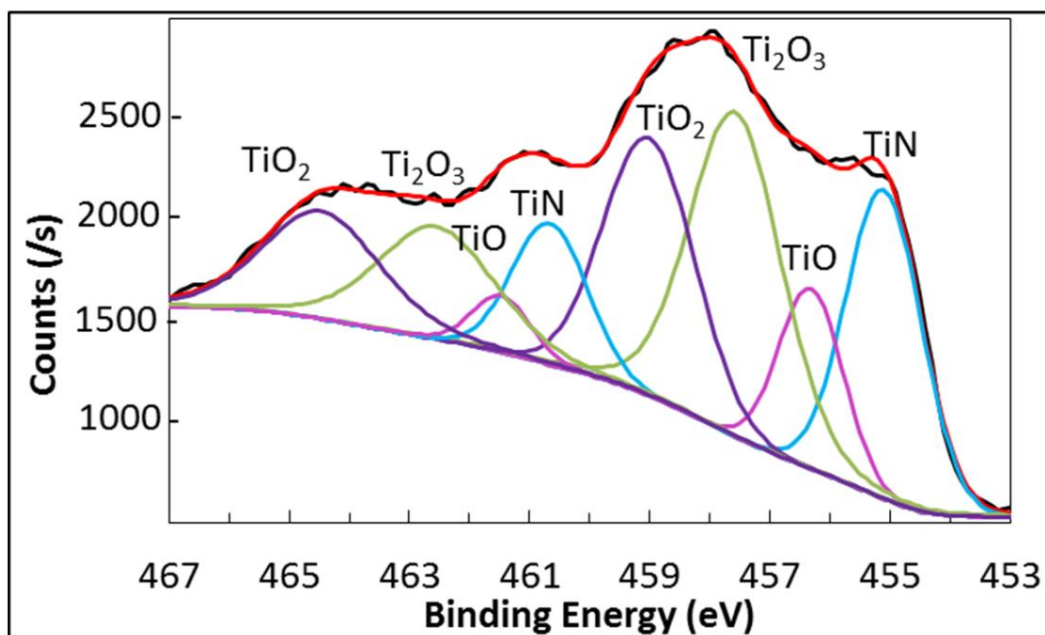


Figure 95: Fitting of Ti2p complex HR spectrum, detected for TiAlN1 sample after 40 burner rig cycles at 850°C [107].

According to literature, the titanium oxides TiO, Ti<sub>2</sub>O<sub>3</sub> and TiO<sub>2</sub> that gives rise to peaks (Ti2p<sub>3/2</sub> and Ti2p<sub>1/2</sub> doublet) with progressively increasing binding energies.

The binding energy of Ti-O bonds in TiO was reported to be 456.2 eV [88], 455.1 eV [154] or 455.3 eV [155]. The Ti<sub>2</sub>O<sub>3</sub> shows a peak at 457.5-458.3 eV [150], [154], which is superimposed to the peak characteristic of TiO<sub>2</sub> placed in the range between 457.9 eV and 458.8 eV [31], [87], [88], [145], [149], [150], [151]. Because of the scattering of literature data about BE of TiO<sub>2</sub> bond and the little information about XPS spectrum of Ti<sub>2</sub>O<sub>3</sub>, the assignation of the two peaks that we observed in the range between 457.5 eV and 459.0 eV was quite puzzling.

In this work, the doublet placed at 456.2 eV and 461.8 eV was assigned to TiO, the doublet at 457.5 eV and 463 eV was assigned to Ti<sub>2</sub>O<sub>3</sub> and the doublet at 459 eV and at 464.6 eV was assigned to TiO<sub>2</sub>. Finally, the Ti-N doublet was observed at 455.1 eV (Ti2p<sub>3/2</sub>) and at 460.8 eV (Ti2p<sub>1/2</sub>).

The XPS data are summarized in **Table 11** and **Table 12**. The **Table 11** shows the chemical compositions in atomic percentages of the sample surface before and after oxidation, while the **Table 12** reports the kind of chemical bonds and species, which were observed during XPS analysis.

**Table 11:** XPS surface analysis of specimens before and after burner rig test (40 cycles up to 850° C and 950° C) [107].

| Sample  | O    | Al   | Ti   | N    | Others (% at.)                   |
|---|------|------|------|------|----------------------------------|
| <b>as processed samples</b>                                     |      |      |      |      |                                  |
| <b>TiAl</b>   | 0.8  | 46.8 | 43.3 | 0    | Nb= 4.5 and Cr= 4.7              |
| <b>TiAlN1</b>   | 1.7  | 23.7 | 22.7 | 50.1 | Ar= bal.                         |
| <b>TiAlN2</b>   | 0.7  | 21.7 | 23.9 | 52.2 | Ar= bal.                         |
| <b>TiAlN3</b>   | 0.7  | 24.0 | 22.9 | 50.7 | Ar= bal.                         |
| <b>samples after 40 cycles at 850°C in Butner Rig apparatus</b> |      |      |      |      |                                  |
| <b>TiAl</b>   | 63.4 | 17.2 | 15.7 | -    | Nb=0.7 and Cr=1.4<br>Ar, C= bal. |
| <b>TiAlN1</b>   | 52.5 | 16.7 | 18.4 | 12.0 | Ar= bal.                         |
| <b>TiAlN2</b>   | 51.7 | 17.8 | 18.5 | 12.0 | -                                |
| <b>TiAlN3</b>   | 7.4  | 21.8 | 22.3 | 46.2 | Ar= bal.                         |
| <b>samples after 40 cycles at 950°C in Butner Rig apparatus</b> |      |      |      |      |                                  |
| <b>TiAl</b>   | 67.6 | 13.7 | 17.8 | -    | -                                |
| <b>TiAlN1</b>   | 62.2 | 29.4 | 7.0  | 1.4  | -                                |
| <b>TiAlN3</b>   | 16.1 | 21   | 21.8 | 41.1 | -                                |

According to XPS survey analysis, the as-processed samples (coated and uncoated) show surface contaminations of oxygen and carbon with very small

percentages. The oxygen contamination is present in sample surfaces because of oxygen adsorption, and formation of a small amount of a mixture of titanium oxide and aluminium oxide. Anyway, the as processed sample surfaces were sputtered by argon in XPS chamber. In this case, the sample surfaces were cleaned until the carbon contamination disappeared quasi completely. For each sample, cleaning was performed by argon sputtering for different times, but in general sputtering time was about 7-15 min.

After the sputtering an atomic ratio between Ti and Al close to 1:1 was found on the surface of uncoated samples while for the coated samples the Ti:Al:N atomic ratio was consistent with the presence of a  $(\text{Ti}_{0.5}\text{Al}_{0.5})\text{N}$  coating.

**Table 12:** Chemical bonds and species detected by XPS in the samples before and after burner rig test (40 cycles up to 850° C and 950° C) [107].

| Sample  | O                                   | Al  | Ti  | N                     |
|---|-------------------------------------|---|---|-----------------------|
|   | <b>chemical bonds, (species)</b>    |   |   |                       |
| <b>TiAl alloy</b>                                   | O-(Al,Ti)                           | Al-M  | Ti-M; Ti-O  | -                     |
| <b>TiAl oxidized at 850°C and at 950°C</b>          | O-Ti;<br>O-Al;<br>(O <sub>2</sub> ) | Al-O (Al <sub>2</sub> O <sub>3</sub> )                  | Ti-O,<br>(TiO <sub>2</sub> , TiO)   | -                     |
| <b>TiAlN (1/2/3)</b>                                | O-(Al,Ti)                           | Al-N, (AlN);<br>Al-O, (Al <sub>2</sub> O <sub>3</sub> ) | Ti-N,(TiN);<br>Ti-O,(TiO)   | N-(Al,Ti),<br>(TiAlN) |
| <b>TiAlN (1/2/3) oxidized at 850°C and at 950°C</b> | O-Ti;<br>O-Al;<br>(O <sub>2</sub> ) | Al-O,(Al <sub>2</sub> O <sub>3</sub> );<br>Al-N,(AlN)   | Ti-O,(TiO,<br>TiO <sub>2</sub> ,Ti <sub>2</sub> O <sub>3</sub> );<br>Ti-N,(TiN) | N-(Al,Ti),<br>(TiAlN) |

After short-term cycling in burner rig apparatus (40 cycles at 850°C and 950°C), the oxygen percentages greatly increased on the all surfaces more and more with the temperature growth. The oxygen percentages in oxidized samples appeared different, since it was bigger on uncoated surface than on the coated surfaces. After oxidation, every peak related to the metallic substrate disappeared in the XPS spectrum of uncoated alloy while evidences of the TiAlN coating were still present within the spectrum of the coated specimens. Aluminium and titanium oxides (with some evidence of the presence of  $Ti^{3+}$  and  $Ti^{2+}$ ) composed the oxide scale. In every case, the XPS of coated oxidized surfaces showed N-(Al,Ti) bonds, which means that the oxide layer was very thin. The oxygen concentration resulting from surface oxidation was consistent with the formation of a mixture of rutile and alumina in the case of uncoated alloy and specimens with TiAlN1 and TiAlN2 coatings. The main formation of these oxides was also confirmed by the HR XPS spectra. The atomic ratio between aluminium and titanium in the XPS spectrum of the uncoated alloy, either before or after oxidation, was always close to 1:1, which means that the presence of these two elements in the oxide film reflects their presence in the intermetallic alloy. The Al:Ti ratio still remained close to 1:1 after 40 cycles even for the TiAlN3 sample, which showed only a limited growth of the oxide layer. In contrast, for the TiAlN1 the comparison between the XPS spectra after burner rig testing at 850° C and 950° C showed that the Al:Ti ratio in the oxide scale increased with the oxidation temperature and the growth of the oxide layer. This feature suggests that the oxide film can progressively acquire a passivating character as the oxidation process advances only in the case of coated samples. After the burner rig tests the oxygen concentration on the surface of samples with TiAlN3 coating was much lower than for the TiAlN1 and TiAlN2 samples and contemporaneously a rather high nitrogen concentration was found. This means that the TiAlN3 coating showed higher oxidation resistance and therefore that the not-oxidized nitride coating was still present in the external part of the samples affected by XPS analysis also after burner rig oxidation treatment. On the contrary, XPS did not show clear evidence of significant presence of the nitride coating on TiAlN1 surface after 40 cycles up to 950°C. In addition, after 40 cycles at 850 °C, the Nb and Cr concentrations decreased on the surface of the uncoated samples and these elements disappeared after 40 cycles at 950 °C. Finally, these elements were never detected on the surface of the coated samples, which is not surprising at all, because they were not found inside the nitride coatings as well.

The repetition of XPS analysis after the progressive sputtering of the oxidized layer grown on coated samples put in evidence the difference in thickness of the

oxide layers. The XPS analyses of each coated sample, oxidized during burner rig test at 950°C, are compared after different sputtering time in **Table 13**.

**Table 13:** XPS surface analysis after 40 cycles at 950°C, comparison after different sputtering times.

| Sample   | O<br>(% at.) | Al<br>(% at.) | Ti<br>(% at.) | N<br>(% at.) |
|--|--------------|---------------|---------------|--------------|
| <b>TiAlN1 oxidized</b>                         | 62.2         | 29.4          | 7.0           | 1.4          |
| <b>TiAlN1 oxidized,<br/>(20 min sputtered)</b> | 52.8         | 15            | 21            | 10           |
| <b>TiAlN2 oxidized</b>                         | 62.3         | 31.9          | 4.4           | -            |
| <b>TiAlN2 oxidized,<br/>(20 min sputtered)</b> | 64.1         | 25.2          | 10.7          | -            |
| <b>TiAlN3 oxidized</b>                         | 16.1         | 21            | 21.8          | 41.1         |
| <b>TiAlN3 oxidized,<br/>(8 min sputtered)</b>  | 2.9          | 22.7          | 23.5          | 50.9         |

According to these results, the thickness of oxide layer was greatly higher in TiAlN1 and TiAlN2 than in TiAlN3 samples. After a rather long sputtering (20 minutes), the TiAlN1 and TiAlN2 specimens still showed very high oxygen concentration, while nitrogen started to be detected only in TiAlN1 sample. In the case of TiAlN2 coating a sputtering lasting even 50 minutes was not sufficient to put in evidence the peaks related to the nitride coating. In TiAlN3 case a sputtering time of 8 minutes was sufficient for reducing the oxygen concentration to about 2.9 (% at.) and enhancing the nitrogen concentration to 50.9 (% at.). Therefore, the oxidation kinetics for samples carrying TiAlN coatings with the same composition was found to be very different; the thinner oxide layer growing on the TiAlN3 sample and the thickest one growing on the TiAlN2 specimen.

The differences observed in oxidation resistance between coatings that have the same chemical composition can be only explained on the basis of the processing path adopted for depositing the TiAlN coatings.

The substrate HiPIMS pre-treatment (samples TiAlN2 and TiAlN3) utilized pulses with peak power densities of about  $500 \text{ Wcm}^{-2}$  applied to the TiAl target. This aggressive plasma etching step chosen for TiAlN2 (60 minutes) significantly altered the surface morphology and roughness of the substrate ( $R_a \sim 130 \text{ nm}$  vs  $R_a \sim 10 \text{ nm}$  for TiAlN1). It is recognized that during PVD film growth, an increased substrate surface roughness results in a more defective coverage because of shadowing effects. HiPIMS films however, are extremely dense and smooth thanks to the high energy of the arrival particles, ad-atom mobility and nucleation density increase. The atomic shadowing effect for HiPIMS films during the coating growth is significantly reduced but is still present when the substrate surface roughness is high. Consequently, the grown TiAlN2 coating was probably more defective and highly stressed. Moreover, the surface roughness of the sputtered TiAlN coating increased with the roughness of the TiAl substrate. This resulted in a greater exposed surface area, which favored the oxidation process.

In the TiAlN3 case, a soft plasma etching step (10 minutes) was followed by the introduction of a 300 nm thick TiAl metal interlayer, which resulted in a clearly defined and sharp interface with a coherent TiAlN layer growth. Very likely, the gentle ion etching pre-treatment plus a metal interlayer deposition positively influenced properties such as adhesion and oxidation performance.

For these reasons thermal shock and oxidation resistance of TiAlN coated intermetallic alloy was better investigated through long term cycling (200 cycle at  $950^\circ\text{C}$ ) only for TiAlN1 and TiAlN3 samples [125].

### **3.2.2 Long-term cycling oxidation at $950^\circ \text{C}$ of TiAlN coated and uncoated intermetallics**

The microstructures of TiAlN1 and TiAlN3 samples before and after long-term oxidation are reported in **Figure 96** and **Figure 97** respectively.

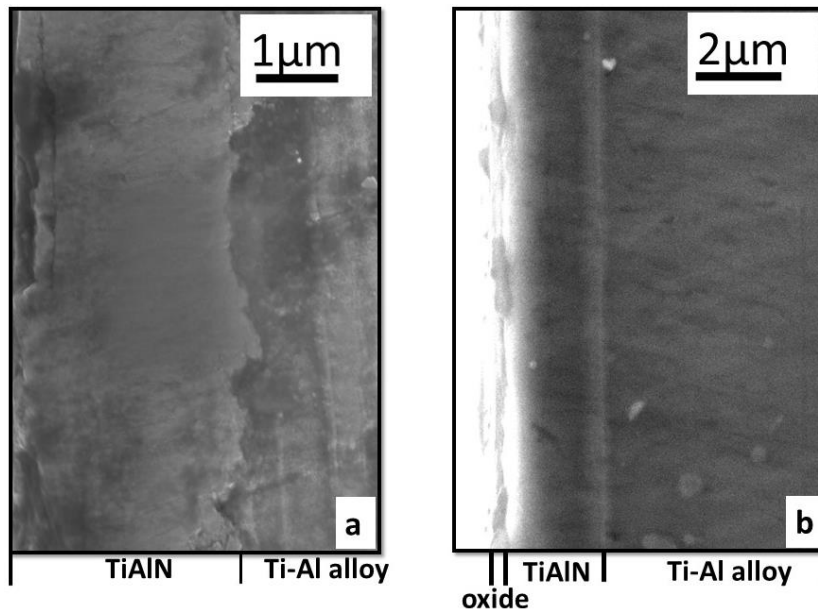


Figure 96: SEM images of TiAlN1 cross-section: (a) before and (b) after 200 cycles at 950 °C in Burner Rig apparatus.

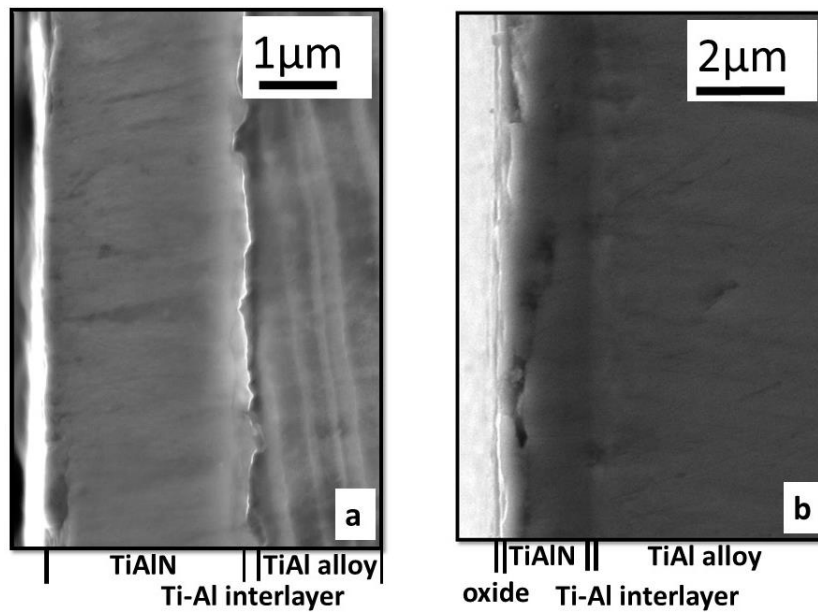


Figure 97: SEM images of TiAlN3 cross-section: (a) before and (b) after 200 cycles at 950 °C in Burner Rig apparatus.

After long-term oxidation, the both coatings were well adhered to the substrate, and spallation phenomena were never observed. This is a very important result since the specimens suffered of repeated thermal shocks during cyclic oxidation; these

shocks are quite severe in particular during the quenching step, that involves a cooling from 950° C to 300° C in about 3 minutes only. Very thin oxide surface layers (about less than 0.5  $\mu\text{m}$  thick) grew on these unchanged coated surfaces.

The XRD patterns of uncoated alloy and coated TiAlN1 sample before and after the long-term burner rig tests are represented in **Figure 98** and **Figure 99** respectively. These last XRD spectra were identical to those recorded for TiAlN2.

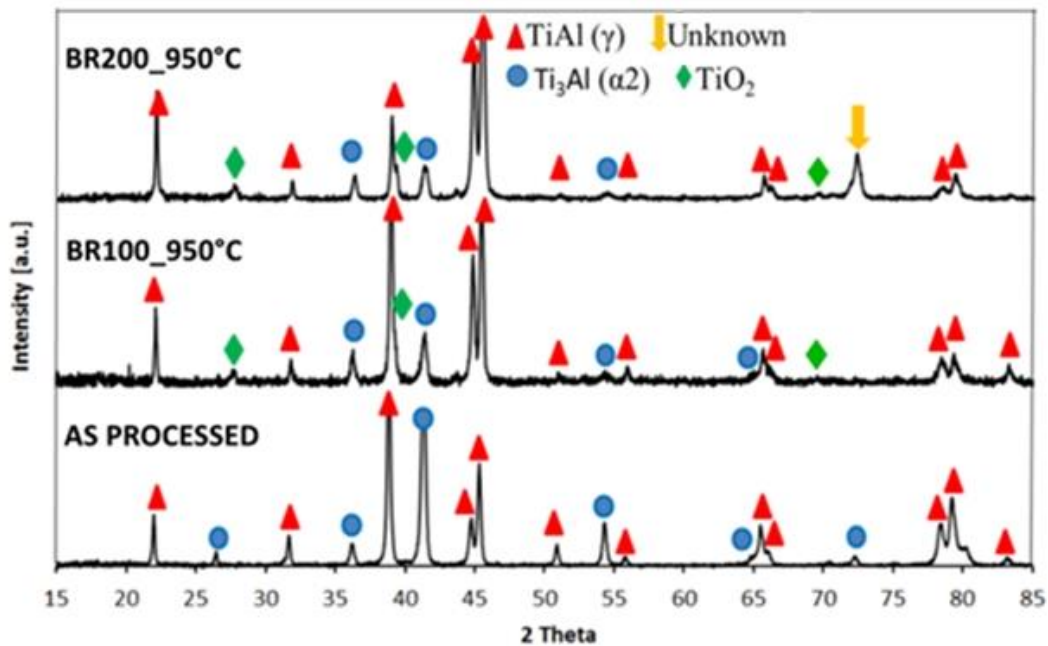


Figure 98: XRD patterns of TiAl substrate before and after 100 and 200 oxidation cycles in burner rig [125].

The as-processed uncoated intermetallic, as explained before, shows two crystalline phases: dominant  $\gamma$ -TiAl phase (with ordered face centred tetragonal L10 structure) and  $\alpha_2$ -Ti<sub>3</sub>Al phase (with ordered hexagonal D019 structure). After cyclic oxidation (consisting of 100 or 200 cycles), the peaks of TiO<sub>2</sub> appeared in the relevant spectra. In literature [156],[157],[104], it was reported that rutile is one of the principal component of the oxide layer grown on Ti-Al intermetallic. In addition, after oxidation of Ti-Al intermetallic, the amorphous alumina or very fine alumina crystal grains form too [2]. In present work, the alumina formation was not observed in the XRD patterns, while its formation was confirmed by XPS analyses. Very likely, as the oxide layer is only a small part of the volume of material affected by the XRD analysis and as there is a tendency to form amorphous alumina (not detectable by XRD) this last phase could not be detected by XRD. Moreover, after

200 oxidation cycles an unidentified peak at  $2\theta \sim 72.3^\circ$  was also observed in the XRD spectrum. This signal probably was due to a contamination accidentally occurred inside the burner rig chamber.

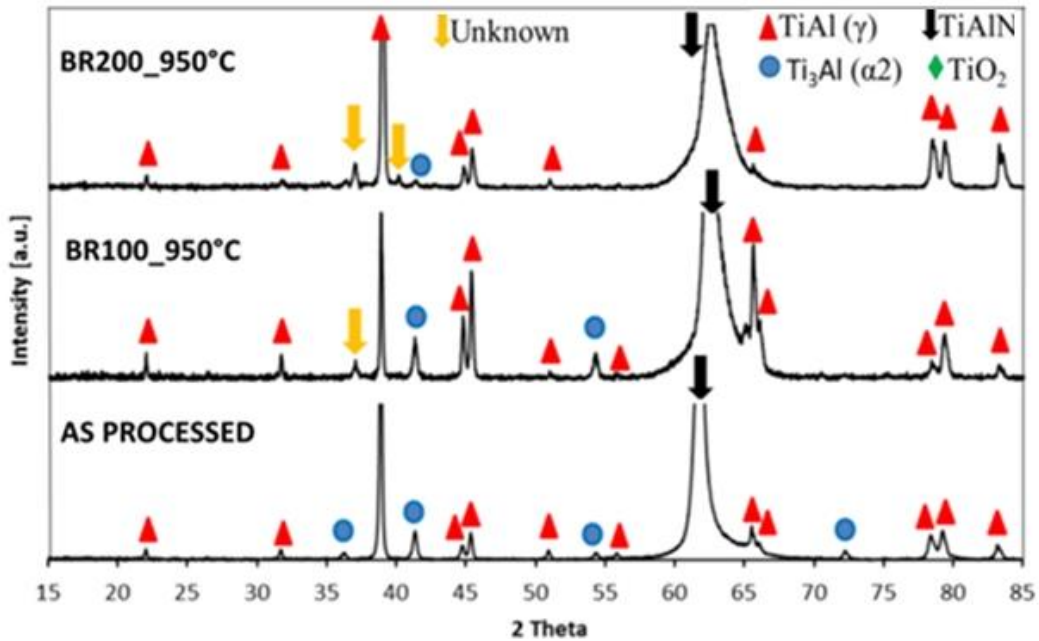


Figure 99: XRD patterns of TiAlN1 samples before and after 100 and 200 oxidation cycles in burner rig [125].

As described before, the XRD patterns of as processed TiAlN coated samples show the presence of several phases:  $\gamma$ ,  $\alpha_2$  and TiAlN (with B1-NaCl structure, card number 58012 of ICSD database). The high intensity of the (220) peak of TiAlN shows that preferred orientation occurred. Since the TiAlN coating thickness is lower than three  $\mu\text{m}$  the peaks relevant to the intermetallic substrate are still well evident. Long-term cyclic oxidation caused only small changes in the XRD patterns of coated samples. It is evident that the TiAlN peak (220) still remained strong, but it slightly shifted towards higher  $2\theta$  values. Probably this shift was due to a change in residual stresses, likely occurring during the thermal cycling, which involves many thermal shocks. The oxide layer growing during cyclic oxidation was not thick enough to impede the X-ray beam to get to the underlying nitride coating and the substrate.

The XPS survey analyses of the surface of uncoated and coated specimens, before and after 100 and 200 thermal cycles at 950 °C in Burner Rig, are compared in **Table 14**.

**Table 14:** XPS elemental analysis of as processed and oxidized samples [125].

| Sample                                  | XPS analysis (% at.) after surface cleaning |      |      |      |                           |
|---|---|------|------|------|---------------------------|
|   | O1s   | Al2p | Ti2p | N1s  | Others                    |
| <b>TiAl as processed</b>                | 0.8   | 46.8 | 47.1 | 0    | Nb=2.1; Cr= 1.9; Ar= bal. |
| <b>TiAl after 100 cycles at 950°C</b>   | 67.5  | 13.1 | 17.0 | 0    | Cr=0.2; Nb=0.1; Ar= bal.  |
| <b>TiAl after 200 cycles at 950°C</b>   | 67.6  | 19.6 | 11.2 | 0    | Cr=1.5; Nb<0.1            |
| <b>TiAlN1 as processed</b>              | 1.7   | 23.7 | 22.7 | 50.1 | Ar= bal.                  |
| <b>TiAlN1 after 100 cycles at 950°C</b> | 69.5  | 20.7 | 8.8  | 0    | Cr=0.8; Ar= bal.          |
| <b>TiAlN1 after 200 cycles at 950°C</b> | 65.6  | 30.7 | 1.9  | 0    | Cr=1.1; Ar= bal.          |
| <b>TiAlN3 as processed</b>              | 0.7   | 24.0 | 22.9 | 50.7 | Ar= bal.                  |
| <b>TiAlN3 after 100 cycles at 950°C</b> | 68.8  | 15.1 | 10.2 | 0    | Cr=2.3; Ar =bal.          |
| <b>TiAlN3 after 200 cycles at 950°C</b> | 62.9  | 20.9 | 15.1 | 0    | Cr=1.1                    |

As processed samples showed some oxygen contaminations, in fact the oxygen concentration on the surface was about 0.8% at. for uncoated substrate, and 1.7 or 0.7 % at. for TiAlN1 and TiAlN3 samples respectively. After prolonged oxidation (100 cycles or 200 cycles at 950°C in Burner Rig), all surfaces were completely oxidized and contained 63-69 % at. of oxygen. Such high oxygen concentrations cannot be explained only with the complete oxidation of Al and Ti to Al<sub>2</sub>O<sub>3</sub> and

TiO<sub>2</sub> respectively. On the other hand, additional oxygen is combined with chromium and some oxygen very likely is adsorbed on the surface. Table 11 also shows that the atomic ratio between Al and Ti and the relative amount of their oxides changed with the oxidation advancement. In the case of the uncoated TiAl sample the Al:Ti atomic ratio was 0.8:1 and 1.8:1 after 100 and 200 oxidation cycles respectively. This means that Al diffused towards the surface exposed to the oxidizing atmosphere more quickly than Ti. The oxide layer formed on the surface of coated samples showed an Al:Ti ratio ranging from 2.4:1 (100 cycles) to 16:1 (200 cycles) for TiAlN1 and from 1.5:1 (100 cycles) to 1.4:1 (200 cycles) for TiAlN3. It is evident that the Al:Ti atomic ratio greatly increased with the oxidation progress in the case of the TiAlN1 sample, while only a small variation was observed for TiAlN3.

Nitrogen was never observed by XPS analysis on the surface of the oxidized TiAlN1 and TiAlN3 samples because the oxide layer was thick enough to mask the underlying TiAlN coating.

After thermal cycling in the burner rig apparatus, the content of chromium within the oxide layer grown on the uncoated intermetallic was always lower than 2 %, but progressively increasing with the treatment time. Chromium was also detected in the oxide layer grown on the coated samples, because of diffusion from the substrate (**Table 14**). On the contrary, only negligible amount of niobium was observed in the oxide layer in every case.

In order to investigate the oxidation progress, the XPS HR spectra were recorded for as processed and oxidized surfaces. These spectra for Al2p, Ti2p, O1s, N1s peaks give more information about chemical bonds formed by Al, Ti, O and N.

The deconvoluted peaks in HRS of the uncoated TiAl sample before and after long-term oxidation are reported in **Figure 100**.

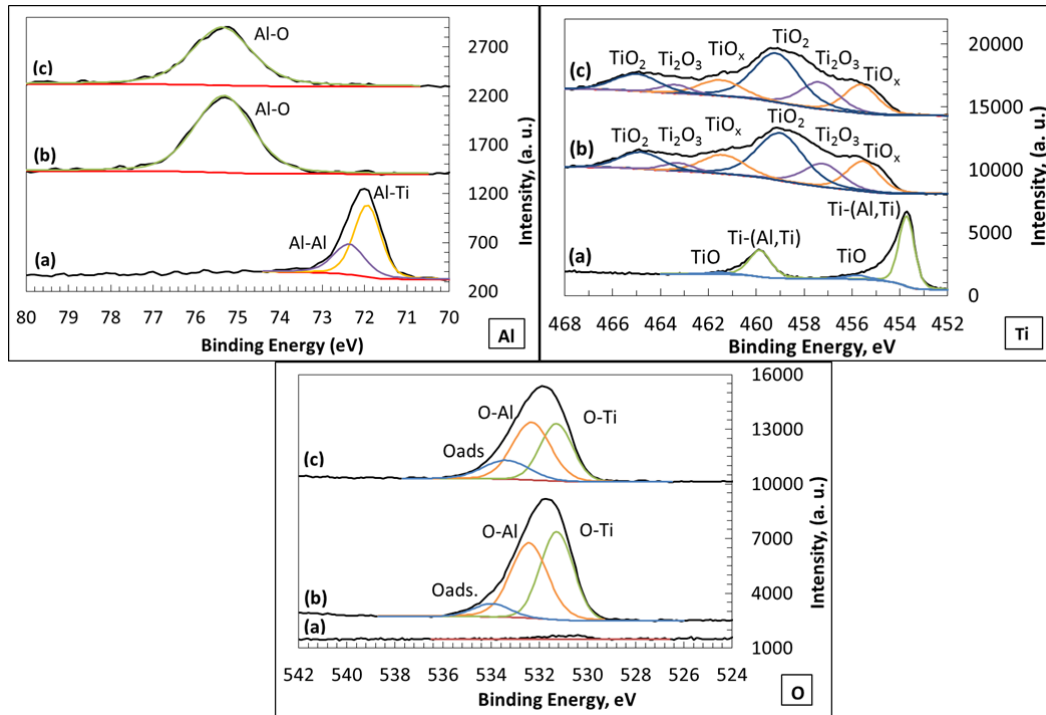


Figure 100: XPS high-resolution surface spectra of uncoated TiAl: (a) as processed; (b) after 100 thermal cycles at 950 °C; (c) after 200 thermal cycles at 950 °C [125].

Before cycling in burner rig, according to the deconvolution of the Al2p peak situated at 72 eV, both Al-Ti and Al-Al metallic bonds were observed on the TiAl uncoated surface. The XPS HR Ti2p spectrum confirmed this result. The Ti-(Al,Ti) bonds show the spin orbit doublet (Ti2p3/2 and Ti2p1/2) placed at 453.7 eV and 459.8 eV. In addition, very weak signals of TiOx doublet were observed at 456 eV (Ti2p3/2) and 461.8 eV (Ti2p1/2). The XPS HR O1s spectra put in evidence only a very weak and broaden signal in the range between 530 eV and 532 eV, which is due to the oxygen contamination and causes the formation of both O-Ti and O-Al bonds.

After 100 or 200 thermal cycles at 950 °C, the intensity of the O-Al and O-Ti peaks significantly increased in the XPS HR O1s spectrum. The broad and complex curve in this spectrum can be deconvoluted into three peaks. A first peak placed at 531 eV can be attributed to the O-Ti bonds in titanium oxides, while the second peak with binding energy of 532.1 eV is due to O-Al bonds in alumina. The third peak situated at 533.8 eV can be attributed to adsorbed O<sub>2</sub>. In the XPS HR Al2p spectrum, the strong peak of Al-O bonds at 75.6 eV (“b” and “c” curves) confirmed the alumina formation. All titanium chemical bonds show a spin orbit doublet (Ti

2p<sub>3/2</sub> and Ti 2p<sub>1/2</sub>) in the XPS HR Ti2p spectrum. In XPS HR Ti2p spectra after oxidation the very similar complex curves (b and c) can be fitted by three doublets. In fact, after severe oxidation (100 and 200 cycles at 950°C), the titanium formed contemporaneously three different bonds with oxygen. As discussed previously, literature allows to identify these bonds. The binding energies of Ti-O bonds in TiO<sub>x</sub>, Ti<sub>2</sub>O<sub>3</sub> and TiO<sub>2</sub> oxides reported in the literature are summarized in **Table 15**, which shows as the binding energy increases with the titanium oxidation state (namely Ti<sup>+2</sup>, Ti<sup>+3</sup> and Ti<sup>+4</sup>).

**Table 15:** Binding energies for Al, Ti, O and N chemical bonds [125].

| XPS HR      | the Binding Energy (eV), from literature data     |  |  |  |  |                                      |
|-------------|---|--|--|--|--|--------------------------------------|
| <b>Al2p</b> | Al-Ti<br>[149]                                    | Al-Al<br>[87]  | Al-N<br>[149]                                  | Al-O<br>[87],[150]                     |  |                                      |
|             | 71.5  | 72.8   | 74.3   | 75.6                                   |  |                                      |
| <b>Ti2p</b> | Ti-(Al,Ti)<br>[152]                               | Ti-N<br>[149],<br>[150],<br>[152]                    | Ti-N sat.<br>[158],<br>[159]                   | (TiO <sub>x</sub> )<br>[152],<br>[155] | (Ti <sub>2</sub> O <sub>3</sub> )<br>[152],<br>[155] | (TiO <sub>2</sub> )<br>[87],<br>[88] |
|             | 453.7   |  | 458  | 455.3-                                 | 457.0-   | 458.3-                               |
|             | 459.8   | 455.8  | 464  | 456.2                                  | 457.1  | 458.7                                |
|             |   | 461.1  |  | 461.7-                                 | 463  | 464.3                                |
|             |   |  | 462.8  |  |  |                                      |
| <b>O1s</b>  | O-Ti<br>[87],[88],<br>[149],[150],<br>[154],[151] | (Al <sub>2</sub> O <sub>3</sub> )<br>[150],<br>[151] | (O <sub>2</sub> ads.)<br>[88],[149],<br>[150], |  |  |                                      |
|             | 529.6-531.2                                       | 532.1  | 531.9-533                                      |  |  |                                      |
| <b>N1s</b>  | N-(Al,Ti)<br>[87],[145],<br>[149],                |  |  |  |  |                                      |
|             | 396.4-398.6                                       |  |  |  |  |                                      |

Some disagreement can be found in the literature data. This is not surprising because, for instance,  $\text{TiO}_x$  is a non-stoichiometric compound with composition ranging from 0.7 to 1.3 of  $\text{TiO}$  [160]. Since the binding energies characteristic of Ti-O bond in titanium oxides are very similar the relevant peaks can be overlapped. In this work, the  $\text{TiO}_2$  doublet was observed in the HRS at 458.8 eV (Ti 2p<sub>3/2</sub>) and 464.6 eV (Ti 2p<sub>1/2</sub>). Similarly, the  $\text{Ti}_2\text{O}_3$  peaks was situated at 457.0 eV and 463.1 eV, and the doublet for  $\text{TiO}_x$  was found at 455.3 eV and 461.5 eV. According to the peak intensities in the XPS HR Ti2p spectrum, the main component of the mixture of titanium oxides was  $\text{TiO}_2$ , even though  $\text{Ti}_2\text{O}_3$  and a non-stoichiometric compound  $\text{TiO}_x$  were also present in not negligible quantities.

The **Figure 101** and **Figure 102** show XPS HR spectrum of  $\text{TiAlN1}$  and  $\text{TiAlN3}$  coated samples respectively. Curves labeled as “a” refer to the as-processed samples while those labeled as “b” and “c” were recorded after 100 and 200 thermal cycles respectively.

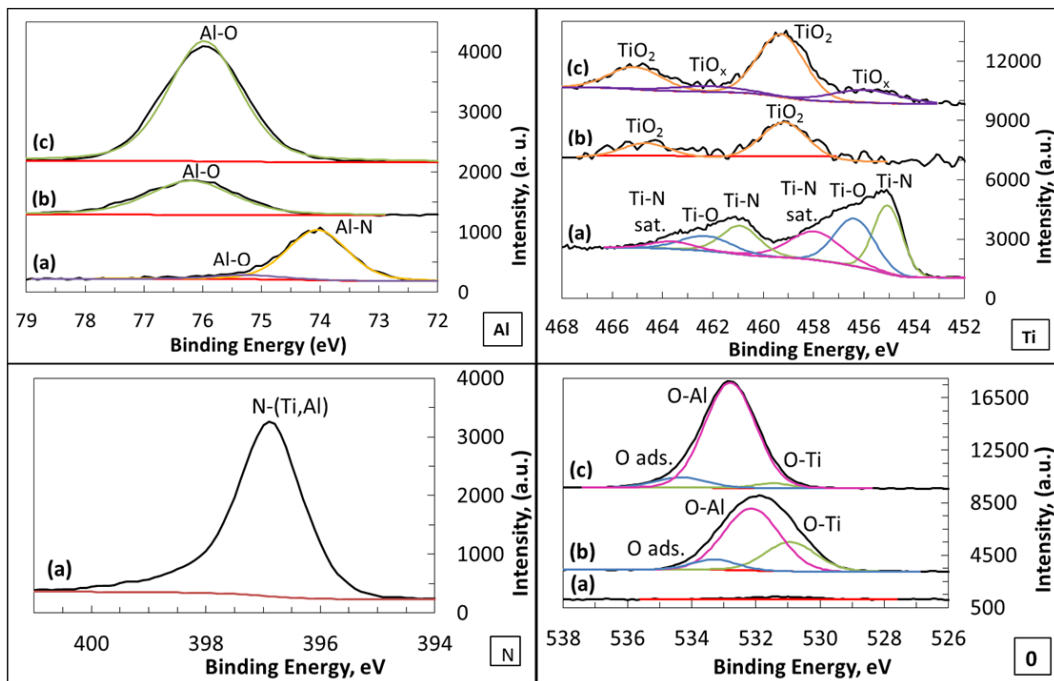


Figure 101: XPS HR spectra of  $\text{TiAlN1}$  sample: (a) as processed; (b) after 100 thermal cycles at  $950^\circ\text{C}$ ; (c) after 200 thermal cycles at  $950^\circ\text{C}$ . XPS HR N1s not observed after cyclic oxidation (Curves (b) and (c) not reported) [125].

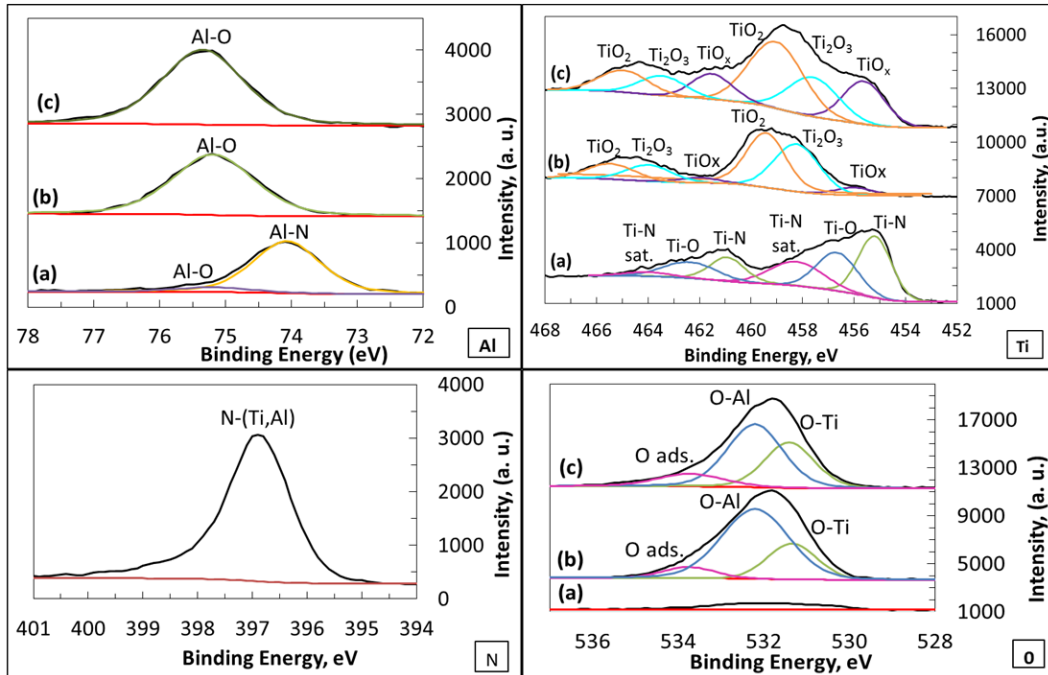


Figure 102: XPS HR of TiAlN<sub>3</sub> sample: (a) as processed; (b) after 100 thermal cycles at 950°C; (c) after 200 thermal cycles at 950°C. XPS HR N1s not observed after cyclic oxidation (Curves (b) and (c) not reported) [125].

As processed coatings, as expected and according to **Table 14**, have the same chemical composition. In N1s, Al2p and Ti2p XPS HR spectra, the N-(Ti,Al), Al-N and Ti-N bonds are always present. In XPS HR N1s spectrum, the N-(Ti,Al) peak was placed at 396.9 eV. In the XPS HR spectra of Al2p, the peak of Al-N bonds was observed at 74.2 eV. The Ti2p HR spectrum of as-processed TiAlN<sub>1</sub> and TiAlN<sub>3</sub> specimens showed that titanium is mainly bonded to nitrogen. The double peak of the Ti-N bonds was found at 455.1 eV and 461.0 eV, while two satellites of these signals were also observed at 458.3 eV and 464.0 eV. In addition, both the as-processed coated surfaces contained also a small quantity of Al and Ti oxides. This is consistent with **Table 14**, showing that oxygen atomic percentages of about 0.7 and 1.7 were observed before cyclic oxidation for TiAlN<sub>3</sub> and TiAlN<sub>1</sub> samples respectively. The XPS HR Al2p spectrum put in evidence the presence of Al-O bonds, since a wide but weak peak was observed in the range 75–76 eV. The XPS HR O1s spectrum confirmed that O-(Ti, Al) bonds formed on the surface of as processed TiAlN<sub>1</sub> and TiAlN<sub>2</sub> samples. The wide and small peak attributable to metal oxides was observed at around 532 eV. Finally, also a doublet for TiO<sub>x</sub>, placed at 456.2 eV and 462.3 eV, was observed in the XPS HR Ti2p, thus confirming the slight oxidation of the sample surface.

The TiAlN1 and TiAlN3 samples after severe oxidation treatments (100 and 200 cycles at 950 °C) showed the formation of a complex oxide scale containing aluminium oxide and different titanium oxides. As expected, the N-(Ti,Al) peak and the Ti-N peak disappeared in the XPS HR N1s and XPS HR Ti2p spectrum respectively. A strong peak of Al-O bond in alumina was observed in XPS HR Al2p spectrum of TiAlN1 and TiAlN3 samples (in the range of 75.6–76 eV), and the corresponding O-Al peak grew in the XPS HR O1s spectrum too. In fact, the complex curve in XPS HR O1s spectrum can be fitted by using three peaks. In the both coated samples, the O-Al bond of alumina situated at 532.1 eV, the O-Ti bond placed at 531 eV and the broad peak of adsorbed oxygen placed in the range 533–534 eV were observed. It is evident that the O-Al peak shows bigger intensity than the O-Ti signal and therefore that the content of alumina is higher than that of titanium oxides. Nevertheless, some differences for alumina formation can be found between TiAlN1 and TiAlN3 samples. After 100 cycles at 950°C, the TiAlN1 coated sample contained both alumina and titanium oxides (**Figure 101**, curve b), while after 200 cycles (**Figure 101**, curve c) the O peak was almost completely constituted by alumina. The **Figure 102** (XPS HR O1s spectrum of TiAlN3 oxidized coating) shows that the quantity of alumina was always bigger than the amount of titanium oxides, but a mixture of these oxides was always present (the quantity of titanium oxide ranging between 1/2 and 2/3 of the alumina amount). The deconvolution of the Ti2p curves in XPS HR Ti2p spectra, shows that several titanium oxides are present on the surface of the oxide layers formed on TiAlN1 and TiAlN3 samples (**Figure 101** and **Figure 102** respectively). TiO<sub>2</sub>, and TiO<sub>x</sub> formed on the surface of TiAlN1 sample, while the oxidized TiAlN3 sample exhibited three oxides (TiO<sub>2</sub>, Ti<sub>2</sub>O<sub>3</sub> and TiO<sub>x</sub>). Each titanium oxide (TiO<sub>2</sub>, Ti<sub>2</sub>O<sub>3</sub> and TiO<sub>x</sub>) showed, as usual, a spin orbit doublet. In both oxidized coated samples, the TiO<sub>2</sub> was the most important titanium oxide found, and its amount increased with the number of thermal cycles. In addition, TiO<sub>x</sub> was observed in minor quantity. The Ti<sub>2</sub>O<sub>3</sub> specie was only present on the TiAlN3 oxidized surface.

In order to compare the thickness of the oxide layers and better investigate their composition depth profile analyses of uncoated and coated surfaces were performed. Before the XPS analysis, each sample surface was previously cleaned by argon sputtering until carbon contamination disappeared. The XPS analysis was repeated after increasing sputtering times. In this manner, curves that depict the variation of chemical concentration with the sputtering time were obtained. These curves show for each element the variation of concentration with the distance from the surface. These concentration profiles are reported in **Figure 103**.

The concentration curves for Cr and Nb are not shown in **Figure 103** because only little amounts of these elements were found inside the oxide scale formed on the samples **Table 14**.

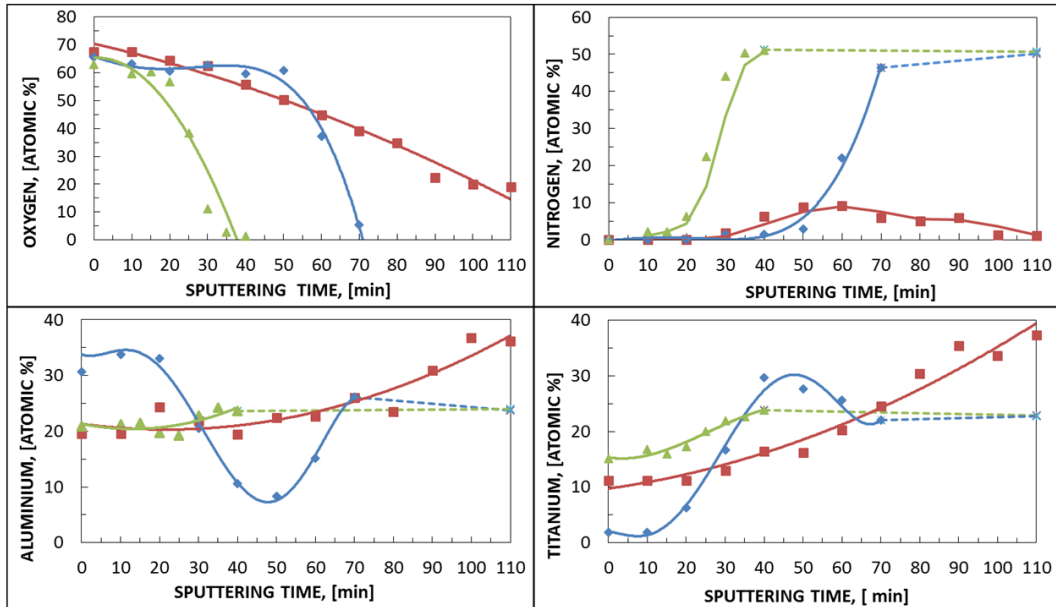


Figure 103: XPS depth profiles, after 200 thermal cycles at 950 °C: red line = TiAl (uncoated alloy), blue line = TiAlN1 coated sample, green line = TiAlN3 coated sample. The dashed lines show the extrapolation of the curves toward the concentration of titanium, aluminium and nitrogen found in the TiAlN coatings [125].

After long term cycling (200 cycles at 950°C in Burner Rig apparatus) continuous oxidized layers formed on the surface of all samples. Each kind of sample showed different concentration profiles and thickness of oxide scale. The sputtering rate was approximately calculated from literature data [161]. According to this XPS database, the sputtering rate is 7.1 nm/min and 4.8 nm/min for  $\text{TiO}_2$  and  $\text{Al}_2\text{O}_3$  respectively. An average sputtering rate for the oxide layers of about 6 nm/min was calculated, assuming that the  $\text{TiO}_2:\text{Al}_2\text{O}_3$  ratio is 1:1. Based on calculated sputtering rate, the oxygen and nitrogen profiles indicated the thickness of the oxide layer grown on the surface of the different specimens.

The external part of all oxidized samples contained mainly oxygen, titanium and aluminium.

Below this external part of the coated surfaces, the oxygen concentration progressively decreases. On the contrary, the nitrogen concentration, which is null in the more external part of the oxide layer, increases progressively with the

distance from the surface. After a first period of sputtering, both oxides and nitride were observed to be contemporaneously present. This is due to the interpenetration of the oxide and the nitride layers resulting from the roughness of the nitride coating surface and the diffusion of oxygen and nitrogen. When the sputtering allowed to reach the nitride coating the nitrogen concentration approached 50% at., while the oxygen concentration became very little.

For example, after 20 min (sputtering time), both coatings showed the higher concentration of oxygen (over 60 % at.), and contemporaneously TiAlN3 sample showed 6.3% at. of nitrogen while TiAlN1 did not contain nitrogen. At this point (which is about 120 nm far from the surface), the oxide layer and nitride coating begin to mix in the case of TiAlN3 sample. Further progressive sputtering led to a decrease of the oxygen concentration and an increase of nitrogen content. In the case of TiAlN1 sample after 50 minutes of sputtering the oxygen concentration was still 60.9%, but contemporaneously the nitrogen concentration was not negligible (2.9%). This means that 50 minutes of sputtering are necessary to move close to the nitride coating of TiAlN1 sample. The higher nitrogen concentration (about 50 % at. corresponding to the content in the nitride coating) was observed after 35 min and 70 min (sputtering time) for TiAlN3 and TiAlN1 samples respectively. This means that the intact coating begins at these points. Therefore, a very thin oxide scale of about 210 nm formed on TiAlN3 sample, while on TiAlN1 sample a scale about 300 nm thick was observed.

In the case of uncoated intermetallic, the depth profile of oxygen showed an almost linear trend since the content of oxygen decreased gradually with the distance from the surface. After very long period of sputtering, about 110 min that corresponded to about 660 nm layer thick, the oxygen concentration was still 18.9% and the nitrogen concentration null. For safety of XPS instrument, the test was stopped at this point. Anyway, the thickness of the oxide layer grown on the uncoated alloy exceeded the thickness of 660 nm.

In addition, nitrogen was found in the middle of the oxide layer formed on uncoated TiAl. In fact, nitrogen appeared in relevant concentration curve at a distance of 150 nm from the surface. The quantity of nitrogen inside the oxide layer grown on uncoated TiAl ranged between 1.1 at.% and 9.2 at.%. A maximum nitrogen concentration of 9.2% was found 360 nm far from the surface. The formation by air oxidation of a mixed layer containing both oxide and nitride was already reported in the case of Ti-46Al-8 Nb alloy oxidation [2].

The oxygen and nitrogen diffusion through the oxide layer (for uncoated specimens) or through the oxide layer and the underlying nitride coating (for coated specimens) led to the formation of diffusion layer. This process involved diffusion from the gaseous atmosphere and inwards transport inside the oxide layer. It is worthwhile studying the formation of an oxygen rich diffusion layer because it is expected to cause intermetallic embrittlement [162]. The diffusion of oxygen and nitrogen towards the substrate was investigated by SEM-EDS semi-quantitative analysis. An area placed on the sample cross section at a distance from the surface between 2.5  $\mu\text{m}$  and 4.5  $\mu\text{m}$  was investigated. This diffusion layer of the uncoated and the coated samples showed very different composition. The presence of a protective nitride coating on the sample surface greatly affected the diffusion process of oxygen, but not that of nitrogen. In case of the uncoated TiAl specimen, significant percentages of oxygen and nitrogen were found in the diffusion layer. Differently, the oxidation of TiAlN1 and TiAlN3 specimens resulted in the formation of a diffusion layer containing some percent of nitrogen and less than 1% of oxygen. The diffusion of oxygen through the oxide layer and the formation of the diffusion layer observed for the uncoated TiAl, but not for coated samples, is consistent with a mechanism for the scale growth involving inwards transport processes. The TiAlN1 and TiAlN3 coatings proved to greatly hinder the diffusion of oxygen towards the intermetallic substrate. In fact XPS analyses performed on the cross-section of TiAlN1 and TiAlN3 samples allowed to assess that after the cyclic oxidation only a small amount of oxygen is present within the nitride coating and EDS analysis performed within the substrate below the coating showed that oxygen concentration was lower than 1%. On the contrary the coatings were not able to avoid the nitrogen diffusion towards the intermetallic substrate.

The influence of nitrogen on the microstructure and the mechanical behaviour of Ti-Al intermetallic alloys is quite complex. The presence of nitrogen in solid solution in precipitates in the  $\gamma$  phase or in the  $\alpha_2$  phase improves micro hardness, compressive yield strength and creep behaviours [163]. The addition of some concentration of nitrogen results in the decrease of fracture strain, in particular for titanium rich alloys while this effect is not so evident for stoichiometric Ti-Al [164].

The aluminium and titanium concentration profiles of the XPS showed that after 200 thermal cycles the aluminium concentration is always higher than that of titanium on the surface of all the oxidized specimens. This outcome demonstrates that also the metallic elements (mainly Al and Ti) diffuses from the sample core towards the surface of the oxide layer. In every case, a preferential diffusion of aluminum with respect to titanium towards the sample surface was observed. This

phenomenon caused the surface enrichment of aluminum, progressively occurring with the oxide layer growth. Nevertheless the Al:Ti atomic ratio is quite different for the three kinds of samples. In particular, the concentration of Al is about 19 times higher than that of titanium on the surface of TiAlN1 coated sample. The preferential diffusion of aluminium caused the surface enrichment of aluminium, and its depletion at the core of the oxide layer. For instance, a zone of aluminium depletion was observed 300 nm far from the surface in the case of TiAlN1 sample.

### 3.2.3 Oxidation behaviour of TaAlN coated 48-2-2 intermetallic alloy

As reported in the state of the art section TaN surface coating is believed to grant advantages with respect to TiN also in terms of oxidation protection and the oxidation resistance of TiAlN films should be improved by doping them with tantalum. For these reasons, also a TaAlN coating was deposited in the surface of the intermetallics alloy 48-2-2 with the aim of improving its oxidation resistance.

The oxidation behaviour of this coated material was compared to that of the bare Ti-48Al-2Cr-2Nb alloy through a first oxidation test performed under flowing air (100 l/h) at 900°C.

The EDS analysis of as processed and oxidized substrates are reported in **Figure 104** and **Figure 105** respectively. According to the nominal composition the EDS shows that the alloy mainly consists of titanium and aluminium, while chromium and niobium are present in little quantity. After oxidation, the oxygen appeared on the alloy surface in significant quantity, which means that alloys surface was strongly oxidized after 30 minutes at 900°C. The distribution of chemical elements (Ti, Al and O) in cross-section of uncoated intermetallic alloy can be appreciated by EDS maps (**Figure 106**). Of course, the concentration of Ti and Al is lower in the oxide layer than in the substrate because of the presence of oxygen. SEM images of top and cross-section of TiAl substrate are shown in **Figure 107** and **Figure 108** respectively. The surface of oxidized alloy exhibits a rather uniform morphology. The sample cross-section shows the presence of an oxide layer with thickness of about 2.5 µm. The oxygen map obtained on the cross-section puts in evidence that oxygen is also present well below the oxide scale, in fact, oxygen was found inside and external zone about 4.7 µm thick. Then oxygen penetrates through the oxide layer and give rise to a diffusion zone about 2 µm thick, placed below the oxide layer.

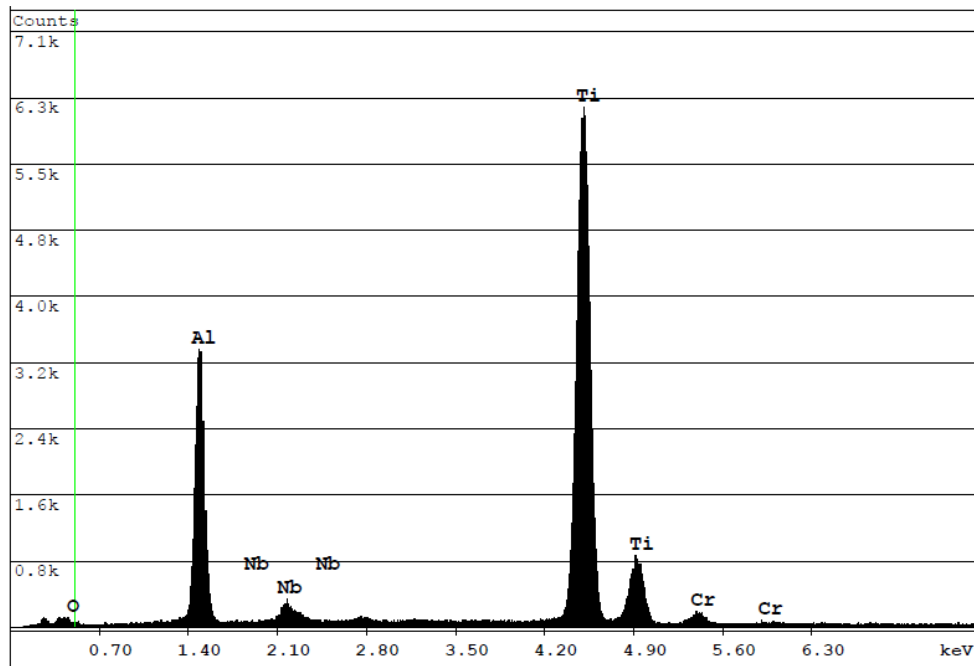


Figure 104: EDS of as-processed Ti-48Al-2Cr-2Nb surface.

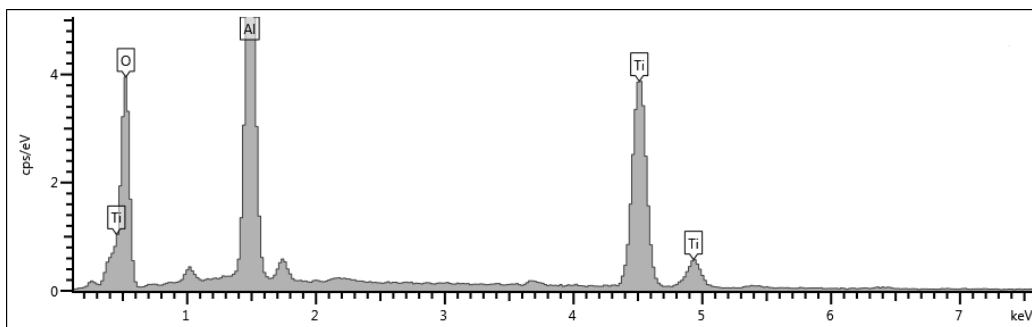


Figure 105: EDS of Ti-48Al-2Cr-2Nb oxidized at 900°C for 30 min.

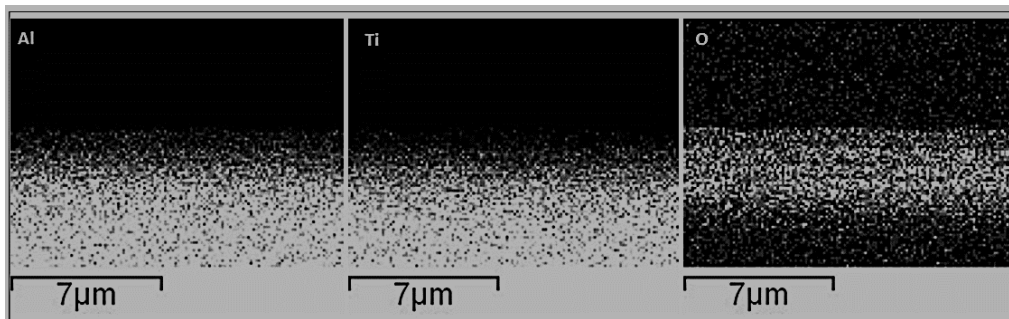


Figure 106: EDS cross-section of Ti-48Al-2Cr-2Nb oxidized at 900°C for 30 minutes.

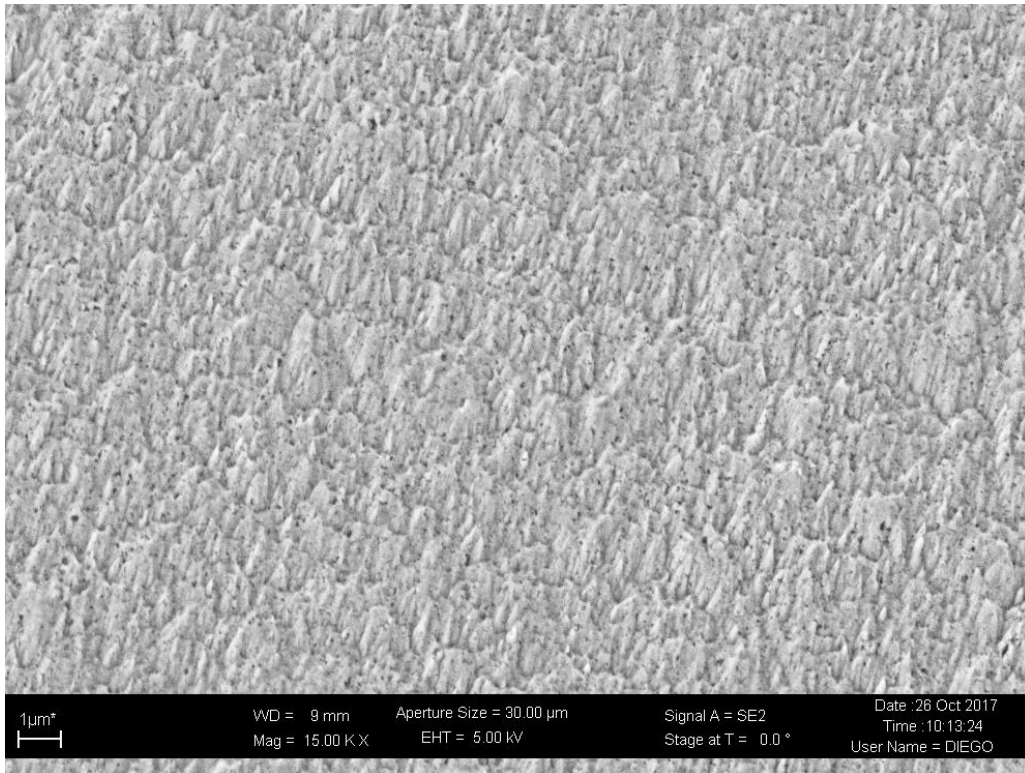


Figure 107: SEM image of surface of intermetallic alloy after oxidation at 900°C for 30 minutes.

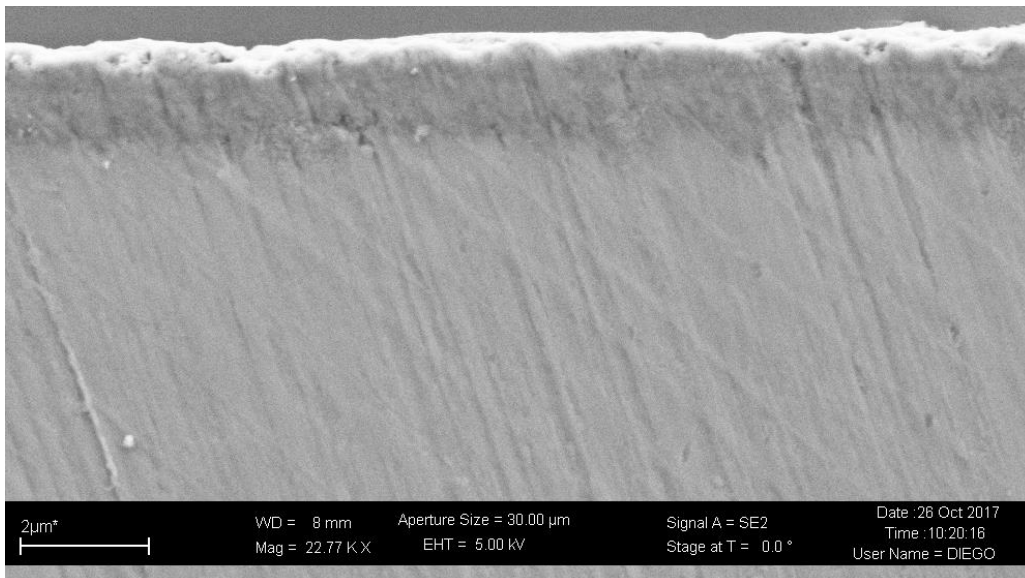


Figure 108: SEM image of cross-section of uncoated 48-2-2 intermetallic alloy after oxidation at 900 °C for 30 minutes (oxide layer a bit less than 2 μm thick).

The EDS analyses for samples with TaAlN coating, as-processed and oxidized, are reported in **Figure 109** and **Figure 110** respectively. According to EDS analysis the coating composition (at. %) is N= 55.98%, Al= 19.28%, Ta= 24.74%. Small contamination by oxygen can be also inferred on the basis of EDS for as-processed coating (**Figure 109**).

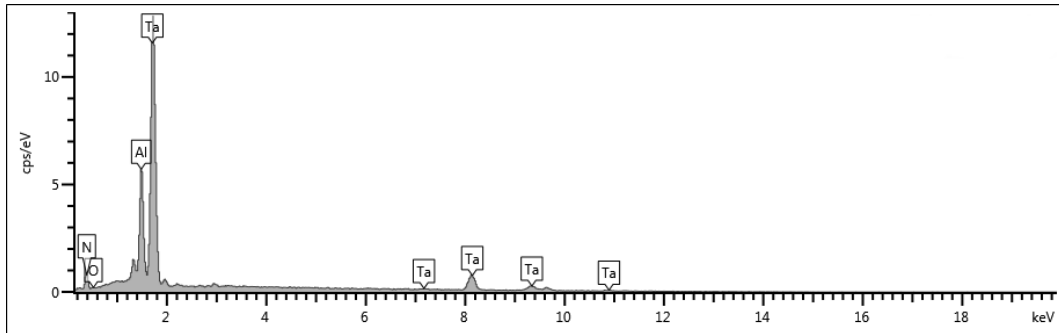


Figure 109: EDS spectrum of surface of as-processed TaAlN coated sample.

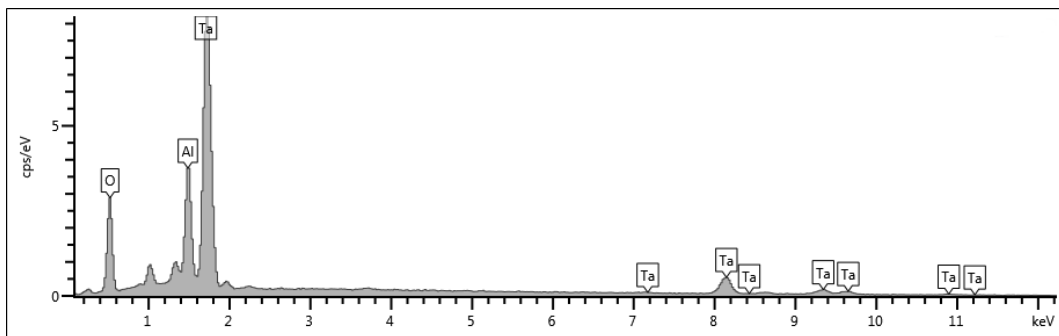


Figure 110: EDS of TaAlN coated sample after oxidation at 900°C for 30 minutes.

The SEM images of samples carrying the TaAlN coating after oxidation, surface and cross-section, are showed in **Figure 111** and **Figure 112** respectively.

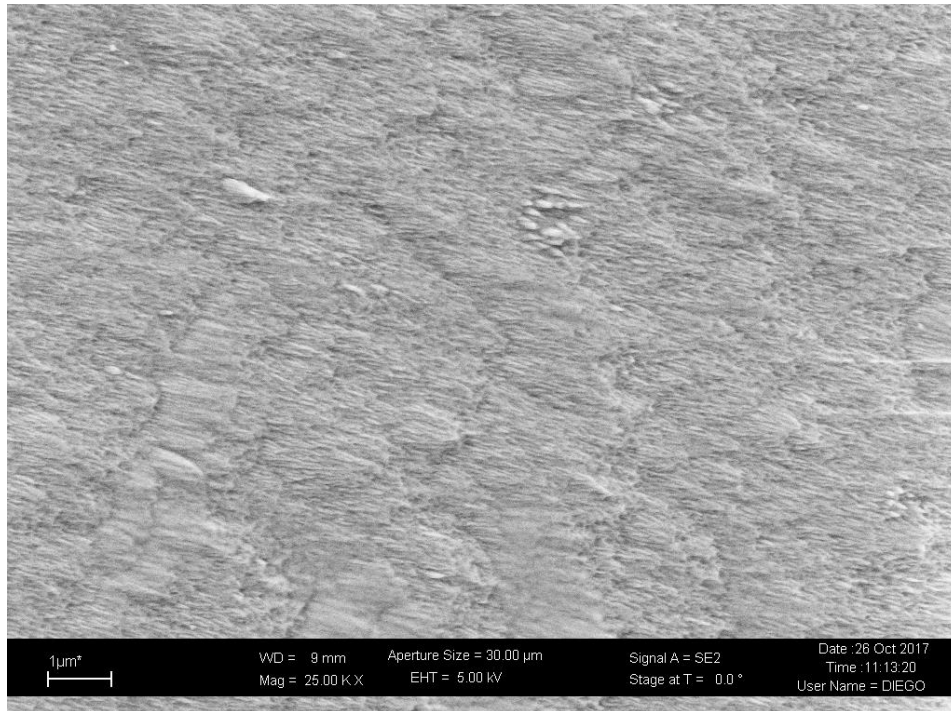


Figure 111: SEM surface image of TaAlN coated sample after oxidation at 900°C for 30 minutes.

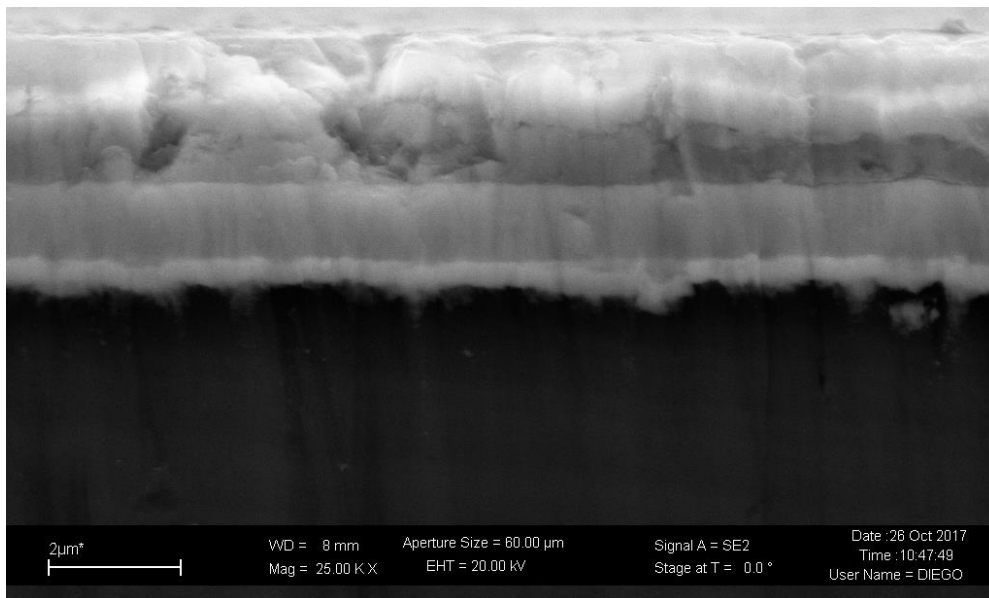


Figure 112: SEM cross-section image of TaAlN coated sample after oxidation at 900°C for 30 min (the up layer is an oxide scale about 2 μm thick grown on remaining TaAlN coating 1.2 μm thick, and the lower layer is the TiAl interlayer about 0.4 μm thick).

The cross section of oxidised sample shows that a continuous oxide layer grew on the nitride surface. The thickness of this oxide layer was about 2.5  $\mu\text{m}$  (**Figure 112**) and therefore the same observed after oxidation (under the same conditions) for the uncoated alloy. Below the scale it is possible to observe the nitride coating 1,6  $\mu\text{m}$  thick. Since the thickness of the as-deposited TaAlN coating was about 2-2.5  $\mu\text{m}$ , it can be concluded the oxide layer growth causes the consumption of part of the nitride coating. On the other hand, since the thickness of the oxide layer is much greater than the decrease of thickness of the nitride coating it is clear that the scale forms through a mechanism of outward diffusion of metallic elements. Al diffuses from the substrate towards the surface passing across the nitride layer, while Ta moves from the nitride layer towards the scale.

The EDS maps of cross-section of oxidized samples bearing the TaAlN coating, showed in the Figure 113, are consistent with these findings. It is evident that Al is present all over the cross section but its concentration decreases moving from the intermetallic alloy to the nitride layer, but does not change appreciably passing from the nitride coating to the oxide layer. Obviously tantalum is absent inside the substrate; its concentration seems higher in the nitride coating with respect to the oxide layer. Oxygen can be detected in a zone close to the surface and about 5  $\mu\text{m}$  thick; since the thickness of the oxide layer was about 2.5  $\mu\text{m}$  and that of the nitride coating after oxidation 1,6  $\mu\text{m}$  thick it seems that oxygen can diffuse inwards reaching the substrate place below the nitride coating.

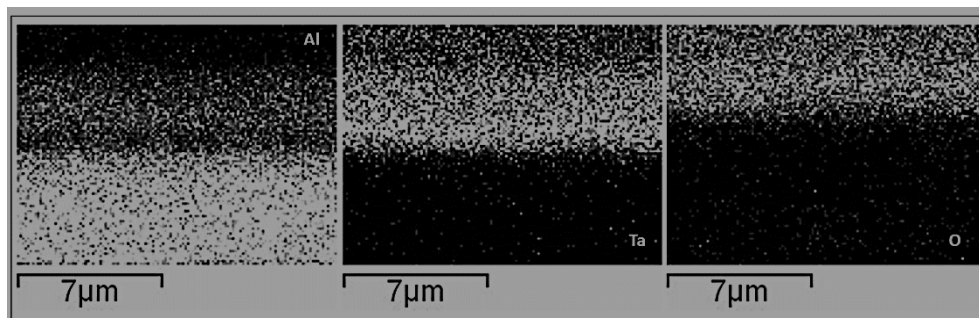


Figure 113: EDS cross-section of sample with TaAlN coating oxidized at 900°C for 30 minutes.

The XRD patterns of as-processed and oxidized samples with TaAlN coating (reported in **Figure 114** and **Figure 115** respectively) helps to better understand the composition of both coating and external oxide layer.

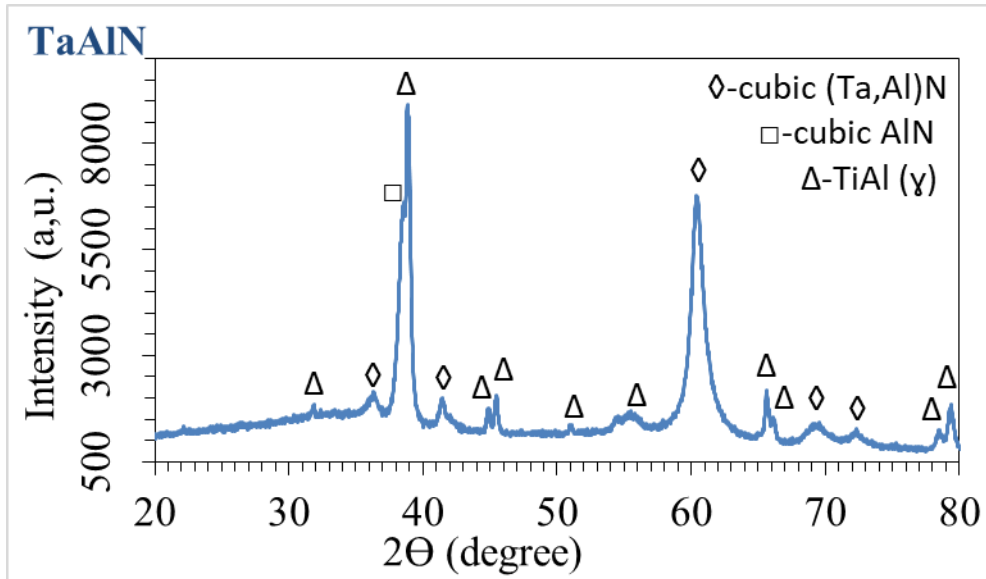


Figure 114: XRD plot of surface of as-processed samples with TaAlN coating.

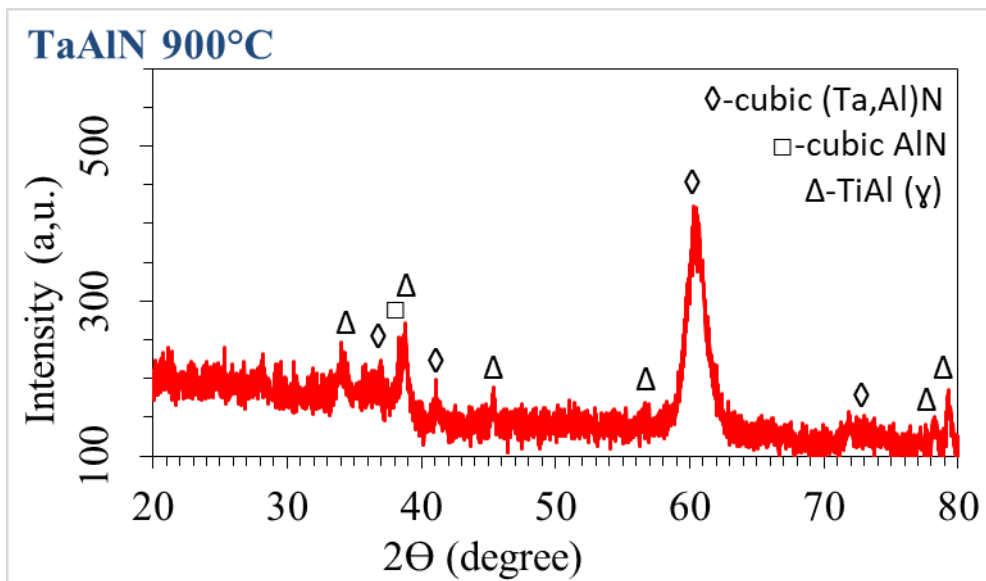


Figure 115: XRD plot of surface of with TaAlN coating after oxidation at 900°C for 30 min in air.

The XRD patterns of as-processed and oxidized coating shows the reflexes characteristic of face-centred-cubic (f.c.c.) TaN which are shifted because of the formation of the solid solution (Ta, Al)N [96]. According to literature, the lattice constants of f.c.c. AlN and TaN are 0.412 nm [ICDD 25–1495] and 0.43399 nm [ICDD 49–1283] respectively. TaN and AlN show similar XRD patterns where the

reflexes of TaN are systematically shifted towards lower diffraction angles with respect to the corresponding reflexes of AlN. When a (Ta,Al)N solid solution forms the peaks are placed at intermediate angles with respect to those characteristic of TaN and AlN [96]. In addition, some peaks belonging to TiAl ( $\gamma$ ) phase are also present, which means that the X-ray beam penetrates well below the surface reaching the TiAl substrate. In this work, the reflexes attributable to the solid solution between TaN and AlN were founded at 36.1 (111), 41.5 (200), 60.5 (220) and 72.5 (311) (2-theta degree). The intensity of (220) peak is much higher than that expected for a spectrum of powders. This feature shows that the nitride layer grows according to a preferential orientation of crystals, as was previously observed also for TiAlN coatings deposited with the same technique. The weak peak observed at around 38 (2-theta degree), as a shoulder of the main peak of  $\gamma$ -TiAl hardly could be attributed to the solid solution, while its position is consistent with the (111) reflex of cubic AlN. This last outcome would suggest that not all Al enter in the (Ta,Al)N solid solution.

These results are in agreement with the literature. In the Ta-N phase diagram, the  $\delta$ -TaN is a metastable phase at room temperature. The  $\delta$ -TaN frequently appears during magnetron sputtering deposition. In addition, a small addition of Al into TaN stabilized the  $\delta$ -TaN phase. In TaN lattice, the aluminium atoms are located at interstitial positions and do not replace the Ta atoms at substitutional positions in the  $\delta$ -TaN structure [96].

The XRD pattern obtained after oxidation shows that the intensity of the peaks belonging to both the nitride coating and the substrate greatly decreases because the oxide layer covers the surface. However, any peak attributable to crystalline oxides was not observed. Very likely not-well crystallized or amorphous oxides forms, as also suggested by the background noise of the relevant XRD pattern. The composition of the oxide layer can be better investigating by using XPS technique.

The XPS survey spectra of as-processed and oxidized samples with TaAlN coating are reported in **Figure 116** and **Figure 117**.

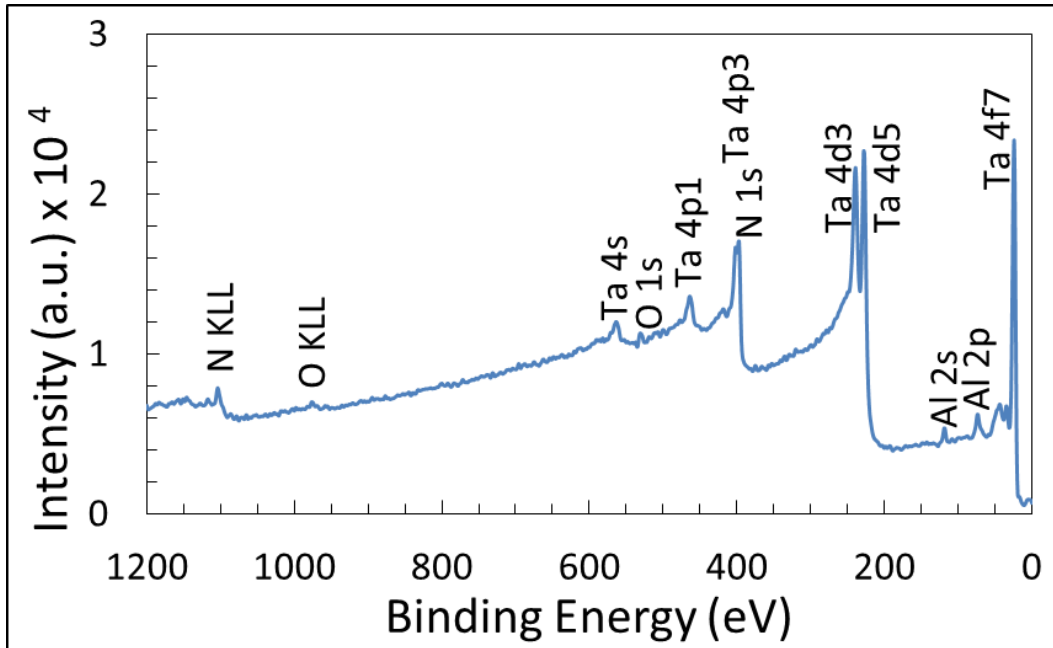


Figure 116: Survey spectrum of as-processed sample with TaAlN coating.

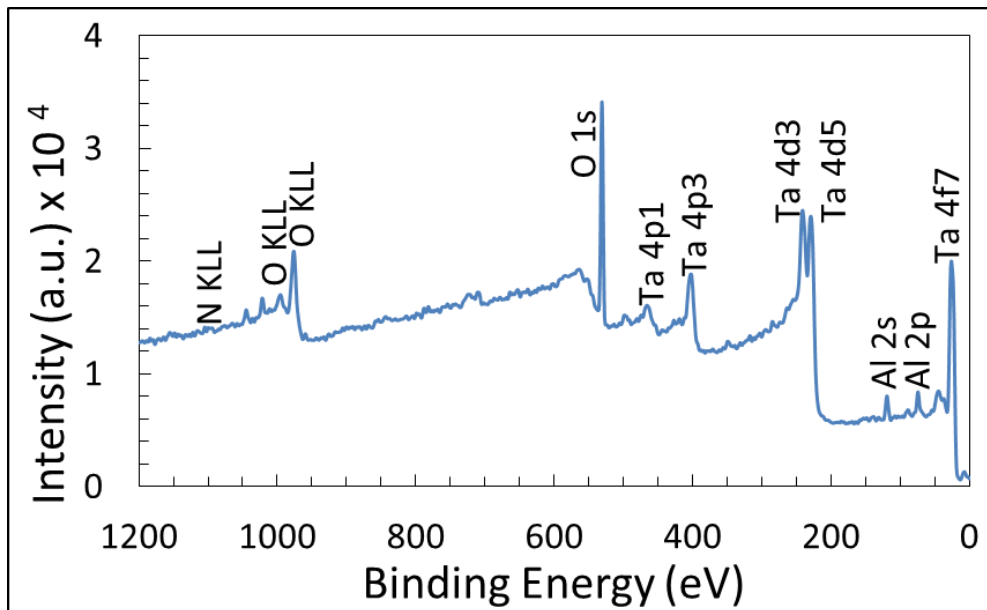


Figure 117: Survey spectrum of sample with TaAlN coating oxidised at 900°C for 30 min.

As processed coated sample shows in the relevant XPS spectrum the N peak at 400 eV (**Figure 116**).

In this survey spectrum, the peaks of tantalum and aluminium are also present. A very strong O peak at about at 540 eV grew in the spectrum of oxidized samples with TiAlN coating (**Figure 117**). This survey spectrum obviously exhibits the Ta and Al peaks too, thus showing that the oxide layer consists of a mixture of oxides of these elements.

The XPS HR analysis of as-processed and oxidised coated samples are presented in **Figure 118** and **Figure 119** respectively. In **Table 16**, the binding energies for chemical bonds formed by Ta, Al, N and O, reported in the literature, are summarized.

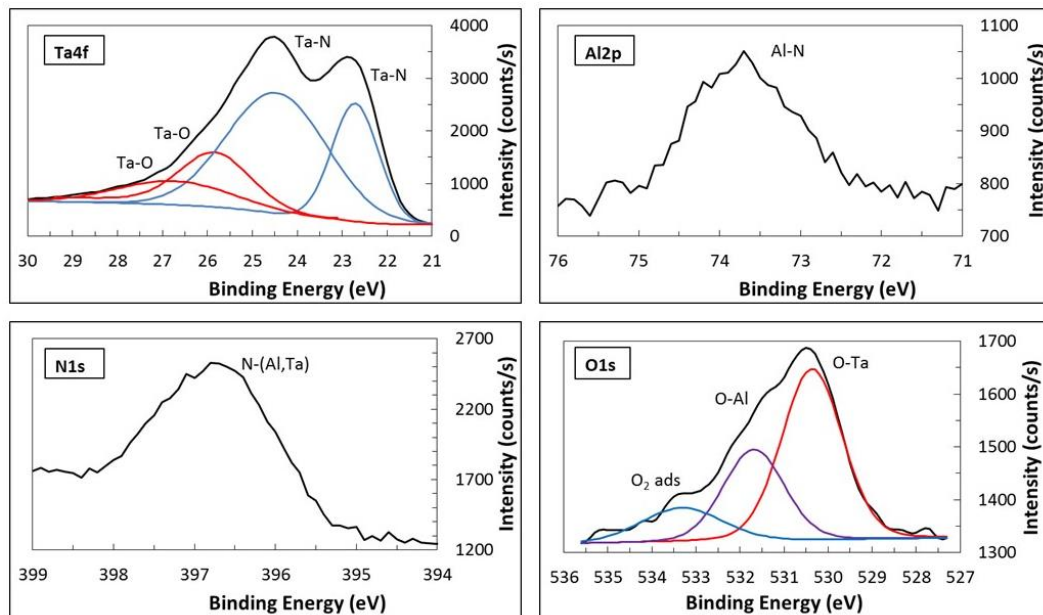


Figure 118: XPS HR spectra of as-processed samples with TaAlN coating.

According to Ta4f XPS HR plot, tantalum formed two different bonds, both represented by doublets (**Figure 118**). The double peak related to Ta-N bond is placed at 22.75 eV( $4f_{7/2}$ ) and 25.3 eV( $4f_{5/2}$ ). In the literature (**Table 16**), this doublet was reported to be in wide range at 22.5 eV-24 eV( $4f_{7/2}$ ) and 24.9 eV-26 eV( $4f_{5/2}$ ). The TaAlN coating shows some oxygen contamination. The Ta-O doublet can be observed in Ta4f XPS HR plot, the peaks show their maximum at 26eV( $4f_{7/2}$ ) and 27.3eV( $4f_{5/2}$ ). However, the second peak is very broad and is placed in the range between 25eV and 30 eV. According to previous works (**Table 16**), the Ta-O binding energy for Ta<sub>2</sub>O<sub>5</sub> oxide was founded at 25.9 eV-27.2eV( $4f_{7/2}$ ) and 28.4eV-29.1eV( $4f_{5/2}$ ).

The Al2p HR XPS plot shows a not well defined single peak at 73.8eV (**Figure 118**). This peak can be attributed at Al-N bond. From **Table 16**, the Al-N binding energy is 74.3 eV [125]. In this plot, evidence of bonds between aluminum and oxygen cannot be found. In literature the Al-O bound was founded at 75.6 eV [165],[125].

The N1s HR XPS plot shows only one peak for N-(Al, Ta) bonds at 396.7 eV (**Figure 118**). The N-(Al, Ta) peak should be placed at 396.4 eV-398.6 eV according to literature [125].

The O1s HR XPS plot can be fitted by using three peaks belonging to different species: O-Ta, O-Al and adsorbed O<sub>2</sub> (**Figure 118**). The O-Ta bond situated at 530.3 eV, can be attributed to Ta<sub>2</sub>O<sub>5</sub> formation. The O-Al bond gave rise to a peak at 531.8 eV and the peak of O<sub>2</sub> was found at 533.5 eV. **Table 16** shows consistent literature binding energies : the O-Ta bond has energy in the range of 529.8 eV-532 eV; the O-Al bond was observed at 532.1 eV [125]; while adsorbed O<sub>2</sub> was founded at 532 eV-533 eV [166].

The oxidized samples carrying TaAlN coating showed the formation of O-Ta and O-Al bonds in the external part of the oxide layer (**Figure 119**).

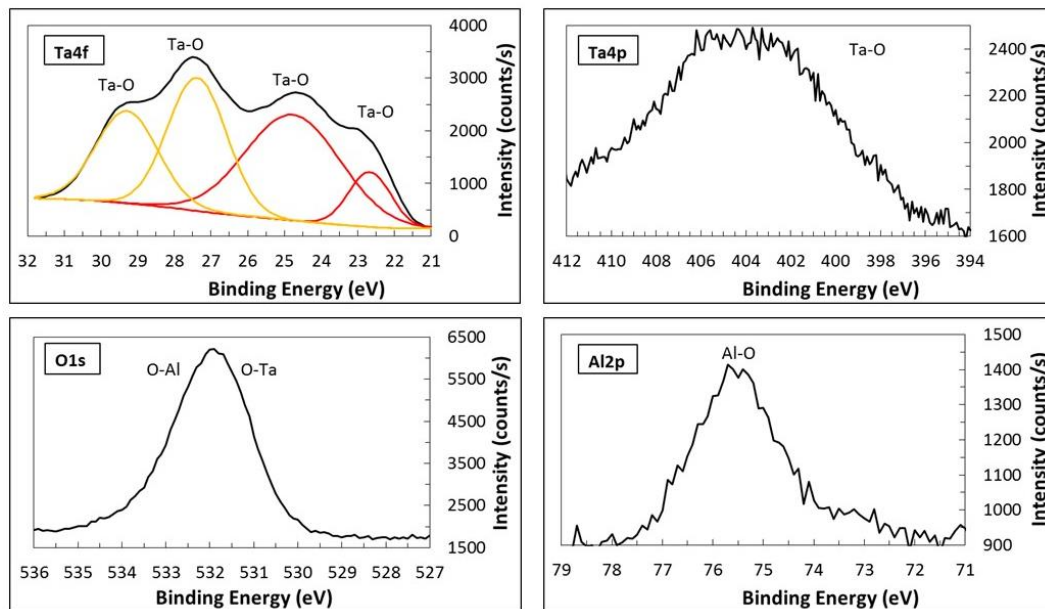


Figure 119: XPS HR spectra of samples with TaAlN coating oxidised at 900°C for 30 min.

**Table 16:** Binding energies for Ta, Al, N and O chemical bonds.

| <b>XPS<br/>HR</b> | <b>Binding Energy parameters of chemical bonds, eV<br/>(from literature data)</b>   |   |   |  |
|-------------------|---|---|---|--|
| <b>Ta4f</b>       | Ta –Ta:<br>22.1 [167];<br>22.6(4f <sub>7/2</sub> ) and<br>24.5(4f <sub>5/2</sub> )[168];<br>21.8 (4f <sub>7/2</sub> ) and<br>23.7(4f <sub>5/2</sub> )[165];<br>21.8 (4f <sub>7/2</sub> ) and<br>23.8 (4f <sub>5/2</sub> ) [169] | Ta-O(TaO <sub>x</sub> ):<br>23.3 and<br>24.8[167];<br>24.7[170] | Ta-O(Ta <sub>2</sub> O <sub>5</sub> ):<br>25.9[167];<br>27.2(4f <sub>7/2</sub> ) and<br>29.1(4f <sub>5/2</sub> )[168];<br>27(4f <sub>7/2</sub> ) and<br>29(4f <sub>5/2</sub> )[165];<br>26.5[170];<br>26.5(4f <sub>7/2</sub> ) and<br>28.4(4f <sub>5/2</sub> )[171] | Ta-N(TaN):<br>23.2(4f <sub>7/2</sub> )[170];<br>23[165];<br>23.6 and<br>25.5[172];<br>22.5(4f <sub>7/2</sub> ) and<br>24.9(4f <sub>5/2</sub> )[169];<br>24(4f <sub>7/2</sub> ) and<br>26(4f <sub>5/2</sub> )[173];<br><br>Ta <sub>1+x</sub> N:<br>22.5 [167] |
| <b>Ta4p</b>       | Ta-N(TaN): 401[167]; 402[174]; 405(4p <sub>3/2</sub> )[165];<br>403-404(4p <sub>3/2</sub> )[170]  |   |   | Ta-O(Ta <sub>2</sub> O <sub>5</sub> ):<br>404.6[166]   |
| <b>Ta4d</b>       | Ta-N(TaN <sub>x</sub> ): 228 and 239[174]   |   |   |  |
| <b>O1s</b>        | O-Ta:<br>530.7[167];<br>531.3[168];<br>529.8[170]   | Ta <sub>2</sub> O <sub>5</sub> :<br>530.6 and<br>532.0[171]     | O-Al:<br>532.1[125]   | O <sub>2</sub> :<br>532-533[166]   |
| <b>N1s</b>        | N-Ta(TaN):<br>397[165];<br>396.6[170];<br>402[174]  | N-O:<br>398.2[167]  | N-(Al,Ta):<br>396.4-<br>398.6[125]  | N-Metal:<br>397[165]   |
| <b>Al2p</b>       | Al-Al:<br>72.5 (2p <sub>3/2</sub> ) and<br>73(2p <sub>1/2</sub> )[165];<br>72.8[125]  | Al-N:<br>74.3[125]  | Al-O:<br>75.6[165];<br>75.6[125]  |  |

The Ta4f HR XPS plot shows that tantalum was bonded with oxygen. On the top of oxide layer grown on TaAlN coating, two kinds of Ta-O bonds (each resulting in a doublet) formed, which corresponded to TaO<sub>x</sub> and Ta<sub>2</sub>O<sub>5</sub> species (**Figure 119**). The doublet for TaO<sub>x</sub> was localised at 22.75 eV and 24.8 eV; while in literature the doublet for TaO<sub>x</sub> was observed at 23.3 eV and 24.8 eV [167]. The Ta-O doublet for Ta<sub>2</sub>O<sub>5</sub> was observed in Ta 4f HR spectrum at 27.3 eV (4f<sub>7/2</sub>) and 29.3 eV (4f<sub>5/2</sub>) (**Figure 119**). Ta-O binding energy for Ta<sub>2</sub>O<sub>5</sub> was observed in Ta4p<sub>3/2</sub> spectrum at 404.6 eV, Which is coherent with literature data [166].

A single peak for Al-O bond was detected at 75.5 eV in the Al2p XPS HR plot. In literature the relevant binding energy is reported to be 75.6 eV [125],[165]. The O1s HR XPS plot confirmed that the O-Al and O-Ta bonds formed on the top of oxidized surface of samples with TaAlN coating. The relevant peaks were superimposed in the O1s HR spectrum; the binding energy of O-Al bond was founded at 532 eV, while that of O-Ta was observed at 531.8 eV (**Figure 119**). **Table 16** shows that the binding energies concerning these bonds are generally situated around 532 eV: 529.8 eV -531.3 (O-Ta bond), 530.6 eV and 532 eV (O-Ta bond in Ta<sub>2</sub>O<sub>5</sub>), 532.1eV(O-Al).

# Chapter 4

## Conclusions

### 4.1 Oxidation behaviour of Ti-Al intermetallic alloys

The oxidation resistance of some Ti-Al intermetallic alloys of second and third generation (Ti-48Al-2Cr-2Nb at.%, Ti-48Al-2Nb-0.7Cr-0.3Si at.%, Ti-43.5Al-4Nb-1Mo at.% and Ti-47Al-2Cr-8Nb at.%), which have been proposed for industrial applications up to 850°C, have been investigated in a wide range of temperature.

After TGA isothermal tests at different temperatures (850°C-1000°C) for 10 hours in air the oxide scale in every case was mainly constituted by rutile and alpha alumina. The oxide layer of Ti-43.5Al-4Nb-1Mo and Ti-47Al-2Cr-8Nb alloys, which contain 4% at. and 8% at. of Nb respectively, also contained niobium oxide.

The presence inside the scale of all the other alloying elements was also assessed by EDS and XPS. Some of them showed a concentration gradient within the surface layer. In particular the outermost part of the oxide layer showed enhanced content of Ti, Cr and Si.

Spallation of the oxide layers was observed to occur under different conditions depending on the kind of alloy. This phenomenon limits the maximum working temperature of the different alloys. Spallation started to occur at 900°C for Ti-48Al-2Cr-2Nb and Ti-48Al-2Nb-0.7Cr-0.3Si, at 950-1000°C for Ti-43.5Al-4Nb-1Mo and at 1000° C for Ti-47Al-2Cr-8Nb. Spallation occurred more easily in the case of alloys that showed high growth rate of the oxide layer.

The oxidation kinetics of all the four Ti-Al alloys was controlled by diffusion processes, that occurred with different rates within oxide layers showing different composition. In fact, the growth of the oxide layers followed a parabolic rate law, at least as long as important exfoliation phenomena do not happen.

The kinetic parameters (both parabolic rate constant and activation energy) were experimentally investigated and allowed to establish the following ranking (from the worst to the best) for the oxidation resistance of the TiAl alloys examined: Ti-48Al-2Cr-2Nb, Ti-48Al-2Nb-0.7Cr-0.3Si, Ti-43.5Al-4Nb-1Mo, Ti-47Al-2Cr-8Nb.

The parabolic rate constant values for the oxidation of these alloys increased with the temperature increase (as expected), and they were always between those characteristics for the oxidation of pure titanium and pure aluminium. The activation energy values for the oxidation of these alloys were: 216.30 kJmol<sup>-1</sup> (Ti-48Al-2Cr-2Nb), 256.57 kJmol<sup>-1</sup> (Ti-48Al-2Nb-0.7Cr-0.3Si), 285.12 kJmol<sup>-1</sup> (Ti-43.5Al-4Nb-1Mo) and 298.4 kJmol<sup>-1</sup> (Ti-47Al-2Cr-8Nb). These values are higher than that reported in literature for pure titanium and consistent with most of literature data available for similar Ti-Al intermetallic alloys, but constantly lower than that attributed to the binary alloy Ti-48.6Al (400 kJmol<sup>-1</sup>). Therefore, the alloying elements, which are added to improve the mechanical properties, decrease the oxidation resistance with respect to binary Ti-48.6Al. In addition, these alloying elements differently affect the oxidation behaviour.

The alloys with higher content of Nb and Mo showed better oxidation behaviour than Ti-48Al-2Cr-2Nb and Ti-48Al-2Nb-0.7Cr-0.3Si, thus indirectly confirming that these elements play a role of in the oxidation mechanism. The different behaviour of these last two alloys (Ti-48Al-2Cr-2Nb and Ti-48Al-2Nb-0.7Cr-0.3Si) can be explained with the different concentration of Cr (displaying a detrimental effect) and the addition in the second alloy of Si, that is believed to improve the oxidation resistance [102].

## 4.2 TiAlN ceramic coatings

In order to improve the oxidation resistance of Ti-48Al-2Cr-2Nb (which showed the worse oxidation resistance among the alloys under investigation), TiAlN coatings were deposited by reactive High Power Impulse Magnetron Sputtering (HiPIMS) technique. Oxidation resistance and coating adhesion, which are among the major requirements for environmental barrier coatings of turbine engine components, were found to be very good for the TiAlN coating under investigation. In addition, the procedure adopted for the preparation of the surface of the TiAl substrate before the coating deposition affected the oxidation behaviour.

All the TiAlN coatings significantly increased the oxidation resistance over that of the Ti-48Al-2Cr-2Nb substrate. In particular, a coating obtained by combining a soft HiPIMS plasma etching and the deposition of a TiAl interlayer before the processing of a TiAlN film resulted in a greater reduction of the oxidation rate. This improved performance was attributed to the growth of a coherent dense TiAlN film with a reduced flaw concentration.

The TiAlN barrier deposited by HiPIMS displayed very good thermal stability, as any evidence of spinodal decomposition was not observed after testing the specimens at temperatures up to 950°C for rather long periods.

The thickness of the oxide film grown on coated samples was measured after prolonged cyclic oxidation. A gentle surface etching and the deposition of a TiAl interlayer before the TiAlN processing allowed to reduce the oxide layer thickness from 300 nm to 120 nm. In every case, the thickness of the oxide layer formed on coated samples was very smaller than that observed for the uncoated intermetallic alloy (over 660 nm).

The oxide layers always consisted of alumina and several titanium oxides ( $\text{TiO}_2$ ,  $\text{Ti}_2\text{O}_3$ ,  $\text{TiO}_x$ ). Alumina and rutile became the main components of the oxide films with the oxidation advancement. Moreover, after prolonged oxidation the ratio between  $\text{Al}_2\text{O}_3$  and  $\text{TiO}_2$  was very different for the uncoated intermetallic and the coated samples. The oxide scale grown on the uncoated alloy contained similar amounts of aluminum and titanium oxides (a mixture of  $\text{TiO}_2$ ,  $\text{Ti}_2\text{O}_3$  and  $\text{TiO}_x$ ). In the case of oxidation of the coated samples containing the TiAl interlayer alumina was the main component of the oxide film, but several titanium oxides were also detected. The oxide layer formed on the other coated samples was chiefly constituted by alumina and rutile, with the amount of alumina progressively increasing with the oxidation time. In fact, after 200 oxidation cycles the external part of the oxide film was made almost completely by alumina. Consequently an underlying zone of Al depletion formed near the interface between the oxide film and the nitride coating. In every case the increase of alumina content on the sample surface is expected provide progressively enhanced passivation with the advancement of the oxidation process. These findings suggest an outward mechanism of growth for the oxide layer, since the enrichment in aluminum of the surface can only be caused by the different diffusion rate of Al and Ti.

Also nitrogen and oxygen can diffuse inwards and cross the oxide layer (uncoated samples) and the underlying nitride coatings (coated samples). For all the

samples significant amounts of nitrogen were detected in the diffusion layer formed within the intermetallic alloy. This means that neither the oxide scale nor the nitride coating are able to avoid the inward diffusion of nitrogen. On the contrary, oxygen was able to diffuse through the oxide layer formed on uncoated samples but only negligible amounts of oxygen were observed inside the diffusion layer placed below the TiAlN films. This means that the TiAlN coating hindered the inwards diffusion of oxygen.

The intermetallic alloy seems to undergo oxidation according to a complex mechanism involving outwards diffusion of Al and Ti and inwards diffusion of oxygen. On the contrary the outwards diffusion of Al and Ti seems chiefly responsible for the growth of the oxide layer when the samples are protected by the nitride coatings.

Conclusively the HiPIMS technique allowed to obtain coatings showing thermal stability, oxidation resistance and strong interfaces with the intermetallic substrate. In fact, hundreds of severe thermal shocks involved in the cyclic oxidation testing never caused the coating damage or its loss of adhesion. Therefore, the HiPIMS TiAlN coatings show potential for oxidation protection of Ti-Al alloys, also at temperatures significantly exceeding the operating temperature of second generation intermetallic alloys.

The optimized processing of TiAlN coating (after deposition of TiAl interlayer) should be adopted for alloys designed for applications at higher temperatures and the coating effectiveness also confirmed in this new cases. The tendency of the scale to suffer spallation should be investigated after very long-term oxidation and then after the growth of very thick oxide layers.

### **4.3 TaAlN ceramic coatings**

Literature findings pushed to investigate also TaAlN coating, as an alternative to TiAlN protective layers. The TaAlN coating was deposited on Ti-48Al-2Cr-2Nb alloy by reactive High Power Impulse Magnetron Sputtering technique. The as-processed TaAlN coating mainly consisted of cubic (Ta,Al)N, with the possible presence of a small amount of cubic AlN too.

After a preliminary oxidation test, which was performed under flowing air (100 l/h) at 900°C for 30 minutes, the TaAlN coating appeared not spalled and only poorly damaged. However the comparison between TaAlN-coated and uncoated

samples showed that this coating is not able to decrease the oxidation rate. The oxidation scale for both uncoated and TaAlN-coated specimens showed similar thickness (about 2.5 $\mu\text{m}$ ). The oxide layer grown on the TaAlN film consisted in a mixture of Ta<sub>2</sub>O<sub>5</sub>, TaO<sub>x</sub> and Al<sub>2</sub>O<sub>3</sub> oxides, not well crystallized or amorphous. In addition, the TaAlN coating was not able to block the oxygen diffusion towards the intermetallic substrate. For the reasons above mentioned this protection layer showed to be less effective than TiAlN film, and therefore it was not submitted to further investigations.

## References

- [1] “ANSYS-CFX Gas Turbine Combustor.” [Online]. Available: <http://cfd2012.com/ansys-cfx-gas-turbine-combustor.html>.
- [2] M. Mitoraj, E. Godlewska, O. Heintz, N. Geoffroy, S. Fontana, and S. Chevalier, “Scale composition and oxidation mechanism of the Ti-46Al-8Nb alloy in air at 700 and 800 °C,” *Intermetallics*, vol. 19, no. 1, pp. 39–47, 2011.
- [3] B. P. Bewlay, S. Nag, A. Suzuki, and M. J. Weimer, “TiAl alloys in commercial aircraft engines,” *Mater. High Temp.*, vol. 33, no. 4–5, pp. 549–559, 2016.
- [4] K. Kothari, R. Radhakrishnan, and N. M. Wereley, “Advances in gamma titanium aluminides and their manufacturing techniques,” *Prog. Aerosp. Sci.*, vol. 55, pp. 1–16, 2012.
- [5] J. Dai, J. Zhu, C. Chen, and F. Weng, “High temperature oxidation behavior and research status of modifications on improving high temperature oxidation resistance of titanium alloys and titanium aluminides: A review,” *J. Alloys Compd.*, vol. 685, pp. 784–798, 2016.
- [6] C. Leyens, R. Braun, M. Fröhlich, and P. E. Hovsepian, “Recent progress in the coating protection of gamma titanium aluminides,” *Jom*, vol. 58, no. 1, pp. 17–21, 2006.
- [7] R. Pflumm, A. Donchev, S. Mayer, H. Clemens, and M. Schütze, “High-temperature oxidation behavior of multi-phase Mo-containing  $\gamma$ -TiAl-based alloys,” *Intermetallics*, vol. 53, pp. 45–55, 2014.
- [8] T. Tetsui, “Gamma Ti aluminides for non-aerospace applications,” *Curr. Opin. Solid State Mater. Sci.*, vol. 4, no. 3, pp. 243–248, 1999.
- [9] D. M. Dimiduk, P. L. Martin, and R. Dutton, “Accelerated insertion of materials: Gamma alloys pose challenges, but are really not unique,” in *Gamma Titanium Aluminides 2003*, 2003, pp. 15–22.
- [10] H. Baur, D. B. Wortberg, and H. Clemens, “Gamma Titanium Aluminides 2003,” in *Y.W. Kim, H. Clemens, A.H. Rosenberger*, 2003.

- [11] Y. Koyanagi, S. Ueta, and T. Noda, "Development of TiAl alloy with high creep strength and manufacturability for a turbine wheel," 2011.
- [12] B. P. Bewlay, M. Weimer, T. Kelly, A. Suzuki, and P. R. Subramanian, "Intermetallic-based alloys-science, technology, and applications," in *1516*, 2012, pp. 49–58.
- [13] "Pratt and Whitney PW1100G Geared Turbofan Engine." [Online]. Available: <http://theflyingengineer.com/flightdeck/pw1100g-gtf/>.
- [14] U. Habel *et al.*, "Forged Intermetallic  $\gamma$ -TiAl Based Alloy Low Pressure Turbine Blade in the Geared Turbofan," pp. 1223–1227, 2016.
- [15] Y. Kim, "Ordered Intermetallic Alloys , Part III: Gamma Titanium Aluminides," *JOM*, no. July, pp. 30–31, 1994.
- [16] H. Anada and Y. Shida, "Effect of Mo addition on the oxidation behaviour of Tial intermetallic compound," *Mater. Trans. JIM*, vol. 36, no. 4, pp. 533–539, 1995.
- [17] H. Clemens and S. Mayer, "Design, processing, microstructure, properties, and applications of advanced intermetallic TiAl alloys," *Adv. Eng. Mater.*, vol. 15, no. 4, pp. 191–215, 2013.
- [18] S. Biamino *et al.*, "Electron beam melting of Ti-48Al-2Cr-2Nb alloy: Microstructure and mechanical properties investigation," *Intermetallics*, vol. 19, no. 6, pp. 776–781, 2011.
- [19] G. Baudana *et al.*, "Electron Beam Melting of Ti-48Al-2Nb-0.7Cr-0.3Si: Feasibility investigation," *Intermetallics*, vol. 73, pp. 43–49, 2016.
- [20] M. Ternier *et al.*, "Electron Beam Melting of High Niobium Containing TiAl Alloy : Feasibility Investigation," *steel Res. Int.*, vol. 83, no. 10, pp. 943–949, 2012.
- [21] M. Ternier, "Innovative materials for high temperature structural applications: 3rd Generation  $\gamma$ -TiAl fabricated by Electron Beam Melting," Politecnico di Torino, 2014.
- [22] D. Kim *et al.*, "Oxidation behaviour of gamma titanium aluminides with or without protective coatings," *Int. Mater. Rev.*, vol. 59, no. 6, pp. 297–325, 2014.
- [23] G. L. Chen, X. J. Xu, Z. K. Teng, Y. L. Wang, and J. P. Lin, "Microsegregation in high Nb containing TiAl alloy ingots beyond

- laboratory scale,” vol. 15, pp. 625–631, 2007.
- [24] Z. C. Liu, J. P. Lin, S. J. Li, and G. L. Chen, “Effects of Nb and Al on the microstructures and mechanical properties of high Nb containing TiAl base alloys,” vol. 10, pp. 653–659, 2002.
- [25] D. Pilone and F. Felli, “Isothermal oxidation behaviour of TiAl-Cr-Nb-B alloys produced by induction melting,” *Intermetallics*, vol. 26, pp. 36–39, 2012.
- [26] I. C. I. Okafor and R. G. Reddy, “The oxidation behavior of high-temperature aluminides,” *Jom*, vol. 51, pp. 35–40, 1999.
- [27] S. A. Kekare and P. B. Aswath, “Oxidation of TiAl based intermetallics,” *J. Mater. Sci.*, vol. 32, pp. 2485–2499, 1997.
- [28] D. Pilone, F. Felli, and A. Brotzu, “High temperature oxidation behaviour of TiAl-Cr-Nb-Mo alloys,” *Intermetallics*, vol. 43, pp. 131–137, 2013.
- [29] S. Taniguchi and T. Shibata, “Influence of additional elements on the oxidation behaviour of TiAl,” *Intermetallics*, vol. 4, no. 96, pp. 85–93, 1996.
- [30] J. W. Fergus, “Review of the effect of alloy composition on the growth rates of scales formed during oxidation of gamma titanium aluminide alloys,” *Mater. Sci. Eng. A*, vol. 338, no. 1–2, pp. 108–125, 2002.
- [31] V. Maurice, G. Despert, S. Zanna, P. Josso, M. P. Bacos, and P. Marcus, “XPS study of the initial stages of oxidation of  $\alpha_2$ -Ti<sub>3</sub>Al and  $\gamma$ -TiAl-TiAl intermetallic alloys,” *Acta Mater.*, vol. 55, no. 10, pp. 3315–3325, 2007.
- [32] Y. Shida and H. Anada, “Role of W, Mo, Nb and Si in oxidation of TiAl in air at high temperature,” *Nippon Kinzoku Gakkaishi/Journal of the Japan Institute of Metals*, vol. 58, no. 7, pp. 754–762, 1994.
- [33] H. Jiang, “Effect of Nb on the high temperature oxidation of Ti-(0–50 at.%) Al,” *Scr. Mater.*, vol. 46, pp. 639–643, 2002.
- [34] T. Izumi, T. Yoshioka, S. Hayashi, and T. Narita, “Oxidation behavior of sulfidation processed TiAl-2 at.%X (X=Si, Mn, Ni, Ge, Y, Zr, La, and Ta) alloys at 1173 K in air,” *Intermetallics*, vol. 13, no. 7, pp. 694–703, 2005.
- [35] H. ren JIANG *et al.*, “Effects of Nb and Si on high temperature oxidation of TiAl,” *Trans. Nonferrous Met. Soc. China (English Ed.)*, vol. 18, no. 3, pp. 512–517, 2008.

- [36] Z. Tiebang *et al.*, “Synergistic Effect of Nb and Mo on Oxidation Behavior of TiAl-Based Alloys,” *Rare Met. Mater. Eng.*, vol. 1, 2012.
- [37] X. Y. Li, S. Taniguchi, Y. Matsunaga, K. Nakagawa, and K. Fujita, “Influence of siliconizing on the oxidation behavior of a  $\gamma$ -TiAl based alloy,” *Intermetallics*, vol. 11, no. 2, pp. 143–150, 2003.
- [38] F. M. A. Ebach-Stahl, R. Braun, and C. Leyens:, “Oxidation protective coatings for  $\gamma$ -TiAl-recent trends,” *Materwiss. Werksttech.*, vol. 38, no. 9, pp. 667–673, 2007.
- [39] D. Wei, P. Zhang, Z. Yao, W. Liang, Q. Miao, and Z. Xu, “Oxidation of double-glow plasma chromising coating on TC4 titanium alloys,” *Corros. Sci.*, vol. 66, pp. 43–50, 2013.
- [40] W. Wenbo, X. Zhong, H. Zhiyong, W. Zhenxia, and Z. Pingze, “Effect of niobium surface alloying on the antioxidation of Ti-6Al-4V,” *Rare Met. Mater. Eng.*, vol. 36, no. 5, pp. 869–873, 2007.
- [41] G. Chaoli, B. Haifeng, L. Xiao-ping, and Z. Ping, “Process of double glow surface plasma niobizing on TiAl alloy,” *Trans. Mater. Heat Treat.*, vol. 36, no. 2, pp. 57–60, 2007.
- [42] H. Yuehui, H. Boyun, Q. Zaohul, and L. Yexiang, “Improvement of oxidation resistance of TiAl based alloy at the elevated temperature by carburization,” *Chin J Mater Res*, vol. 10, no. 6, pp. 603–607, 1996.
- [43] X. Wei and L. Xiaoping, “High-temperature oxidation experimental of Mo surface alloying on TiAl based alloy,” *Total Corros. Control*, vol. 24, no. 1, pp. 23–24, 2010.
- [44] T. Izumi, T. Yoshioka, S. Hayashi, and T. Narita, “Oxidation behavior of sulfidation processed TiAl-2 at.% X (X= Si, Mn, Ni, Ge, Y, Zr, La, and Ta) alloys at 1173 K in air,” *Intermetallics*, vol. 13, pp. 694–703, 2005.
- [45] S. Taniguchi *et al.*, “Influence of implantation of Al, Si, Cr or Mo ions on the oxidation behavior of TiAl under thermal cycle conditions,” *Mater. Sci. Eng. A*, vol. 266, pp. 267–275, 1999.
- [46] H. Songxiao, Z. Zhu, X. Jinsheng, and Y. Guansen, “Influence of Nb ion implantation on oxidation resistance of high temperature titanium alloy at 650 °C,” *Rare Met. Mater. Eng.*, vol. 18, no. 3, pp. 162–167, 1999.
- [47] X. Y. Li *et al.*, “Oxidation behavior of TiAl protected by Al and Nb combined ion implantation at high temperature,” *Nucl. instruments methods*

- Phys. Res. b*, vol. 187, pp. 207–214, 2002.
- [48] X. Y. Li *et al.*, “Effect of C, Nb and C+Nb combined ion implantation on the oxidation resistance of  $\gamma$ -TiAl based alloy,” *Mater. Sci. Eng. A*, vol. 316 (1/2), no. 187, pp. 224–230, 2001.
- [49] X. Y. Li *et al.*, “Oxidation behavior of TiAl protected by Si+ Nb combined ion implantation,” *Intermetallics*, vol. 9, no. 5, pp. 443–449, 2001.
- [50] U. Hornauer *et al.*, “Improvement of the high temperature oxidation resistance of Ti50Al via ion-implantation,” *Nucl. instruments methods Phys. Res. b*, vol. 148, pp. 858–862, 1999.
- [51] H. E. Zschau, M. Schütze, H. Baumann, and K. Bethge, “Application of ion beam analysis for the control of the improvement of the oxidation resistance of TiAl at 900 °C in air by fluorine ion implantation and HF-treatment,” *Nucl. instruments methods Phys. Res. b*, vol. 240, pp. 137–141, 2005.
- [52] H. E. Zschau, M. Schütze, H. Baumann, and K. Bethge, “Surface modification of titanium aluminides with fluorine to improve their application for high temperature service condition,” *Nucl. instruments methods Phys. Res. b*, vol. 257, pp. 383–387, 2007.
- [53] A. Donchev, E. Richter, and M. Schutze, “Improving the oxidation resistance of TiAl-alloy with fluorine,” *J. Alloys Compd.*, vol. 452, pp. 7–10, 2008.
- [54] X. Yanhui, “Laser Surface Alloying with C and C+Nb in a TiAl Alloy and its Oxidation Resistance at High Temperature and Wear Resistance Properties,” Xiangtan University, 2003.
- [55] S. Dechun, X. Li, and L. Keyong, “Improvement in resistance to high temperature oxidation of titanium alloy by laser surface alloying with Al+Nb,” *Chinese J. Lasers*, vol. 24, no. 3, pp. 281–285, 1997.
- [56] J. Dai, H. Yu, J. Zhu, F. Weng, and C. Chen, “Mechanical properties and high temperature oxidation behavior of Ti-Al coating reinforced by nitrides on Ti-6Al-4V alloy,” *Surf. Rev. Lett.*, vol. 23, no. 4, p. 1650031–1–1650031–9., 2016.
- [57] S. Kim, D. Paik, I. Kim, H. Kim, and K. Park, “Effect of aluminising on high temperature oxidation resistance of TiAl compounds,” *Mater. Sci. Technol.*, vol. 14, pp. 822–825, 1998.
- [58] Z. D. Xiang, S. Rose, and P. K. Datta, “Pack deposition of coherent aluminide coatings on  $\gamma$ -TiAl for enhancing its high temperature oxidation

- resistance,” vol. 161, pp. 286–292, 2002.
- [59] V. Gauthier, F. Dettenwanger, M. Schütze, V. Shemet, and W. J. Quadackers, “Oxidation-resistant aluminide coatings on  $\gamma$ -TiAl,” *Oxid. Met.*, vol. 59, no. 3–4, pp. 233–255, 2003.
- [60] C. Zhou, H. Xu, S. Gong, and K. Y. Kim, “A study of aluminide coatings on TiAl alloys by the pack cementation method,” *Mater. Sci. Eng.*, vol. 341, pp. 169–173, 2003.
- [61] A. G. Evans, D. R. Mumm, J. W. Hutchinson, G. H. Meier, and F. S. Pettit, “Mechanisms controlling the durability of thermal barrier coatings,” *Prog. Mater. Sci.*, vol. 46, pp. 505–553, 2001.
- [62] C. G. Levi, E. Sommer, S. G. Terry, A. Catanoiu, and M. Ruhle, “Alumina grown during deposition of thermal barrier coatings on NiCrAlY,” *J. Am. Chem. Soc.*, vol. 86, no. 4, pp. 676–685, 2003.
- [63] B. M.P., “The oxidation and protection of gamma titanium aluminides,” *JOM*, vol. 48, no. 11, pp. 46–50, 1996.
- [64] Z. Tang, F. Wang, and W. Wu, “Effect of a sputtered TiAlCr coating on the oxidation resistance of TiAl intermetallic compound,” *Oxid. Met.*, vol. 48, no. 5–6, pp. 511–525, 1997.
- [65] Z. Tang, F. Wang, and W. Wu, “The effects of several coatings on cyclic oxidation resistance of TiAl intermetallics,” *Surf. Coat. Technol.*, vol. 110, pp. 57–61, 1998.
- [66] Z. Tang, F. Wang, and W. Wu, “Effect of MCrAlY overlay coatings on oxidation resistance of TiAl intermetallics,” *Surf. Coat. Technol.*, vol. 99, no. 248–252, 1998.
- [67] Q.-M. Wang, M.-H. Ming, P.-L. Ke, J. Gong, C. Sun, and L.-S. Wen, “Oxidation protection of NiCoCrAlY coatings on  $\gamma$ -TiAl,” *Trans. Nonferrous Met. Soc. China*, vol. 15, no. 2, pp. 423–426, 2005.
- [68] Y. X. Cheng, W. Wang, S. L. Zhu, L. Xin, and F. H. Wang, “Arc ion plated-Cr<sub>2</sub>O<sub>3</sub> intermediate film as a diffusion barrier between NiCrAlY and  $\gamma$ -TiAl,” *Intermetallics*, vol. 18, pp. 736–739, 2010.
- [69] D. J. Kim, D. Y. Seo, X. Huang, Q. Yang, and Y.-W. Kim, “Cyclic oxidation behaviour of a beta gamma powder metallurgy TiAl–4Nb–3Mn alloy coated with a NiCrAlY coating,” *Surf. Coat. Technol.*, vol. 206, pp. 3048–3054, 2011.

- [70] D. J. Kim, X. Huang, D. Y. Seo, and Y.-W. Kim, "Cyclic oxidation and interdiffusion behaviour of a NiCrAlY coated powder metallurgy beta gamma TiAl-2Nb-2Mo alloy," *Oxid. Met.*, vol. 78, pp. 31–50, 2012.
- [71] D. J. Kim, "The estimation of delamination life of the plasma-sprayed thermal barrier coating for gas turbine blade," Sungkyunkwan University, Suwon, Korea, 2008.
- [72] V. Gauthier, F. Dettenwanger, and M. Schütze, "Oxidation behavior of  $\gamma$ -TiAl coated with zirconia thermal barriers," vol. 10, pp. 667–674, 2002.
- [73] H. A. Jehn, "Improvement of the corrosion resistance of PVD hard coating – substrate systems," vol. 125, pp. 212–217, 2000.
- [74] M. Xuelian, "Fabrication of the Low Oxygen Partial Pressure Fusing Coating Formed on Ti-6Al-4V Alloy and the Performance Analysis," Jilin University, Changchun, 2008.
- [75] J. P. Kim, H. G. Jung, and K. Y. Kim, "Al+Y codeposition using EB-PVD method for improvement of high-temperature oxidation resistance of TiAl," *Surf. Coat. Technol.*, vol. 112, pp. 91–97, 1999.
- [76] C. Zhou, F. Cai, H. Xu, and S. Gong, "Cyclic oxidation behavior of Al-Cu-Fe-Cr quasicrystalline coating on titanium alloy," *Mater. Sci. Eng. A*, vol. 386, pp. 362–366, 2004.
- [77] C. Leyens, M. Schmidt, M. Peters, and W. A. Kaysser, "Sputtered intermetallic Ti-Al-X coatings: phase formation and oxidation behavior," *Mater. Sci. Eng.*, vol. 239–240, pp. 680–687, 1997.
- [78] J. K. Lee, H. N. Lee, H. K. Lee, M. H. Oh, and D. M. Wee, "Effects of Al-21Ti-23Cr coatings on oxidation and mechanical properties of TiAl alloy," *Surf. Coat. Technol.*, vol. 155, no. 59–66, 2002.
- [79] C. Zhou, Y. Yang, S. Gong, and H. Xu, "Effect of Ti-Al-Cr coatings on the high temperature oxidation behavior of TiAl alloys," *Mater. Sci. Eng. A*, vol. 307, pp. 182–187, 2001.
- [80] A. E. Stahl, C. Eilers, N. Laska, and R. Braun, "Cyclic oxidation behaviour of the titanium alloys Ti-6242 and Ti-17 with Ti-Al-Cr-Y coatings at 600 and 700 °C in air," *Surf. Coat. Technol.*, vol. 223, pp. 24–31, 2013.
- [81] J. K. Lee, M. H. Oh, and D. M. Wee, "Long-term oxidation properties of Al-Ti-Cr two-phase alloys as coating materials for TiAl alloys," *Intermetallics*, vol. 10, pp. 347–352, 2002.

- [82] L. C., P. M., H. P., and M. W.-D., "Materials for Advanced Power Engineering," in *Materials for Advanced Power Engineering*, J. Leconte-Beckets, M. Catton, F. Schubert, and P. J. Eunis, Eds. Juelich, Germany: Schriften des Forschungszentrum Jülich, pp. 465–474.
- [83] R. Qiang and H. Shejun, "Effects of Ti<sub>0.5</sub>Al<sub>0.5</sub>N coatings on the protecting against oxidation for titanium alloys," *Rare Met. Mater. Eng.*, vol. 29, no. 2, pp. 154–161, 2010.
- [84] R. Qiang, H. Shejun, and H. Xianqi, "Preparation and oxidation resistance of Ti<sub>0.75</sub>Al<sub>0.25</sub>N coatings deposited on titanium alloy," *Heat Treat. Met.*, vol. 35, no. 6, pp. 88–92, 2010.
- [85] C. Qian, X. Li, T. Yingyuan, Z. Shenglong, and W. Fuhui, "Effect of nitride coatings on the cyclic oxidation behavior of Ti6Al4V alloy," *J. Chinese Soc. Corros. Prot.*, vol. 32, no. 1, pp. 7–12, 2012.
- [86] W. Baoyun, L. Zhengxian, Y. Peng, D. Jihong, and J. Shouchang, "Microstructure and inoxidizability of TiN/TiAlN coating on TC4 by arc ion plating," *Titan. Ind. Prog.*, vol. 25, no. 2, pp. 32–36, 2008.
- [87] L. Ipaz, W. Aperador, J. Caicedo, J. Esteve, and G. Zambrano, "A Practical Application of X-Ray Spectroscopy in Ti-Al-N and Cr-Al-N Thin Films," in *X-Ray Spectroscopy*, S. K. Sharma, Ed. InTech, 2010, p. 280.
- [88] J. F. Marco, J. R. Gancedo, M. A. Auger, O. Sánchez, and J. M. Albella, "Chemical stability of TiN, TiAlN and AlN layers in aggressive SO<sub>2</sub> environments," *Surf. Interface Anal.*, vol. 37, no. 12, pp. 1082–1091, 2005.
- [89] R. Qiang, H. Shejun, H. Nacan, and H. Xianqi, "Properties of TiAlCrN coating prepared by arc ion plating," *Heat Treat. Met.*, vol. 33, no. 3, pp. 51–54, 2008.
- [90] Y. X. Leng *et al.*, "Biomedical properties of tantalum nitride films synthesized by reactive magnetron sputtering," *Thin Solid Films*, vol. 398–399, pp. 471–475, 2001.
- [91] C. L. Liu, P. K. Chu, G. Q. Lin, and M. Qi, "Anti-corrosion characteristics of nitride-coated AISI 316L stainless steel coronary stents," *Surf. Coatings Technol.*, vol. 201, pp. 2802–2806, 2006.
- [92] R. Westergård, M. Bromark, M. Larsson, P. Hedenqvist, and S. Hogmark, "Mechanical and tribological characterization of DC magnetron sputtered tantalum nitride thin films," *Surf. Coatings Technol.*, vol. 97, pp. 779–784, 1997.

- [93] S. Xu, P. Munroe, J. Xu, and Z.-H. Xie, "The microstructure and mechanical properties of tantalum nitride coatings deposited by a plasma assisted bias sputtering deposition process," *Surf. Coatings Technol.*, vol. 307, pp. 470–475, 2016.
- [94] M. Pfeiler *et al.*, "On the effect of Ta on improved oxidation resistance of Ti-Al-Ta-N coatings," *J. Vac. Sci. Technol. A Vacuum, Surfaces, Film.*, vol. 27, pp. 554–560, 2009.
- [95] Y. Yang, Y. X. Xu, L. Chen, and P. H. Mayrhofer, "Improved Ti-Al-N coatings through Ta alloying and multilayer architecture," *Surf. Coatings Technol.*, vol. 328, no. September, pp. 428–435, 2017.
- [96] Y.-I. Chen, J.-H. Lin, and C.-C. Chou, "Oxidation resistance and mechanical properties of Ta-Al-N coatings," *Surf. Coatings Technol.*, vol. 303, pp. 41–47, 2016.
- [97] R. Baoyi, Z. Xuejun, G. Feng, P. Jianping, and F. Naixian, "Preparation of amorphous SiO<sub>2</sub> coating and its protection for Ti-22Al-26Nb alloy at high temperature," *Mater. Metall. Eng. J.*, vol. 8, no. 3, pp. 188–192, 2009.
- [98] Z. Xiao *et al.*, "Oxidation protection of commercial-purity titanium by Na<sub>2</sub>O-CaO-SiO<sub>2</sub> and SiO<sub>2</sub>-Al<sub>2</sub>O<sub>3</sub>-CaO-Na<sub>2</sub>O glass-ceramic coatings," *Ceram. Int.*, vol. 41, pp. 325–331, 2015.
- [99] T. Moskalewicz, F. Smeacetto, and A. Czysrk-Afilemonowicz, "Microstructure, properties and oxidation behavior of the glass-ceramic based coating on near- $\alpha$  titanium alloy," *Surf. Coat. Technol.*, vol. 203, pp. 2249–2253, 2009.
- [100] S. Sarkar, S. Datta, S. Das, and D. Basu, "Oxidation protection of gamma-titanium aluminide using glass ceramic coatings," *Surf. Coat. Technol.*, vol. 203, pp. 1797–1825, 2009.
- [101] G. Chunhong, T. Zhaolin, W. Fuhui, W. Weitao, and L. Shiqiong, "Effect of enamel coating on oxidation and hot corrosion resistance of Ti-24Al-14Nb-3V," *J. Mater. Eng. Perform.*, vol. 14, no. suppl., pp. 75–80, 2001.
- [102] O. Ostrovskaya, C. Badini, G. Baudana, E. Padovano, and S. Biamino, "Thermogravimetric investigation on oxidation kinetics of complex Ti-Al alloys," *Intermetallics*, no. May, pp. 1–7, 2017.
- [103] G. Baudana, " $\gamma$ -Titanium Aluminide Alloys for Aircraft and Automotive Engine Components Applications Processed by Electron Beam Melting," Politecnico di Torino, 2018.

- [104] M. Terner *et al.*, “Initial Oxidation Behavior in Air of TiAl-2Nb and TiAl-8Nb Alloys Produced by Electron Beam Melting,” *J. Mater. Eng. Perform.*, vol. 24, no. 10, pp. 3982–3988, 2015.
- [105] G. Baudana *et al.*, “Intermetallics Electron Beam Melting of Ti-48Al-2Nb-0.7Cr-0.3Si: Feasibility investigation,” *Intermetallics*, vol. 73, pp. 43–49, 2016.
- [106] D. Lundin and K. Sarakinos, “An introduction to thin film processing using high-power impulse magnetron sputtering,” *J. Mater. Res.*, vol. 27, no. 5, pp. 780–792, 2012.
- [107] C. Badini *et al.*, “Thermal shock and oxidation behavior of HiPIMS TiAlN coatings grown on Ti-48Al-2Cr-2Nb intermetallic alloy,” *Materials (Basel)*, vol. 9, no. 12, 2016.
- [108] V. Kouznetsov, K. Macák, J. M. Schneider, U. Helmersson, and I. Petrov, “A novel pulsed magnetron sputter technique utilizing very high target power densities,” *Surf. Coat. Technol.*, vol. 122, pp. 290–293, 1999.
- [109] A. Anders, “A review comparing cathodic arcs and high power impulse magnetron sputtering (HiPIMS),” *Surf. Coat. Technol.*, vol. 257, pp. 308–325, 2014.
- [110] U. Helmersson, M. Lattemann, J. Bohlmark, A. P. Ehiasarian, and J. T. Gudmundsson, “Ionized physical vapor deposition (IPVD): A review of technology and applications,” *Thin Solid Films*, vol. 513, no. 1–2, pp. 1–24, 2006.
- [111] J. Bohlmark, “Fundamentals of High Power Impulse Magnetron Sputtering,” Linköping University, Sweden, 2005.
- [112] K. Sarakinos, J. Alami, and S. Konstantinidis, “High power pulsed magnetron sputtering: A review on scientific and engineering state of the art,” *Surf. Coatings Technol.*, vol. 204, no. 11, pp. 1661–1684, 2010.
- [113] J. T. Gudmundsson, N. Brenning, D. Lundin, and U. Helmersson, “High power impulse magnetron sputtering discharge,” *J. Vac. Sci. Technol. A Vacuum, Surfaces, Film.*, vol. 30, no. 3, p. 030801/1-030801/34, 2012.
- [114] A. P. Ehiasarian, R. New, W.-D. Münz, L. Hultman, U. Helmersson, and V. Kouznetsov, “Influence of high power densities on the composition of pulsed magnetron plasmas,” *Vacuum*, vol. 65, no. 2, pp. 147–154, 2002.
- [115] O. Lemmer, W. Kölker, S. Bolz, and C. Schiffrers, “HiPIMS ‘goes

- production', actual status & outlook," *IOP Conf. Ser. Mater. Sci. Eng.*, vol. 39, no. 1, pp. 1–3, 2012.
- [116] A. P. Ehiasarian, J. G. Wen, and I. Petrov, "Interface microstructure engineering by high power impulse magnetron sputtering for the enhancement of adhesion," *J. Appl. Phys.*, vol. 101, p. 54301, 2007.
- [117] J. Alami, "Enhanced ionized sputtering in HIPIMS: An innovative deposition technique for the next generation superior industrial coatings," *Vak. Forsch. und Prax.*, vol. 25, no. 5, pp. 19–23, 2013.
- [118] J. T. Gudmundsson, J. Alami, and U. Helmersson, "Spatial and temporal behavior of the plasma parameters in a pulsed magnetron discharge," *Surf. Coatings Technol.*, vol. 161, no. 2–3, pp. 249–256, 2002.
- [119] J. Alami, K. Sarakinos, G. Mark, and M. Wuttig, "On the deposition rate in a high power pulsed magnetron sputtering discharge," *Appl. Phys. Lett.*, vol. 89, no. 15, pp. 1–4, 2006.
- [120] D. J. Christie, "Target material pathways model for high power pulsed magnetron sputtering," *J. Vac. Sci. Technol. A Vacuum, Surfaces, Film*, 23, vol. 330, 2005.
- [121] I. Petrov, P. B. Barna, L. Hultman, and J. E. Greene, "Microstructural evolution during film growth," *J. Vac. Sci. Technol. A Vacuum, Surfaces, Film.*, vol. 21, no. 5, pp. 117–128, 2003.
- [122] J. Dalla Torre *et al.*, "Microstructure of thin tantalum films sputtered onto inclined substrates: Experiments and atomistic simulations," *J. Appl. Phys.*, vol. 94, no. 1, pp. 263–271, 2003.
- [123] W. Ensinger, "Low energy ion assist during deposition — an effective tool for controlling thin film microstructure," *Nucl. Instruments Methods Phys. Res. Sect. B Beam Interact. with Mater. Atoms*, vol. 127–128, no. 97, pp. 796–808, 1997.
- [124] M. Aiempanakit, "Reactive High Power Impulse Magnetron Sputtering of Metal Oxides," Linköping University, Sweden, 2013.
- [125] C. Badini, S. M. Deambrosis, O. Ostrovskaya, V. Zin, E. Padovano, and E. Miorin, "Cyclic oxidation in burner rig of TiAlN coating deposited on Ti-48Al-2Cr- 2Nb by reactive HiPIMS," *Ceram. Int.*, vol. 43, no. 7, pp. 5417–5426, 2017.
- [126] M. Lattemann, A. P. Ehiasarian, J. Bohlmark, P. Å. O. Persson, and U.

- Helmersson, "Investigation of high power impulse magnetron sputtering pretreated interfaces for adhesion enhancement of hard coatings on steel," *Surf. Coatings Technol.*, vol. 200, no. 22–23 SPEC. ISS., pp. 6495–6499, 2006.
- [127] I. Encyclopedia Britannica, "Bragg law. Crystals." [Online]. Available: <https://www.britannica.com/science/Bragg-law>.
- [128] I. SlidePlayer, "X-Ray diffraction analysis." [Online]. Available: <http://slideplayer.com/>.
- [129] The State University of New York at Oswego, "online textbook." [Online]. Available: <https://cellularphysiology.wikispaces.com/>.
- [130] The University of Glasgow. Imaging Spectroscopy and Analysis Centre, "Scanning Electron Microscopy (SEM)." [Online]. Available: <https://www.gla.ac.uk/>.
- [131] canadian centre for welding and joining, "Scanning Electron Microscopy and Energy Dispersion Spectroscopy." [Online]. Available: <https://sites.ualberta.ca/~ccwj/>.
- [132] LinkedIn Corporation, "X-ray photoelectron spectroscopy." [Online]. Available: <https://www.slideshare.net/>.
- [133] "X-ray photoelectron spectroscopy." [Online]. Available: <https://www.ifw-dresden.de/institutes/ikm/research-teams-and-topics/micro-and-nanostructures/available-methods/xps/>.
- [134] A. Ház, M. Jablonský, A. Orságová, and I. Šurina, "Determination of Temperature Regions," in *4th International Conference Renewable Energy Sources 2013*, 2013, pp. 1–6.
- [135] European standard, "ISO 1071-335: Advanced technical ceramics - Methods of test for ceramic coatings - Determination of adhesion and other mechanical failure modes by a scratch test." 2005.
- [136] I. Rotaru, B. Istrate, M. Benchea, A. Tufescu, and D. Olaru, "Mechanical and structural characteristics of p ( HEMA ) hydrogel for lumbar disc prosthesis," *Teh. - New Technol. Prod. Mach. Manuf. Technol.*, no. August 2016, pp. 112–119, 2013.
- [137] I. Paul N. Gardner Company, "Progressive Load Scratch Test." [Online]. Available: <https://www.gardco.com/pages/adhesion/fischerscope.cfm>.

- [138] C. Wagner, "Theoretical Analysis of the Diffusion Processes Determining the Oxidation Rate of Alloys," *Electrochem. Soc. J.*, vol. 99, p. 369, 1952.
- [139] E. Godlewska, M. Mitoraj, and J. Morgiel, "Reaction and diffusion phenomena upon oxidation of a ( $\gamma + \alpha_2$ ) TiAlNb alloy in air," *Mater. High Temp.*, vol. 26, no. 1, pp. 99–103, 2009.
- [140] K. Przybylski, J. Prazuch, T. Brylewski, and E. Durda, "High temperature oxidation behaviour of TiAl8Nb alloy," *Arch. Metall. Mater.*, vol. 58, no. 2, pp. 477–480, 2013.
- [141] H. ren JIANG *et al.*, "Effects of Nb and Si on high temperature oxidation of TiAl," *Trans. Nonferrous Met. Soc. China (English Ed.)*, vol. 18, pp. 512–517, 2008.
- [142] P. Panjan, B. Navinsek, M. Cekada, and A. Zalar, "Oxidation behavior of TiAlN coating sputtered at low temperature," *Vacuum*, vol. 53, pp. 127–131, 1999.
- [143] C. M. Koller, R. Hollerwerger, R. Rauchbauer, P. Polcik, J. Paulitsch, and P. H. Mayrhofer, "Conference Paper of 18th Plansee Seminar," in *Thermal stability and oxidation resistance of TiAlN/TaAlN multilayer coating*.
- [144] L. Chen, J. Paulitsch, Y. Du, and P. H. Mayrhofer, "Thermal stability and oxidation resistance of Ti–Al–N coatings," *Surf. Coat. Technol.*, vol. 206, pp. 2954–2960, 2012.
- [145] S. M. Ha, M. H. Park, and S. H. Kim, "Magnetron sputtering of TiAlN films for inkjet printhead resistors," *J. Ceram. Process. Res.*, vol. 13, pp. 16–21, 2012.
- [146] T. Ikeda and H. Satoh, "Phase formation and characterization of hard coatings in the Ti–Al–N system prepared by the cathodic arc ion plating method," *Thin Solid Films*, vol. 195, pp. 99–110, 1991.
- [147] S. Inamura, K. Nobugai, and F. Kanamaru, "The preparation of NaCl-type Ti<sub>1-x</sub>Al<sub>x</sub>N solid solution," *J. Solid State Chem.*, vol. 68, pp. 124–127, 1987.
- [148] A. P. Ehiasarian, "High-power impulse magnetron sputtering and its applications," *Pure Appl. Chem.*, vol. 82, pp. 1247–1258, 2010.
- [149] R. Ananthakumar, B. Subramanian, A. Kobayashi, and M. Jayachandran, "Electrochemical corrosion and materials properties of reactively sputtered TiN/TiAlN multilayer coatings," *Ceram. Int.*, vol. 38, pp. 477–485, 2012.

- [150] J. T. Chen *et al.*, “Characterization and temperature controlling property of TiAlN coatings deposited by reactive magnetron co-sputtering,” *J. Alloy. Compd.*, vol. 472, pp. 91–96, 2009.
- [151] A. Rizzo *et al.*, “Improved properties of TiAlN coatings through the multilayer structure,” *Surf. Coat. Technol.*, vol. 235, pp. 475–483, 2013.
- [152] M. C. Biesinger, L. W. M. Lau, A. R. Gerson, and R. S. C. Smart, “Resolving surface chemical states in XPS analysis of first row transition metals, oxides and hydroxides: Sc, Ti, V, Cu and Zn,” *Appl. Surf. Sci.*, vol. 257, pp. 887–898, 2010.
- [153] A. Rizzo *et al.*, “Surface & Coatings Technology Improved properties of TiAlN coatings through the multilayer structure,” *Surf. Coat. Technol.*, vol. 235, pp. 475–483, 2013.
- [154] G. Lu, S. L. Bernasek, and J. Schwartz, “Oxidation of a polycrystalline titanium surface by oxygen and water,” *Surf. Sci.*, vol. 458, pp. 80–90, 2000.
- [155] Y. Fu, H. Du, S. Zhang, and W. Huang, “XPS characterization of surface and interfacial structure of sputtered TiNi films on Si substrate,” *Mater. Sci. Eng. A*, vol. 403, pp. 25–31, 2005.
- [156] J. D. Sunderkötter *et al.*, “The high-temperature oxidation behaviour of Ti-47Al-2Cr-0.2Si and Ti-48Al-2Cr-2Nb compared with Ti-48Al-2Cr,” *Intermetallics*, vol. 5, pp. 525–534, 1997.
- [157] V. A. C. Haanappel, J. D. Sunderkötter, and M. F. Stroosnijder, “The isothermal and cyclic high temperature oxidation behaviour of Ti-48Al-2Mn-2Nb compared with Ti-48Al-2Cr-2Nb and Ti-48Al-2Cr,” *Intermetallics*, vol. 7, pp. 529–541, 1999.
- [158] N. C. Tompkins and H. G. Saha, “Titanium nitride oxidation chemistry: An x-ray photoelectron spectroscopy study,” *J. Appl. Phys.*, vol. 72, pp. 3072–3079, 1992.
- [159] D. Jaeger and J. Patscheider, “A complete and self-consistent evaluation of XPS spectra of TiN,” *J. Electron. Spectrosc. Relat. Phenom.*, vol. 185, pp. 523–534, 2012.
- [160] M. D. Banus, T. B. Reed, and A. J. Strauss, “Electrical and magnetic properties of TiO and VO,” *Phys. Rev. Lett. B*, vol. 5, pp. 2775–2784, 1972.
- [161] “XPS database. Scientific Ionbeam.”

- [162] M. Thomas *et al.*, “Effects of exposure at 700 °C on RT tensile properties in a PM  $\gamma$ -TiAl alloy,” *Intermetallics*, vol. 14, pp. 1143–1150, 2006.
- [163] F. Pedrix, M.-F. Trichet, J.-L. Bonnetien, M. Cornet, and J. Bigot, “Influence of nitrogen on the microstructure and mechanical properties of Ti-48Al alloy,” *Intermetallics*, vol. 9, pp. 147–155, 2001.
- [164] T. Kawabata, M. Tadano, and O. Izumi, “Effect of carbon and nitrogen on mechanical properties of Ti-Al alloys,” *ISIJ Int.*, vol. 31, pp. 1161–1167, 1991.
- [165] “XPS simplified.” [Online]. Available: <http://xpssimplified.com/>.
- [166] A. V. Naumkin, A. Kraut-Vass, S. W. Gaarenstroom, and C. J. Powell, “NIST X-ray Photoelectron Spectroscopy Database,” *The U.S. Secretary of Commerce on behalf of the United States of America*, 2012. [Online]. Available: <https://srdata.nist.gov/xps/XPSDetailPage.aspx?AllDataNo=31687>.
- [167] J. A. Wilks and J. A. Kelber, “Nitridation of organo-silicate glass: A self-limiting process for PVD Ta<sub>1+x</sub>N/Ta barrier formation,” *Appl. Surf. Sci.*, vol. 255, pp. 9543–9547, 2009.
- [168] E. Atanassova, G. Tyuliev, A. Paskaleva, D. Spassov, and K. Kostov, “XPS study of N<sub>2</sub> annealing effect on thermal Ta<sub>2</sub>O<sub>5</sub> layers on Si,” *Appl. Surf. Sci.*, vol. 225, pp. 86–99, 2004.
- [169] K. Sasaki, A. Noya, and T. Umezawa, “Stoichiometry of Ta – N Film and Its Application for Diffusion Barrier in the Al<sub>3</sub>Ta / Ta – N / Si Contact System,” *japanese J. Appl. Phys.*, vol. 29, no. no 6, pp. 1043–1047, 1990.
- [170] X. Zhao, N. P. Magtoto, and J. A. Kelber, “Chemical vapor deposition of tantalum nitride with tert -butylimino tris ( diethylamino ) tantalum and atomic hydrogen,” *Thin Solid Films*, vol. 478, pp. 188–195, 2005.
- [171] X. Yu, Z. Li, J. Liu, and P. Hu, “Ta-O-C chemical bond enhancing charge separation between Ta<sup>4+</sup> doped Ta<sub>2</sub>O<sub>5</sub> quantum dots and cotton-like g-C<sub>3</sub>N<sub>4</sub>,” *Appl. Catal. B, Environ.*, vol. 205, pp. 271–280, 2017.
- [172] A. Arranz and C. Palacio, “Composition of tantalum nitride thin films grown by low-energy nitrogen implantation : a factor analysis study of the Ta 4 f XPS core level,” *Physics, Appl.*, vol. A. 81, pp. 1405–1410, 2005.
- [173] M. . H. Tsai, S. C. Sun, T. H. Chiu, C. . E. Tsai, and S. H. Chuang, “Metalorganic chemical vapor deposition of tantalum nitride by

- tertbutylimidotris ( diethylamido ) tantalum for advanced metallization Metalorganic chemical vapor deposition of tantalum nitride by tertbutylimidotris ( diethylamido ) tantalum for advanced m,” *appl. phys. lett.*, vol. 67, no. 8, pp. 1128–1130, 1995.
- [174] H. Kawasaki, K. Doi, J. Namba, Y. Suda, T. Ohshima, and K. Ebihara, “Characterization of Tantalum Nitride Thin Films Fabricated by Pulsed Nd : YAG Laser Deposition Method,” *J. Appl. Phys.*, vol. 40, no. 4A, pp. 2391–2394, 2001.

